X- 71004

FLIGHT MECHANICS/ESTIMATION THEORY SYMPOSIUM

AUGUST 1975

GSFC —— **GODDARD SPACE FLIGHT CENTER** ——
GREENBELT, MARYLAND

FLIGHT MECHANICS/ESTIMATION
THEORY SYMPOSIUM

Compiled by

Carmelo E. Velez
Systems Development and
Analysis Branch

August 1975

GODDARD SPACE FLIGHT CENTER
Greenbelt, Maryland

The requirement for the use of the International System of Units (SI) has been waived for this document under the authority of NPD 2220.4, paragraph 5.d.

EDITOR'S NOTE

The papers presented herein have been derived primarily from transcripts taken at the Flight Mechanics/Estimation Theory Symposium held October 15 to 16, 1974, and April 15 to 16, 1975, at Goddard Space Flight Center. In order to achieve a uniform format, a considerable amount of editing was needed and in the interest of time, only a subset of all the papers presented were prepared for this publication. Abstracts of all the papers are included however, and attempts will be made to improve the handling of conference material so that in future proceedings all papers presented will be published.

CONTENTS

CONTENTS (continued)

CONTENTS (continued)

CONTENTS (continued)

THE DETERMINATION OF ORBITS USING
PICARD ITERATION

Rajendra Prasad Mikkilineni and Terry Feagin
University of Tennessee Space Institute
Tullahoma, Tennessee

The topic of this presentation is the determination of orbits using Picard iteration, which is a direct extension of the classical method of Picard that has been used in finding approximate solutions of nonlinear differential equations for a variety of problems. The application of the Picard method of successive approximations to the initial value and the two-point boundary value problems is given below.

The initial value problem,

$$\dot{z} = F(z, t)$$

$$z(t_1) = c, \qquad\qquad n = 1, 2, \ldots$$

is solved by means of the iterative scheme,

$$\dot{z}_n = F(z_{n-1}, t)$$

$$z_n(t_1) = c,$$

whereby the n*th* approximation to the state vector z is computed from the $(n-1)$ approximation (beginning with some initial approximation, $z_0(t)$). The computation involves performing a simple integration or quadrature at each stage of the iterative process. The constant of integration is chosen such that each iterate satisfies the initial condition, $z(t_1) = c$.

Similarly, the two-point boundary value problem,

$$\dot{z} = F(z, t)$$

$$g(z(t_1), z(t_2)) = 0,$$

is solved by means of the iterative scheme,

$$\dot{z}_n = F(z_{n-1}, t)$$

$$g(z_n(t_1), z_n(t_2)) = 0, \qquad\qquad n = 1, 2, \ldots$$

where g denotes certain constraints or boundary conditions that must be satisfied by the solution at t_1 and t_2.

This paper presents an investigation of the suitability of this type of iterative scheme for the problem of estimating orbits. In the estimation problem, we again have to solve the differential equation for the state. However, we are now given a set of imprecise observations, $y(t_i) \; {}_{i=1}^m$, which are, in general, nonlinear functions of the state. The problem is to find a $z(t)$ which comes close (in some sense) to satisfying the observations. The estimation problem can thus be written as

$$\dot{z} = F(z, t)$$

subject to the condition that $z(t)$ minimizes some function Q, where

$$Q = Q[z(t_1), z(t_2), \ldots, z(t_m), y(t_1), y(t_2), \ldots, y(t_m)].$$

For instance, Q could be the sum of the squares of the residuals (the residual being the difference between the observed and the computed values of the observations). Again, the iteration is set up.

$$\dot{z}_n = F(z_{n-1}, t),$$

now choosing the constant of integration for $z_n(t)$ such that

$$Q[z_n(t_1), z_n(t_2), \ldots, z_n(t_m), y(t_1), \ldots, y(t_m)]$$

is minimized. As before, each stage of the iteration requires that a quadrature is performed. In order to perform the integration, we have chosen to approximate the right-hand side, $F(z_{n-1}, t)$, by a series of Chebyshev polynomials, $T_j(\tau)$, and to integrate term-by-term. Thus, the approximation

$$F(z_{n-1}, t) \cong \sum_{j=0}^{N}{}' \; b_j T_j(\tau)$$

is made where $\tau = 1 - 2t/(t_m - t_1)$ is normalized time. The coefficients of the series are determined readily using the orthogonality properties from the relation

$$b_j = \sum_{k=0}^{N}{}'' \; F(\tau_k) T_j(\tau_k)$$

where $\tau j = \cos(j\pi/N)$. The integration can be performed by manipulating these coefficients, giving

$$z_n \cong \sum_{j=0}^{N}{}' \; a_j T_j(\tau)$$

2

where

$$a_j = (b_{j-1} - b_{j+1})/2j \qquad \text{for } j = 1, 2, \dots N$$

and a_0 = the arbitrary constant of integration that is determined from the requirement that Q be minimized.

We will now consider the application of this technique to an orbit estimation problem, namely, the determination of the orbit of an earth satellite from observations of the range and range rate by several tracking stations.

There are no external forces except the gravity field of the earth. The equations of motion for the satellite are written as a set of six, first-order equations for the six state variables: x, y, z, u, v, and w. For instance, $R_s(t_i)$ represents the range observed at t_i from the fifth tracking station, and range rate is the time derivative of the range denoted by $\dot{R}_s(t_i)$; these are given. For the computer simulation presented here, we have taken the nominal values of the range and the range rate and added random noise. The standard deviations assumed are 30 meters in range and about 50 cm per second in range rate.

For this particular problem, the Q function should be considered. This is the sum of the weighted squares of the residuals:

$$Q = \sum_{s=1}^{s} \sum_{i=1}^{m} [R_s(t_i) - g_s(t_i)]^2 \, W_{si}$$

$$+ \sum_{s=1}^{s_1} \sum_{i=1}^{m_1} [\dot{R}_s(t_i) - \dot{g}_s(t_i)]^2 \, W_{si}$$

where

$$\begin{aligned}
g_s(t_i) = \big\{ &[x(t_i) - x_s(t_i)]^2 \\
+ &[y(t_i) - y_s(t_i)]^2 \\
+ &[z(t_i) - z_s(t_i)]^2 \big\}^{1/2}
\end{aligned}$$

and

$x_s(t_i), y_s(t_i), z_s(t_i)$ = the fifth station coordinates at t_i,

$R_s(t_i)$ = the range from the particular tracking station,

g_s = the range computed using the present iterate,

$\dot{R}_s(t_i)$ = observed range rate, and

W_{si} = weight for the particular observation.

We can see that g_s is the function of the state at t_i, and x_s represents the coordinates of the station itself. The minimization of this function Q with respect to the integration constant is carried out using Newton's method.

Table 1 provides the data for the three tracking stations we have assumed. The longitude and latitude, number of observations, and the total interval considered—about 1500 seconds—are listed. The elliptic orbit considered has an eccentricity of 0.0557, with a semimajor axis of about 7178 km. This corresponds to a perigee at 400 km altitude, an apogee at 1200 km altitude, and an inclination of 20° to the equatorial plane.

Table 1
Station and Orbit Data

Parameters	Station		
	1	2	3
Latitude (deg)	18.0	12.0	10.0
Longitude (deg)	0.0	28.0	14.0
Number of Observations	10	20	30
Interval Between Observations (s)	168.0	79.0	52.0
Semimajor Axis (km)	a = 7178.145		
Eccentricity	e = 0.0557		
Inclination (deg)	i = 20.0		
Longitude of Ascending Node	Ω = 0.0		
Argument of Perigee	ω = 0.0		

Some of the results obtained are depicted in figure 1, which shows the error as a function of time for different iterations. The initial guess is off by about 70 km from the true solution, and with two iterations the error is brought down to something like 15 km.

In order to see the convergence properly, the log of absolute error is plotted as a function of the iteration number in figure 2. The error is plotted for several points along the trajectory. The first point is T = 0, and the last point is T = 1513.1. It is seen that the convergence is linear as was expected because of its relation to the classical Picard method.

One of the disadvantages of this method is that the convergence is obtained only for arcs of length less than about one-third of a revolution. Another problem is that of developing a procedure for connecting two successive arcs.

4
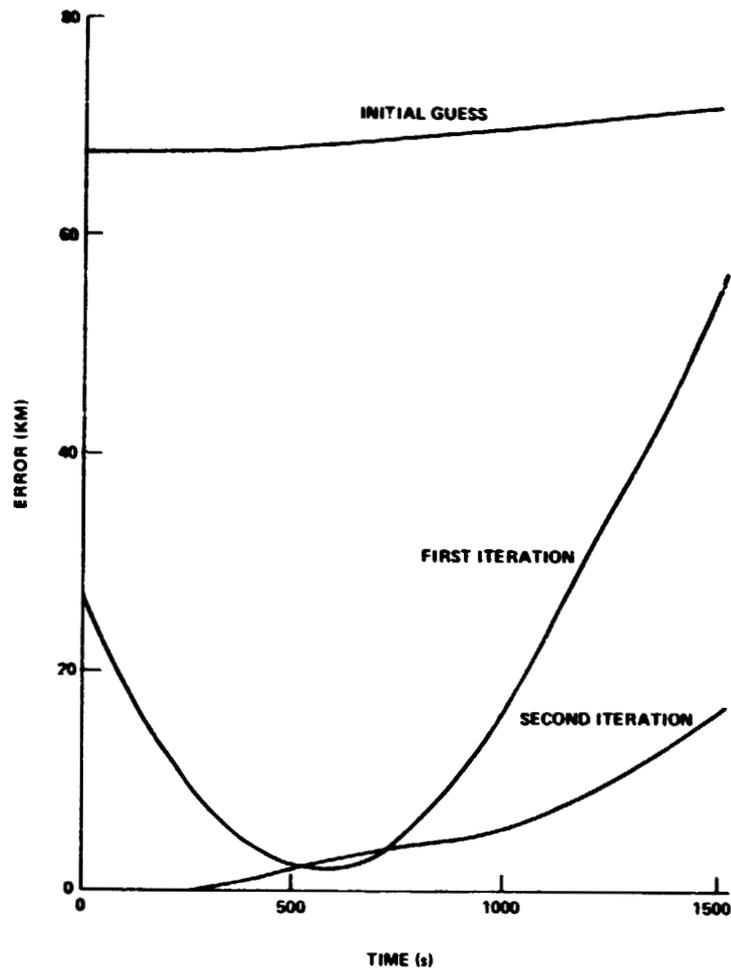
Figure 1. Error as a function of time for different iterations (elliptic orbit).

On the other hand, there are many advantages: For example, the method is quite simple and does not require the linear perturbation equations. The solution is in the form of a polynomial and is convenient to store. There is no interpolation required, should the solution be needed at some intermediate point. The error in representing this by a polynomial can, of course, be estimated by observing the last few terms of the polynomial. Also, the method is not sensitive to a poor initial guess. As we have seen here, the initial guess was off by about 70 km and even then the process will converge without difficulty.

The question is, is this method really more efficient than a more traditional approach to solving a problem? Actually, we have not compared it with the existing methods. However, we have some estimates on the time taken for this particular problem—it takes about 30 seconds on the IBM 360/65.
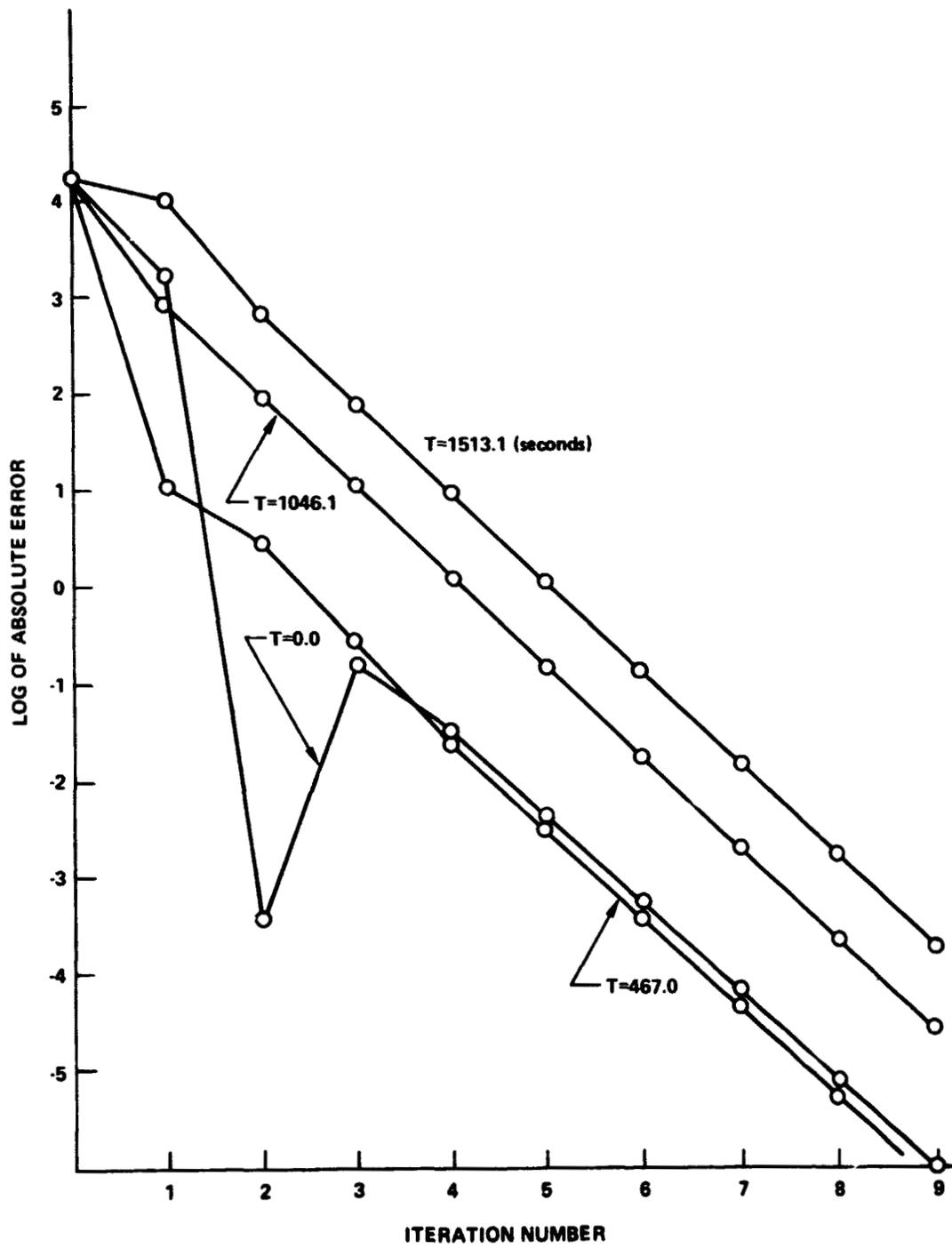
Figure 2. Convergence of the method for an elliptic orbit.

A FINITE ELEMENT GRAVITY FIELD?

J. L. Junkins
University of Virginia
Charlottesville, Virginia

The paper details an approach for constructing a globally valid, piecewise continuous family of locally valid potential functions. The thesis put forth here is that the higher frequency terms of the geopotential can be more efficiently computed from such locally convergent approximations (typically three variable power series of order less than 5) than from any globally convergent gravity representation. This approach appears to be a step in the direction of voiding the recent trend that the better model we have of the geopotential, the more expensive it is to integrate orbits with it! Numerical experiments conducted thus far confirm the validity of the approach and that acceleration errors of 0 (10^{-10} km/s^2) are achievable. The trade-offs involved in selecting the finite element shape and size, and the order of the local approximations versus resulting accuracy, computational speed, and storage requirements are currently under study.

MEAN RATES OF THE ORBITAL ELEMENTS OF A SATELLITE PERTURBED BY A LENS SHAPED MASCON

M. I. Ananda
Jet Propulsion Laboratories
Pasadena, California

A set of mean orbital rates are computed for a satellite perturbed by a lens shaped mascon. A disturbing potential in terms of the orbital elements of the satellite and the mascon parameters is developed. The partial derivatives of the potential with respect to the orbital elements are formed. These partials are averaged over the period of the satellite orbit to eliminate the short periodic terms. The averaged partials are substituted into the variation of parameters equations to give the mean orbital rates. In the limiting case, when the radius of the lens shaped mascon reaches zero the mean orbital rate due to a point mass is obtained. The orbital rates developed by the method described here are compared against the rates obtained by numerical differencing. The method developed here is used to reduce the Apollo-15 and -16 subsatellite data for lunar farside gravity determination.

ON THE FORMULATION OF THE GRAVITATIONAL
POTENTIAL IN TERMS OF EQUINOCTIAL VARIABLES*

Paul J. Cefola
Computer Sciences Corporation
Silver Spring, Maryland

One year ago I presented a paper at this symposium that described some work we had been doing with the method of averaging. One of the aspects of that paper had to do with a particular choice of nonsingular variables that were called equinoctial variables. In particular, we investigated analytical averaging techniques in the equinoctial coordinate frame. Some very good results were obtained, and we developed some expressions for fairly low-order perturbations. We developed explicit expressions for the disturbing potential for the zonal harmonics up to J_4 and the third-body harmonics up to $(a/R_3)^6$, where a is the semimajor axis of the orbit and R_3 is the distance to the third body.

After that we reconsidered the problem and decided that one of the shortcomings of that work was the lack of general expressions for the disturbing potential. This lack was a problem for several reasons: First, serious problems were encountered in extending the results to higher degree terms. The need to extend the results occurs, for example, in mission analysis, where the problem of including the effect of one higher degree third-body term or including the effect of an additional zonal harmonic occurs frequently. Second, having explicit expressions for each term made software development complicated because, for each new term, additional software was required, and there was the possibility of errors at each step.

These are some of the reasons why it was desirable to develop general results for the disturbing potential in this coordinate frame, and that is what I propose to discuss now. We are going to consider the gravitational potential and will use several special functions—the Legendre and associated Legendre polynomials and the Q_{nm}, which are called the derived Legendre functions. Recently there has been a fair amount of interest in these functions in the context of the gravitational potential. (For example, Pines, 1973.) The various disturbing potential expansions are listed below.

Disturbing Function Expansions

Perturbation	n*th* Term

Third-body harmonics

$$\frac{\mu_3}{R_3} \left(\frac{a}{R_3}\right)^n \left(\frac{r}{a}\right)^n \, P_n(\cos\psi)$$

Zonal harmonics

$$-J_n \frac{\mu}{a} \left(\frac{R_e}{a}\right)^n \left(\frac{a}{r}\right)^{n+1} P_n(\cos\psi)$$

Arbitrary geopotential term (n, m)

$$\frac{\mu}{a} \left(\frac{R_e}{a}\right)^n \left(\frac{a}{r}\right)^{n+1} P_{nm}(\cos\psi)$$

$$(C_{nm}\cos m\lambda + S_{nm}\sin m\lambda)$$

$$\lambda = \alpha - \theta$$

Here we are considering the third-body harmonics and the zonal harmonics, in particular. (It was originally planned to have some expressions for the tesseral case, but they are still in the process of being checked.) We have introduced the semimajor axis into these expressions, even though it is not required, because we are going to average these expressions and want to use existing results in two-body mechanics. For the third-body harmonics, the ψ angle will be the angle between the vector to the satellite and the vector to the third body. In the case of zonal harmonics, ψ will be the colatitude.

In averaging these potentials, a two-step process is used. The purpose of step 1 is to obtain expressions for the Legendre functions in terms of equinoctial orbital elements. In step 2, the averaging is performed.

One of the important questions in deriving potentials in terms of classical or equinoctial elements is how to get the fast variable motion into the potential. There are several different options, and they have a direct effect upon the amount of manipulation and on the complexity of the final results. Also related to these options is the level of accuracy that can be achieved. For third-body harmonics, there are really two options: We can use the mean anomaly for both the satellite and for the third body and end up with a very general potential. This was done by Kaula in 1966. Or we can use direction cosines (relative to an orbital reference frame) to get the location of the third body. If direction cosines are used, there is not quite the flexibility in modeling that is had with the Kaula approach, but the expressions are a lot more compact. In our work with the method of averaging, the use of the direction cosines is quite appropriate.

For zonal harmonics, we bring in the motion of the fast variable by using the orbital true longitude. For the arbitrary geopotential term, by which is meant tesserals, there are two options that are somewhat related to the two options that exist for third-body harmonics: We can use the mean variable for the satellite and Greenwich sidereal time, which is particularly appropriate for the study of resonance cases; or we can use the true longitude of the

10

satellite and Greenwich sidereal time, which appears to be most appropriate if we want to assume that the central body rotational angle is fixed during the averaging. Such a potential might be particularly appropriate for lunar satellites.

Several expressions for cos ψ are listed below. These correspond to various attempts to develop the third-body potential. The first expression listed for cos ψ in terms of right ascension and declination of the satellite and the third body was used by Kaula. He then used the addition theorem and the definition of the inclination function to obtain expressions for the Legendre polynomials in terms of the classical elements. These results have great generality because we can impose all types of resonance constraints on them, yet they are also very complex.

<center>Expressions for Cosine ψ</center>

$$\cos \psi = \alpha \cos v + \beta \sin v$$
$$\alpha = \hat{R}_3 \cdot \hat{P}, \beta = \hat{R}_3 \cdot \hat{Q}$$

$$\cos \psi = \alpha \cos u + \beta \sin u$$
$$u = v + \omega, \alpha = \hat{R}_3 \cdot \hat{N}, \beta = \hat{R}_3 \cdot \hat{M}$$

$$\cos \psi = \alpha \cos L + \beta \sin L$$
$$L = v + \omega + \Omega, \alpha = \hat{R}_3 \cdot \hat{f}, \beta = \hat{R}_3 \cdot \hat{g}$$

More recent work in third-body perturbations uses the concept of expressing third-body motion by direction cosines relative to an orbital coordinate frame. Kaufman in 1970 and Lorell and Liu in 1971, in particular, worked with the apsidal coordinate frame. Subsequently, Kozai worked with a coordinate frame where the orbital x-axis was along the nodal crossing and the third axis was in the orbit plane. Essentially, he used the argument of latitude as his fast variable. At about the same time, we used the true longitude as our fast variable and also used the direction cosines of the third body relative to the equinoctial coordinate frame (FGW), in which the x-axis points at the origin of the latitudes.

One of the problems involved in working with Legendre polynomials and, in particular, with the direction cosines formulation, was that there did not appear to be an addition theorem for that case. In most of the work using that approach, the basic recursion relationships have been used to generate the Legendre functions. There have not been general formulas for the required Legendre functions with the argument $\alpha \cos L + \beta \sin L$. This is the same problem I reported on a year ago. Recently, we took another look at the addition theorem, looked at the expressions in terms of the direction cosines, and found that we could reformulate the problem in such a way that the addition theorem still applied; the steps in that derivation are shown in equations 1 and 2.

First, we introduce a phase angle, L', and define the trigonometric functions—cos L' and sin L'—to fit the form of the addition theorem. Then α, δ, α_3, and δ_3 must be defined.

$$\alpha = L \qquad\qquad\qquad \cos \delta = 1$$
$$\alpha_3 = L' \qquad\qquad\qquad \sin \delta = 0 \qquad\qquad (1)$$
$$\cos \delta_3 = \sqrt{\alpha^2 + \beta^2} \qquad\qquad \sin \delta_3 = \sqrt{1 - \alpha^2 - \beta^2} = \gamma$$

Here those angles are treated as arbitrary quantities. By substituting equation 1 into the addition theorem:

$$P_n (\cos \psi) = P_n(0) \, P_n(\gamma) + 2 \sum_{m=1}^{n} \frac{(n-m)!}{(n+m)!} P_{nm}(0) \, P_{nm}(\gamma) \cos m (L - L'). \qquad (2)$$

In equation 2, γ is the direction cosine of the third body relative to the vector normal to the orbit plane.

If we define some C_m and S_m polynomials in α and β similar to the w⌐ ˙ Pines did in 1973, the addition theorem can be simplified. The final result is

$$P_n(\cos \psi) = P_n(0) \, P_n(\gamma) + 2 \sum_{m=1}^{n} \frac{(n-m)!}{(n+m)!} \, P_{nm}(0) \, Q_{nm}(\gamma) \, [C_m(\alpha,\beta) \cos m L + S_m(\alpha,\beta) \sin m L] \quad (3)$$

where

$$C_m(\alpha,\beta) = \mathrm{Re} \, (\alpha + j\beta)^m \qquad\qquad (4)$$

and

$$S_m(\alpha,\beta) = I_m (\alpha + j\beta)^m \qquad\qquad (5)$$

Because $P_{nm} = 0$ for $n - m$ equal to an odd integer, Q_{nm} gives even powers of the γ function. It can be expressed quite well in terms of a polynomial in α and β. Again, it is finite, so we have a general form, a modified addition theorem, that is useful in this case.

To give an idea of what these polynomials look like, the first one that appears in the third-body perturbation is evaluated as follows:

$$P_2(\alpha \cos L + \beta \sin L) = -\frac{1}{4} \, (3\gamma^2 - 1) + \frac{3}{4} \, [(\alpha^2 - \beta^2) \cos 2L + 2\alpha\beta \sin 2L]$$
$$= \frac{1}{2} \left[\frac{3}{2} \, (\alpha^2 + \beta^2) + \frac{3}{2} \, (\alpha^2 - \beta^2) \cos 2L + 3\alpha\beta \sin 2L - 1 \right]. \qquad (6)$$

This checks against the results that were presented in our paper a year ago. It has been checked for several cases and gives exactly the results obtained previously through very long and arduous manipulations; in fact, some errors were found in those previous results through comparison with the general formula.

Another major point of this paper is to emphasize the computation of the potential by using the recursion formula, and below are listed the recursion formulas (equations 7 to 10) that are appropriate to the computation of P_m ($\alpha \cos L + \beta \sin L$).

$$(n + 1) P_{n+1}(\gamma) \quad = \quad (2n + 1)\gamma P_n(\gamma) - n P_{n-1}(\gamma) \tag{7}$$

$$(n - m) Q_{nm}(\gamma) \quad = \quad (2n - 1)\gamma Q_{n-1,m}(\gamma) - (m + n - 1) Q_{n-2,m}(\gamma) \tag{8}$$

$$C_{m+1}(\alpha,\beta) \quad = \quad \alpha C_m(\alpha,\beta) - \beta S_m(\alpha,\beta) \tag{9}$$

$$S_{m+1}(\alpha,\beta) \quad = \quad \beta C_m(\alpha,\beta) + \alpha S_m(\alpha,\beta) \tag{10}$$

Equation 7 is the standard recursion for the Legendre polynomials, and equation 8 is the recursion for the derived Legendre functions (this is given in Ananda and Broucke, 1973, and Pines, 1973). Equations 9 and 10 are the recursions for the C_m and S_m polynomials, respectively.

The final formula for the averaged potential also has the same C_m and S_m polynomials, with k and h as the argument, and the same recursions will still apply. We are interested in obtaining averaged potentials, and we want to average with respect to a time-oriented variable, so we average with respect to the mean longitude. In equation 11, we take the standard formula for the average of $(r/a)^n \cos m\, v$ and recast it in terms of the true longitude:

$$\frac{1}{2\pi} \int_0^{2\pi} \left(\frac{r}{a}\right)^n e^{imL} d\lambda$$

$$= \left(-\frac{1}{2}\right)^m \left(\frac{n+m+1}{m}\right) (k + jh)^m F\left(\frac{m-n-1}{2}, \frac{m-n}{2}, m+1, h^2+k^2\right). \tag{11}$$

It should be noted that the formulas are a hypergeometric series and that the polynomial previously referred to as appearing in these integrals has the argument $k + jh$. The symbol j is the square root of -1.

We wanted to obtain a recursion formula for computing the right-hand sides of these integrals, and it happens that one has already been derived and is presented in Cook's paper on the PROD program (1973). The formula for these integrals is as follows:

$$\frac{1}{2\pi} \int_0^{2\pi} \left(\frac{r}{a}\right)^n e^{imL} d\lambda = \left(-\frac{1}{2}\right)^m \left(\frac{n+m+1}{m}\right) (k + ih)^m B^m_{m+2} (h^2+k^2) \tag{12}$$

where

$$B^\varrho_\varrho = 0,\ B^{\varrho-1} = 1,\ B^{\bar{k}-1}_\varrho = B^{\bar{k}}_\varrho + \frac{(\varrho+\bar{k})(\varrho-\bar{k}-1)}{4\bar{k}(\bar{k}+1)} (h^2+k^2) B^{\bar{k}+1}_\varrho$$

So along with $P_n (\alpha \cos L + \beta \sin L)$, the hypogeometric series and the eccentricity polynomials can be reached recursively.

The following is a result for the nth term in the third-body potential expressed in terms of equinoctial elements and the direction cosines:

$$\frac{\mu_3}{R_3} \left(\frac{a}{R_3} \right)^n P_n(0) P_n (\gamma) B_{n+2}^0 (h^2 + k^2)$$

$$+ 2 \frac{\mu_3}{R_3} \left(\frac{a}{R_3} \right)^n \sum_{m=1}^{n} V_{n,m} B_{n+2}^m (h^2 + k^2) Q_{n,m} (\gamma) [C_m (\alpha,\beta) C_m (k,h) + S_m (\alpha,\beta) S_m (k,h)]$$

where

$$V_{n,m} = \left(- \frac{1}{2} \right)^m P_{n,m} (0) \frac{(n-m)!}{(n+m)!} \left(\frac{n+m+1}{m} \right) . \tag{13}$$

All of the terms in equation 13 can be obtained recursively. In writing a program, we would probably initially compute the coefficients $V_{n,m}$ and then store them as data at the beginning of the program. We do not obtain all of the terms indicated in the equation. We get approximately $(n/2)$ terms in that summation because some of the associated Legendre functions with zero argument are zero, depending on whether $n - m$ is an even or odd number. We have a finite, closed-form expression, and we verified several of the results presented a year ago with this formula. The next step is to show how the same analysis is done for zonal harmonics. The potential due to the nth zonal harmonic is

$$- J_n \frac{\mu}{a} \left(\frac{R_e}{a} \right)^n \left(\frac{a}{r} \right)^{n+1} P_n (\cos \psi) \tag{14}$$

where ψ is the colatitude. Cos ψ can be expressed in classical elements by

$$\cos \psi = \sin i \sin (v + \omega) . \tag{15}$$

In equation 15, i is the inclination and v is the true anomaly. We can express $\cos \psi$ quite well in terms of the equinoctial elements as is shown in the next equation.

$$\cos \psi = \frac{-2p}{1 + p^2 + q^2} \cos L + \frac{2q}{1 + p^2 + q^2} \sin L \tag{16}$$

In equation 16, p and q are equinoctial elements. If we assume auxiliary variables defined by

14

$$\alpha \equiv \frac{-2p}{1 + p^2 + q^2}$$

(17)

and

$$\beta \equiv \frac{2q}{1 + p^2 + q^2},$$

the argument of the Legendre function in equation 14 has the same form as it did in the third-body case, and we can use the addition theorem we derived previously for P_n ($\alpha \cos L + \beta \sin L$).

For averaging over the mean longitude, we have to somewhat modify our averaging formula. We could use the previous averaging formula with negative values of n, but that would result in an infinite series in the eccentricity, which can be seen by examining the hypogeometric series involved. Essentially, we made a quadratic transformation in the hypogeometric series, changed the arguments a little, introduced a variable x defined as $1/\sqrt{1 - h^2 - k^2}$, and found that we could get a finite series in the eccentricity and x for the required integrals:

$$\frac{1}{2\pi} \int_0^{2\pi} \left(\frac{a}{r}\right)^{n+1} e^{imL} \, d\lambda = \left(\frac{1}{2}\right)^m \binom{n-1}{m} x^{2n-1} (k + ih)^m B_n^m (h^2 + k^2). \quad (18)$$

We also use the same polynomials, the $P_{m,n}$ polynomials in this case, which can be used in computing the potential for both third-body and zonal effects. There will be another saving in computation if both effects are included.

Next we give a general expression for the potential due to a zonal harmonic, that is, the averaged potential in terms of the same eccentricity functions, derived Legendre functions, and the same α-β polynomials:

$$- J_n \left(\frac{\mu}{a}\right)\left(\frac{R_e}{a}\right)^n \quad P_n (0) P_n (\gamma) x^{2n-1} B_m^0 (h^2 + k^2)$$

(19)

$$-2J_n \left(\frac{\mu}{a}\right)\left(\frac{R_e}{a}\right)^n \sum_{m=1}^{n-1} W_{n,m} x^{2n-1} B_n^m (h^2 + k^2) Q_{n,m} (\gamma) [C_m (\alpha,\beta) C_m (k,h) + S_m (\alpha,\beta) S_m (k,h)]$$

where

$$W_{n,m} = \left(\frac{1}{2}\right)^m P_{n,m} (0) \frac{(n-m)!}{(n+m)!} \binom{n-1}{m}$$

Again, everything can be derived recursively; terms that are useful in the the third-body case are useful here, and terms that are useful for the lower order zonal harmonics can be used to

compute the higher order ones. Therefore, I suspect that a very efficient computation pro-
gram can be built using this formula, with the added advantage of having only one formula
rather than many to verify.

REFERENCES

Ananda, M. P. and R. Broucke, 1973, *Poisson Series Solutions for Oblateness Perturbations
of a Satellite*, Jet Propulsion Laboratory Technical Memorandum 391-432, April.

Cook, G. E., 1973, "Basic Theory for PROD, a Program for Computing the Develo   t
of Satellite Orbits," *Celestial Mechanics*, 7(3), April, pp. 301-314.

Kaula, W. M., 1966, *Theory of Satellite Geology*, Blaisdell Publishing Corp., Waltham, Mass.

Pines, S., 1973, "Uniform Representation of the Gravitational Potential and Its Derivatives,"
AIAA Journal, 11 (11), November, pp. 1508-1511.

SOME RECENT INVESTIGATIONS IN NUMERICAL AVERAGING

David Wexler

Aerospace Corporation

Los Angeles, California

Our interest in averaging techniques stems from a requirement to conduct large-scale mission planning exercises on a system of computers that gets overloaded whenever such a study arises. These studies have been conducted at Aerospace using a Cowell propagator simply because of the necessity for accuracy in a high drag environment. However, due to limited computer resources, a project has been initiated to develop a better method, which will involve using an existing algorithm or developing a new one.

This paper presents two topics, the first of which concerns a feasibility study that was conducted using two programs, MAESTRO and PECOS, to see if averaging could be accurate. The second topic concerns some continuing investigations and some new ideas, generally untested. It is assumed that the idea of averaging with respect to trajectory propagation is familiar to everyone so it will not be reviewed here.

The MAESTRO program, developed by Chauncey Uphoff and Dave Lutzky of Analytical Mechanics Associates, was obtained by Aerospace for a feasibility test. It was initially designed as an interplanetary mission analysis tool for the Radio Astronomy Explorer-2 (RAE-2) lunar orbiter. Several choices of variables and propagating techniques are available in MAESTRO. For instance, a Cowell integrator, an Encke integrator, and several variation-of-parameter techniques, including the numerical averaging of the Gaussian variation-of-parameter (VOP) equations, are available.

The forces in the program are given in the radial, circumferential, and polar directions. MAESTRO has a fairly simple exponential atmosphere and has a precision averaging startup, which means that osculating initial conditions in several choices of reference frames can be input and the program will automatically provide the initial mean state.

The Aerospace version of MAESTRO has been merged with a program called PECOS. PECOS, itself, is a test bed for orbit planning simulations. The interplanetary calculations were stripped out of MAESTRO and the force evaluations from PECOS are now used by both MAESTRO and PECOS.

The output can be plotted by an auxiliary pr g available at Aerospace. In particular, overlays of PECOS precision and MAESTRO averaging output can easily he accomplished for comparison purposes. Two versions of mean-to-osculating are used.

On output, the Kozai form is used, and within the averaging quadrature, the Iszak form is used. There is no particular reason for this order except for the program's historical development. Fortunately, Iszak is very good for use under the quadrature because it is nonsingular at low eccentricity.

With present program limitations, only certain parameter sets and integration types from MAESTRO are available. For instance, the Cowell integration is not available. Only two out of the original eight techniques are being used. They include the integration of a parameter set which is nonsingular at low eccentricity. This set is similar to, but not exactly the same as, the equinoctial elements. The averaging technique uses the same elements.

The initial conditions for the test case that were used for the feasibility study were chosen from typical orbits of interest to Aerospace. They were initially compiled for Terry Harter to run at GSFC on a test using the Goddard Trajectory Determination System (GTDS). At Aerospace they were run by Stan Navickas in the Mission Analysis Department with the MAESTRO/PECOS software.

Table 1 shows that the four cases here have perigees ranging from 67 to 92 n.m. and apogees ranging from 156 to 223 n.m. The inclinations are all between 90° and 110.5°. The lifetimes range from about 4.5 days to 2 months: case A-1 has a 2-month lifetime and case B-1 has a 4.5-day lifetime, and those are the two cases that will be discussed here.

Figures 1, 2, and 3 are time histories of elements for case A-1, which had approximately a 2-month lifetime. The computer runs were limited to 7 days because it is so expensive to run the Cowell integration in PECOS. This is the orbit which does the least of the four test cases.

Table 1
Initial Conditions for Four Test Cases

Case	Perigee H_p(n.m.)	Apogee H_A(n.m.)	Inclination (deg)	C_D A/W(ft^2/lb)
A1	92	156	96.43	0.0007295 (0.002099)
A2	85	161	94.55	0.0007295 (0.002099)
B1	67	207	96.57	0.0062981 (0.001286)
B2	69	223	110.5	0.0062981 (0.001286)

The semimajor axis is plotted in figure 1. The oscillating line is the output from the Cowell technique in PECOS, and the line down the center is the mean element output from MAESTRO. There has been no correction to put the short-period variations back on.

Figure 2 is the eccentricity from the same trajectory. Again the oscillating curve is the output from the Cowell integration translated into Kepler elements. Figure 3 is the argument of perigee. Figures 4, 5, and 6 are for case B-1, which dies in 4.5 days. The dark line down the center is the mean output from MAESTRO. It can be seen that the program tracks the elements all the way to the end of the lifetime.

Figure 6 is the argument of perigee, and, as expected, the envelope of the oscillations grows rapidly as it approaches the end of the lifetime and the eccentricity drops. The orbit becomes circular, so the argument of perigee begins to oscillate more and more wildly. But the mean argument of perigee is still being tracked and follows the center of the oscillation envelope.

Figures 7, 8, and 9 give the comparison between the Cowell integration and the corrected average propagation at about 4 days into the case having a 4.5-day lifetime. The orbit is generally tracked. The phasing and the magnitude have tracked quite well at the end of 4 days. I am very hesitant to interpret the small errors there, because we have a problem with the interpolator in PECOS/MAESTRO right now. The step sizes in the integration for the averaging process are 90 minutes, but the output is roughly every 2 minutes.

If the output of mean elements were plotted on a finer scale, it would be seen that the result has a small wiggle. This wiggle is probably due to the interpolator. There is some suspicion that the errors in the oscillating elements are due to that wiggle, but that is still a qualitative judgment. The important thing is that the orbit is being tracked.

We interpreted these plots as proof that the averaging technique does work. At this point, there had been no attempt whatsoever to make this program efficient. MAESTRO was simply merged into a larger system using some of the logic from that larger system, so timings from these runs were totally meaningless. Using the results proving the feasibility of the technique, we decided to go ahead and attempt to modify MAESTRO to make it a stand-alone version that would be efficient, using essentially the same logic that it has always had, but using a more accurate force model than it had when it was developed for GSFC. The modifications and developments which will go into this further study will be discussed now.

The purpose of the current investigation is to increase the accuracy and, if possible, to decrease the computation time; this will of course involve a compromise between the two. Currently, we are developing MAESTRO as a stand-alone version with modification for accuracy in a high drag environment, to run on the CDC 7600. The next step will be to replace the independent variable with the true anomaly and to remove the fast variable. Another concurrent activity, being handled by Dave Lutzky of Vector Sciences, is treating the short period effects within the averaging quadrature and for output with a Fourier expansion from which the coefficients of the harmonics are computed automatically and

19

numerically. This is work which was developed under funds from GSFC. The results will be inserted into MAESTRO to see if they will help to make the program more efficient and accurate.

Now I would like to discuss some of the work I am doing. It is all formal at this time, none of it has been implemented in the program yet.

One of the disadvantages of using time as the independent parameter is that the averaging period is always difficult to interpret. For instance, it is possible to use the mean motion, which is determined by the initial oscillating elements or by the initial mean elements, to determine the period. But, however it is done, it will probably be difficult to be consistent and to initially choose the right time.

Another problem is that the equations for the averaged elements have a term in their exact form which depends upon the time rate of the period. This is generally referred to as the Leibnitz term, and it depends upon the time rate of the period, the values of the true elements at both ends of the averaging period, and on the mean element at the midpoint of the averaging interval.

Still another problem arises if constant time steps are chosen: For instance, if the integration step is chosen as the initial period of the orbit, then, farther on down the line, the time step will no longer correspond to the period, and there will be drift with respect to perigee or any geometric event in the orbit. If the true anomaly is chosen as the independent parameter, none of the above disadvantages apply. Another effect is that we get automatic regularization of the orbit sampling. Points are automatically clustered near perigee where most of the action occurs for the high drag situation.

It is also possible to make repeated use of terms in the mean-to-osculating transformations, particularly if step size is chosen properly within the averaging quadrature. Also, the mean-to-osculating formulas appear in closed form, at least to first order in J_2. This is due simply to the fact that the disturbing potential can be expressed in a finite number of terms, depending upon the true anomaly.

In changing the propagation algorithm, we wanted to choose a state vector which is nonsingular for low eccentricity and inclination. For convenience, we chose to use the same state that MAESTRO now uses, except for the fast variable. If the independent variable is now chosen as the true anomaly, then the angle-time relationship must be tracked through an equation other than the one we had before. If the new fast variable is itself chosen as the time, we then have a new differential equation:

$$\frac{dt}{df} = h/r^2 + \text{perturbations}.$$

Because this leaves us with large oscillations, it is a poor choice for averaging. Suppose that, instead, the parameter Q (Stern, 1960) is chosen:

$$Q = M + \omega + \Omega - \bar{n}t$$

$$\bar{n} = (-2\epsilon)^{3/2} / \mu$$

where ϵ is the orbital energy. Then $\bar{n}$ determines the period of the true anomaly. The Q will always be a slow variable, and, in fact, for the Kepler problem, it is a constant.

The equations for the new system are given by

$$\frac{dE}{df} = \frac{dE}{dt} \frac{dt}{df} = F_E (E, t, f) \frac{dt}{df}$$

where E is any element

$$\dot{E} = F_E (E, t, f).$$

The exact averaged equations are

$$\bar{E} = \frac{1}{2\pi} \int_{f-\pi}^{f+\pi} E(f') \, df'$$

$$\frac{d\bar{E}}{df} = \frac{1}{2\pi} \int_{f-\pi}^{f+\pi} F_E (E, f', t) \, df' \frac{dt}{df'}$$

To make averaging efficient, the force evaluation is accomplished by approximating the elements in the integrand to the mean elements, plus a correction, as in the standard second-order averaging technique. Also, since the time no longer appears explicitly in the state, it must be the result of a similar correcting transformation. This means that the mean-to-osculating transformation is required at every step, as it is in all second-order averaging techniques.

Formally, the mean-to-osculating transformations are simple to derive. The equations needed are indicated below in abbreviated form:

$$E^* = \bar{E} + \delta E_p$$

If it is assumed that Δf is $2\pi/2K$, then values of the trigonometric functions of the harmonics of the true anomaly can be tabulated and never recalculated, because the same values will be repeated in true anomaly from revolution to revolution. This should save a significant amount of calculation and make for an efficient mean-to-osculating transformation.

In the equations,

$$\frac{dE}{df} = CONST + \sum_{1}^{N} (A_n \cos nf + B_n \sin nf)$$

and

$$\delta E_P = \sum_{1}^{N} (-A_n \sin nf + B_n \cos nf)/n,$$

A_n and B_n are derived from the Lagrange planetary equations with the J_2 perturbation only. The $[A_n, B_n]$ are slowly varying functions of the state vector and supposedly would not need to be recalculated more than once per revolution, and probably not that often. This depends upon the strength of the perturbations.

The evaluation of $d\overline{Q}/df$ is fairly obvious, and it is used here as an example: The forcing function, F_Q, is $(\dot{M} + \dot{\omega} + \dot{\Omega} - n) + (n - \bar{n}) - \bar{n}t$. Time appears explicitly, which may create some difficulties, at least formally, although it is doubtful that numerically this will give any trouble. The factor dt/df, which appears in the integrand, is given by

$$\frac{dt}{df} = \frac{h}{r^2} + \text{perturbations.}$$

However, since all the parameters in the state are slow (there is no fast variable), probably the two-body rate, or just h/r^2, is good enough for the function dt/df. That will probably require some experimentation, but, since there is no fast variable, there is no purpose in carrying higher order terms in this factor. The term $\bar{n}$ is related to the time derivative of the energy, and that relates (at least in its dominant term) to the time rate of the semimajor axis due to drag for the cases where drag is the most important perturbation aside from J_2. The quantity $(n - \bar{n})$ is proportional to the disturbing potential and $(\dot{M} + \dot{\omega} + \dot{\Omega} - n)$ is given by the Gaussian VOP equations. The MAESTRO propagator will be used as the basic software tool in the implementation of these techniques.

Still to be considered are techniques for calculating an accurate argument of perigee at low eccentricity. There are some problems because there is a mix of the true mean anomaly and the mean argument of perigee in one of the transformations; some experimentation is still required.

The exponential instability in Q, which is due to the presence of $\bar{n}t$, must also be investigated. This is a problem which will most likely be more apparent on computers with short word lengths. With the CDC computers and their essentially infinite word lengths, we have tried experimenting to see when we can make the equations blow up in a simple form, and we have been unable to find the instability numerically. That may give us trouble, though, and it will require more experimentation to see if there really is a problem.
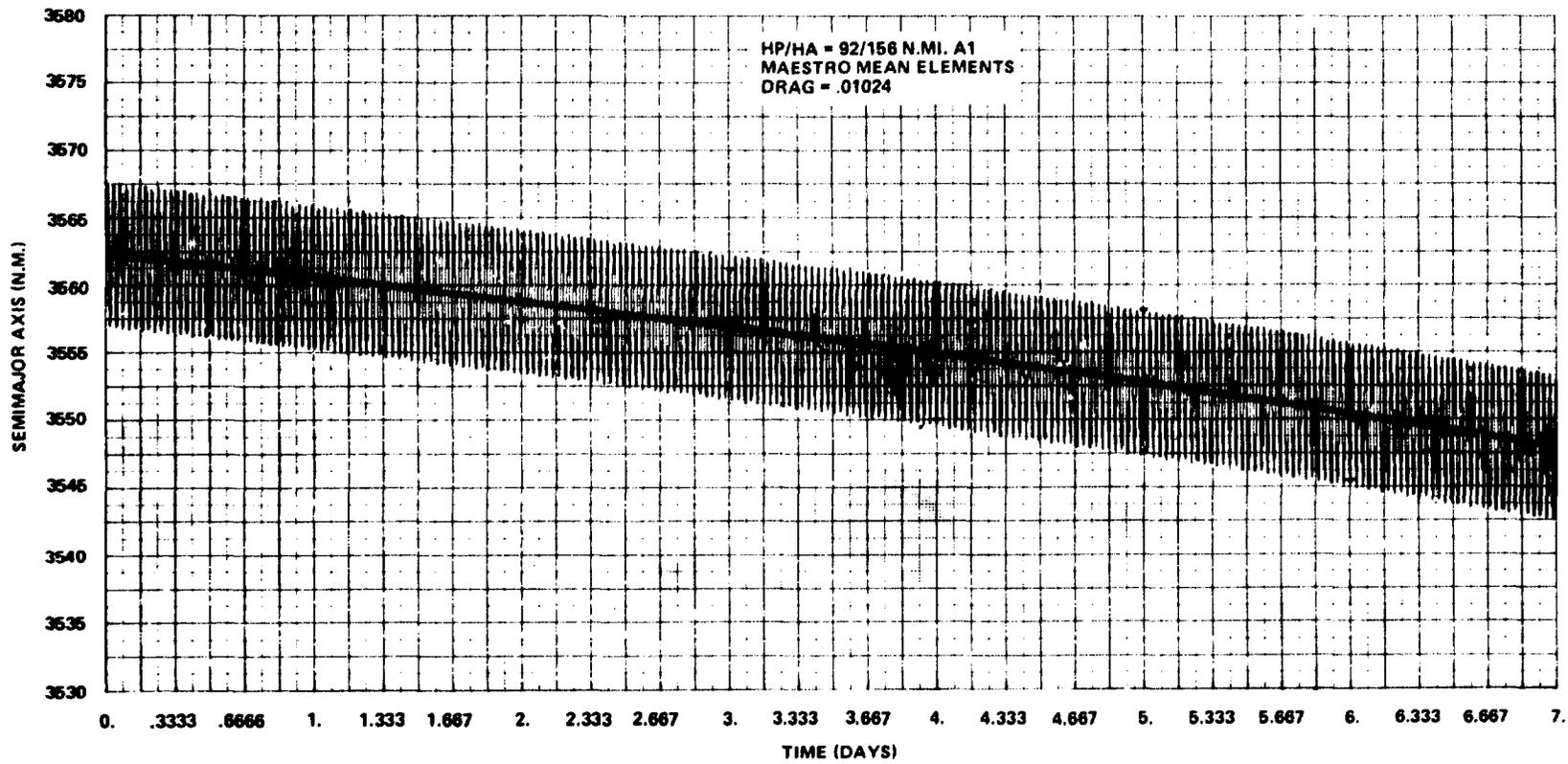
Figure 1. Comparison of PECOS and MAESTRO semimajor axis plots for case A-1.
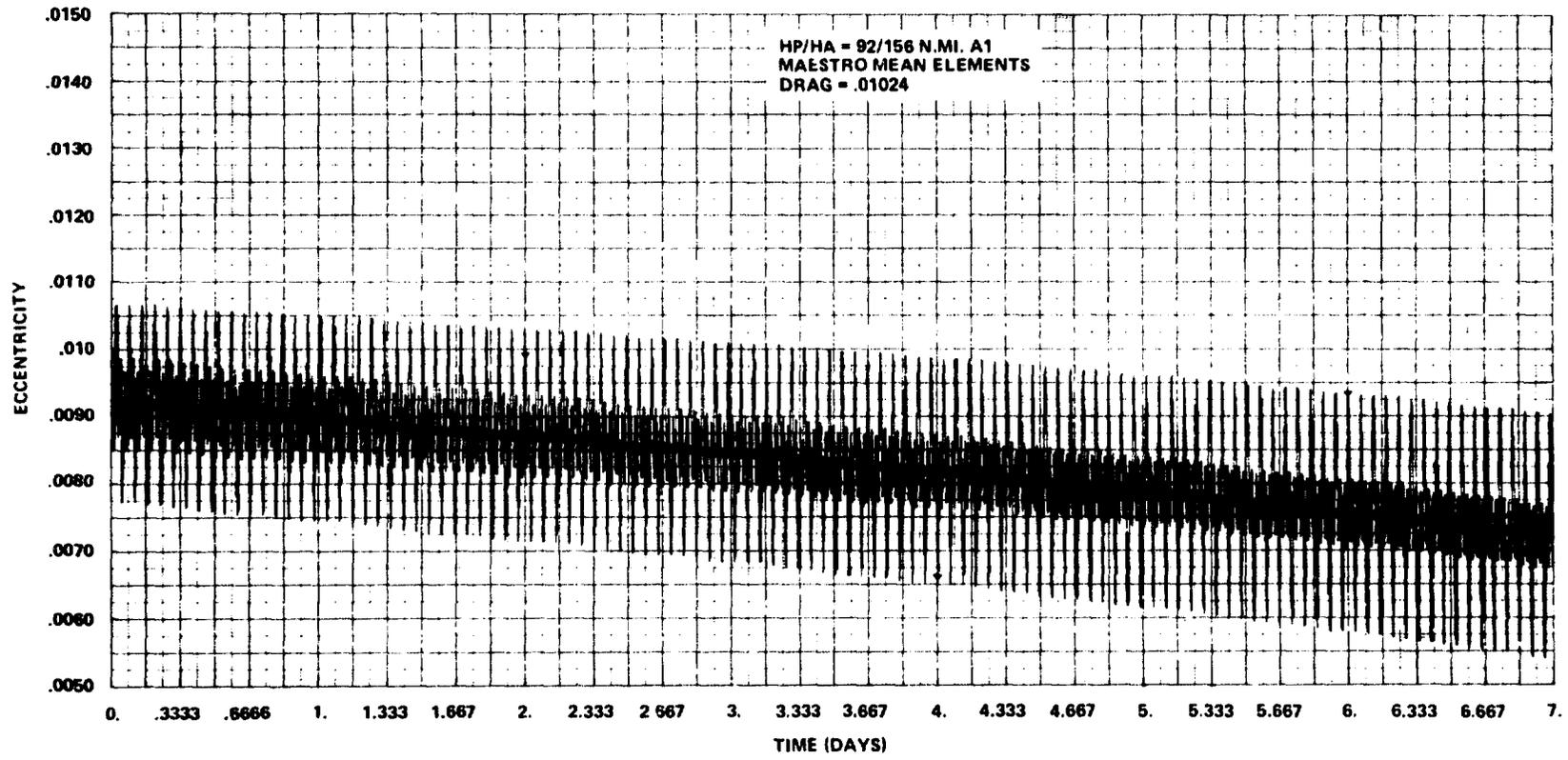
Figure 2. Comparison of PECOS and MAESTRO eccentricity plots for case A-1.
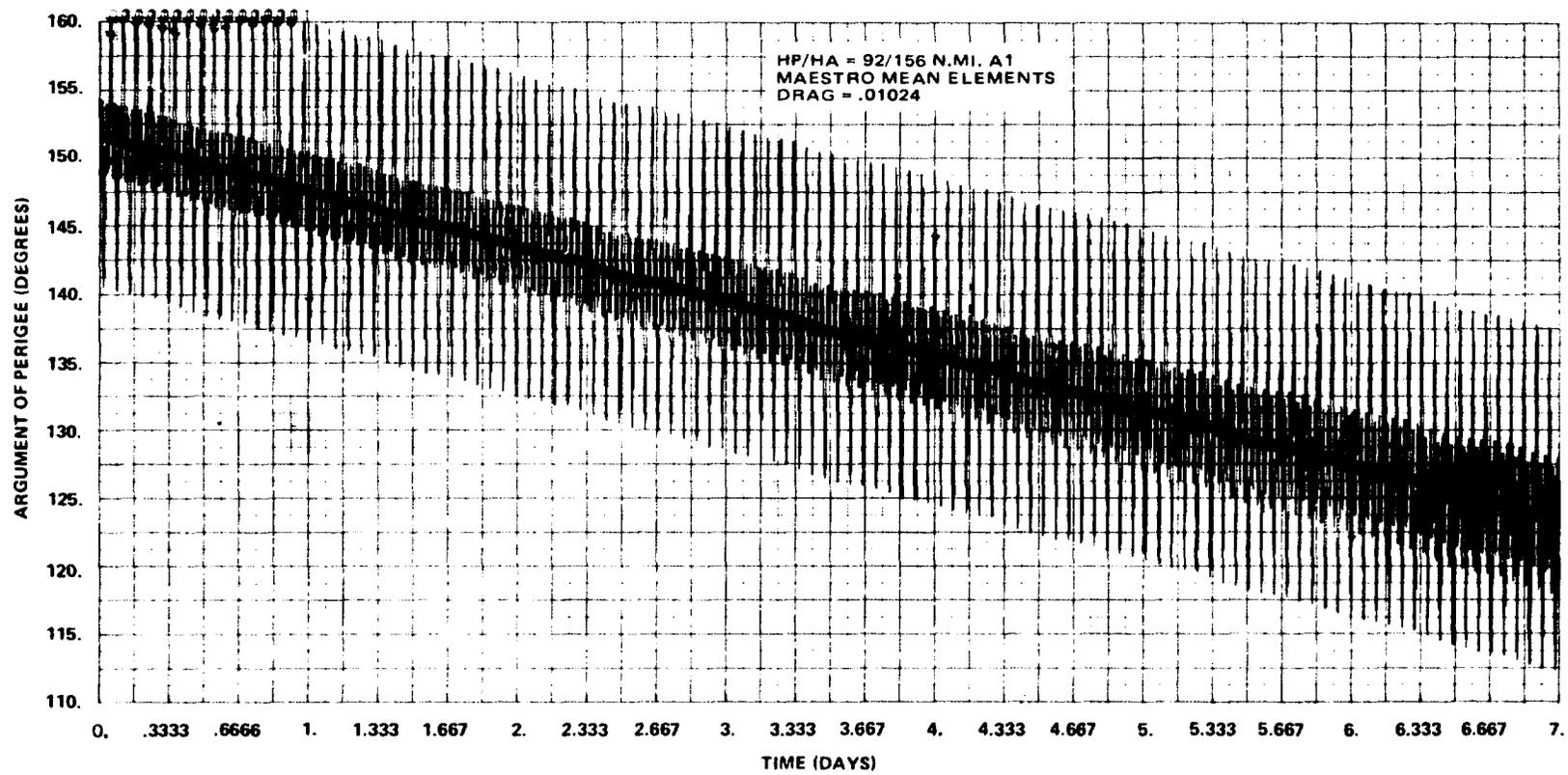
Figure 3. Comparison of PECOS and MAESTRO argument of perigee plots for case A-1.
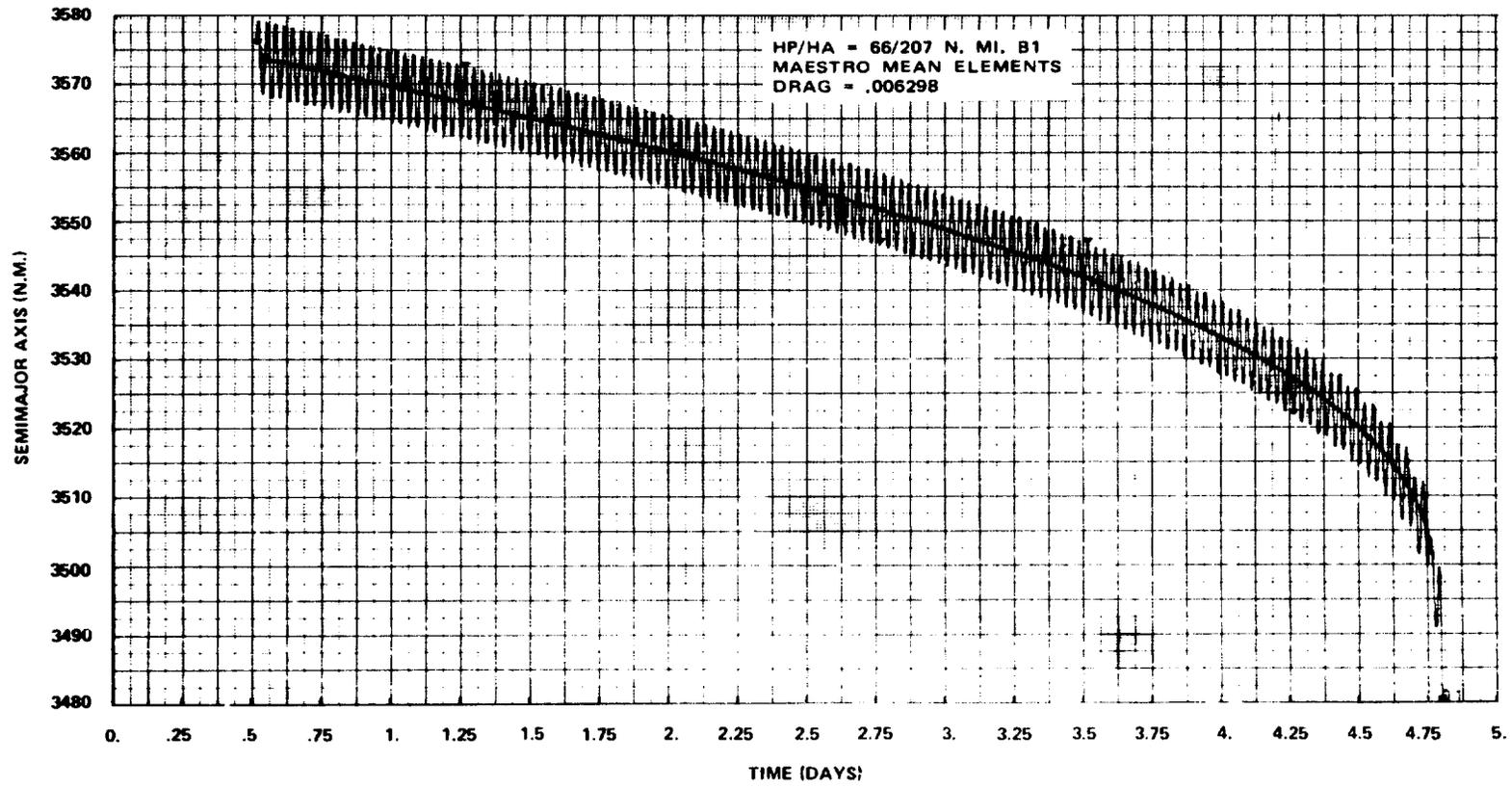
Figure 4. Comparison of PECOS and MAESTRO semimajor axis plots for case B-1.
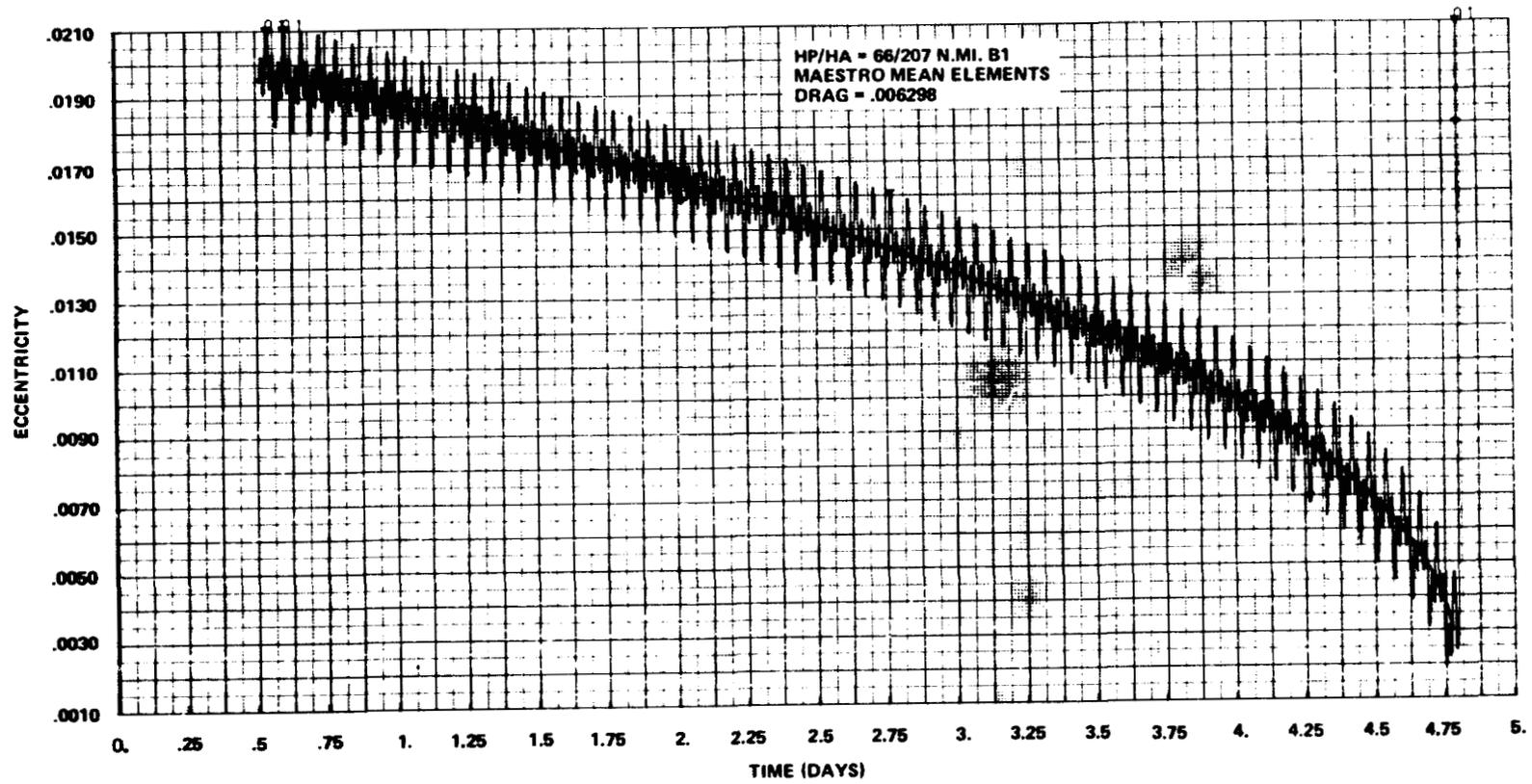
Figure 5. Comparison of PECOS and MAESTRO eccentricity plots for case B-1.
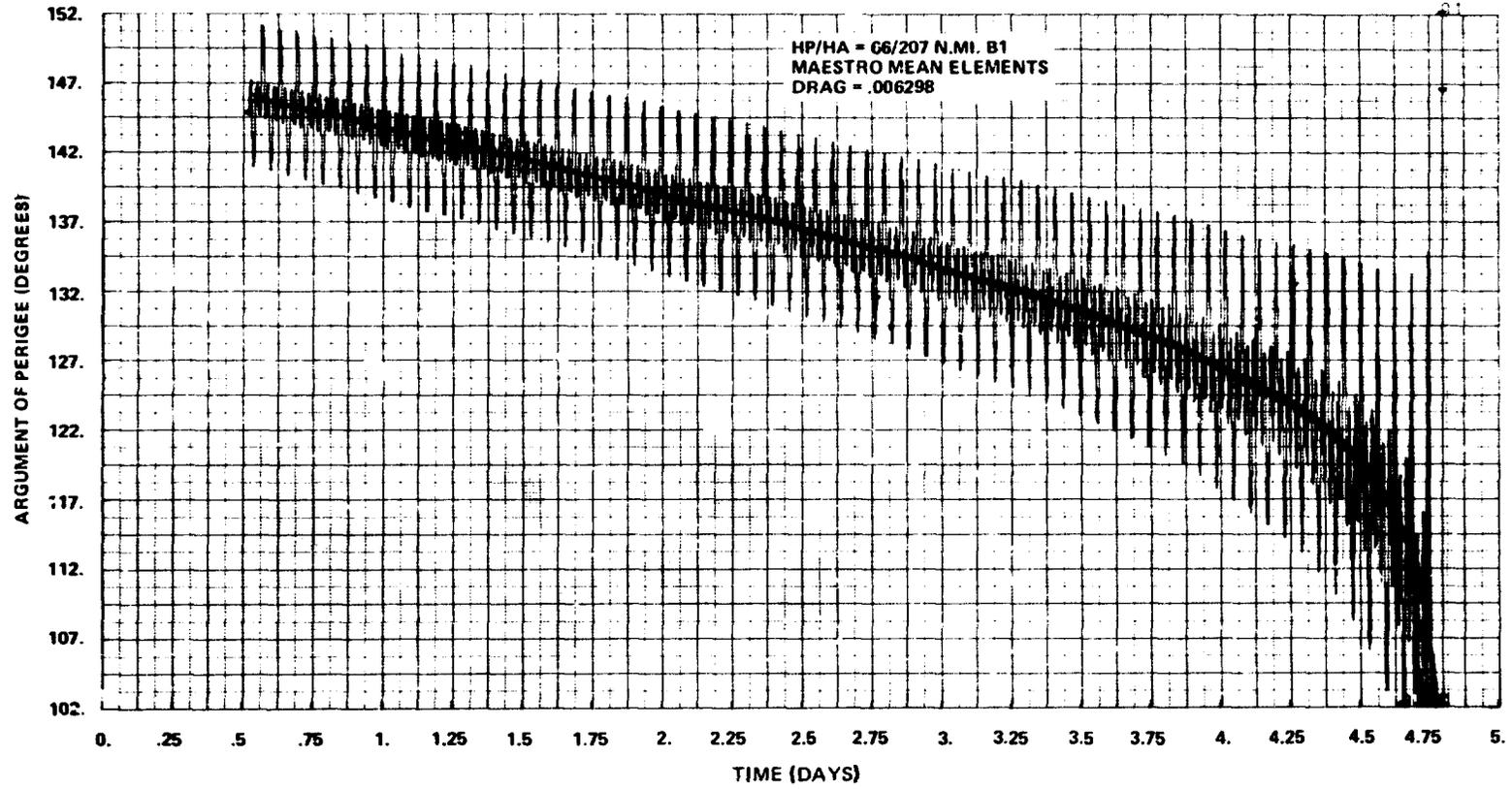
Figure 6. Comparison of PECOS and MAESTRO argument of perigee plots for case B-1.
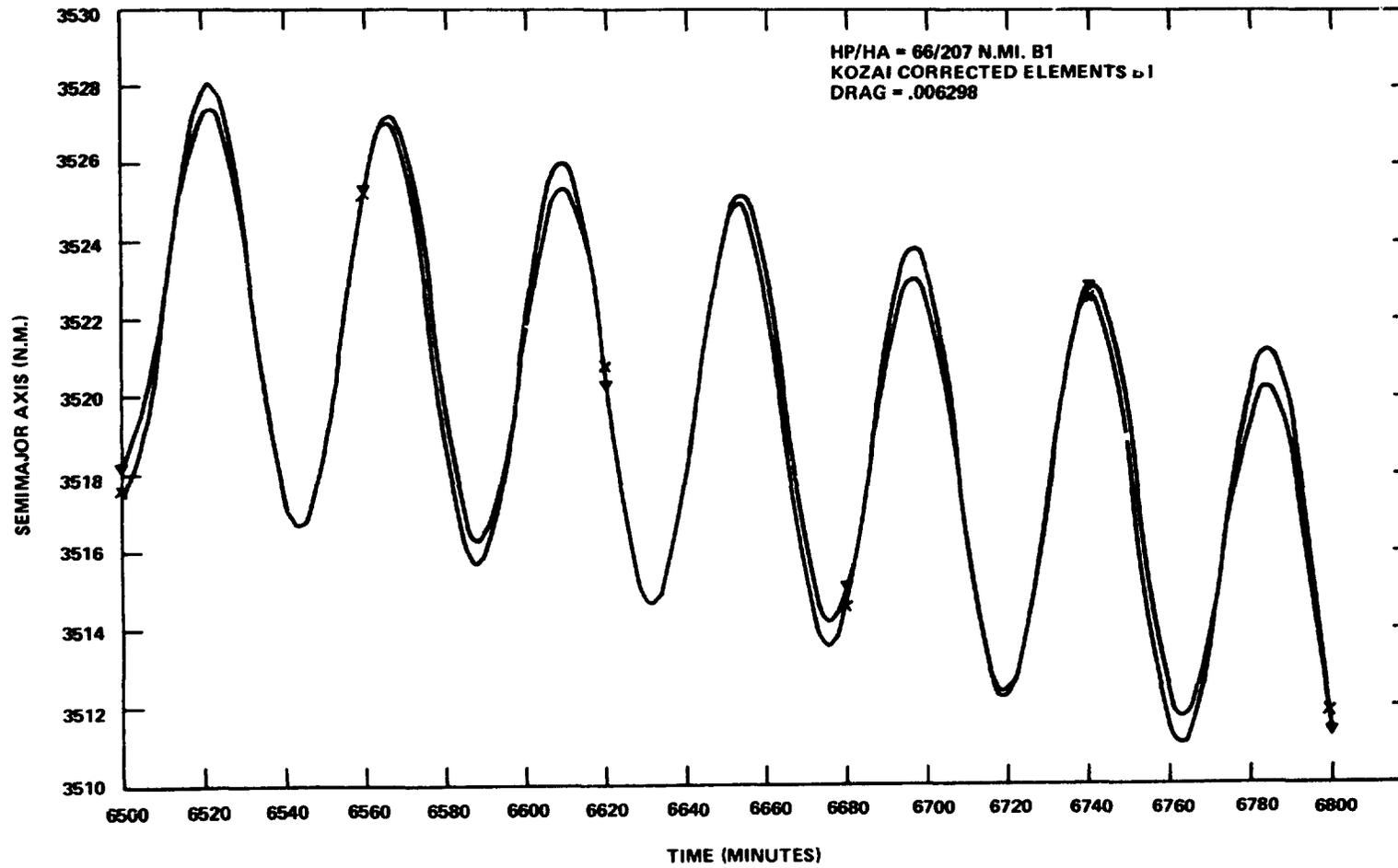
Figure 7. Comparison of Cowell integration and short period recovery for semimajor axis.
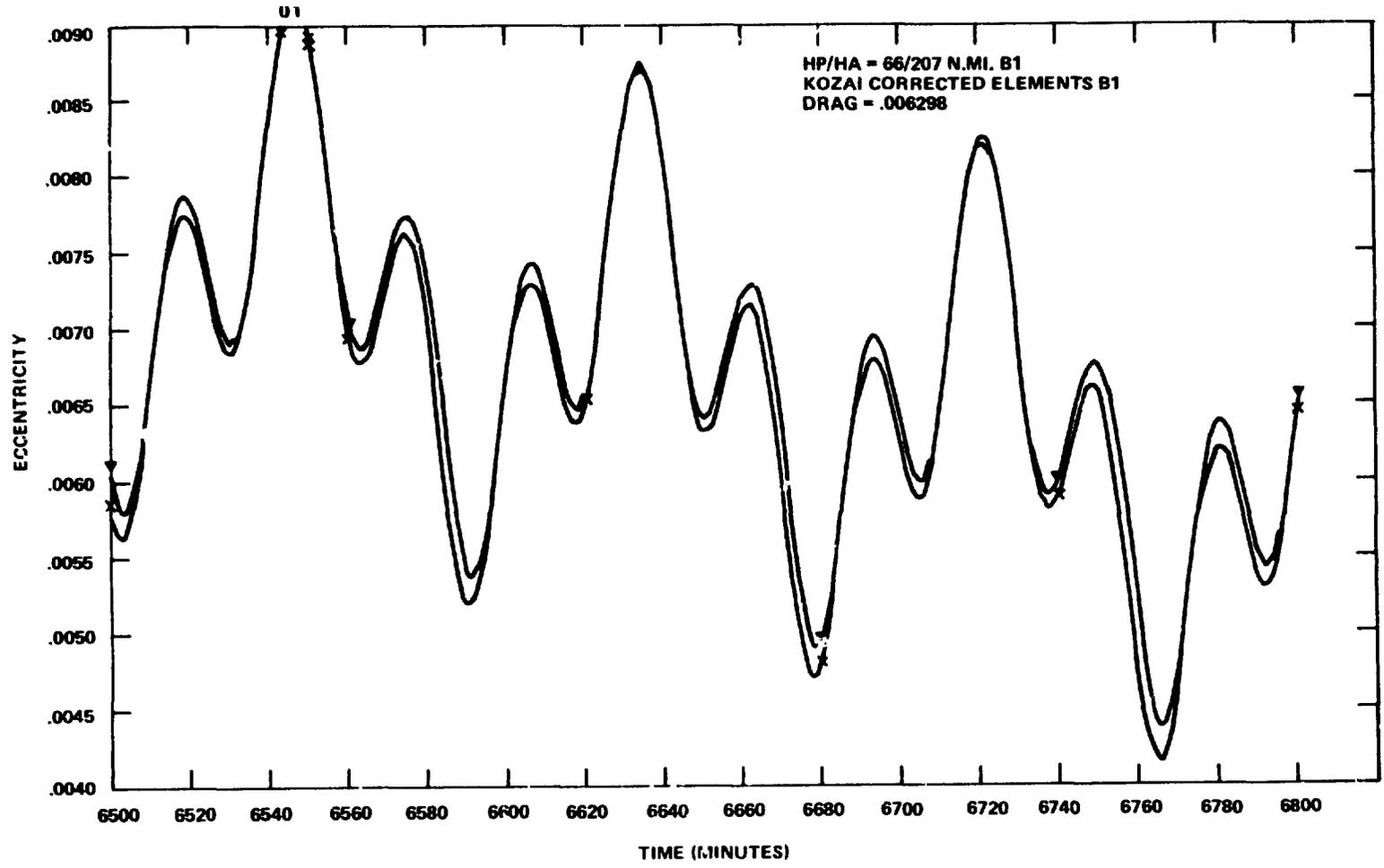
Figure 8. Comparison of Cowell integration and short period recovery for eccentricity.
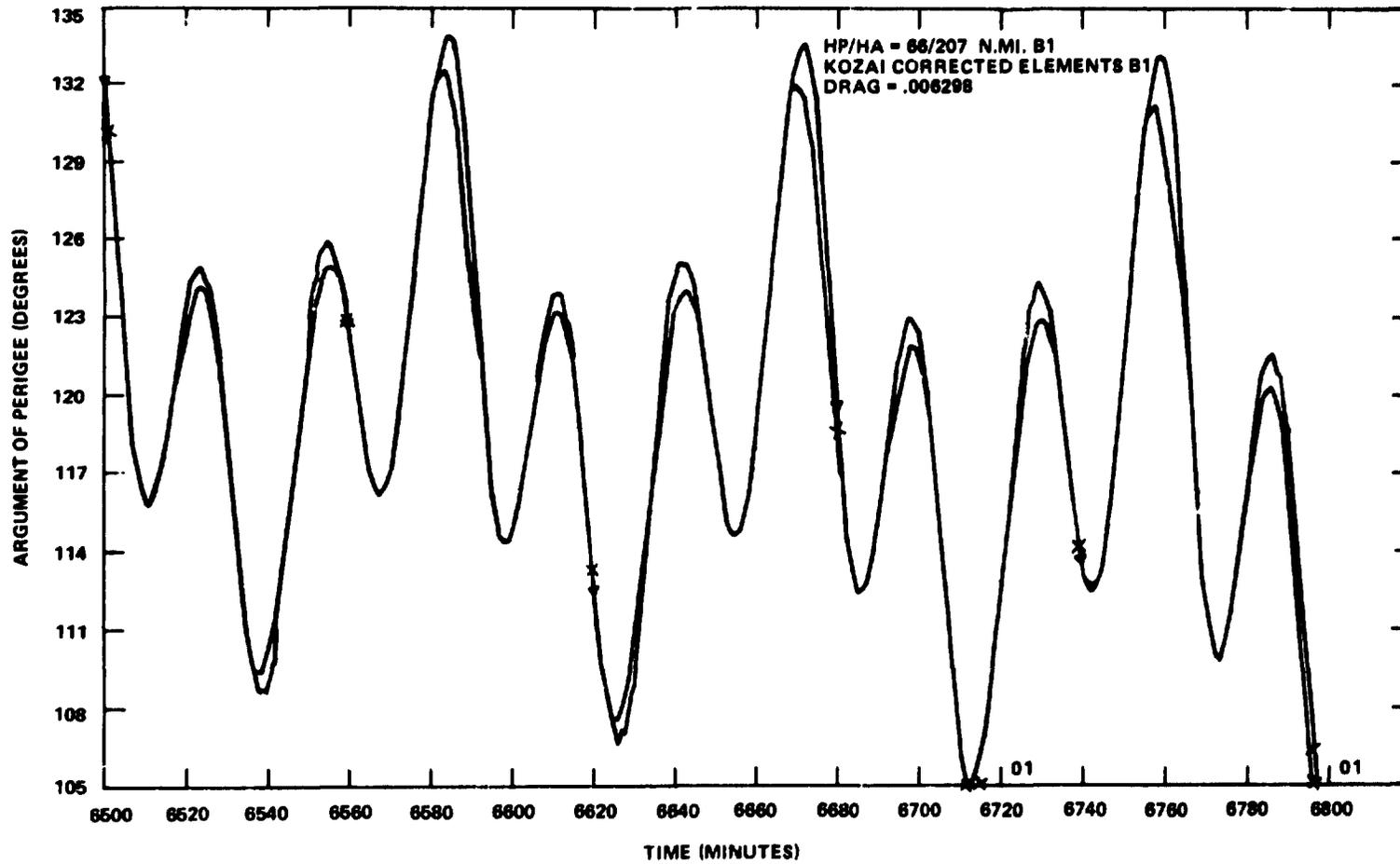
Figure 9. Comparison of Cowell integration and short period recovery for argument perigee.

31

REFERENCES

Izsak, I., 1963, "A Note on Perturbation Theory," *Astron. J.*, **68**, October, pp. 559-561.

Stern, T. F., 1960, *An Introduction to Celestial Mechanics*, Interscience Publishers, N.Y., p. 127.

Uphoff, C., 1973, "Numerical Averaging in Orbit Prediction," *AIAA Journal*, **V.** (II), November, pp. 1513-1516.

AUTONOMOUS NAVIGATION FOR ARTIFICIAL SATELLITES

Pranav S. Desai
Computer Sciences Corporation
Silver Spring, Maryland

The term "autonomous navigation" refers to the possibility of providing a satellite with the sufficient number and type of sensors, as well as computational hardware and software, to enable it to track itself. In other words, there is no ground tracking involved.

There are two classes of such autonomous navigation: passive and active. Passive means that the satellite does not get cooperation from the ground or from other satellites; active means that the satellite does get active cooperation from either the ground or from another satellite like the Trackir   'ata Relay Satellite Systen   RSS). This active cooperation could come in the   .adio signals, laser beams, ο, other kinds of signals or beacons.

The basic reason for usi. ℓ .tonomous navigation is to reduce the necessity for ground tracking, thereby reducing the over. ''ding of ground tracking facilities and also reducing the cost. There are also other technical reasons. For example, with a fast satellite, if there is a gap in the ground tracking data set, especially if there are drag and other prominent effects present, an autonomous navigation system could increase the accuracy of prediction between the two data sets. Another reason could be that the reaction time for noticing changes in the satellite orbit would be reduced by autonomous navigation, even if it is used as a backup to ground tracking.

This work is a conceptualization effort made by Don Novak, Paul Beaudet, and the author at Computer Sciences Corporation. The literature is not exhaustive, but it should be noted that Howard Garcia's paper has a summary of sensors as well as some discussion of the new sensor interferometer landmark tracker.

The following considerations are important in such a feasibility study: First of all, it is necessary to be aware of what types of sensors are available (or could be made available) on a satellite to help in autonomous navigation. Then the observability arising from combinations or configurations of these sensors should be checked. In other words, it should be determined whether a given set of sensors is sufficient under various conditions for determination of attitude and orbit of the satellite. The accuracy of the selected system and its reliability should then be studied to determine that, should one of the components fail, the other components would be enough to back it up. The choice of sensors basically depends on the estimation algorithm, in that we might choose either a coupled attitude and orbit determination scheme or a decoupled scheme. The computational hardware is still another factor.

Some potential sensors for use in autonomous navigation are listed below, but this is by no means an exhaustive list. Some satellites that have used, or are presently using, these sensors are listed:

- Inertial measurement unit–ATS-F, OAO-2, OAO-C

- Star mapper–ATS-F, CTS, OAO-2, OAO-C, OSO-I, OSO-7, SAS-B, SAS-C, SSS-A

- Magnetometer–AE, AEROS, GEOS-C, OSO-I, OSO-7, SAS-A, SAS-B, SAS-C

- Solar sensor–SE, AEROS, ATS-F, CTS, GEOS-C, IMP-H, I, J, RAE-2, SAS-B, C, SSS-A, Nimbus

- Horizon sensors-optical–IMP-H, I, J, RAE-2, SSS-A

- Horizon sensors-infrared–AE, AEROS, ATS-F, CTS, SAS-C, TIROS, Nimbus

- Interferometer landmark tracker–ATS-F

- Scanner/camera–SMS, Nimbus, Landsat

The first is an inertial measurement unit, which is a system of gyros and accelerometers for determining inertial attitude and inertial acceleration of the spacecraft; it has been used on the Orbiting Astronomical Observatory (OAO). The star mapper is probably the most accurate of the attitude sensors for determining inertial attitude and has been used on many satellites. The magnetometer determines attitude with respect to the magnetic field of the earth, or the central body, and if there is a good model available for the magnetic field of the central body, it indirectly determines the satellite attitude. The solar sensor comes in many varieties, but basically it provides angles to the sun from the spacecraft frame. Horizon sensors can be either optical or infrared. For example, an optical horizon sensor was used on the Radio Astronomy Explorer-2 (RAE-2) mission; but infrared is more common and is used in a large number of missions. The interferometer landmark tracker (ILT), a new type of sensor, will be discussed later.

So far the discussion has been limited to attitude-type sensors; however, they are by no means the only sensors that could be used for autonomous navigation. We could consider using non-attitude- or non-navigational-type sensors, including meteorological cameras and scanners that could be used in a landmark determination scheme, in which there is currently an interest.

There are two other sensors to be considered: the one-way Doppler and the image correlator (IC); however, the image correlator has not yet been put on board. The one-way Doppler would determine range rate to known radio stations on the ground or to a tracking satellite. The image correlator is an advanced version of the landmark determination-type scheme where a computer would determine, through pattern recognition, the direction cosines in the spacecraft axes to a known landmark.

It is also necessary to decide how to combine the sensors for autonomous navigation, and a decision has to be made as to whether attitude and orbit should be determined in a coupled or decoupled scheme. There is an argument in favor of a decoupled scheme because orbital parameters, on the whole, vary less rapidly than attitude parameters. Therefore, longer spans of data can be used for orbit determination than for attitude. A coupled scheme would not take into account this difference in the memory span requirement of the two. However, an initial determination could very well be coupled, so perhaps the best method would be to first determine a coarse orbit and attitude in a coupled determination, followed by fine attitude determination, followed by fine orbit determination. So, for this discussion, it is assumed that we are going to determine attitude first, then orbit.

The ILT (figure 1a) has a pair of antennas (at A and B), and its function is to determine the phase difference between the received signals that arrive at the antennas. The ILT must be initialized as to what radio signal frequency it is looking for, which means that the approximate position in orbit must be known. If the satellite is geosynchronous, orbit determination does not have to be done continuously.

ANTENNAS AT A, B (BASELINE AB = d)

(a)

(b)
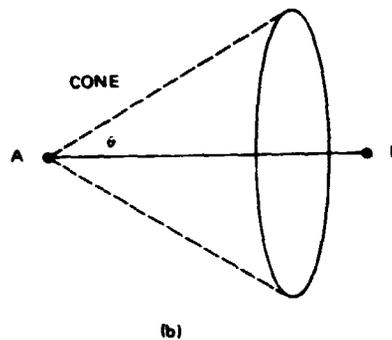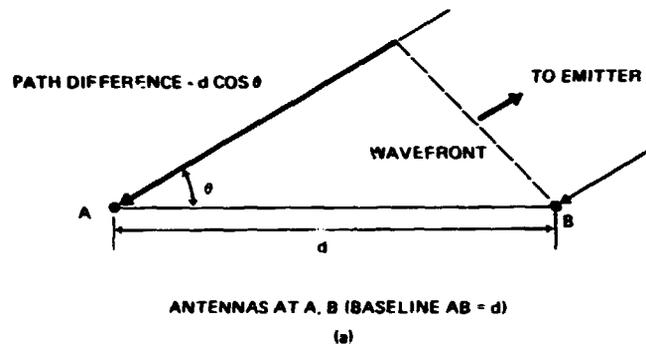
Figure 1. Interferometer landmark trackers phase shift geometry and circle of ambiguity. (a) ILT phase shift geometry; (b) ILT circle of ambiguity.

We determine the path difference, $d \cos \theta$, by determining the phase difference, because the two are proportional, and this gives us the angle θ between the direction line to the emitter and the baseline of the ILT. However, as seen in figure 1b, there is a conical ambiguity left in the direction to the emitter, because that angle is all that is known. To reduce ambiguity, we also have another pair of antennas (not shown in figure) where the baseline is perpendicular to the first baseline; we will have an intersection of two cones and, therefore, will reduce the ambiguity to just two lines. A little further analysis, perhaps over a period of time or using multiple landmark determination, might reduce the twofold ambiguity as well.

In figure 2, we begin examining some sensor configurations from the point of view of observability. Suppose we were trying to determine the satellite inertial attitude using a star sensor that determines the direction to one star only, and then supplement that with a landmark determination scheme. In other words, the direction cosines in the spacecraft axis to one landmark on the central body are determined using either the ILT or some other means such as a scanner or a camera.
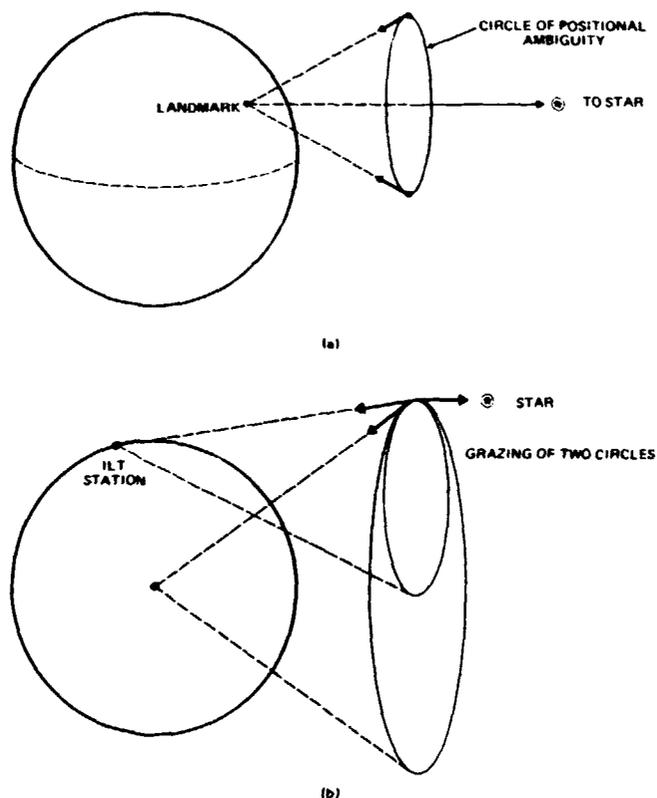
Figure 2. Star sensor configuration. (a) One-star, single landmark symmetry; (b) poor resolution geometry.

In a scheme like this, the star determines the satellite attitude ambiguous to the roll around the axis from the satellite to the star. Normally, the roll ambiguity is further reduced by having a second star, but suppose that second star is replaced by a landmark. In that case, all that is known is the angle between the star direction and the landmark direction, and that does not give the absolute attitude of the spacecraft unless its position is known. Spacecraft position can be ambiguous to within that circle (figure 2a), in fact, to within the whole cone, which indirectly results in ambiguity in the attitude. That would be considered an untenable or unobservable condition.

Suppose we tried to reduce the ambiguity by looking at the central body horizon and obtaining indirectly the direction to the center of the central body. This could remove the ambiguity, but occasionally there is a situation where the resolution is poor, because we are now on two circles that graze, and as can be seen in figure 2b, the graze is quite large. If the ILT station was not placed in the plane formed by the line to the center of the central body and the line to the star, then the circles would intersect at two points instead of grazing, and that would be a better resolution geometry.

Based on this discussion, we can eliminate as untenable those configurations for attitude determination which use only one star and one landmark and such other combinations which are conceptually equivalent, for example:

- One star—ILT/IC (single station)

- Sun—ILT/IC (single station)

- One star—central body horizon

- Sun—central body horizon

- Moon horizon—central body horizon

- Moon ILT—central body ILT (single station)

The following are weakly-orbit-coupled configurations for attitude determination:

- One star—central body horizon—ILT/IC (single station)

- Sun—central body horizon—ILT/IC (single station)

- Moon horizon—central body horizon—ILT/IC (single station)

- One star—ILT/IC (multiple stations)

- Sun—ILT/IC (multiple stations)

- Moon horizon—ILT/IC (multiple stations)

- Moon ILT—central body ILT (multiple stations)

We are still speaking of attitude determination, and we would like it to be orbit decoupled, but these configurations are weakly orbit coupled in the sense that the ILT, for example, would need to be initialized with an approximate knowledge of orbit so that we would know which station to tune to. This list includes a one star/central body horizon/one landmark configuration as well as a one-star/multiple station configuration for the same reason. In summary, to have orbit decoupled attitude determination, perhaps two star sensors would be needed, and they could have an associated inertial measurement unit to back them up.

We will now examine the information that can be derived by determining the direction to the landmark in the spacecraft frame. Figure 3 shows the spacecraft position, the line from the spacecraft to a known landmark, and θ and γ, which are the latitude and longitude of the landmark. The unknown subpoint of the satellite is $(\theta_\theta, \gamma_0)$, the distance of the satellite is r, and the satellite-to-landmark range is ρ. The following equations are based on the fact that this line intersects this sphere, and they show that the direction cosines of that line ought to be 1_x, 1_y, 1_z, in the earth frame of reference:

$$\cos\theta\,\cos\gamma = \rho\ell_x + r\cos\theta_0\,\cos\gamma_0 \tag{1}$$

$$\cos\theta\,\sin\gamma = \rho\ell_y + r\cos\theta_0\,\sin\gamma_0 \tag{2}$$

$$\sin\theta = \rho\ell_z + r\sin\theta_0 \tag{3}$$

$$\rho = -r\left[\hat{\ell}\cdot\hat{r} + \sqrt{(\hat{\ell}\cdot\hat{r})^2 - (1 - 1/r^2)}\right]$$

where

$$\hat{\ell}\cdot\hat{r} \equiv \ell_x\cos\theta_0\,\cos\gamma_0 + \ell_y\cos\theta_0\,\sin\gamma_0 + \ell_z\sin\theta_0.$$

Equations 1 to 3 can be solved to get the range explicitly; therefore, for every landmark, the three equations reduce to two equations. If θ and γ, the position of the landmark on the earth, are known, then there are three unknowns: r, θ_θ, and γ_0. If we are interested in orbit determination, and the attitude is already determined, then we have three unknowns and two equations per landmark, so that we need at least two landmarks for orbit or position determination.

If we could determine the subpoint $(\theta_\theta, \gamma_0)$ on a continuous basis, then, by studying a history of the subpoint, we could get a track of the satellite on the ground and its characteristics would suggest a period. By using Kepler's Third Law, for example, the semimajor axis could be derived indirectly from the period. In that case, even one landmark is, in principle, sufficient for orbit determination.

38
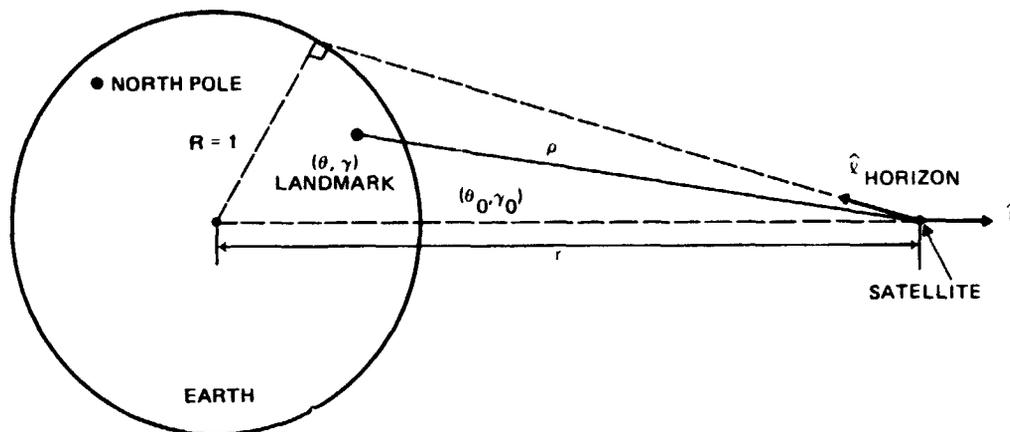
Figure 3. Spacecraft/landmark geometry.

We have assumed that attitude was already known, but suppose we were trying to use this ILT for a coupled attitude and orbit determination, perhaps in a coarse way, for preliminary locking on. How many unknowns would then be had?

In figure 3, we have these directional cosines to the landmark, which are supposed to be in the geographic frame. What we really would know from the satellite instruments would be the direction cosines in the satellite frame of reference. Therefore, indirectly there are three unknowns involved here which represent the transformation from the satellite frame to the geographic frame, which essentially means the satellite attitude, that is, the three attitude angles of the satellite. We then have six unknowns—the three satellite attitude angles plus three positional unknowns—and two equations per landmark, so we still would need only three landmarks. If we had strategically located a sufficient number of landmarks, accounting for possible cloud cover, even then perhaps just a few would be enough for a coupled attitude and orbit determination. (Expressions for the sensitivity of this kind of determination have been developed in our report and are available for anyone interested in performing their error analysis.)

In summary, it seems that by using a variety of sensors it is conceptually possible to have autonomous navigation. However, the details would have to be worked out for each type of orbit. For example, a geosynchronous orbit would require a different type of configuration, perhaps, than the 2-hour satellite, so we do not have a general conclusion or recommendation valid for all types of satellites.

The second part of this paper presents a standardized autonomous navigation system (figure 4) which was designed by Computer Sciences Corporation personnel for possible future use in a standardized type of satellite. In the base are the computer, electronics, and some gyro hardware. On the two sides of that base are two gimbal units. The right-hand gimbal unit is a two-star sensor, located near the beam splitter, which would determine the satellite's inertial attitude. The main navigational unit (lower left) consists of a gimbal unit with three arrays of infrared detectors arranged conically at the tip of the unit. One small section of that array is high resolution, and two outside sections are low resolution. This is supposed to determine three directions to three points on the horizon of the central body.
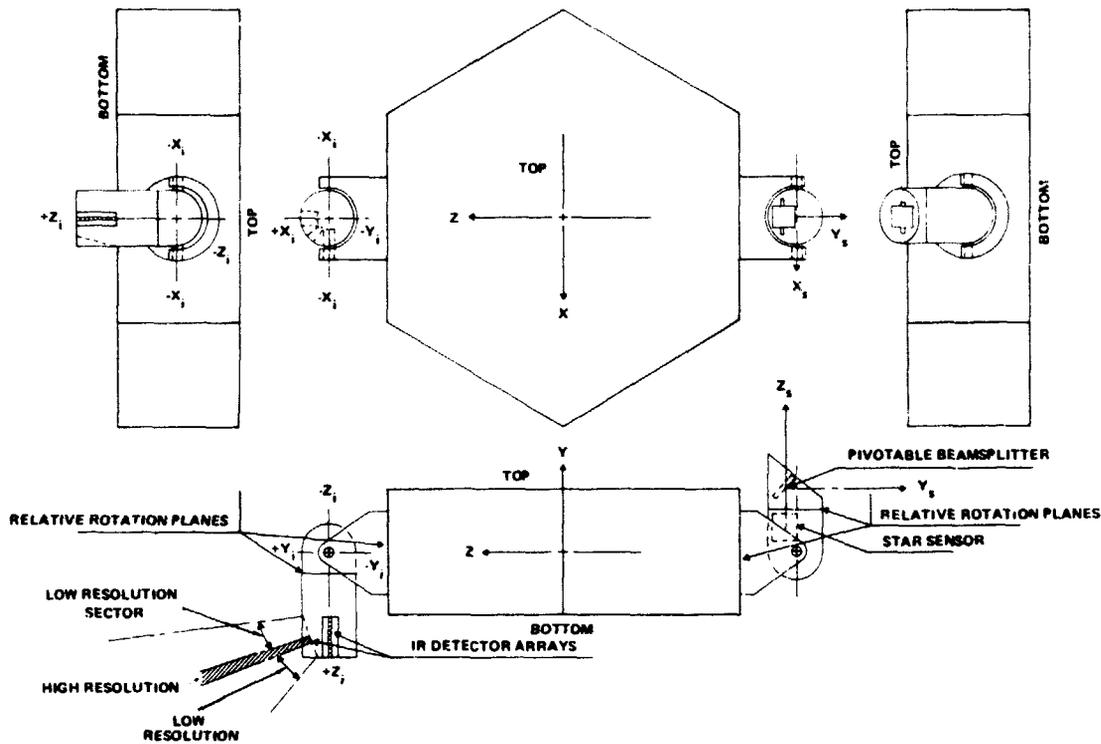
Figure 4. Possible configuration for the proposed standardized autonomous navigation system.

As seen in figure 5, three lines of sight to the central body horizon determine a unique cone, so that the satellite position is known. The following are the equations for x_i, y_i, z_i, the central body coordinates in the spacecraft axes:

$$h_{11}x_i + h_{12}y_i + h_{13}z_i = (r^2 - R^2)^{1/2}$$

$$h_{21}x_i + h_{22}y_i + h_{23}z_i = (r^2 - R^2)^{1/2}$$

$$h_{31}x_i + h_{32}y_i + h_{33}z_i = (r^2 - R^2)^{1/2}$$

By using the information from the star sensors, the equations can be transformed into inertial coordinates.

Figures 6 and 7 show the degree of accuracy we can get from this system. Depending on the angular accuracy of the IR detectors, different errors are obtained at different altitudes. At 1000 km altitude, and with a 0.1° angular precision, we have less than a 10-km error, in fact, close to a 5-km error in altitude (figure 7). In figure 6, the horizontal component error, the curves are flatter, but again we have the same order of magnitude accuracy.
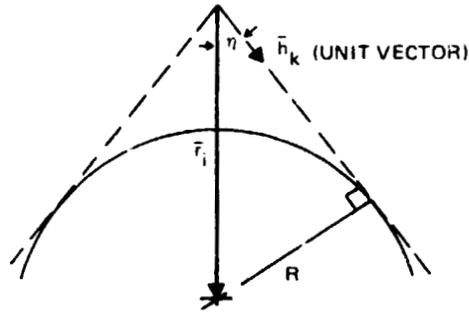
Figure 5. Three lines of sight to the central body horizon determine a unique cone.
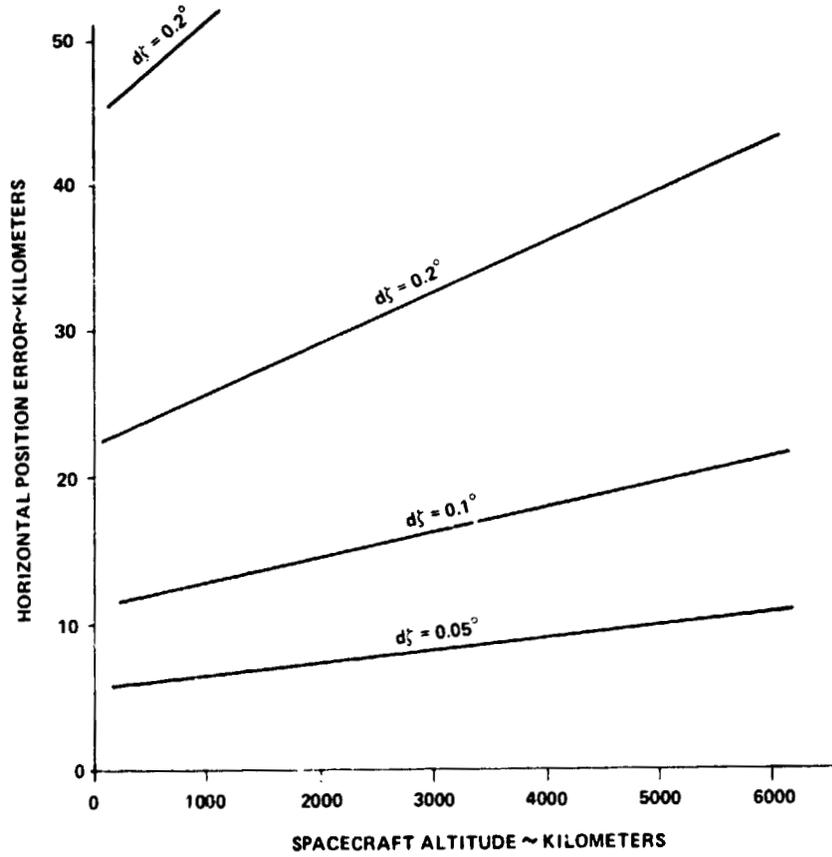
Figure 6. Variation of the position horizontal component error.
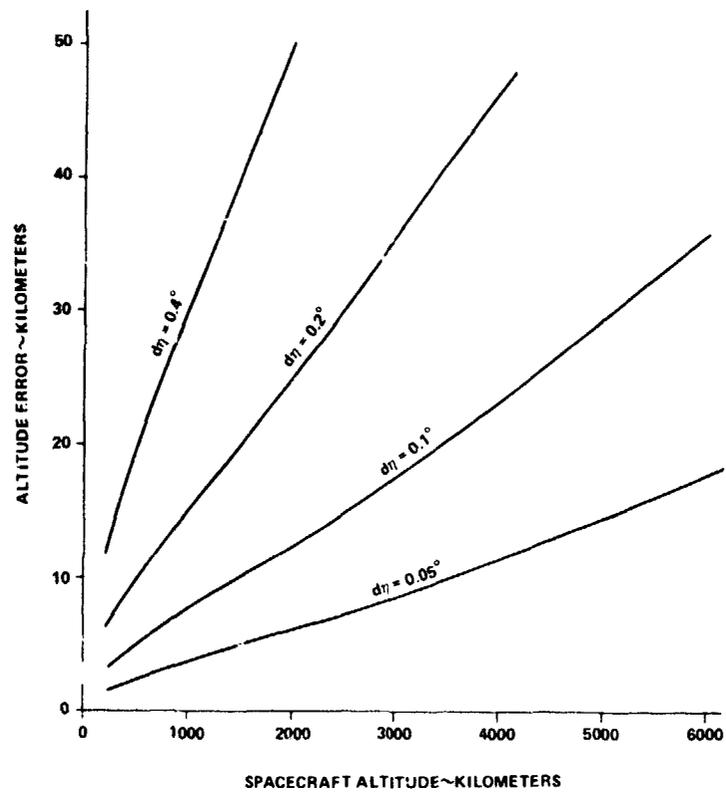
Figure 7. Variations in altitude error
as a function of altitude.

BIBLIOGRAPHY

Dambeck, W. J., *Geostationary Satellite Position and Attitude Determination Using Picture Landmarks*, NOAA TM NESS-21, August 1972.

Garcia, H. A., "An Analysis of Recent Advances in Autonomous Navigation," (Presented at AIAA Guidance and Control Conference, Key Biscayne, Florida, 1973).

Reznikov, B. A., "Parametric Observability of Space Vehicles," *Kosmich. Issled.*, 6 (3), p. 338, 1968.

IDEAL ELEMENTS FOR PERTURBED KEPLERIAN MOTIONS

A. Deprit
University of Cincinnati
Cincinnati, Ohio

The motion is referred to Hansen's ideal frame, its attitude being defined by its Eulerian parameters. The parameters selected to determine the motion in the orbital plane cause no singularities or indeterminacies for small eccentricities; they have been chosen with a view of making the right-hand members of the equations as simple to program as possible.

N76-10172

SOME RESULTS IN THE FUNDAMENTAL GEOMETRIC THEORY OF ONBOARD DIRECTIONAL SENSORS

Bertrand T. Fang
Wolf Research and Development Corporation
Riverdale, Maryland

Earlier in the symposium, Dr. Velez mentioned the need for standardizing the many different kinds of attitude sensors. The primary attitude sensors now in use are directional sensors, which means that they sense or measure certain external reference directions relative to the spacecraft body. Interferometers, magnetometers, horizon scanners, and star trackers are examples of such sensors, and this paper will take a very elementary look at some of their fundamental geometric properties, with the hope that, by studying the basic geometry, we can derive a set of equations which are applicable to different kinds of sensors.

First we will look at the basic ingredients of directional information, the manner in which the observation equations govern these basic ingredients and convey attitude and orbit information, and also the manner in which errors enter into these equations. The second topic to be discussed is attitude observability; in other words, what combinations of these direction measurements will resolve attitude unambiguously. Lastly, we will consider some of the concepts developed to study horizon sensors. Horizon scanners are of interest because they also present orbit information and are somewhat unique in that the measurement is not actually a particular vector, but rather a scanning vector, which is tangent to the spherical earth.

In analyzing these different directional sensors very carefully, it is found that, although there are many different kinds of sensors, the directional information can be divided into two very simple types, the first of which is given by the scalar product of two vectors as shown in figure 1.

For this measurement, we have the direction R, which is the radiation from the transmitting station, and also a spaceborne antenna, which is a direction fixed onto the spacecraft. The measurement is the phase difference of the radiation arriving at the two ends of the antenna baseline and is given by the dot product of the reference direction R, which is a unit vector from the transmitting station to the spacecraft, and the unit vector K, which is the spacecraft-fixed direction. This measurement may be represented as the following observation equation:

$$y_1 = \cos\theta = \left(\frac{\lambda}{L}\right)\left(\frac{\Delta\phi}{2\pi}\right) = \bar{R} \cdot \bar{K}$$

$$= [R^I]^T [K^I] = [R^I]^T [A_{I/B}] [K^B]$$

The superscripts I and B refer to the inertial and spacecraft axes, respectively, and $A_{I/B}$ is the direction cosine matrix relating the spacecraft and inertial axes and containing all of the attitude information. On the left-hand side of the equation, y_1 is the measured quantity: K^B is a spacecraft-fixed unit vector and is therefore a known quantity. Therefore, the attitude matrix, $A_{I/B}$, is the only unknown quantity in this equation.
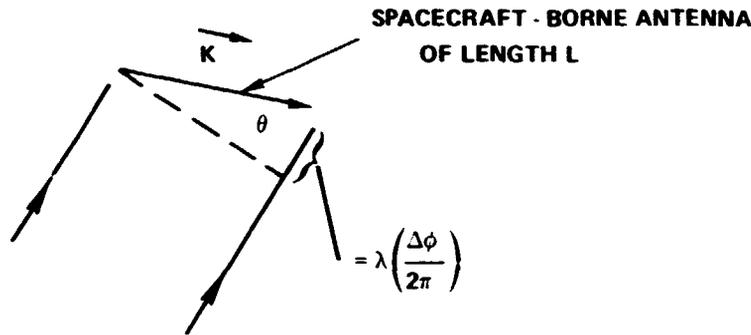
Figure 1. Attitude determination measurement as made by a short-baseline interferometer on the ATS-6 spacecraft.

Figure 2 shows the second type of direction measurement, made by the digital solar aspect sensor used on the Atmospheric Explorer Spacecraft. The vector R represents the line-of-sight from the spacecraft to the sun; i, j, and k are orthogonal unit vectors along spacecraft-fixed directions; and solar aspect angle E_S is specified by the cross-product of R and K. This measurement may be represented by the following equations:

$$y_2 = \sin E_S = \frac{\bar{R} \times \bar{K}}{|R \times K|} \cdot \bar{i} = \frac{\bar{R} \cdot \bar{j}}{\sqrt{1-(R \cdot K)^2}} = \frac{[R^I]^T [A_{I/B}] [J^B]}{\sqrt{1-([R^I]^T [A_{I/B}] [K^B])^2}}$$

and

$$y_3 = \cos E_S = \frac{[R^I]^T [A_{I/B}] [I^B]}{\sqrt{1-([R^I]^T [A_{I/B}] [k^B])^2}}$$

45

Being scalar equations, this second class of measurement contains more information than the first class, although it is necessary that

$$y_2^2 + y_3^2 = 1.$$

It should be noted that y_2 and y_3 are related in a more complicated nonlinear way to the attitude matrix, $A_{I/B}$.
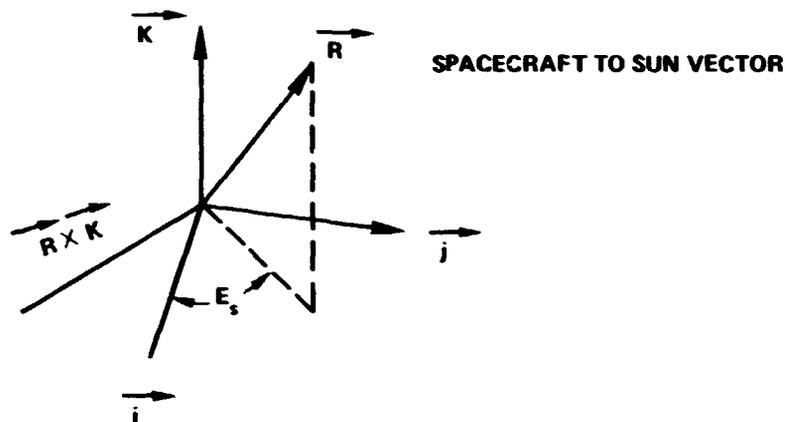
Figure 2. Orbit determination measurement as made by the digital solar aspect sensor on the AE spacecraft.

The various problems of interest may be classified as follows by referring to the measurement equations: In the usual attitude determination problem, only the attitude matrix, $A_{I/B}$, is considered an unknown. In the orbit determination problem, only the reference vector, R, is assumed unknown. In coupled attitude/orbit determination, both of these quantities are unknown. It is known that there are three unknown parameters for the attitude and three unknown parameters for the orbital position; therefore, in theory, at least six equations are needed to determine orbit as well as attitude. One good point about this type of equation is that it is applicable in general to different kinds of sensors; whatever errors exist must enter into appropriate quantities in these equations.

The first type of error to be considered is timing error; that is, instead of making the measurement at time t, the actual measurement is made at time (t + Δt). With the timing error considered, the first measurement equation assumes the following form:

$$y_1(t + \Delta t) = [R^1(t + \Delta t)] \, [A_{I/B}(t + \Delta t)] \, [K^B]$$

$$\cong [R^1(t)] \, [A_{I/B}(t + \Delta t)] \, [K^B]$$

$$\cong [R^1(t)] \, [A_{I/B}(t)] \, \left([K^B] + \Delta t \, [\Omega^B] \times [K^B]\right)$$

It can be seen that, generally, timing error does not have much effect on the reference direction sensed. The main effect is that, instead of measuring the component of R along the K direction, the measurement equation is measuring the component along a rotated K direction as a result of the spacecraft angular velocity, e^B. The following equation shows how errors in given quantities enter into the measurement equation:

$$y_1 + \Delta y_1 = \left([R^1] + [\Delta R^1]\right)^T [A_{B/1}^1] \left([K]^B + [\Delta K]^B\right).$$

On the left-hand side of the equation, Δy_1 could stand for instrument reading errors, biases, and so on. It is independent of particular instruments: that is, for different instruments, we may simply have a different bias, and so on. The second quantity, ΔR^1, represents the uncertainty about the reference direction. There may also be uncertainties because the instrument is not sensing the true direction: for instance, ionospheric refractions will result in terms like this. The last term, ΔK^B, represents the instrument alignment errors. So it can be seen that equations of this sort will be applicable to all different sensors, with any errors entering only into the ∂ quantities.

The next topic to be considered is attitude observability. The first basic principle we are concerned with here is that attitude is a relative notion, for although we generally refer to the attitude of spacecraft in inertial space, we could also refer to the attitude of the inertial space relative to the spacecraft. The information contained in one description is, of course, readily transformed to the other, but, conceptually, it often might be clearer to look at the problem one way rather than the other.

Another basic fact is that an attitude has three degrees of freedom and requires at least three independent measurements for determination. In addition, if all three independent measurements are related to only a single reference direction, the attitude cannot be resolved without ambiguity. This should be obvious, since, for a rigid body, the position of any three noncolinear points (or equivalently, two noncolinear vectors) are required to determine its attitude. So if two reference directions in inertial space are known, the attitude of inertial space relative to the spacecraft, and, therefore, the attitude of the spacecraft itself, is known. For directional sensors, of course, attitude observability is equivalent to the observability of two reference directions.

The following equation is an example of the analytical formulation of observability. The unit vectors e_1, e_2, and e_3 represent three reference directions.

$$\bar{e}_1 \cdot \bar{e}_1 = \bar{e}_2 \cdot \bar{e}_2 = \bar{e}_3 \cdot \bar{e}_3 = 1$$

$$\bar{e}_1 \cdot \bar{e}_2 = \alpha, \bar{e}_2 \cdot \bar{e}_3 = \beta, \bar{e}_1 \cdot \bar{e}_3 = \gamma$$

Assume that they are unit vectors and are known in inertial space. The components of these vectors along three spacecraft-fixed directions, r_1, r_2, and r_3, are measured, that is,

$$\bar{e}_1 \cdot \bar{r}_1 = m, \bar{e}_2 \cdot \bar{r}_2 = n, \bar{e}_3 \cdot \bar{r}_3 = p.$$

Taken together, these represent nine nonlinear equations for the nine components of e_1, e_2, and e_3. The attitude observability is equivalent to the uniqueness of the real solutions of these equations, which are not very easy. Since we are not concerned with error at this time, any measurement would correspond to an attitude. Thus there is no inconsistency, and the only concern is whether there is no uniqueness of solution.

In general, the analytical determination of observability is difficult. Figure 3a shows a graphical construction which can help a great deal in providing insight into these problems. In the figure, vector e is a reference direction, and vector r is a spacecraft-fixed direction. A measurement of the component of e along the direction r will limit the reference direction to lie on a small circle, which is the intersection of a plane with the sphere. It would be very convenient to represent directions as well as attitudes on a unit sphere.

Figure 3b shows the second type of measurement, mentioned before, which gives the angle ϕ. In terms of geometry on the unit sphere, it is a half great circle, which represents all possible directions with the same meridional angle ϕ. Since this is a half great circle, it does provide a little more information than the first type of measurement.

Figure 4 shows the result of multiple measurements. It is assumed that two small circle measurements have been made, or that two components of a reference vector have been measured, which can be represented as the intersection of two small circles. In general, there is a twofold ambiguity, because after two components of a unit vector have been measured, the third component is determined up to an ambiguity in its sign. This is reflected by the two points of intersection as indicated in the figure.

Figure 5 shows what happens with half great circle measurements. In general, the intersection of two half great circles would completely define a direction. But these figures show that a combination of the second type of measurement, which is a half great circle, with the first type of measurement, which is a small circle, may still leave some ambiguity.

When two reference directions are available, the results are as seen in figure 6. There are three small circle measurements which give two possible positions of the direction e_1, as shown by the intersection of two circles. The reference direction e_2 must lie on a small circle centered at e_2 as shown in the figure. In addition, A and B intersect, A and C

48

(a)   (b)
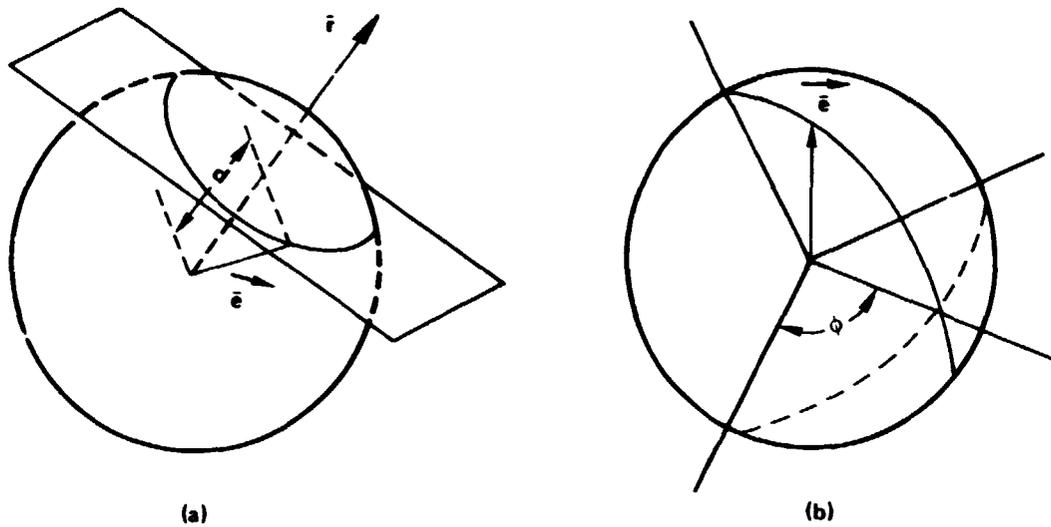
Figure 3. Graphical construction on a unit sphere. (a) Small circle representing all possible $\bar{e}$ which has component d along $\bar{r}$; (b) half great circle representing all possible directions with the same meridional angle ϕ.
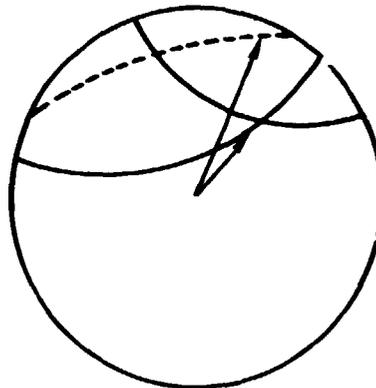
Figure 4. Intersection of two small circles gives two possible directions for $\bar{e}$; only components along linearly independent directions are independent measurements.

do not intersect, and e_1 is known. Also, e_2 has two possible positions, which means there is still some ambiguity in the attitude.

The first conclusion arrived at through these arguments is that, generally, five independent small circle measurements are required to determine attitude. Three of the measurements define one vector completely, and the other measurement, together with the known angle between the two reference directions, determines the other reference direction. Secondly, if we want to obtain attitudes from three measurements, then at least two of these measurements must be great circle measurements. A third conclusion is that, in general, three

49
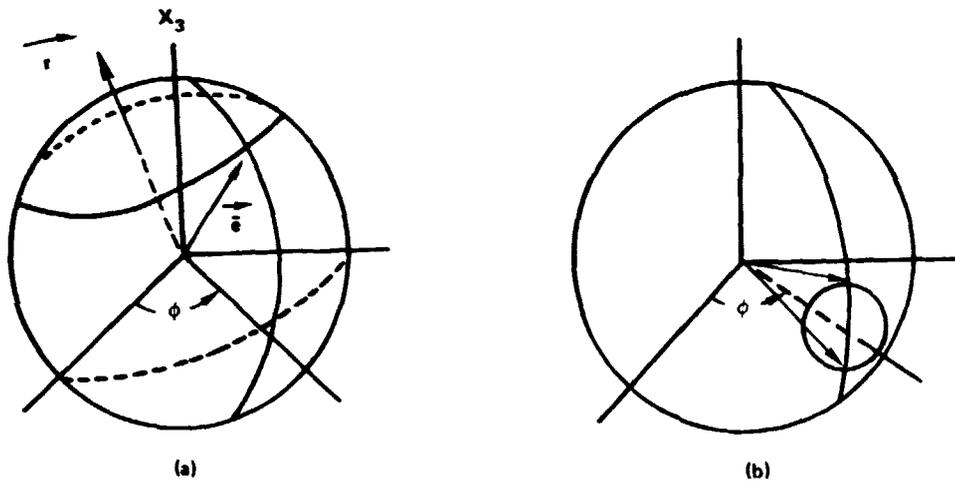
Figure 5. Half great circle measurements. (a) The X_3-r plane is perpendicular to the great circle plane, and $\bar{e}$ is determined uniquely; (b) two possible directions for $\bar{e}$.
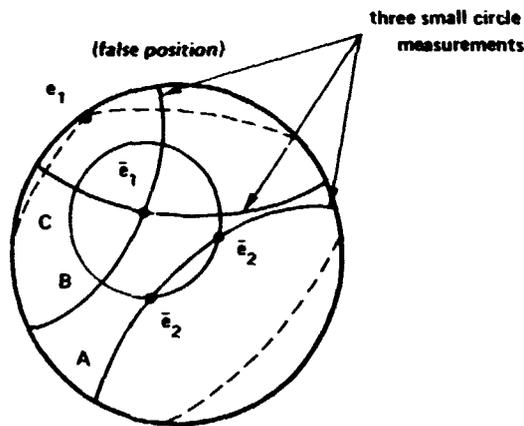
Figure 6. Three small circle measurements concerning two reference directions $\bar{e}_1$ and $\bar{e}_2$.

half great circle measurements plus any additional measurement would result in attitude without ambiguity.

It can also be concluded that attitude measurement based on three small circle measurements of three reference directions requires that the sensors not be on the same plane. This is easy to understand if we invert the role of the attitude of the spacecraft and the attitude of the inertial space; it can then be seen that this case is really the same as that covered by the first conclusion.

Other conclusions are as follows: In general, the symmetrical placement of sensors increases the chance of attitude ambiguity. Although attitude observability is very difficult

50

to determine analytically, a mechanical model of a unit sphere can be constructed, which will readily resolve attitude observability without difficulty. Lastly, although sometimes more than three measurements are required to determine the three attitude parameters, four or five measurements available may also provide some redundancy for data smoothing.

Figure 7 introduces the topic of horizon scanners. The reference direction for the horizon scanner is the local vertical, and when a horizon scanner measurement is made, it means that the scanning ray is tangent to the spherical earth. The information available is the angle between the scanning ray and the local vertical. The measurement equation is given by

$$\cos \theta = \sqrt{1 - \left(\frac{r_e}{r_e + h(\tau)}\right)^2} = -\overline{R(\tau)} \cdot \overline{s(\tau)}$$

$$= \cos a \sin \phi (\tau) - \sin a \cos \phi (\tau) \cos \left\{ \psi (\tau) + \lambda (\tau) \right\} .$$

where

a   =   the half cone angle of the scanner,

τ =   time of horizon crossing,

ϕ =   pitch angle of the scanning axle.

ψ =   roll angle of the spacecraft,

λ =   scanner roll angle, and

h   =   spacecraft altitude.

It is evident from the above equation and from what has been said previously that the horizon measurement does not convey any information concerning the yaw about local vertical.

There is a measurement equation like the above for each horizon transit. Since the scanning speed is fast, it may be assumed in a first approximation that neither the spacecraft altitude nor the attitude has changed from horizon entry to horizon exit. It may then be deduced immediately from the two measurement equations at entry and exit that the spacecraft has a roll angle,

$$\psi = -\left(\lambda + \frac{\Delta \lambda}{\alpha}\right)$$

and a pitch angle,

$$\phi = \mu + \alpha$$

51

or

$$\phi = \pi - \mu + \alpha,$$

where

$$\sin \mu = \left\{ \frac{1 - \left(\dfrac{r_e}{r_e + h}\right)^2}{1 - \sin^2 a \sin^2 \dfrac{\Delta\lambda}{\alpha}} \right\}^{\frac{1}{2}},$$

$$\tan \alpha = \tan a \cos \frac{\Delta\lambda}{\alpha},$$

and $\Delta\lambda$ is the earth width angle as seen by the scanner.
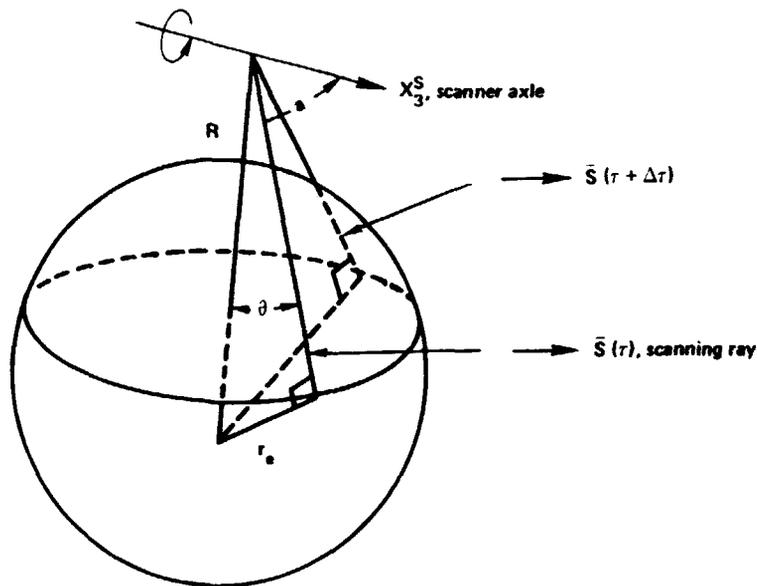
Figure 7. Horizon scanner geometry.

The existence of two possible pitch angles is easy to understand if it is realized that the two horizon measurements are now nothing but two small circle measurements about the local vertical. The extension of this result to higher approximations with the consideration of small attitude changes is straightforward and, in that case, the horizon measurements will relate to the spacecraft attitude as well as attitude rate.

Sometimes two scanners with different half cone angles a' and a'' are mounted on the same axle. In that case, the first approximation pitch angle becomes

52

$$\phi = \tan^{-1} \left(\frac{\sin a' \cos \dfrac{\Delta\lambda'}{\alpha} - \sin a'' \cos \dfrac{\Delta\lambda''}{\alpha}}{\cos a' - \cos a''} \right)$$

The redundancy eliminates the pitch angle ambiguity and the need for altitude information and also provides smoothing for the roll information.

Actual measurements are often transit times rather than scanning angles and earth width. The time information is transformed to angular information using the scanning rate, and any bias in scanning rate will amplify with time. Therefore, without periodic reinitializations, the spacecraft roll, which is directly related to the scanning angle, cannot be determined accurately. On the other hand, the pitch angle is related to the earth width and is more susceptible to triggering errors.

DESCRIPTION OF THE ROTATIONAL MOTION OF A NONSYMMETRIC RIGID BODY IN TERMS OF EULER ANGLES, DIRECTION COSINES, AND EULER PARAMETERS

H. S. Morton
University of Virginia
Charlottesville, Virginia

The rotational motion of a nonsymmetric rigid body can be described by a set of three time-dependent Euler angles. In the torque-free case, the natural angles are the 1-2-1 or the 1-3-1 Euler angles if the angular momentum axis coincides with the space 1-axis, the 2-3-2 or 2-1-2 angles if it coincides with the space 2-axis, or the 3-1-3 or 3-2-3 angles if it coincides with the space 3-axis. In each case, the first angle satisfies a differential equation whose solution can be simply expressed in terms of theta functions, which can be readily computed with the aid of rapidly-converging series. One can then determine the nine direction cosines and/or four Euler parameters, whose transformation properties are more convenient than the Euler angles. The 2-3-2 or 2-1-2 angles offer certain advantages if the body 2-axis is the principal axis of intermediate inertia. The analytic torque-free solutions provide a good base for studying the motion of a nonsymmetric rigid body in the presence of perturbing torques.

ATTITUDE CAPTURE PROCEDURES FOR GEOS-C

G. M. Lerner
Computer Sciences Corporation
Silver Spring, Maryland

The scientific objective of the GEOS-C mission is to perform experiments to apply geodetic satellite techniques to solid-earth physics and oceanography. A spaceborne radar altimeter will map the topography of the ocean surface with a relative accuracy of ±1 meter.

To meet the objectives of the radar altimeter experiment, GEOS-C will be gravity-gradient stabilized in a nearly circular orbit at an altitude of 843 km. The orbital inclination will be 115° to maximize experimental coverage in the North Atlantic Ocean. A 21.5-ft, extendable scissors-type boom with a 100-lb end mass will provide passive pitch and roll stabilization and a momentum which will provide yaw stabilization. An eddy-current damper and magnetic coil are also provided.

Because no active attitude control hardware is provided and damper time constants are large, a detailed capture strategy has been developed at Computer Sciences Corporation (CSC) in coordination with AVCO and the Johns Hopkins Applied Physics Laboratory. This strategy has evolved from many detailed simulations and requires real-time attitude determination support for the initiation of critical commands.

POTENTIAL GEOSYNCHRONOUS ORBIT/ATTITUDE RESOLUTION USING LANDMARK DATA

C. C. Goad*

Wolf Research and Development Corporation
Riverdale, Maryland

The information content in data other than conventional radar tracking is gaining increased popularity. This paper presents a covariance analysis of reducing the orbit and attitude state from landmarks (ground-truth) data extracted from images taken at geosynchronous altitude.

It is shown that comparable accuracy can be achieved with landmark data alone when compared with current optimistic reductions using conventional types of data.

*Currently at National Oceanographic and Atmospheric Administration, Rockville, Maryland.

DETERMINATION OF ORBITAL POSITION FROM EARTH AND SUN SENSOR DATA ON SMS-A AND IMP-J

H. L. Hooper and M. A. Shear
Computer Sciences Corporation
Silver Spring, Maryland

Attitude data from earth and sun sensors on SMS-A and IMP-J were processed in an attempt to refine the orbital elements as determined from tracking data. The results were checked against additional tracking data and the discrepancies were investigated. The results have implications for the accuracy obtainable with any orbit-dependent attitude sensor.

57

ON-LINE ORBIT DETERMINATION AND ESTIMATION
FOR ATS-6 FROM REDUNDANT ATTITUDE SENSORS

T. S. Englar, Jr.
Business and Technology Systems, Inc.
Seabrook, Maryland

ATS-6 is equipped with an onboard, two-axis interferometer which can provide direction cosines to earth-based transmitters. In addition, the spacecraft carries an earth scanner which can be thought of as an additional two-axis interferometer with transmitter at the earth's center. From the six-direction cosines thus available, both position and attitude determination can be performed. This paper describes a procedure proposed for use both in the SAPPSAC experiment on ATS-6 and in the ATS-6 on-line attitude determination program at GSFC which decouples position determination from spacecraft attitude. The resulting position pseudo-measurement is used in a constant gain Kalman filter for estimation of orbit state. Propagation of the state estimate is accomplished with circular orbit perturbation equations.

58

THE OPTICAL SLIT SENSOR AS A STANDARD SENSOR FOR SPACECRAFT ATTITUDE DETERMINATION

James Wertz
Computer Sciences Corporation
Silver Spring, Maryland

The idea for using an optical slit sensor as a standard sensor for spacecraft attitude determination arose during a brainstorming session of the First Goddard Standardization Meeting on June 6, 1975. This paper describes the basic concept of the slit sensor, indicates what information is available from a single sensor and from two sensors, describes one possible standard sensor package, and compares the standard sensor package with the attitude package flown on the first Synchronous Meteorological Satellite (SMS).

The slit sensor concept is one which has exciting potential as a standard attitude sensor for an enormous variety of missions, specifically, any mission using a spinning spacecraft or where rotating sensors or mirrors could be used. At present we are still in the stage of analytic studies—no experiments or design studies have been made. However, past experience suggests that such sensors are feasible and should be relatively easy and cheap to build.

The basic idea of a slit sensor is simple, as shown in figure 1. It consists of one, or perhaps two, narrow slits with a 180° field of view capable of triggering on both the earth and the sun and distinguishing between them. There is no angle measurement per se. There is simply a voltage change or pulse as the sensor crosses the sun or enters or leaves the di   f the earth. The slit scans the sky by being mounted parallel to the spin axis on a sp... ig spacecraft, by rotating itself, or by looking into rotating mirrors on a nonspinning spacecraft.

The major advantage of such a sensor is that it sees the entire sky. If the earth and the sun are visible, it will see them. Equally important, however, is that the slit sensor returns a wealth of attitude data that is both easy to interpret and particularly amenable to sophisticated analysis techniques.

It is important to keep in mind that the idea presented here is a standard sensor concept rather than a single piece of hardware; that is, we are interested in standardization of style and in manner of use. This implies great cost reduction, with little or no loss, and, in fact, possibly some gain in the versatility for individual missions.

The greatest economy probably comes from the fact that there is only one ground processing package, thus reducing the development costs. On the other hand, the experience

base that is gained provides economy, reliability, and confidence. There will be some degree of package duplication, and this will certainly reduce hardware costs for some missions. At the same time, the mission planner is free to adjust a variety of physical parameters to meet his needs, or to take advantages of advances in hardware or software design. In addition, the mission attitude analyst is free to concentrate his efforts on improving quality and accuracy of results without constantly having to start over by developing new models or combining a variety of old models for each new mission.
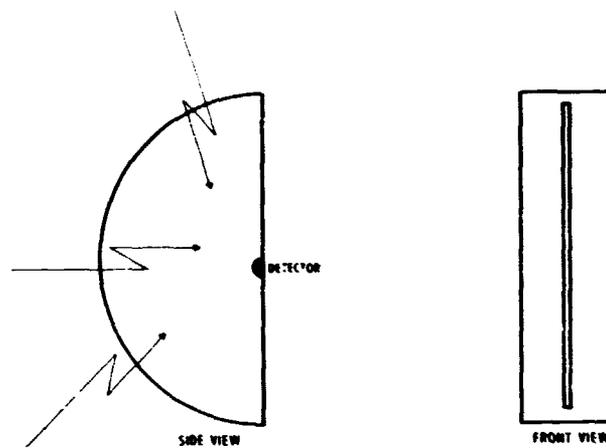
Figure 1. Optical slit sensor.

It has been indicated that a wealth of attitude information is available from the slit sensor or sensor package. Next I will briefly describe the type of information obtained, and then compare it with that available from sensors actually flown on the recently launched SMS-A.

In examining the information available from a single sensor as shown in figure 2, the most obvious data is a dihedral angle from the sun to the earth, measured to the earth midscan (D). However, this could also be measured to earth-in or earth-out for purposes of redundancy. A second type of data is the nadir angle, or the angle from the spin axis of the spacecraft to the center of the earth, which is available from earth-width measurements. Figure 3 is a plot of nadir angle versus earth-width angle, with nadir angle along the vertical axis and earth width along the horizontal axis. As can be seen from the figure, as the earth moves toward the sensor poles, it will subtend a larger dihedral angle. Therefore, the earth-width angle can be used as a measure of the nadir angle.

There are two regions where there is some difficulty with this measurement: In the vicinity of the spin plane, the earth-width measurement is relatively insensitive to the nadir angle, and, in the vicinity of the poles, the sensor never leaves the disk of the earth. Thus, there is not particul. y good attitude information in two regions—along the Equator and in the region of the poles. However, there is a large region in between where high quality attitude information is available.

60

W = EARTH-WIDTH DIHEDRAL ANGLE

D = SUN-TO-EARTH MIDSCAN
    DIHEDRAL ANGLE
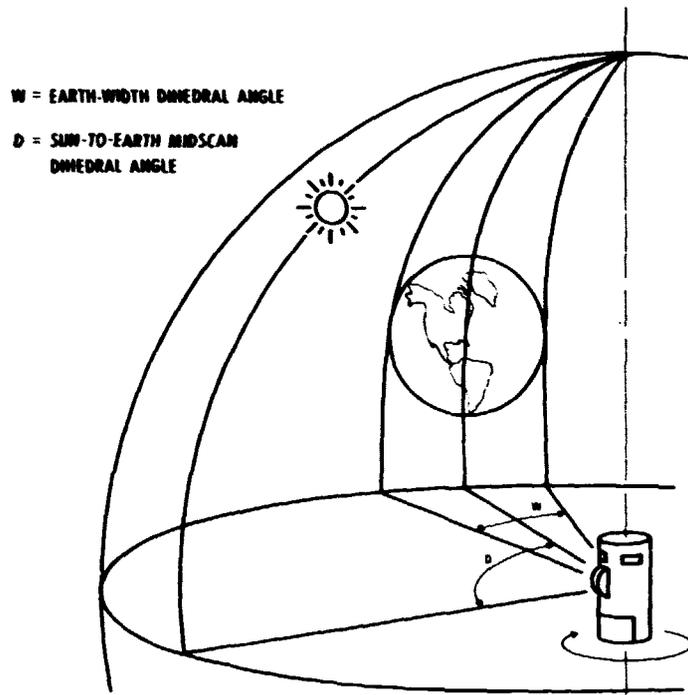
Figure 2. Information available from a single sensor.

Both of these measurements are available from just the presence of simple pulse. If the total illumination following on the slit sensor is monitored, then additional information is available which can provide the nadir angle in the vicinity of the poles. That is, specifically, if the total illumination output from the slit sensor is monitored, then this will be a sinusoidal oscillation. The amplitude of the sine is a measure of the nadir angle, and the phase of the sine relative to the sun is a measure of the dihedral angle from the sun to the center of the earth.

This information alone is sufficient for attitude determination; therefore, we could stop with a single sensor. However, the information would be of relatively poor quality at nadir angles near 90°, which are relatively common, and near the poles the information depends on intensity measurements. Bias determination and in-flight calibration would both be difficult.

Thus, it is worthwhile to consider the nature of information available from a second sensor. In particular, if the second sensor is mounted at an angle to the first, rather than parallel to the spin axis, then there will be a great deal of additional information rather than just redundancy. Slightly different information would be available, depending on whether the second sensor looks into the same hemisphere as the first or is canted somewhat so it can see slightly up or down. For the sake of concreteness, the results of a 360° sensor will be considered, but this is by no means necessary to take advantage of the second sensor.

61
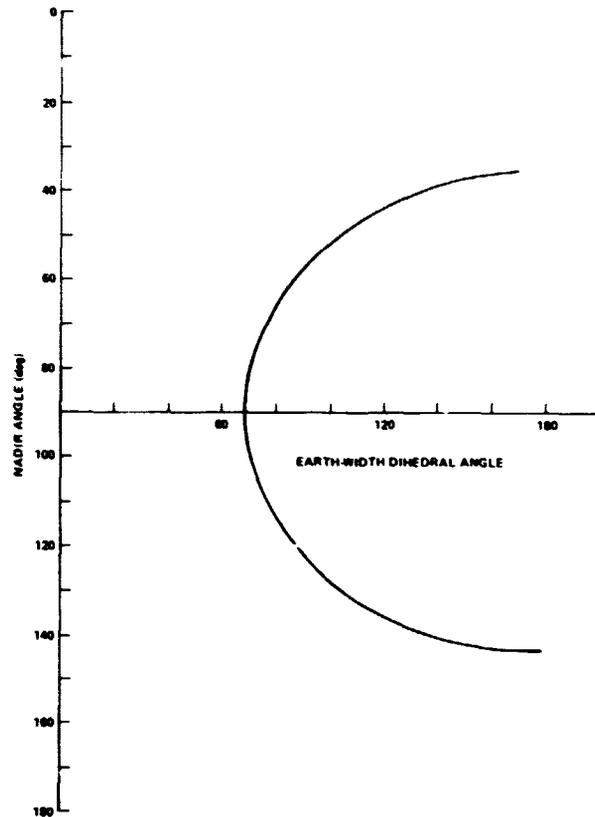
Figure 3. Nadir angle versus earth-width dihedral angle for
vertical slit sensor and 70° diameter earth.

There are measurements available from a second sensor that are similar to those from the
first sensor, but there are important differences as well. The dihedral angle from the sun to
the earth is measured between two planes that do not contain the spin axis, and the nadir
angle from earth widths (shown in figure 4) comes closer to the poles.

Specifically, if ρ is the angular radius of the earth and θ is the angle at which the second
sensor is tilted to the first, then the nadir angle measurement will come within ρ-θ of both
poles. Thus, full sky coverage in the nadir angle is available by tilting the second sensor
at an angle equal to the angular radius of the earth at whatever distance the spacecraft is
operating. The intensity measurements are the same at the pole as well, if we wish to use
them; and the same problem exists around the Equator where the earth width is relatively
insensitive to the nadir angle.

However, in addition to these two measurements, there are two measurements that are
available from two slit sensors which are not available from either sensor singly. In par-
ticular, there is a sun angle from the sensor crossing times, and, as illustrated in figure 5,

62
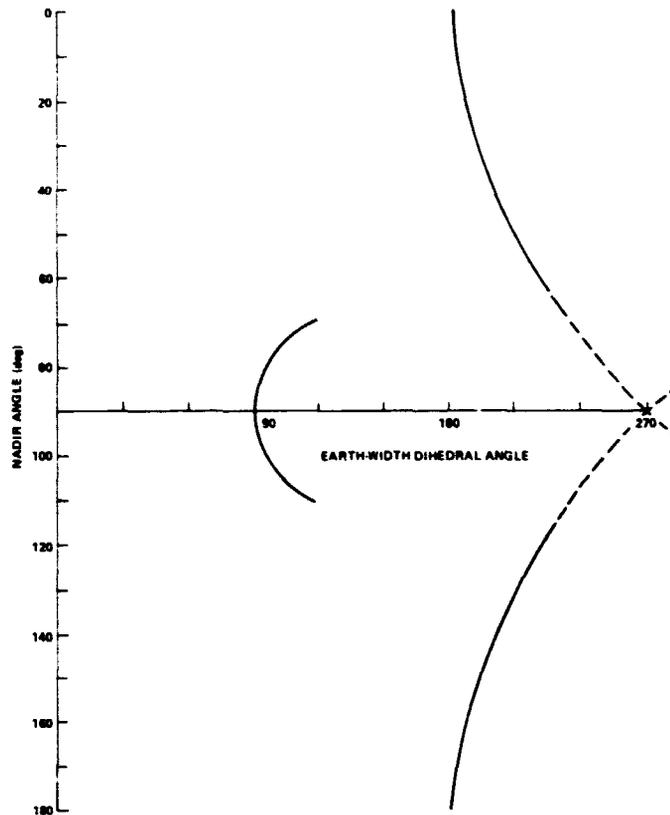
Figure 4. Nadir angle versus earth-width dihedral angle for
360° field of view slit sensor 35° from vertical and 70˝
diameter earth.

there is a third independent measure of the nadir angle from the midscan crossing times.
Here again the nadir angle is the vertical coordinate and the midscan-to-midscan dihedral angle
is the horizontal coordinate. It can be seen in the figure that there is now particularly good
data in the vicinity of the Equator, with good distinction of the nadir angle. In addition,
since the two hemispheres are different, we no longer have the problem of ambiquity about
two possible solutions. Therefore, one needs no a priori information at all in order to use
this procedure to find the attitude.

The following is a summary of the measurements that are available from two nonparallel
slit sensois: There is one sun angle measurement, two independent measurements of the
sun-to-earth midscan dihedral angle, and two earth-in measurements and two earth-out
angles available for redundancy purposes. There are three independent mea. urements of
the nadir angle. In addition, if we are willing to monitor the total illumination falling on
the slit sensor, then there will be two additional independent measurements of the nadir
angle available. So it is seen that two slit sensors provide essentially full sky coverage
with abundant attitude data.
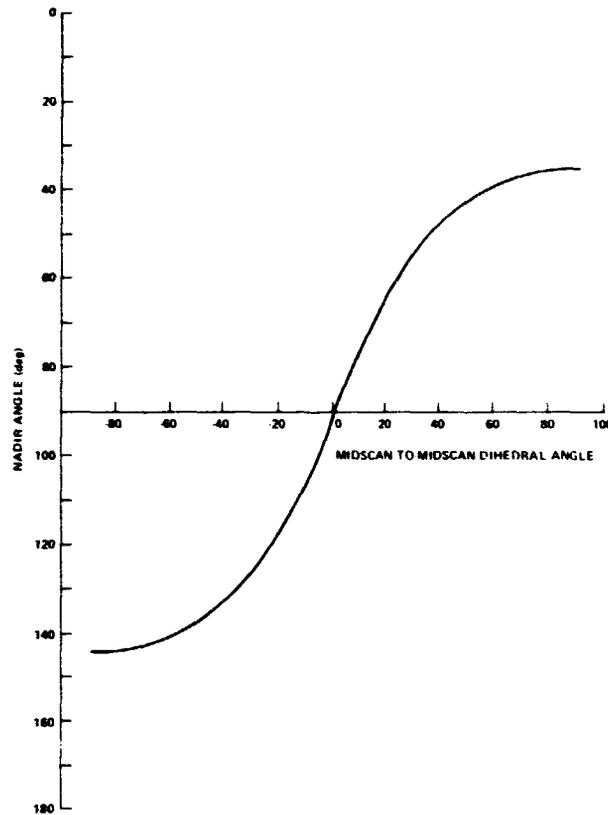
Figure 5. Nadir angle versus dihedral angle from midscan of vertical slit sensor to midscan of 35° off vertical slit sensor for 70° diameter earth.

Given the general concept of attitude determination with a pair of optical slit sensors, it should be possible to incorporate these sensors into a standard attitude package. The key to a standard sensor package is versatility; that is, a variety of sensitivity levels, a variety of spectral regions, and a variety of angular orientations. For example, the most likely spectral region for normal operation would be the infrared, since this provides well-defined earth horizons and intensity levels such that a single sensor could trigger on both the sun and the earth. At the same time, it is desired to incorporate the possibility of other intensity levels and other spectral regions for triggering on different celestial objects.

There are many possible configurations for a standard sensor package. One possible configuration, shown in figure 6, consists of three sensors mounted on a single plate: One sensor would be parallel to the spin axis of the spacecraft and two would be tilted at adjustable angles. In normal operation, the vertical sensor and one of the others would be used for attitude, and the third sensor used purely for purposes of redundancy. Any two sensors could provide high quality attitude information over all, or nearly all, of the celestial sphere, and any one could provide adequate information over most of the celestial sphere.

64
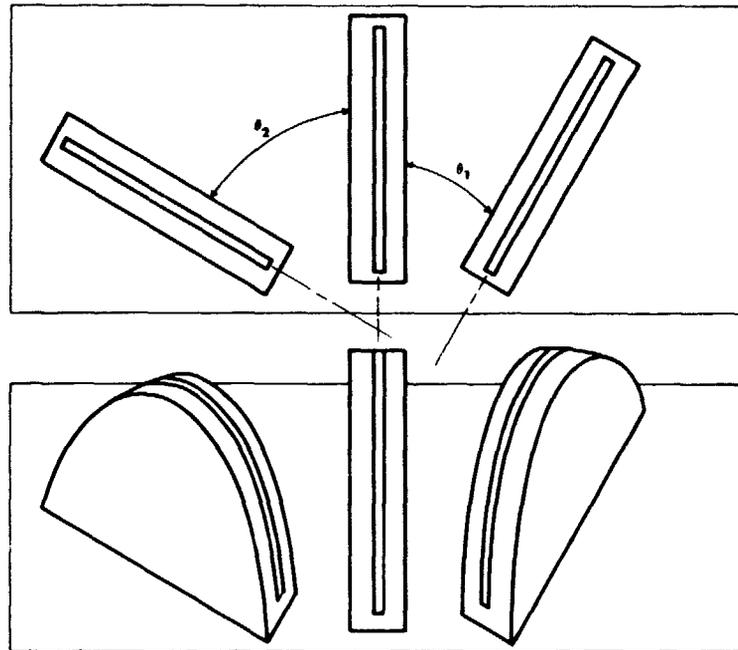
Figure 6. Slit sensor package.

So far we have discussed the general characteristics of slit sensor behavior. Now we will compare the analytic performance of a slit sensor package with the attitude package flown on the first SMS, which was launched on May 19, 1975, into a transfer orbit and was eventually placed in a circular synchronous orbit near the Equator. It should also be pointed out that, relative to Mr. Goad's presentation, we are interested here only in the attitude sensors themselves, and not attitude determination from the visible and infrared spin scan radiometer (VISSR).

There were seven attitude sensors actually flown on the SMS: two sun sensors, each with a field of view of $120°$ and five earth sensors: two primary earth sensors at $4°$ above and below the spin plane that were used for attitude determination in mission orbit and three other sensors that were used primarily for attitude in the transfer orbit. We will compare this with a slit sensor package consisting of three attitude sensors: one sensor that is parallel to the spin axis and two which are tilted, one at $8.5°$ and the other at $30°$ in the opposite direction.

Accurate spacecraft attitudes require that sensor biases be accurately known. Therefore, it is of interest to determine how many biases would need to be measured to use the sensor information with precision. In the package flown there are 20 total biases (two plane tilt, six azimuth, five triggering level, and seven elevation angle), which, as a purely practical matter, tells us that some selection will be necessary. There is essentially no chance of determining 20 biases from the data that are available from the spacecraft. The slit sensor package has a total of eight biases (three plane tilt, two azimuth, and three triggering level) that would need to be determined for all of the sensors to be utilized.

65

In normal circumstances, however, all the sensors in either package will not be fully utilized, and all of the biases will not need to be determined. Specifically, in both cases, a minimum of five biases is required for accurate attitude determination. However, it should also be pointed out that these five minimum biases for the sensor packages flown provide accurate attitudes only near the mission orbit and, in particular, do not provide accurate attitudes during most of the transfer orbit or during any other maneuvers or mishaps that might occur. On the other hand, since one sensor is fully redundant in the slit sensor package, the five minimum biases there provide accurate attitudes over the entire celestial sphere, including both the transfer orbit and the mission orbit.

Given the geometry of the sensor package, it is straightforward to calculate the portion of the celestial sphere covered by each sensor and the variety of independent measurements available for attitude determination. In particular, for the sensor package that is flown, there are two sun angle measurements over 50 percent of the sky and one sun angle measurement over the remaining 50 percent, such that the sun is fully covered with the package flown. In the slit sensor package, there are three sun angle measurements available over 87 percent of the sky, one measurement over 12 percent, and there is no sun angle measurement at all for 1 percent of the sky.

If the attitude is at orbit normal, and if the satellite is in an equatorial orbit, then in the package flown there are four sun-to-earth midscan dihedral angles available, and there are three such angles available with the slit sensor package. However, those three angles with the slit sensor package are available if it is required that the same sensor be used for both sun triggering and earth triggering. If you allow the sun to trigger with one sensor and the earth to trigger with another, then there are a total of nine sun-to-earth dihedral angles with the slit sensor package.

There are two earth-width dihedral angles over 9 percent of the sky with the sensor package flown: There is one measure over just slightly less than half of the sky, and there is no earth-width measurement at all over 42 percent. On the other hand, with the slit sensor package, there are three earth-width measurements over 93 percent of the sky, two over 6 percent, and one measurement over the remaining 1 percent, such that the sky is fully covered.

In addition to this, there are three midscan-to-midscan nadir angle measurements over 93 percent of the sky with the slit sensor package and one measurement over 6 percent. This measurement is not available at all from the attitude package flown.

Thus, the results here indicate that the slit sensor package has substantially more independent attitude measurements over more of the sky than the attitude package flown, even though the package flown has more than twice the number of sensors. From an analytic point of view, the slit sensor package should give better attitude results from this information.

Another characteristic of importance is sensor redundancy. That is, what information is left if the single most critical sensor for a particular measurement or a particular region of the sky is lost. With the sensor package flown, the loss of one critical sensor would be a moderately

serious problem, since we are guaranteed coverage of the earth over only 9 percent of the celestial sphere. The sun presents fewer problems, since there we are guaranteed coverage over 50 percent of the sky. With the slit sensor package, the loss of one critical sensor would be essentially no problem, since one of the sensors was intended to be redundant in any case. The earth and sun sensing are 100 percent covered; the sun angle measurement is at least 87 percent covered.

The loss of two critical sensors would be a very serious problem for the attitude package flown. All of the sun or all of the earth observations could be lost. It would also be a problem for the slit sensor package. All of the sun angle and midscan-to-midscan nadir angle measurements would be lost. However, the sun-to-earth dihedral angle and the er th-width angles would still be available over at least 87 percent of the sky. Thus, it should still be possible to do attitude determination. However, the accuracy or bias determinati... characteristics could be impaired.

If we lose three critical sensors in the slit sensor package, which has only three sensors, the spacecraft is obviously fully blind. In the attitude package flown, the spacecraft would be essentially blind. In some configurations, it is possible that there would be one observation still in existence, however, it is unlikely that attitude determination could be done with that one observation.

Lastly, there is the question of attitude accuracy, which requires a good knowledge of the sensor biases. A major factor in the accuracy with which biases can be determined is the coverage of the celestial sphere for each individual sensor. In the normal course of a mission, there are transfer orbits, inversion maneuvers, and so on. Each sensor will encounter a variety of geometries. As more coverage of the sky is available, more data from these different geometries will be provided, and the biases can be better determined, for two reasons. The most obvious, of course, is that there is more information available. In addition, there is a greater variety of geometries, and, in general, it is the variety of geometries which allows us to distinguish between sensor biases.

Thus, it is worth examining the sky coverage of individual sensors for purposes of bias determination. With the attitude package that was flown on SMS, the sun sensors both covered 75 percent of the sky. When sensing the sun, the slit sensor package would cover anywhere from 87 to 100 percent of the sky. (The parallel sensor would cover 100 percent; the $+8.5°$ sensor, 99 percent; and the $-30°$ sensor 87 percent.) Thus, the two packages would be essentially equivalent in this regard, with a very slight advantage, perhaps, going to the slit sensor package.

However, when sensing the earth, there is a major difference. With the attitude package flown, the earth sensors cover only 20 to 29 percent of the sky. (The $±4°$ sensors would cover 29 percent; the $+20°$ sensor, 28 percent; the $-25°$ sensor, 27 percent; and the $-48°$ sensor, 20 percent.) However, when sensing the earth, the slit sensor package would cover 93 to 100 percent. With the parallel sensor, coverage would increase from 99 to 100 percent if an intensity measurement in the vicinity of the poles is used, rather than simply a pulse

measurement. So it is clear from this information that the slit sensor package would provide much better bias determination, for two reasons: There are fewer biases to be found, and those which are necessary are easier to determine.

Thus, for SMS, it is seen that the slit sensor package has less than one-half the number of sensors that the flown package has, yet these would provide more independent attitude measurements over more of the sky, substantially greater redundancy, and far better bias determination characteristics than the flown sensors. One advantage of the slit sensor package is that it is inherently simple. (It is possible to envision a prototype made out of a tunafish can and a photocell). A second major advantage is that it is exceptionally versatile in two senses: It obviously has full sky coverage, which allows for more independence of mission details, but probably more important is the great mechanical versatility. That is, the same sensor can be used with changes in mechanical or electrical parameters to fit the particular mission at hand. Therefore, a single ground processing package could be used for a large number of missions.

For example, we could change the tilt of the second sensor to provide the best pole-to-pole coverage for a particular mission. On some missions, it might be possible to use a tilted sensor that has two stops for different conditions where accurate attitudes are desired. Also, the triggering levels could be changed to fit the particular needs at hand. In theory, the same sensors aboard the same spacecraft could be used in transfer orbit 322 km (200 miles) above the surface of the earth as halfway to Mars, by simply changing the triggering levels and triggering on Mars and Jupiter as point sources and measuring their nadir angles with respect to the spin axis of the spacecraft.

The slit sensor works on any spinning spacecraft. On any despun spacecraft, it can work by either rotating the sensors or by allowing them to look into one or more rotating mirrors.

It is difficult to find any disadvantages from an analytic point of view, although, of course, such a sensor system may be physically unbuildable. One minor disadvantage is that a slit sensor's response to the earth is not a square wave, as it is with point sensors. It rises to a maximum at the center of the earth and falls off toward the edges, which implies that the slit sensor might yield substantial triggering level biases. However, triggering level biases are by far the easiest to resolve by ground processing, and therefore this is unlikely to be a serious difficulty.

In summary, the optical slit sensor appears to be a versatile idea. It may be remarkably close to what is needed for modern space flight—a single standard attitude sensor with enormous versatility in its application.

68

ON THE DEVELOPMENT OF PRACTICAL NONLINEAR FILTERS

H. W. Sorenson
Applied Systems Corporation
San Diego, California

The general problem of estimating the state of a nonlinear, time-discrete system from noisy measurement data is considered from the point-of-view of developing feasible computational algorithms for evaluating the Bayesian recursion relations. Algorithms which have been proposed are reviewed, the computational implementaion of these algorithms is discussed, general conclusions coming from numerical studies are noted, and areas requiring additional research are defined.

CONVERGENCE CHARACTERIsTICS OF BATCH AND SEQUENTIAL ESTIMATION ALGORITHMS

B. Schutz

University of Texas

Austin. Texas

The convergence rate and radius of convergence of the batch, and the extended sequential estimators are compared. The converge. e behavior of the two processors in the presence of both observable and unobservabe parameters is considered.

MANEUVER STRATEGY DESIGN FOR MARINER/JUPITER/SATURN AUTONOMOUS GUIDANCE AND NAVIGATION

T. Hagar
Jet Propulsion Laboratories
Pasadena, California

Candidate maneuver strategy algorithms for multiple and quasi-adaptive midcourse maneuvering are presented. Application of these techniques to the Mariner/Jupiter/Saturn 1977 mission, and as possible candidates for autonomous navigation and guidance, is discussed.

CONSIDERATIONS FOR LARGE SPACE TELESCOPE
(LST) MISSION EFFECTIVENESS

J. Tuttle
Martin Marietta Corporation
Denver, Colorado

In designing the support systems module for the LST, consideration must be given to hardware limitations and mission design requirements. Special software has been developed to analyze these sometimes conflicting requirements. This talk will discuss the software and analysis made for the LST study.

SOLAR ELECTRIC PROPULSION

Richard W. Barbieri
Goddard Space Flight Center
Greenbelt, Maryland

Solar electric propulsion is certainly not a new concept. Indeed, it has been with us since the early 1900's. But what is new is a growing awareness that solar electric propulsion offers a rather interesting alternative approach to study the earth and its environment and the solar system.

This paper will cover some problems that we face in low-thrust mission analysis. After some preliminary comments about hardware and pe: ormance parameters, concern will be devoted to the development of a nominal low-thrust trajectory and to the guidance and navigation problem.

To put things into perspective, we should first discuss the major components of a solar electric propulsion system. It can be broken down into three major subsystems: One is a primary power source, which could be made up of batteries, solar cells, and reactors. Its function is to convert thermal or solar energy into electrical power. The second subsystem is a power conditioner and electrical control, which supplies specified levels of voltage and power to the heaters, valves, and thruster electrodes. In effect, it is an electrical power distribution center. The third subsystem is the engine, in which are included the thruster, fuel tanks, and propellant and control system.

Figure 1 shows a comparison of some performance parameters of both chemical and ion propulsion systems. It can be seen that the chemical systems have a thrust-to-weight ratio ranging from about 10 to 10^{-3} g, operating with a specific i.t ·ulse (I_{SP}) in a range of perhaps 90 to 250 seconds. The ion propulsion systems, on the other hand, operate with a thrust-to-weight ratio of about 10^{-4} to about 10^{-6} g, with a specific impulse ranging from 2000 or 3000 seconds up to as high as about 11,000 seconds.

The nuclear propulsion systems fit in this range of 1 to 10 g. Arc jets also fit into this range and overlap the chemical systems and ion propulsion systems as far as thrust-to-weight ratio is concerned.

The low thrust system then provides a very high total velocity increment, and it does this by providing ΔV at a very low acceleration over a long period of time at very high specific impulse. The high specific impulse in effect translates to a smaller amount of propellant that has to be carried on board.
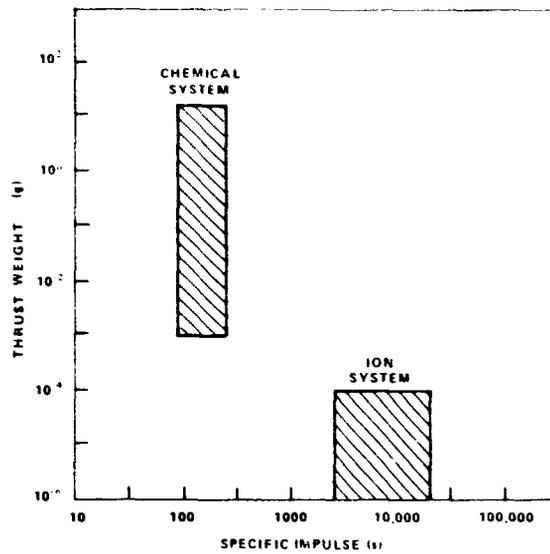
Figure 1. Comparison of performance parameters
of chemical and ion propulsion systems.

Figure 2 shows what might be expected from a low-thrust propulsion system. The terminal mass-to-initial mass ratio is plotted against flight time in days; parameters are given for specific impulse and also for input power to the thruster-to-initial mass ratio (P/M_0).

The Solar Electric Rocket Test-C (SERT-C) mission is a study to place a spacecraft into a 3100-km circular orbit and slowly spiral out to geosynchronous orbit. The spacecraft will lift off with roughly 821 kg (1810 lb), with a specific impulse of roughly 3000 seconds for the transfer orbit engines, which are about 30-millipound thrusters, and with an expected flight time of about 290 days. The SERT-C has a P/M_0 ratio of roughly 4.2 and a terminal mass-to-initial mass ratio of about 0.85. It will get into synchronous orbit with roughly 703 kg (1550 lb) after lifting off with about 821 kg (1810 lb), a fairly high payload ratio.

At the beginning of prelaunch analysis is the task of generating a nominal trajectory, which is usually optimal in some sense. This is where we encounter our first set of problems.

There are certain phenomena peculiar to low-thrust problems, which must be modeled if we are to simulate a low-thrust trajectory with any semblance of accuracy: The first three items—geopotential, N-body, and solar radiation pressure—are not really peculiar to low-thrust systems but certainly must be included in a nominal trajectory algorithm. We have some experience with ballistic high-thrust-type missions with these three items.

The next item, solar array interactions with the environment, are peculiar to low-thrust systems, since the array is the source of power to all spacecraft systems. A model of the radiation belt is required here, and the development of such a model will be akin to the development of the atmospheric density models we have had over the last 15 years. In both cases, we try to construct models for stochastic processes. Atmospheric scientists may

74
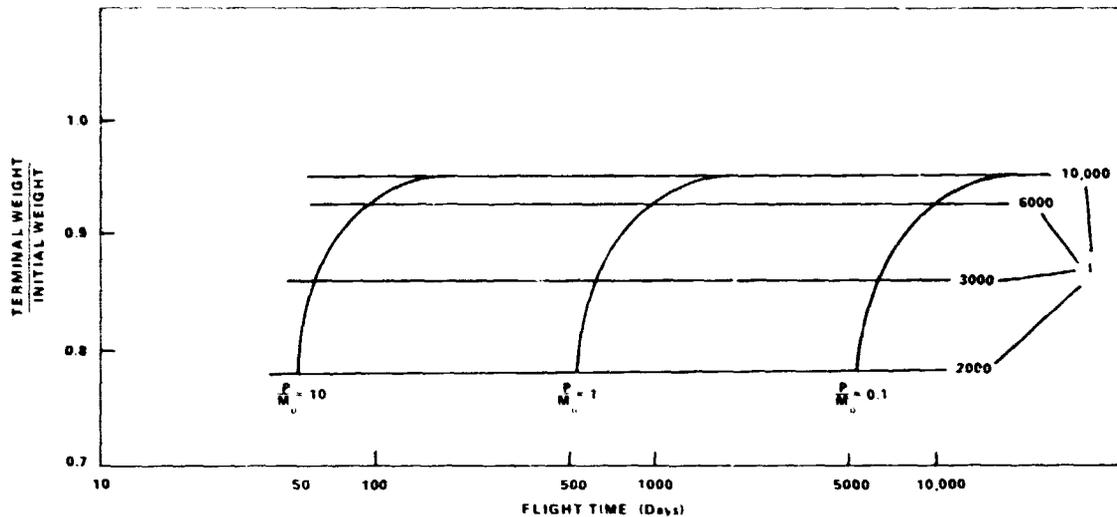
Figure 2. Parameters of low-thrust propulsion system.

have ex| ertise in the development of radiation belt models, but those of us who are concerned with guidance and control and spacecraft systems are relatively unfamiliar with these models: for instance, what kind of assumptions must be made to develop a working model to be inserted into a trajectory generator algorithm.

Another phenomenon to be considered is the solar array degradation, which is closely related to the radiation belt model. For example, silicon solar cells can withstand a radiation dosage of perhaps 10^{14} 1-MeV electrons. However, the radiation that might be experienced is perhaps two orders of magnitude larger than that. Such a dose, 10^{16} 1-MeV electrons, will have dire consequences on the available power to the thruster s. In particular, it could degrade the solar array power by as much as 40 to 50 percent of its beginning-of-life power, which, for the SERT-C mission, for example, is about 9 kW. Consequently, we are forced to protect the solar cells with a thin coating of material about 76 to 152 μm (0.003 to 0.006 inch) thick. Even so, the degradation must be modeled and will be a strong function of the thickness of the protective coating and of the type of material used in this coating.

The last item to be considered is shadowing, which has been encountered before with regard to solar radiation pressure. Now we must be concerned about it to determine the solar array and thruster performance during passage through shadow regions, in particular, during the thruster on/off times. The question is how long it takes the system to get up to full power after passage through shadow, and it happens that we do not have an answer at this time. Upon exit from shadow, for example, we know that it is going to take at least 10 minutes to go through a preheat and controlled loop sequence. It is after this time that the thruster will operate at full power, which is expected to be a function of duration in shadow.

the behavior of the a priori thruster biases after restarting the ons are that such biases remain the same after restart, but detailed investigations warranted. The implication is that if such biases do change, then, for

75

the earth orbiting mission with solar occultation and thruster restarts quite frequent, the orbit determination process must reestimate these biases. Such frequent estimations could lead to significant orbit uncertainty, and this, in turn, has serious implications on the guidance policy.

Having made these comments about the trajectory generation problem, we now turn our attention to the guidance and navigation aspects. I think it is safe to say that, of the small amount of work that has been done in the past in low-thrust mission analysis, little has been devoted to guidance and navigation. The problems here are difficult, and the opportunities for optimization studies abound.

Environment and degradation models have already been mentioned. The same models which reside in the trajectory generator algorithm could certainly be used in the guidance and navigation algorithm. It must be emphasized that, in missions of this type, guidance and navigation are strongly coupled together because of the presence of a stochastic, continuously acting force.

Another aspect of guidance and navigation is the thrust vector model, which can be structured as a constant, as a constant plus noise, as a first- or second-order Markov process, or as a fully stochastic phenomenon. The first option is quite unrealistic. The fourth option leads us to extremely difficult mathematical problems, since it forces us to integrate random non-linear differential equations—nonlinear differential equations are difficult enough. Thrust magnitude depends on ion beam current, total accelerating potential, mass utilization efficiency, effective specific impulse, and numerous other parameters, each possessing a bias and time-varying components, which, when combined, may yield a standard deviation of about 5 percent of nominal thrust magnitude. But this is just a preliminary estimate. It could possibly get worse than 5 percent. The pointing error, on the other hand, is a function of launch vibration, thermal distortion of the grids, and accelerated grid wear, in addition to improper knowledge or measurement of the thruster misalignments, gyro drift, misalignment, and other parameters. Therefore, modeling the thrust vector as a constant is not realistic.

The next item is thruster orientation with respect to the solar array. If the engines are not gimballed, then the optimal orientation of the solar panels will not induce an optimum orientation of the thrust vector and vice versa. This problem is one that really warrants many trade-off studies. Even if engines are gimballed and some freedom for the thrusters is allowed, optimization and trade-off studies must be carried out with respect to the relative orientation of the thrusters with respect to the solar array at various points of the mission.

The last point to be discussed is the type and number of observations, two factors strongly affecting the navigation accuracy, which significantly impacts the guidance policy. One particular data type is that obtained from accelerometers. Because a low-thrust vehicle is thrusting over long periods of time, and because small deviations in the thrust direction and magnitude significantly alter the trajectory over these long periods, it becomes important

to evaluate the influence such data have on navigation error. Implied here is another problem: When extremely sensitive accelerometers (sensing 10^{-10} to 10^{-11} g with 2-arc-second accuracy) become flight-ready, a heavy burden is going to be placed upon attitude control sensor accuracy and measurement process.

If only one accelerometer is placed on board along the nominal thrust axis, then information about mass flow rate becomes available (provided thrust magnitude is known fairly well); however, no information about thrust misalignment is available. On the other hand, it is expected that the navigation problems can be alleviated somewhat by placement of three highly sensitive accelerometers on board to reduce thrust vector misalignments. Such an alleviation is contingent upon precision alignment with respect to attitude control sensors. Thrust direction with respect to the accelerometer axis can then be accurately determined, depending upon accelerometer accuracy, and referenced to inertial coordinates by the attitude control system. This is an area where very little work has been done and numerous studies must be made using not only earth-based data but also onboard navigation sensors.

I would like to close by saying that the overall problem of low-thrust mission analysis is quite fascinating with new and nontrivial aspects requiring the development of new technology. This is an area where it is necessary to reconsider a lot of the concepts that might have been formed in studying ballistic high-thrust-type mission analysis. The problems are not insurmountable, but they are going to be very time-consuming to overcome.

This paper has discussed some of the mathematical models which are needed. In addition, there is the orbit determination problem where data types must be evaluated and used in combination with an optimal filter. Deciding upon a particular filter is not as easy as it might seem, taking into account the thrust-vector-related biases and time-varying components that must be estimated. The strong coupling between navigation and guidance and the problems it poses to the attitude control system are crucial.

DISCUSSION

VOICE: What kind of funding is available to study these types of problems? They sound very interesting.

BARBIERI: The funding right now is nebulous, at best. At this time we are not quite sure where we stand with regard to funding for low-thrust mission analysis.

VOICE: Is anyone in particular interested in pushing this concept further?

HOUGHY: Yes. There is a possibility of a new start for solar electric research and development in the 1976 budget, but there is a very low probability of it actually coming into being. If it does not happen in the 1976 new start, it will probably be continued as a low level technology-type effort. The primary person who would be supporting it, should it stay at low level technology, would be Jim Lazar at the Office of Aeronautics and Space Technology. From our point of view, there is a wide degree of uncertainty as to where we are going right now. We have to wait until we get a reading from the Office of Management and Budget on how they feel about it.

LOW THRUST OPTIMAL GUIDANCE FOR GEOCENTRIC MISSIONS

T. Edelbaum and S. W. Sheppard
Massachusetts Institute of Technology Charles Stark Drapper Laboratories
Cambridge, Massachusetts

Low thrust propulsion appears to have useful application as a means of satellite maneuvering in a strong gravity field. This thesis investigates the usefulness of one possible guidance scheme for such applications by means of a computer simulation. The guidance scheme uses some of the recent optimal trajectory theory applied to a particular class of orbit transfers. These transfers, between inclined circular orbits, are considered because they typify many mission objectives and have a relatively simple optimal solution. The optimal solution is presented here along with a mathematical approach to solving it on a computer. The simulation program, which investigates the effects of an oblate gravity field on the guidance, is also presented. However, oblateness was found to cause relatively small errors and "closed-loop" guidance offered no significant improvement over "open-loop."

RECENT INTERPLANETARY LOW THRUST STUDIES AT AMA

F. I. Mann
Analytical Mechanics Associates, Inc.
Seabrook, Maryland

Performance characteri. tics of optimal low thrust rendezvous missions to the comets Giacobini-Zinner, Borrelly, and Tempel (2) with launches in the 1981-1986 time period are discussed.

Also discussed are performance characteristics of optimal low thrust extra-ecliptic missions, including launch declination effects and the importance of optimizing the launch date.

GEOMETRIES DESCRIBING AN ORBITER'S RELATIVE MOTION

J. B. Eades, Jr.
Analytical Mechanics Associates, Inc.
Seabrook, Maryland

Analytical solutions to a set of modified Euler-Hill equations lead to interesting geometric descriptions of a relative motion. Traces on the displacement and hodograph planes, defining a time history of the motion state, tell much of what can be expected from the solution to any relative motion problem.

The neoclassic solution of Clohessy and Wiltshire (for intercept) has been extended to include effects of forces and general initial values. These results are depicted on both the "local rotating" frame of reference and the companion "inertially oriented" one.

General results for the relative motion state will be described, some special cases will be noted, and examples of uses of these results will be mentioned.

STABILITY OF RELATIVE MOTION

V. Szebehely
University of Texas
Austin, Texas

The equations of the relative motion of two bodies in a given force-field are formulated, and it is shown that the conventional methods of representation lead to instability at rendezvous in the Earth's gravitational field. A method for selecting new dependent and independent variables is offered in order to stabilize the equations of relative motion.

N76-10175

LONG PERIOD NODAL MOTION OF SUN SYNCHRONOUS ORBITS

Kenneth I. Duck
Goddard Space Flight Center
Greenbelt, Maryland

The sun synchronous orbit has been used since the early 1960s for almost every meteorological satellite launched as well as for the two Earth Resources Technology Satellites (Landsat-1 and Landsat-2). This well known orbit concept makes use of the earth's oblateness to induce a precession of the orbit line-of-nodes in order to maintain a fixed angular orientation of the orbit plane relative to the mean sun. The sun synchronous orbit, even though it has been used for many years, will continue to be used for most earth observation and remote sensing applications because:

- The satellite passes through each latitude point at the same local time thus ensuring similar ground lighting conditions on each pass and consequently facilitates data comparisons.

- The average spacecraft solar array angle of incidence to the sun remains within a fixed boundary thus ensuring the availability of electric power.

- The orbits (altitude and inclination) can be chosen such that the majority of the earth's surface can be mapped with near north-south contiguous swaths in a fixed period with repeatability.

The long-period perturbations which disturb sun synchronous orbits have not been the subject of detailed investigations in comparison to geosynchronous orbits where the literature abounds with material. The disturbances acting on sun synchronous orbits has not been examined in detail for several reasons:

- With the exception of the Landsat satellite, previous sun synchronous vehicles have not had orbit adjustment capability to fight the perturbations.

- The spacecraft hardware design lifetimes (1 to 2 years) have been sufficiently short that the perturbations could be neglected without significantly degrading mission performance.

- Prior to the use of inertial guidance on the Delta launch vehicle, injection uncertainties were sufficiently large so as to mask any perturbation effects present.

The assessment of the perturbations acting on sun synchronous orbits becomes more significant when longer lifetime spacecraft are developed as anticipated over the next 10 to 20 years.

C.2

With improvements in hardware technology and reliability and the on-orbit refurbishment capability associated with the advent of Space Shuttle, operational satellite lifetimes could easily exceed 5 years. This increase in lifetime is almost a reality today as most earth orbiting spacecraft launched in recent years have exceeded their design life.

The object of the study documented here was to determine which perturbations significantly affected the long term nodal motion of sun synchronous orbits and then construct an approximate model which described the phenomena observed. Many computer simulations were made with several independent computer programs to assess the relative effect of various combinations of perturbations. Typical of the perturbations included in the simulations were zonal and tesseral gravitational harmonics, third-body gravitational disturbances induced by the sun and moon, and atmospheric drag. It was observed that a model consisting of even-zonal harmonics through order 4 and solar gravity dominated the nodal motion. It was further observed that for long runs the orbit inclination and orientation of the line-of-nodes exhibited an oscillating behavior each having the same period. For all the cases run, the inclination amplitude was very small (always less than 1 degree); however, the nodal motion could be quite large. Due to these observations, it was felt that a resonance existed between the inclination and the nodal motion. The mean daily rate of change in inclination due to solar gravity (in radians/mean solar day) was found by analytic averaging to be

$$\frac{di}{dT} = 16200 \frac{\eta_s^2}{\eta} (1 + \cos i_s)^2 \sin i \sin 2 \Omega_{oc}$$

where

η_s = mean motion of earth about the sun

η = mean motion of satellite about the earth

i_s = solar obliquity

Ω_{oc} = o'clock angle, the angle between the longitude of the ascending node and the mean sun used computing local time

i = orbit inclination

The precession rate of the line-of-nodes due to zonal harmonics through order 4 (assuming a circular orbit) is

$$\dot{\Omega} = A \cos i + B \cos^3 i$$

where

$$A = -\frac{3}{2} n J_2 \left(\frac{Rc}{a}\right)^2 \left[1 - J_2 \left(\frac{Rc}{a}\right)^2 \left(1 - \frac{15}{8} \frac{J_4}{J_2^2}\right)\right]$$

$$B = -\frac{3}{8} n J_2^2 \left(\frac{Rc}{a}\right)^4 \left(19 - \frac{35}{2} \frac{J_4}{J_2^2}\right)$$

and

J_2, J_4 = zonal gravitational coefficients

Rc = mean equatorial radius of the earth

a = orbit semimajor axis

Differentiating $\dot{\Omega}$, substituting di/dt, and noting that

$$\dot{\Omega}_{oc} = \dot{\Omega} - \dot{\phi}_s$$

where $\dot{\phi}_s \approx 0.9856$ °/day, then

$$\ddot{\Omega}_{oc} = -16200 \frac{n_s^2}{n} (1 + \cos i_s)^2 \sin^2 i (\bar{A} - 3\bar{B} \cos^2 i) \sin 2 \Omega_{oc}$$

where $\bar{A}, \bar{B}$ are A and B in radians/mean solar day.

Examination of $\ddot{\Omega}_{oc}$ shows that for altitude regions where drag can be neglected, and assuming that $\sin^2 i$ is approximately constant,

$$\ddot{\Omega}_{oc} \approx k \sin 2 \Omega_{oc}$$

a form of the familiar pendulum equation. It is known that systems which are characterized by the above equation can exhibit libration or circulatory characteristics. Both characteristics can be observed on the phase plane plot (figure 1) made for ITOS-type orbits. It is observed that this system has stable equilibria which correspond to orbits whose line-of-nodes lie through the 6:00 a.m. and 6:00 p.m. points. The pendulum equation can be solved analytically using elliptic functions with a typical solution for a quarter cycle oscillation being

$$\Omega_{oc} = \frac{1}{2} \cos^{-1} \left[-1 + \frac{2m \, cn^2 \, (\sqrt{2k} \, T)}{1 - m \, sn^2 \, (\sqrt{2k} \, T)}\right]$$

84.

where

$$m = 1/2 (1 + \cos 2\, \Omega_{oco})$$

$$o \leq T \leq P_L/4$$

$$o \leq \Omega_{oc} \leq 90°$$

Note that P_L denotes the libration period and Ω_{oco} denotes the value of o'clock angle where $\dot{\Omega}_{oc} = 0$. The libration period, P_L is

$$P_L = \frac{4\, K(m)}{\sqrt{2k}}$$

where $K\,(m)$ denotes a complete elliptic integral of the first kind. Figure 2 shows the o'clock angle libration period for ITOS-type orbits ($h = 1489$ km, $i = 101.9°$). It is seen that the libration period increases from 26 years as the reference o'clock angle moves from one of the stable equilibria toward one of the unstable ones. Investigation of the libration period has shown that the minimum libration period lies between 22 to 30 years for sun synchronous orbits between 200 and 2000 km.
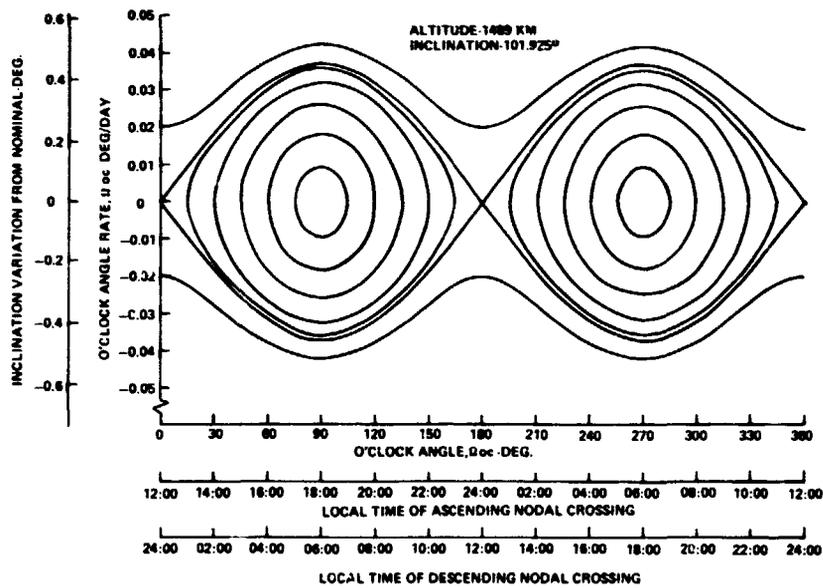
Figure 1. O'clock angle motion in phase space for ITOS-type orbit.
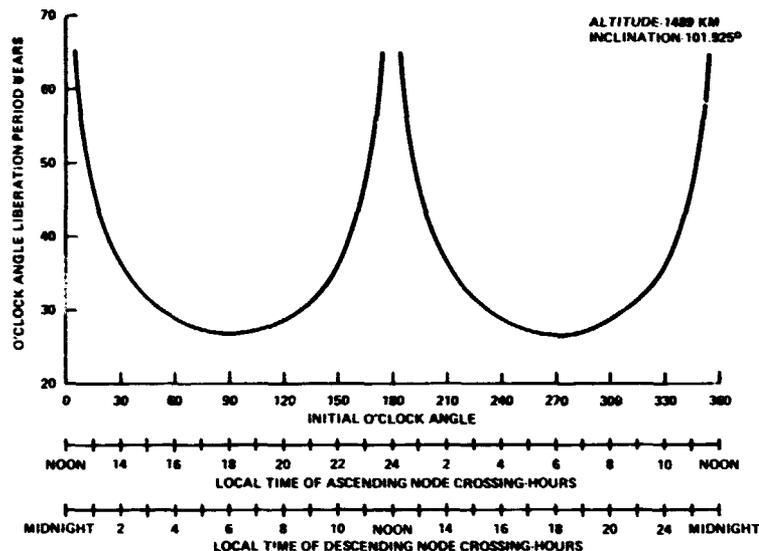
Figure 2. Libration period for ITOS-type orbit.

The pendulum analogy has been compared with both simulation and flight spacecraft data. Figure 3 compares the approximate solution with several simulations having various combinations of perturbations. The reference orbit in this comparison is the ITOS-type (h = 1489 km, i = 101.9°) having an ascending nodal crossing at 3:00 p.m. local time. It is seen that there is excellent agreement between the pendulum analogy and those simulations which include zonal harmonics and solar gravity.

The remaining figures (4 through 9) compare the o'clock angle time history generated using the pendulum model with that obtained from Brouwer mean elements for several flight spacecraft. In examining these comparisons one observes that there are two curves representing approximate nodal drift propagation. The dashed curve is the propagation calculated using a set of orbit elements at the initial epoch for the particular satellite. The solid curve uses an iterated value of inclination to improve the agreement. This approach was taken because of the large relative uncertainty in measuring the inclination. It is seen in all cases that excellent agreement is obtained. In examining these data, note that the ESSA-2 solution (figure 4) is a case where the motion lies in the circulatory region in phase space while the other solutions lie in the libration region. The ESSA-8 solution (figure 7) exhibits the turnaround expected for the libration motion. The final observation to be noted is for Nimbus-5 (figure 9) where the node is located near one of the unstable equilibria. There is still good agreement for this case where the disturbing acceleration is near zero.

In conclusion, the nodal motion of sun synchronous orbits has been investigated and found to exhibit the characteristics of a pendulum. This pendulum motion results from solar

86

gravity inducing an inclination oscillation which couples into the nodal precession induced by the earth's oblateness. The pendulum model has been compared with simulations and flight data with excellent correlation observed.
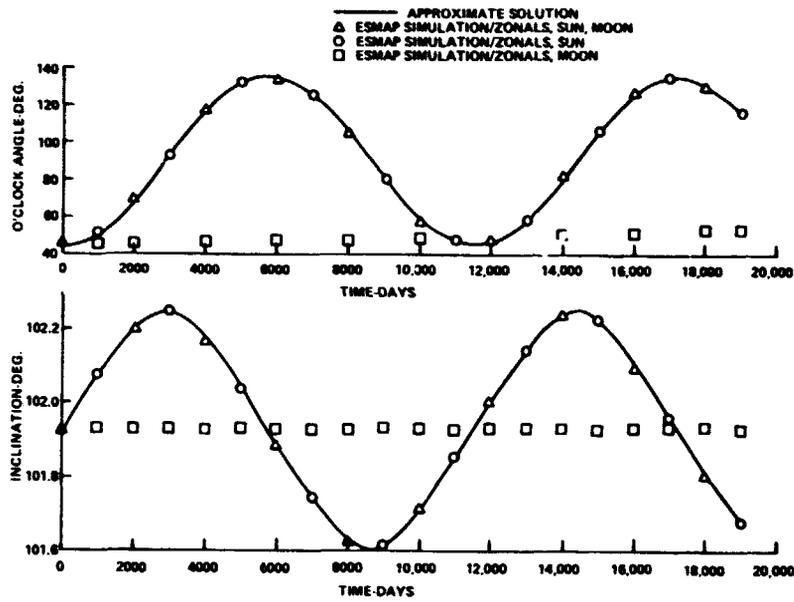
Figure 3. Approximate solution.
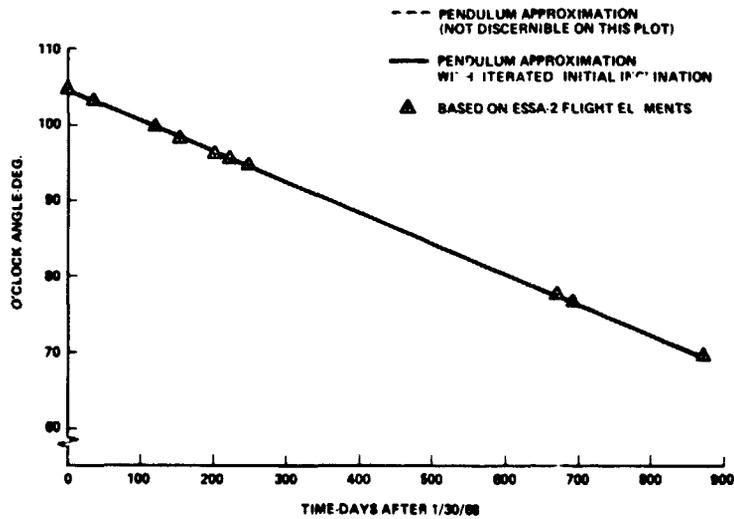
Figure 4. ESSA-2 pendulum solution comparison.
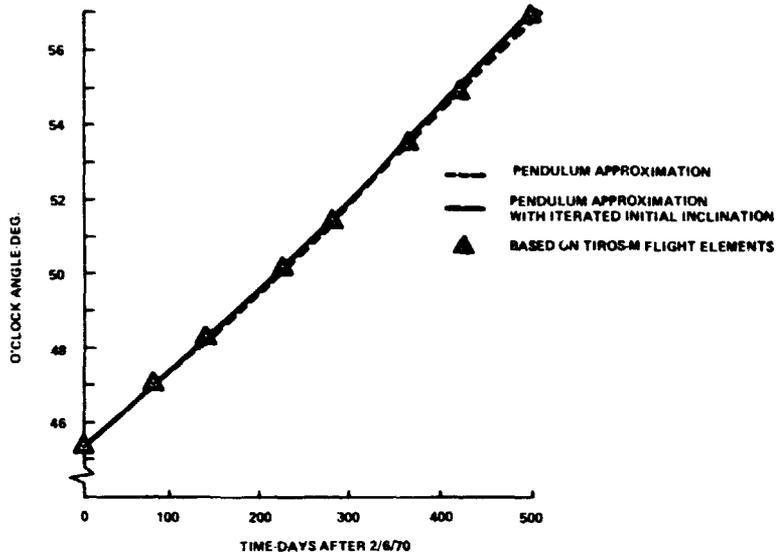
Figure 5. Tiros-M pendulum solution comparison.
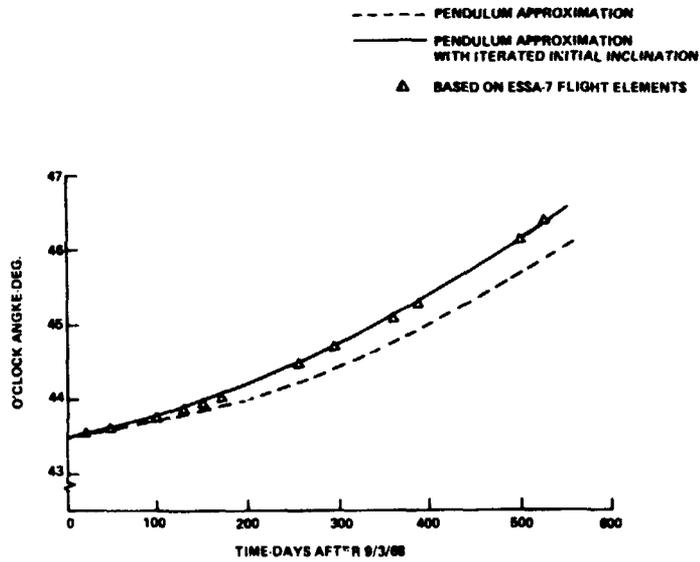
Figure 6. ESSA-7 pendulum solution comparison.
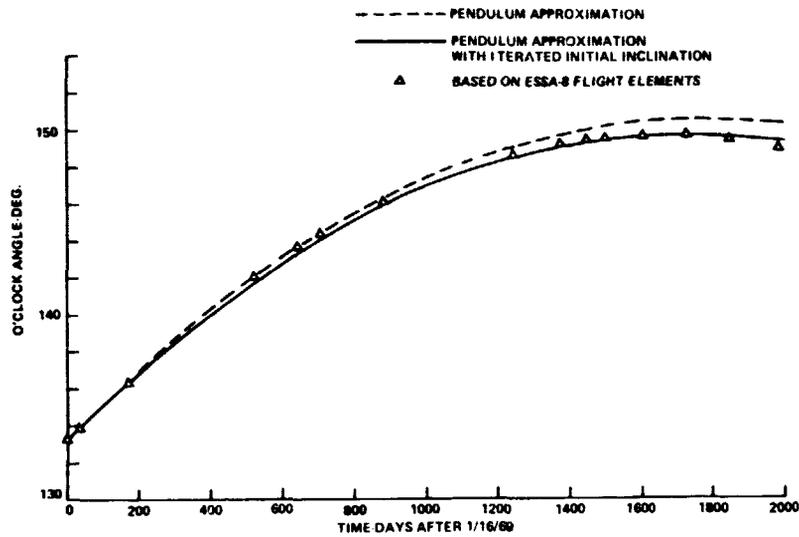
Figure 7. ESSA-8 pendulum solution comparison.
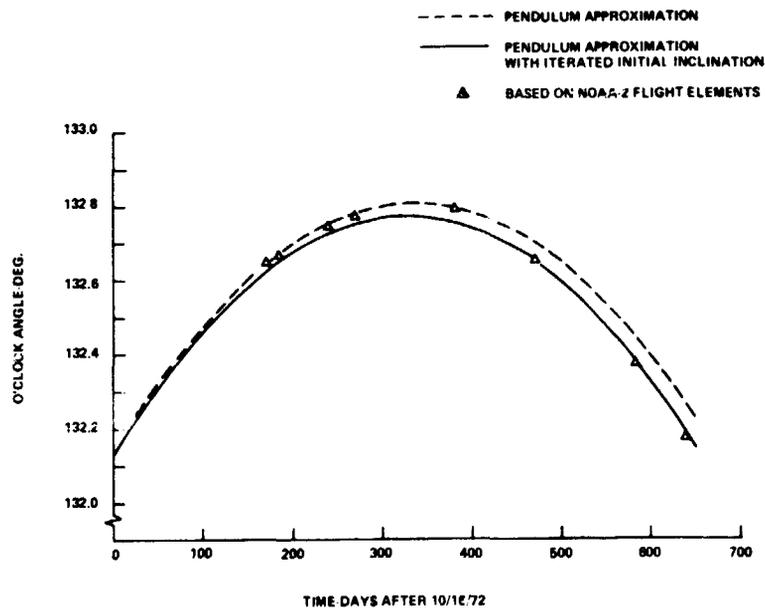
Figure 8. NOAA-2 pendulum solution comparison.
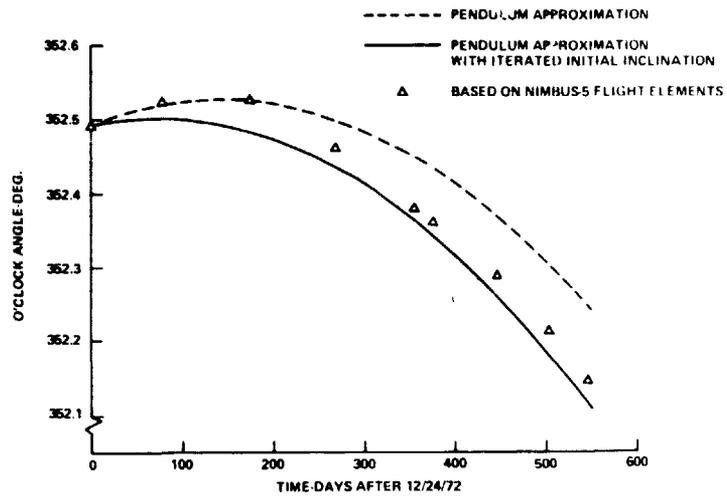
Figure 9. Nimbus-5 pendulum solution comparison.

90

COMPARISON THEOREMS, NUMERICAL INTEGRATION, AND SATELLITE ORBITS

Arnold Stokes
Georgetown University
Washington, D.C.

Consider the equation

$$\dot{x} = X(x). \tag{1}$$

Assume that the behavior of the family of solutions is known, expressed by the estimate

$$|x(t, x_0) - x(t, x_1)| \leqslant K_0 f(t) |x_1 - x_0|, \, t \geqslant 0,$$

Here K_0 is constant, and f is normalized by $f(0) = 1$, $f(t) \geqslant 1$. The function $f(t)$ then expresses the stability or instability of (1), so that stability is equivalent to $f \equiv 1$, and a typical instability would be $f(t) = t + 1$.

Suppose we wish to numerically compute a particular solution of (1), say $x(t, x_0)$, for some fixed x_0. A remarkable theorem of Babuska asserts (under reasonable assumptions on X) that if a strongly stable difference scheme is used, numerical integration of (1) with $x(0) = x_0$ is equivalent to obtaining an exact (theoretical) solution of

$$\dot{y} = X(y) + G(t, y), \tag{2}$$

where $y(0) = x_1$, (here $|x_1 - x_0|$ is the starting error), and $|G(t, y)| \leqslant \eta$, (here η (small) reflects the discretization and truncation error).

Babuska used this result to obtain global error bounds for (2), assuming $x(t, x_0)$ is a uniformly asymptotically stable solution of (1). Here we wish to compare solutions of (1) with solutions of (2), with particular attention given to the effect of different types of $f(t)$.

To develop the comparison, a converse theorem using Lyapunov functions due to Yoshizawa and Hale is applied. Let $z = x - x(t, x_0)$, then (1) becomes

$$\dot{z} = Z(t, z), \tag{3}$$

and the new estimate becomes

$$|z(t, t_0, z_0) - z(t, t_0, z_1)| \leqslant K_0 f(t) |z_1 - z_0|$$

$$= K_0 f(t_0) \frac{f(t)}{f(t_0)} \ |z_1 - z_0|$$

(4)

$$= K(t_0) \ |z_1 - z_0| \exp(\alpha(t) - \alpha(t_0))$$

where $K(t_0) = K_0 \ f(t_0)$, $\alpha(t) = \log f(t)$.

Then one can show there exists a function $V(t, z)$ satisfying

$$|z| \leqslant V(t, z) \leqslant K(t) \ |z|.$$
(a)

$$|V(t, z) - V(t, y)| \leqslant K(t) \ |z - y|, \text{ and}$$
(b)

$$\left| \dot{V}_3 \right| \leqslant \dot{\alpha} V = \frac{\dot{f}}{f} V$$
(c)

where $\dot{V}_3$ denotes the derivative of V along solutions of (3). Note that (a) and (c) allow one to recover (4), using standard theorems. Further, it is easy to show, using (b) that

$$\dot{V}_2 \leqslant \dot{\alpha} V + K(t)\eta = \frac{\dot{f} V}{t} + K_0 \ f(t)\eta.$$

Then an immediate consequence is that

$$|y(t, x_1) - x(t, x_0)| < K_0 \ f(t) \left[|x_1 - x_0| + \eta t \right]$$

So we see that the term $K_0 \ f(t) \ |x_1 - x_0|$ reflects the propagation of the starting error, and the term $\eta K_0 \ f(t)$ gives an estimate of the effects of the discretization and truncation error.

Evidently, it is better to integrate a stable system, $f \equiv 1$, than an unstable system, $f(t) \equiv t + 1$. A simple example is the unperturbed two-body problem, which is unstable, as the difference between two periodic solutions of different periods grows (at least locally) like $t + 1$. An example of a stable problem is the stabilized Kepler problem, as given by Baumgarte and Stiefel, where now all solutions have the same period.

To extend the above to perturbed problems, consider

$$\dot{x} = X(x) + \epsilon X_1(t, x)$$

(5)

Assume that in some region R, $|X_1(t, x)| \leq M$. Here one supposes this region R contains the solution of interest and is large enough so that continued integration would not be of interest long before the integrated solution leaves R.

This assumption will allow the effect of f (t) on the error to be observed, for now we consider

$$\dot{y} = X (y) + \epsilon X_1 (t, y) + G (t, y), \tag{6}$$

and $y (0) = x_1$, $|G (t, y)| \leqslant \eta$ as before.

The same V-function leads to the estimate

$$|y (t, x_1) - x (t, x_0)| \leqslant K_0 f (t) \left[|x_1 - x_0| + t (\eta + \epsilon M) \right] ,$$

which is valid as long as both solutions remain in R. Again one can see the different error estimates obtained for $f \equiv 1$ or $f = t + 1$. Remark: The foregoing gives upper bounds on the error. The strength of the conclusion then rests on the sharpness of the upper bounds, for one cannot conclude $\text{Error}_1 < \text{Error}_2$ on the basis that a crude upper bound of the first is less than a crude upper bound of the second.

However, by considering simple examples, one can see that at least in these cases, numerical integration of a stable system gives an error growth $0 (\eta t)$, while for an unstable problem, the error grows like $0 (\eta t^2)$. So to that extent the foregoing estimates seem reasonable.

Further, numerical experiments are being conducted at Goddard Space Flight Center using the stabilization techniques of Baumgarte and Stiefel, and the results should give further insight into the significance of the above results.

In this regard, perhaps it should be observed that a similar approach to obtain lower bounds does not seem possible, as the difference of two almost periodic functions will, in general, have an arbitrarily small lower bound.

Note that the above estimates can also be obtained in more complicated problems, with such means as time-dependent potentials. Details will appear in a forthcoming paper.

OPTIMAL EXPLICIT RUNGE-KUTTA METHODS

D. Bettis and D. Hall
University of Texas
Austin, Texas

Optimal explicit Runge-Kutta methods are developed for solving the initial value problem for systems of ordinary differential equations. These methods have an optimal estimate of the local truncation error term, thereby allowing the option of implementing a variable-step strategy. The coefficients of the Runge-Kutta method are selected so that the local truncation error is minimized and that the absolute stability region is maximized.

N76-10177

STABILIZATION BY MODIFICATION OF THE LAGRANGIAN*

Joachim W. Baumgarte
Mechanik-Zentrum, Technische Universität Braunschweig
Braunschweig, Federal Republic of Germany and Swiss Federal Institute of Technology
Zürich, Switzerland

ABSTRACT

In order to reduce the error growth during a numerical integration, a method of stabilization of the differential equations of the Keplerian motion is offered. It is characterized by the use of the eccentric anomaly as an independent variable in such a way that the time transformation is given by a generalized Lagrange formalism. The control terms in the equations of motion obtained by this modified Lagrangian give immediately a completely Lyapunov-stable set of differential equations. In contrast to other publications, here the equation of time integration is modified by a control term which leads to an integral which defined the time element for the perturbed Keplerian motion.

INTRODUCTION

It is well known that the classical differential equations of the Keplerian motion are unstable in the sense of Lyapunov. In general, Lyapunov-unstable differential equations develop more unavoidable numerical errors during a numerical integration than Lyapunov-stable equations do. We consider here the stabilization of the differential equations of Keplerian motion with the aim of improving the accuracy and efficiency during the numerical integration. We propose a stabilization method which is purely conservative in contrast to other methods (Baumgarte, 1972a). It is characteristic for all conservative methods, that they make the revolution time independent of the initial conditions (Baumgarte, 1974).

GENERALIZED LAGRANGIAN

In this method the stabilization goes hand in hand with the introduction of a new independent variable s instead of the time t. This procedure is called time transformation and s is called fictitious time. Furthermore, we will require that our stabilized equations of motion be developed from the Lagrangian formalism. But, here we have to use an appropriately

---

modified generalized Lagrangian formalism. In order to introduce, instead of t, the fictitious time s as a new independent variable, we have to use, instead of the original Lagrangian L

$$L = L(q_i, \dot{q}_i, t), \qquad\qquad i = 1, 2, \ldots, n, \qquad\qquad (1)$$

where q_i are the coordinates and dot means differentiation with respect to t, the following generalized Lagrangian L^*:

$$L^* = ht' + \mu \left\{ L\left(q_i, \frac{q_i'}{\mu}, t\right) - h \right\} \qquad\qquad (2)$$

In equation (2) the prime means differentiation with respect to the independent variable s. The time t is now a dependent variable (time coordinate). Together with t appears its conjugated momentum h, which represents physically the negative total energy.

Furthermore, we consider only the case, where

$$\mu = \mu(q_i, h) > 0 \qquad\qquad (3)$$

is a freely chosen positive function only dependent on q_i and h. Later we will see that μ may be interpreted as the local scale of the time transformation. More general dependences of the scale μ are also of interest but shall not be considered further here. Our special choice of μ retains the equivalence between Lagrangian and Hamiltonian formalism. This choice has two consequences:

1. The transformed kinetic energy in an inertial system is also a quadratic form in the velocity components q_i' with respect to the fictitious time s.

2. A conservative system remains conservative after the time transformation.

With these restrictions we obtain the differential equations of motion in the following form:

$$\frac{d}{ds}\left(\frac{\partial L^*}{\partial q_i'}\right) - \frac{\partial L^*}{\partial q_i} = 0 \qquad\qquad (4a)$$

$$\frac{d}{ds}\left(\frac{\partial L^*}{\partial t'}\right) - \frac{\partial L^*}{\partial t} = 0 \qquad\qquad (4b)$$

$$\frac{d}{ds}\left(\frac{\partial L^*}{\partial h'}\right) - \frac{\partial L^*}{\partial h} = 0 \quad\longrightarrow\quad \frac{\partial L^*}{\partial h} = 0 \qquad\qquad (4c)$$

Relative to the system (4a, b, c) the following remarks are in order:

*   Equation (4a) states the equations of motion, which are also given by the original Lagrangian $L(q_i, \dot{q}_i, t)$ after changing from t to s, but which are

96

distinguished only by control terms (Baumgarte, 1972b). This fact will be observed later in the special case of the Kepler problem.

⊙ Equation (4b) gives:

$$h' = \mu (q_i, h) \frac{\partial}{\partial t} L (q_i, q_i', h, t),$$ (5)

which asserts the energy relation. In the conservative
case, where the original Lagrangian L does not depend explicitly
on the time t, we get h = constant.

● From equation (4c) there follows:

$$t' = \mu + \left\{ h \frac{\partial \mu}{\partial h} - \frac{\partial}{\partial h} (\mu L) \right\}.$$ (6)

It will be obvious that the expression in the bracket is a control term, which represents the energy relation. This control term vanishes in the exact solution of the equations of motion, in such a way that $t' = \mu$. Therefore, it follows as previously promised that μ is the local scale of the time transformation.

EXAMPLE: KEPLERIAN MOTION

We consider now the Keplerian problem and use Cartesian coordinates. We will choose the scale μ in such a way that the fictitious time s will be for a pure Keplerian motion the eccentric anomaly. Only by doing this can we obtain both Lyapunov-stable differential equations and equivalence between Lagrange and Hamilton. We, therefore, choose:

$$\mu = \frac{r}{\sqrt{2h}}, r = |\underline{x}|,$$ (7)

where r is the distance.

Before we establish the generalized Lagrangian L*, we first write the original Lagrangian L. With the mass m = 1, K as the gravitational parameter, L has the form:

$$L = \frac{1}{2} |\underline{\dot{x}}|^2 + \frac{K^2}{r}.$$ (8)

With the help of equation (2) we now obtain as the generalized Lagrangian L*:

$$L^* = ht' + \frac{\sqrt{2h}}{2r} |\underline{x}'|^2 + \frac{K^2}{\sqrt{2h}} - \sqrt{\frac{h}{2}} r.$$ (9)

97

With (9) the stabilized equations of motion are:

$$\underline{x}'' = \frac{(\underline{x}, \underline{x}')}{r^2} \, \underline{x}' - \frac{1}{2} \left[\frac{|\underline{x}'|^2}{r^2} + 1 \right] \underline{x} \qquad (10a)$$

$$h' = 0 \qquad (10b)$$

$$5 \quad t' = \frac{1}{2\sqrt{2h}} \left\{ \frac{K^2}{h} + r - \frac{|\underline{x}'|^2}{r} \right\} \qquad (10c)$$

(10a) requires that $h' = 0$. It is essential that in contrast to an earlier publication (Baumgarte, 1972b) the vector-equation for $\underline{x}''$ does not depend on h. This means the revolution time is the fixed number 2π and this implies Lyapunov-stability for the $\underline{x}''$ - equation.

From (10b) there follows h = constant. The constant h is computed from the initial conditions and is placed in the computer as a fixed value. This is the presupposition that now in contrast to earlier publications (Baumgarte, 1972b) the time integration (10c) is Lyapunov-stable. The expression:

$$\frac{1}{2\sqrt{2h}} \left\{ r - \frac{|\underline{x}'|^2}{r} \right\},$$

a part of the right hand side of (10c), is proportional to the difference between potential and kinetic energy. Therefore, the mean value with respect to the fictitious time s of this difference vanishes because we have an oscillator problem in principle. Consequently, the expression $K^2 /(2h)^{3/2}$ in (10c) represents the exact mean value of the right hand side of (10c). This fact implies Lyapunov-stability also for the time integration.

CONTROL TERMS AND LYAPUNOV-STABILITY

In order to show the effect of the stabilization by the control terms, in the classical Keplerian equations

$$\ddot{\underline{x}} = - \frac{K^2}{r^3} \, \underline{x} , \qquad \cdot = \frac{d}{dt} , \qquad (11)$$

we substitute in place of the independent variable t the fictitious time s by using $dt/ds = t' = r/\sqrt{2h}$. Because h = constant we obtain:

$$\underline{x}'' - \frac{(\underline{x}, \underline{x}')}{r^2} \, \underline{x}' + \frac{K^2}{2h} \frac{\underline{x}}{r} = 0 \qquad (12a)$$

98

$$h' = 0 \tag{12b}$$

$$t' - \frac{r}{\sqrt{2h}} = 0. \tag{12c}$$

We now transpose system (10) in such a way that we can see clearly that system (12) differs from system (10) only by control terms which are the right hand sides of equations (13a) and (13c).

$$\underline{x}'' - \frac{(\underline{x}, \underline{x}')}{r^2} \underline{x}' + \frac{K^2}{2h} \frac{\underline{x}}{r} = - \left\{ \frac{|\underline{x}'|^2}{2r^2} - \frac{K^2}{2hr} + \frac{1}{2} \right\} \underline{x} \tag{13a}$$

$$h' = 0 \tag{13b}$$

$$t' - \frac{r}{\sqrt{2h}} = - \left\{ \frac{|\underline{x}'|^2}{2r^2} - \frac{K^2}{2hr} + \frac{1}{2} \right\} \frac{r}{\sqrt{2h}}. \tag{13c}$$

In the control terms in (13a) and (13c) the same bracket appears as a factor, which is analytically zero with respect to the energy relation.

Equation (13c) or (10c) can be integrated. We find as an integral of motion:

$$t = \frac{1}{\sqrt{2h}} \left[\frac{K^2}{2h} s - \frac{(\underline{x}, \underline{x}')}{r} \right] + C. \tag{14}$$

The control terms in (13a, c) produce the Lyapunov-stability under the supposition that the constant h is computed once and for all from the initial conditions. The proof for the stability of the complete system (13) or (10), respectively, (with respect to h = constant, whereby this constant is to be computed, finally, by the initial conditions) can easily be carried out by making the transformation into action and angle variables, because the equivalence between Lagrange and Hamilton exists. By doing this, the generalized Hamiltonian, obtained from the generalized Lagrangian by making a Legendre transformation, will be linear in the action variables, which implies Lyapunov-stability (Baumgarte, 1972b). Another proof follows from the equivalence of the system (10a, b) together with (14), to the corresponding equations of the KS-transformation (Stiefel and Scheifele, 1971).

We will call attention to the fact that the dependence of the time transformation $t' = r\sqrt{2h}$ on the momentum h makes possible the elimination of the instability under the presupposition that $h' = 0$ is integrated exactly.

In the case of perturbed Keplerian motion, the stabilized system (13) or (10) is modified by additional perturbation terms. In equation (14), C is no longer constant but becomes the slowly varying time element (Baumgarte, 1972b; Stiefel and Scheifele, 1971).

Numerical experiments have always shown a reduction in error in the numerical integration. It appears that the positive effects of the stabilization of the pure Keplerian motion carry over to the perturbed problem.

We will finally remark that the KS-transformation can be performed directly in the generalized Lagrangiar L* by inserting

$$r^2 = \sum x_i^2 = \left(\sum u_j^2\right)^2, \frac{\sum x_i'^2}{r} = 4\sum u_j'^2, \begin{matrix} i = 1, 2, 3 \\ j = 1, 2, 3, 4, \end{matrix} \tag{15}$$

thereby giving immediately the analogous complete, stabilized, set of differential equations which leads directly to the KS-elements (Stiefel and Scheifele, 1971).

REFERENCES

Baumgarte. J., 1972a, "Computer Methods" *Applied Mechanics and Engineering*, **1**, pp. 1-16.

Baumgarte, J., 1972b, *Celestial Mechanics*, **5**, pp. 490-501.

Baumgarte, J. and E. Stiefel, 1974, *Celestial Mechanics*, **10**, pp. 71-85.

Stiefel, E. L. and G. Scheifele, 1971, *Linear and Regular Celestial Mechanics*, Springer, Berlin - Heidelberg - New York.

AVERAGED INITIAL CARTESIAN COORDINATES
FOR
LONG LIFETIME SATELLITE STUDIES

S. Pines

Analytical Mechanics Associates, Inc.
Seabrook, Maryland

SUMMARY

A set of initial Cartesian coordinates, which are free of ambiguities and resonance singularities, is developed to study satellite mission requirements and dispersions over long lifetimes.

The method outlined herein possesses two distinct advantages over most other averaging procedures. First, the averaging is carried out numerically using Gaussian quadratures, thus avoiding tedious expansions and the resulting resonances for critical inclinations, etc. Secondly, by using the initial rectangular Cartesian coordinates, conventional, existing acceleration perturbation routines can be absorbed into the program without further modifications, thus making the method easily adaptable to the addition of new perturbation effects.

The averaged nonlinear differential equations are integrated by means of a Runge Kutta method. A typical step size of several orbits permits rapid integration of long lifetime orbits in a short computing time.

INTRODUCTION

Several sets of averaged elements (Lorell, 1970; Broucke and Cefola, 1972; Uphoff, 1973) are in use for satellite lifetime studies. These usually suffer from ambiguities and resonance singularities for low inclinations, near circular orbit, near polar orbits, critical inclination resonances, and such. Moreover, it is necessary to develop the perturbation representations in these element coordinate systems, which often requires ingenuity and is difficult in application. The Cartesian coordinates have been extensively utilized and routines are available to numerically generate most of the significant perturbations. The initial conditions of the Cartesian solution of the classical two-body problem have been developed for variation of parameters (Pines, 1961; Christensen, 1970; Godal and Johansen, 1968), but has not found wide application. With the advent of averaging as a tool for eliminating long tedious numerical integrations in computing solutions, this study was undertaken to reestablish the initial Cartesian coordinates as a useful set of parameters for orbital analysis.

THE INITIAL CONDITION CARTESIAN ELEMENTS

The equations of motion of the satellite in the planetary reference frame are given by

$$\ddot{R} = -\mu \frac{R}{r^3} + F \tag{1}$$

where F represents the perturbation forces other than the central attraction of the principal body.

The initial Cartesian coordinate parameters which describe the motion are given in terms of the position and velocity vectors in Cartesian coordinates by

$$\dot{R}_0 = -\dot{f}R + f\dot{R} \tag{2}$$

where f, g, $\dot{g}$, $\dot{f}$ are given as functions of the difference in eccentric anomaly, θ, as

$$f = 1 - \frac{a(1 - \cos\theta)}{r_0}$$

$$g = \frac{1}{\mu}(r\sqrt{\mu a}\,\sin\theta - d\,a(1 - \cos\theta))$$

$$\dot{f} = -\frac{\sqrt{\mu a}\,\sin\theta}{r_0 r}$$

$$\dot{g} = 1 - \frac{a(1 - \cos\theta)}{r} \tag{3}$$

$$d = R \cdot \dot{R}$$

$$d_0 = R_0 \cdot \dot{R}_0 = -\sqrt{\mu a}\,\sin\theta\left(1 - \frac{r}{a}\right) + d\cos\theta$$

$$r_0 = a(1 - \cos\theta) + r\cos\theta - \frac{d}{\sqrt{\mu}}\sqrt{a}\,\sin\theta$$

$$\frac{1}{a} = \frac{2}{r_0} - \frac{R_0 \cdot \dot{R}_0}{\mu} = \frac{2}{r} - \frac{\dot{R} \cdot \dot{R}}{\mu}$$

The relationship of the time increment to θ, in the absence of perturbations, is given by a form of Kepler's equation

102

$$t - t_0 = \frac{a^{3/2}}{\sqrt{\mu}} \left\{ \theta - \sin\theta + \frac{r}{a} \sin\theta - \frac{d}{\sqrt{\mu a}} (1 - \cos\theta) \right\} \qquad (4)$$

The differential equations for the variation of R_0 and $\dot{R}_0$ under the action of F are generated in Pines (1961) from the conditions that

$$\frac{d}{d\tau} R = 0$$

and   (5)

$$\frac{d}{d\tau} \dot{R} = F$$

Thus, we have

$$\frac{d}{d\tau} R_0 = \dot{g}_\tau R - g_\tau \dot{R} - gF$$

$$\frac{d}{d\tau} \dot{R}_0 = - \dot{f}_\tau R + f_\tau \dot{R} + fF$$ (6)

Following Godel and Johansen (1968), we choose for the perturbation equation of the difference in eccentric anomaly, θ

$$\theta_\tau = 0 \qquad (7)$$

This serves to eliminate mixed secular terms (see Christensen, 1970) from the perturbation derivatives of $f, g, \dot{f}, \dot{g}$, that arise in Pines (1961) where the time from the initial time was assumed unperturbed,

$$\frac{d}{d\tau} (t - t_0) = 0 \qquad (8)$$

We can replace the vectors $R, \dot{R}$ from (6) using the inverse of (2)

$$R = fR_0 + g\dot{R}_0$$

$$\dot{R} = \dot{f}R_0 + \dot{g}\,\dot{R}_0$$ (9)

$$\frac{d}{d\tau} R_0 = (\dot{g}_\tau f - \dot{f}g_\tau) R_0 + (g\dot{g}_\tau - g_\tau\dot{g}) \dot{R}_0 - gF \qquad (9a)$$

$$\frac{d}{d\tau} \dot{R}_0 = (f_\tau\dot{f} - f\dot{f}_\tau) R_0 + (f_\tau\dot{g} - \dot{f}_\tau g) \dot{R}_0 + fF$$

An important stability condition on (9a) is derived. We have

$$f\dot{g} - g\dot{f} = 1 \tag{10}$$

It follows from the perturbation derivative of (10) that

$$f_\tau \dot{g} - \dot{f}_\tau g = -\dot{g}_\tau f + \dot{f} g_\tau \tag{11}$$

Thus the coefficient of R_0 in the $d/d\tau\, R_0$ expression is the negative of the coefficient of $\dot{R}_0$ in the $d/d\tau\, \dot{R}_0$ expression in Equations (9a). This will reduce the computing work in the averaging process.

Since the perturbation of the transit time is not zero, we require a differential equation for the time. Using (3), (4), and (5), we obtain the perturbation differential equations for the time,

$$\frac{d}{d\tau}(t - t_0) = \frac{1}{\sqrt{\mu}} \left\{ \left(\frac{3}{2} a^{1/2}(\theta - \sin\theta) + \frac{r}{2\sqrt{a}} \sin\theta - \frac{d(1 - \cos\theta)}{\sqrt{\mu}} \right) a_\tau - \frac{a(1 - \cos\theta)}{\sqrt{\mu}} d_\tau \right\} + 1 \tag{12}$$

where

$$a_\tau = 2\, a^2\, \dot{R} \cdot F$$

$$d_\tau = R \cdot F \tag{12a}$$

The perturbation derivatives of f, g, $\dot{f}$, and $\dot{g}$ are given below:

$$f_\tau = \frac{a}{r_0}(1 - \cos\theta)\left(\frac{r_{0_\tau}}{r_0} - \frac{a_\tau}{a} \right)$$

$$g_\tau = \left(\frac{r\sin\theta}{2\sqrt{a\mu}} - \frac{d(1 - \cos\theta)}{\mu} \right) a_\tau - \frac{a(1 - \cos\theta)}{\mu} d_\tau \tag{13}$$

$$\dot{f}_\tau = \dot{f}\left(\frac{a_\tau}{2a} - \frac{r_{0_\tau}}{r_0} \right)$$

$$\dot{g}_\tau = -\frac{(1 - \cos\theta)}{r} a_\tau$$

104

where

$$(r_0)_\tau = (1 - \cos\theta)\, a_\tau - \frac{\sqrt{a}\,\sin\theta}{\sqrt{u}}\,(d_\tau + \frac{d}{2a}\,a_\tau) \tag{13a}$$

We now proceed to the averaged differential equations.

THE AVERAGED EQUATIONS OF MOTION

The principle here is to replace the nonlinear differential equations for $R_0(\tau)$ and $\dot{R}_0(\tau)$ by their average value over a single period of the reference orbit as defined by $R_0(\tau_1)$ and $\dot{R}_0(\tau_1)$.

Let the period of reference orbit be $T(\tau_1)$, then for

$$-\frac{T}{2}(\tau_1) \leqslant \tau \leqslant \frac{T}{2}(\tau_1)$$

$$R_0(\tau) = R_0(\tau_1)$$

$$\dot{R}_0(\tau) = \dot{R}_0(\tau_1) \tag{14}$$

$$t - t_1 = \tau - \tau_1 = \frac{1}{\sqrt{\mu}}\left\{ a^{3/2}(\theta - \sin\theta) + r_0 a^{1/2}\sin\theta + \frac{d_0 a(1 - \cos\theta)}{\sqrt{\mu}}\right\}$$

Thus,

$$\frac{d}{d\tau}\dot{\bar{R}}_0 = \bar{R}_0\,\frac{1}{2\pi}\int_{-\pi}^{\pi}\frac{r}{a}(f\dot{g}_\tau - \dot{f}g_\tau)\,d\theta + \dot{\bar{R}}_0\,\frac{1}{2\pi}\int_{-\pi}^{\pi}\frac{r}{a}(g\dot{g}_\tau - g_\tau\dot{g})\,d\theta - \frac{1}{2\pi}\int_{-\pi}^{\pi}\frac{r}{a}\,gF\,d\theta$$

$$\frac{d}{d\tau}\bar{R}_0 = \bar{R}_0\,\frac{1}{2\pi}\int_{-\pi}^{\pi}\frac{r}{a}(f_\tau\dot{f} - f\dot{f}_\tau)\,d\theta + \dot{\bar{R}}_0\,\frac{1}{2\pi}\int_{-\pi}^{\pi}\frac{r}{a}(f_\tau\dot{g} - f\dot{g}_\tau)\,d\theta + \frac{1}{2\pi}\int_{-\pi}^{\pi}\frac{r}{a}\,fF\,d\theta \tag{15}$$

$$\frac{d}{d\tau}\overline{(t - t_0)} = \frac{1}{2\pi}\int_{-\pi}^{\pi}\frac{r}{a}(t - t_0)_\tau\,d\theta$$

where

$$\frac{r}{a} = 1 - \cos\theta + \frac{r_0}{a}\cos\theta + \frac{d_0}{\sqrt{\mu a}}\sin\theta \tag{15}$$

Equation (15) could be integrated analytically, using Fourier series in θ. However, this would require a representation of F in θ and greatly burden the introduction of additional perturbations. Moreover, mathematical resonances would appear and require special techniques for each resonant term. In this, we follow the lead of Uphoff (1973) and adapt Gaussian quadratures s the technique for evaluating the integrals.

We note that F is a vector in three space, and recalling (11), we need to evaluate only 10 integrals. The average equations become:

$$\frac{d}{d\tau}\bar{R}_0 = a_1\bar{R}_0 + a_2\dot{\bar{R}}_0 + \bar{G}$$

$$\frac{d}{d\tau}\dot{\bar{R}}_0 = a_3\bar{R}_0 - a_1\dot{\bar{R}}_0 + \bar{F} \tag{16}$$

$$\frac{d}{d\tau}(t - t_0) = 1 + a_4$$

where

$$a_1 = \frac{1}{2\pi}\int_{-\pi}^{\pi}\frac{r}{a}(\dot{f}g_r - \dot{f}g_r)\,d\theta$$

$$a_2 = \frac{1}{2\pi}\int_{-\pi}^{\pi}\frac{r}{a}(g\dot{g}_r - g_r\dot{g})\,d\theta$$

$$a_3 = \frac{1}{2\pi}\int_{-\pi}^{\pi}\frac{r}{a}(f_r\dot{f} - f\dot{f}_r)\,d\theta \tag{16a}$$

$$\bar{G} = -\frac{1}{2\pi}\int_{-\pi}^{\pi}\frac{r}{a}\,gF\,d\theta = \left\{\begin{array}{c}\bar{g}_1\\\bar{g}_2\\\bar{g}_3\end{array}\right\}$$

106

$$\bar{F} = \frac{1}{2\pi} \int_{-\pi}^{\pi} \frac{r}{a} f F \, d\theta = \left\{ \begin{array}{c} \bar{f}_1 \\ \bar{f}_2 \\ \bar{f}_3 \end{array} \right\}$$

(16a)
(cont.)

$$a_4 = \frac{1}{2\pi} \int_{-\pi}^{\pi} \frac{r}{a} (t - t_0)_\tau \, d\theta$$

To obtain the averaged $\bar{F}, \bar{G}$ vectors, it is necessary to specify the perturbations. For the purpose of this study, we consider accelerations due to tesseral and zonal harmonics for a rotating planet, third body forces, such as the sun and moon, and drag. The detailed equations are given in Appendix A. It should be noted that where F is a function of R, $\dot{R}$ and t, for the purposes of averaging, these functions are given by the two body equations and Kepler's equation given in (17a) through (17d) referenced to the τ time at the midpoint.

We now consider the numerical integration of the averaged equations. We propose to use a Runge Kutta method with a τ step equal to several periods. It must be borne in mind that the time variable is τ and not time. For each evaluation of the seven derivatives of (16), at a specific τ time, τ_i, we must carry out the averaging procedure. Using $\bar{R}_0(\tau_i) \dot{\bar{R}}_0(\tau_i)$ as the reference orbit, we compute the 10 integrals given by (16a).

The Runge Kutta solution will produce $\bar{R}_0(\tau)$, $\dot{\bar{R}}_0(\tau)$ and $(t - t_0)(\tau)$. To compute an ephemeris of the state, R (t) and $\dot{R}$ (t), we proceed as follows:

Let the period of the $\bar{R}_0(\tau)$, $\dot{\bar{R}}_0(\tau)$ orbit be T (τ),

$$T(\tau) = \frac{2\pi}{\mu} (a(\tau))^{3/2}$$

where   (17a)

$$a(\tau) = \left(\frac{2}{\bar{r}_0(\tau)} - \frac{\dot{\bar{R}}_0(\tau) \cdot \dot{\bar{R}}_0(\tau)}{\mu} \right)^{-1}$$

Let N be the integer part of τ/T (τ), and θ is given by,

$$\theta = 2\pi N + \sigma$$ (17b)

Using Newton's method, solve Kepler's equation for σ

$$\Delta\tau = \tau - NT = \frac{1}{\sqrt{\mu}} \left\{ a^{3/2} (\sigma - \sin\sigma) + r_0 a^{1/2} \sin\sigma + \frac{d_0 a(1 - \cos\sigma)}{\sqrt{\mu}} \right\}$$ (17c)

For any position in the N + 1 revolution, where the incremental eccentric anomaly, θ, lies between 0 and 2π.

Let

$$t = t(\tau) + \frac{a^{3/2}}{\sqrt{\mu}} \left\{ \alpha - \sin \alpha + \frac{r(\tau)}{a} \sin \alpha + \frac{d(\tau)(1 - \cos \alpha)}{\sqrt{\mu a}} \right\} (1 + a_4(\tau))$$

$$R(t) = f(\alpha) R_0(\tau) + g(\alpha) \dot{R}_0(\tau)$$

(17d)

$$\dot{R}(t) = \dot{f}(\alpha) R_0(\tau) + \dot{g}(\alpha) \dot{R}_0(\tau)$$

REFERENCES

Broucke, R. and P. Cefola, 1972, "On the Equinoctial Orbit Elements," *Celestial Mechanics*, 5, (3), pp. 303-310.

Christensen, E., 1970, "A Special Perturbation Analysis of Universal Variables," NASA CR-02532.

Godal, T. and T. V. Johansen, 1968, "Undisturbed Eccentric Anomaly Difference as the Independent Variable in the Perturbation Equations," Proceedings 19th IAF Congress, N. Y., AD158.

Lorell, J., 1970, "Lunar Orbiter Gravity Analysis," *The Moon*, 1, (2), pp. 190-231.

Pines, S., 1961, "Variation of Parameters for Elliptic and Near Circular Orbits," *Astron. Journal*, 66, (1), pp. 5-7.

Pines, S., 1973, "Uniform Representation of the Gravitational Potential and Its Derivatives," *AIAA Journal*, 11, pp. 1508-1511.

Uphoff, C., 1973, "Numerical Averaging in Orbit Prediction," *AIAA Journal*, 11, (11), pp. 1512-1516.

APPENDIX A

We consider several typical perturbations.

Tesseral and Zonal Harmonics.
Let the central body rotate about its polar axis, $\hat{k}$ (t) with a uniform angular rate ω. If the inertial Cartesian coordinates of the vehicle is R, then the unit vector to the vehicle in planet fixed coordinates is given by,

$$u = \hat{k}(t) \cdot \frac{R}{r}$$

$$s = \hat{i}(t) \cdot \frac{R}{r} \tag{A.1}$$

$$w = \hat{j}(t) \cdot \frac{R}{r}$$

where $\hat{i}$ (t) and $\hat{j}$ (t) are orthogonal reference axes fixed in the rotating body equation, perpendicular to the polar axis $\hat{k}$ (t), expressed in the inertial Cartesian system of the vehicle.

Following Pines, (1973), the acceleration in the inertial system is given by

$$F_1 = \alpha_1 \hat{i}(t) + \alpha_2 \hat{j}(t) + \alpha_3 \hat{k}(t) + \alpha_4 \frac{R(t)}{r} \tag{A.2}$$

For the purpose of completeness, we list the α_i coefficients for J_2, J_3, J_4, C_{22}, and S_{22}.

$$\alpha_1(J_2) = \alpha_2(J_2) = \alpha_1(J_3) = \alpha_2(J_3) = \alpha_1(J_4) = \alpha_2(J_4) = 0$$

$$\alpha_4(J_2) = - \frac{\mu a_E^2 \, 3J_2 \, (1 - 5 u^2)}{2r^4}$$

$$\alpha_4(J_3) = - \frac{\mu a_E^2 \, 5J_3 \, (3u - 7 u^3)}{2r^5} \tag{A.3}$$

$$\alpha_4(J_4) = - \frac{\mu a_E^4 \, 15 (-1 + 14u^2 - 21 u^4)}{8 r^6}$$

$$\alpha_3(J_2) = - \frac{\mu a_E^2 \, 3J_2 u}{r^4}$$

$$\alpha_3(J_3) = -\ \frac{\mu a_E^3 \ 3J_3 \ (5u^2 - 1)}{2\ r^5}$$

$$\alpha_3(J_4) = -\ \frac{\mu a_E^4 \ 5J_4 \ (7\ u^3 - 3\ u)}{2\ r^6}$$

$$\alpha_1(C_{22}, S_{22}) = \frac{\mu a_E^2 6}{r^4} \ (wS_{22} + sC_{22})$$

$$\alpha_2(C_{22}, S_{22}) = \frac{\mu a_E^2 6}{r^4} \ (sS_{22} - wC_{22})$$

$$\alpha_3(C_{22}, S_{22}) = 0$$

$$\alpha_4(C_{22}, S_{22}) = -\ \frac{\mu a_E^2 15}{r^4} \ (C_{22}(s^2 - w^2) + 2s\,w\,S_{22})$$

Third Body Acceleration.

Let the gravitational mass coefficient of third body be u_i. Let the ephemeris of the third body, $R_{ci}(t)$, be given with respect to the central planet, about which the vehicle is orbiting, then the indirect acceleration is given by

$$F_2 = -\sum_{i=1}^{M} \frac{\mu_i}{r_{vi}^3} \ R - \sum_{i=1}^{M} \frac{\mu_i}{r_{ci}^3} \left(\frac{r_{ci}^3}{r_{vi}^3} - 1 \right) R_{ci} \tag{A.4}$$

where

$$r_{ci} = |R_{ci}|$$

$$r_{vi} = |R - R_{ci}| \tag{A.5}$$

Atmospheric Drag.

Let ρ be the air density, given as a function of the vehicle position, R, and the time, t. The drag acceleration is given by

$$F_3 = -\frac{1}{2}\rho(R, t) \ \frac{v\, C_D S}{m} \ \dot{R} \tag{A.6}$$

where

$$v = |\mathbf{R}|$$

$$C_D = \text{drag coefficient}$$

$$m = \text{vehicle mass}$$

$$s = \text{effective vehicle drag area.}$$

.

.
.

.

.

111

NONLINEAR COUNTER EXAMPLE FOR BATCH
AND EXTENDED SEQUENTIAL ESTIMATION ALGORITHMS

B. T. Fang
Wolf Research and Development Corporation
Riverdale, Maryland

A simple nonlinear example is presented which shows the well-known iterated batch least-squares and extended sequential estimation algorithms may converge to different estimates. For this example one may even say the extended sequential algorithm converges to the "wrong" value.

ORBIT DETERMINATION IN THE PRESENCE OF
UNCERTAIN ATMOSPHERIC DRAG

B. Tapley, D. Dowd, and B. Schutz
University of Texas
Austin, Texas

Uncertainties in the knowledge of the atmospheric density in the associated drag parameter constitute one of the primary limitations on the accuracy on which the orbits of near earth satellites can be determined and predicted. In most orbit determination programs, the effect of uncertainties in atmospheric drag are determined by adopting a standard atmosphere and estimating the drag parameters, $\beta \ C_D \ A \div m$.

However, for most missions, C_D and A vaiy and the standard atmosphere will contain errors. Each of these factors will lead to errors in the orbit determination and prediction operation. In this presentation, an apprcach for estimating the drag parameter, the effective satellite cross sectional area in the atmospheric density simultaneously with the satellite state, is described.

APPLICATIONS OF SATELLITE-TO-SATELLITE TRACKING
TO ORBIT DETERMINATION AND GEOPOTENTIAL RECOVERY

P. Argentiero, R. Garza-Robles, and M. O'Dell
Goddard Space Flight Center
Greenbelt, Maryland

Recent simulations have demonstrated the applicability of satellite-to-satellite tracking data
to the related problems of orbit determination and geopotential recovery. Specifically,
satellite-to-satellite tracking between an earth orbiting satellite and a satellite at geosyn-
chronous altitude (36000 km) produces long continuous data arcs which are not available
by means of ground-based tracking. This facility, in conjunction with correct estimation
techniques, can yield exceptional orbit determination accuracy. The data type also has
considerable applicability to geopotential determination when the low satellite has a high
inclination.

ORBIT DETERMINATION APPLICATIONS OF SATELLITE-TO-SATELLITE TRACKING

Attention is focused on the difficult problem of determining GEOS-C altitude with an
average accuracy of 1 m. Error sources considered were ground-station survey error, data
bias, epoch state errors for the high and low satellite, errors in spherical harmonic coefficients
of the geopotential field to degree, and order 8. Standard covariance analysis software was
utilized to determine that survey error and data bias were insignificant error sources, but
that uncertainty in relay satellite state caused radial errors of the order of 100 m. Geopo-
tential uncertainty caused an average radial error of 6 m. When the high and the low satellites
are estimated and other error sources ignored, the average radial error is 6.2 meters. To
identify the geopotential terms to be estimated in order to satisfy the constraint of 1 meter
altitude resolution, a recursive procedure is implemented. If N-dominant geopotential terms
along with GEOS-C and ATS-6 satellite states are estimated, and if the 1 meter radial
error constraint is not satisfied, the geopotential term from among the unadjusted set which
causes maximum radial aliasing is added to the estimated set of parameters. If the constraint
is still unsatisfied, the recursive procedure continues. This recursive procedure has been
automated within the covariance analysis software. The result of the procedure when applied
to the GEOS-C orbit determination problem is that after 31 dominant geopotential terms
are recursively identified and added to the estimated state along with GEOS-C and ATS-6
state, an average radial error of 1 meter is achieved.

GEOPOTENTIAL RECOVERY APPLICATIONS

During the GEOS-C mission it is planned to track GEOS-C from ATS-6 from widely separated geosynchronous positions of 94°W and 34°E. The resultant data set should be almost globally distributed. Simulations demonstrate that it is possible to estimate from this data set coefficients of the spherical harmonic representation of the geopotential field to degree and order 8 with an accuracy on an order of magnitude superior to that presently obtainable.

N76-10180

LARGE ANGLE SATELLITE ATTITUDE MANEUVERS

John E. Cochran* and John L. Junkins†
The University of Virginia
Charlottesville, Virginia

ABSTRAC

Two methods are proposed for performing large angle reorientation maneuvers. The first method is based upon Euler's Rotation Theorem; an arbitrary reorientation is ideally accomplished by rotating the spacecraft about a line (the "Euler Axis" or "Principal Line") which is fixed in both the body and in space. This scheme has been found to be best suited for the case in which the initial and desired attitude states have small angular velocities. A detailed evaluation of the associated feedback control laws and sensitivity to disturbances has been carried out, assuming the control system to consist of four single-gimbal control moment gyros (CMGs). These results indicate that the proposed scheme is feasible with realistic physical constraints on the CMG torque source. The second scheme is more general in that a general class of transition trajectories is introduced which, in principle, allows transfer between arbitrary orientation and angular velocity states. The method generates transition maneuvers in which the uncontrolled (free) initial and final states are matched in orientation and angular velocity. The forced transition trajectory is obtained by using a weighted average of the unforced forward integration of the initial state and the unforced backward integration of the desired state.

Our current effort is centered around practical validation of this second class of maneuvers. Of particular concern is enforcement of given control system constraints and methods for suboptimization by proper selection of maneuver initiation and termination times. Analogous reorientation strategies which force smooth transition in angular momentum and/or rotational energy are also under consideration.

DISCUSSION

Many spacecraft must perform one or more reorientations or attitude changes during their lifetimes. The ways in which these maneuvers are performed are obviously important from the standpoint of conservation of energy. However, often the optimality of a maneuver in

---

*Visiting Associate Professor, Associate Professor, Aerospace Engineering Department, Auburn University, Auburn, Alabama.
†Associate Professor.

terms of the energy required to perform it may be of lesser importance than the time and computational power needed to define it. That is, often, finding the optimal maneuver strategy may not be desirable or even possible within the constraints imposed.

In this paper, two methods for defining "good," nominal, large-angle attitude maneuvers for spacecraft are presented. Nei'' er of the methods is generally optimal (although in special cases they would be), but both offer the advantages of being (1) relatively easy to use and (2) explicit, rather than iterative. The first method, which is well-suited for the case of quiescent initial and final rotational states, is based on Euler's Rotation Theorem, that is, it is a single axis maneuver. The second method, which may be used when the initial and/or final rotational states are not quiescent, is based on the use of transition trajectories in a phase space of dimension eight, where the redundant dimensions are due to the choice of four parameter descriptions of orientation.

SINGLE AXIS MANEUVERS

The idea of utilizing single axis rotations for arbitrary reorientations is not a new idea (Meyer, 1966). For example, the Apollo Command and Service Module were reoriented with a single rotation about the required Euler axis (Crisp et al., 1967). Such m: neuvers are not necessarily optimal, in fact, Dixon et al. (1970) have shown that single axis maneuvers of axisymmetric spacecraft through the use of thrusters are generally more costly in terms of fuel used than two-impulse maneuvers designed to minimize fuel expended. They are, on the other hand, more easy to define than optimal maneuvers, and if the spacecraft is asymmetric, no closed-form optimal maneuver strategy comparable to that of Dix(. et al. (1970) is available.

One important concept, used to some extent in both methods, is that of Euler, or eigenaxis, rotations. Figure 1 is included to illustrate this concept. On the left hand side of figure 1 are shown a centroidal body-fixed system Cxyz and the associated unit vector triad $(\hat{u}_1, \hat{u}_2, \hat{u}_3)$ as well as the Euler axis for a particular reorientation. The Cxyz system pictured on the right-hand side is a rotationally inertial coordinate system which is used along with the displaced Cxyz system to indicate how the Euler axis rotation proceeds.

Figure 2 provides some information concerning how the attitude of a moving trihedral $C\,\hat{e}_1\,\hat{e}_2\,\hat{e}_3$ with respect to a fixed trihedral $C\,\hat{e}_1'\,\hat{e}_2'\,\hat{e}_3'$ can be defined. The rotation matrix $\underline{A}$, whose elements are direction cosines relating the two trihedrals, can be constructed using Euler angles, say ψ, θ, and ϕ or alternatively using Euler parameters, here indicated by $\alpha_0, \alpha_1, \alpha_2$, and α_3. Furthermore, the Euler parameters are intimately related to the principal rotation angle ϕ and the direction cosines ℓ_1, ℓ_2, and ℓ_3 of the principal line, i.e., the Euler axis (or equivalently, the eigenaxis corresponding to the unit eigenvalue of $\underline{A}$).

Assuming that $\underline{A}$ is specified, the four parameters α_0, α_1, α_2, and α_3 can be determined in a noniterative fashion. Then, for single axis rotations, the direction of the Euler axis can be determined as well as the required principal angle. For control of single axis rotations in the presence of disturbing torques, it is advantageous to define an eigenaxis system as

117
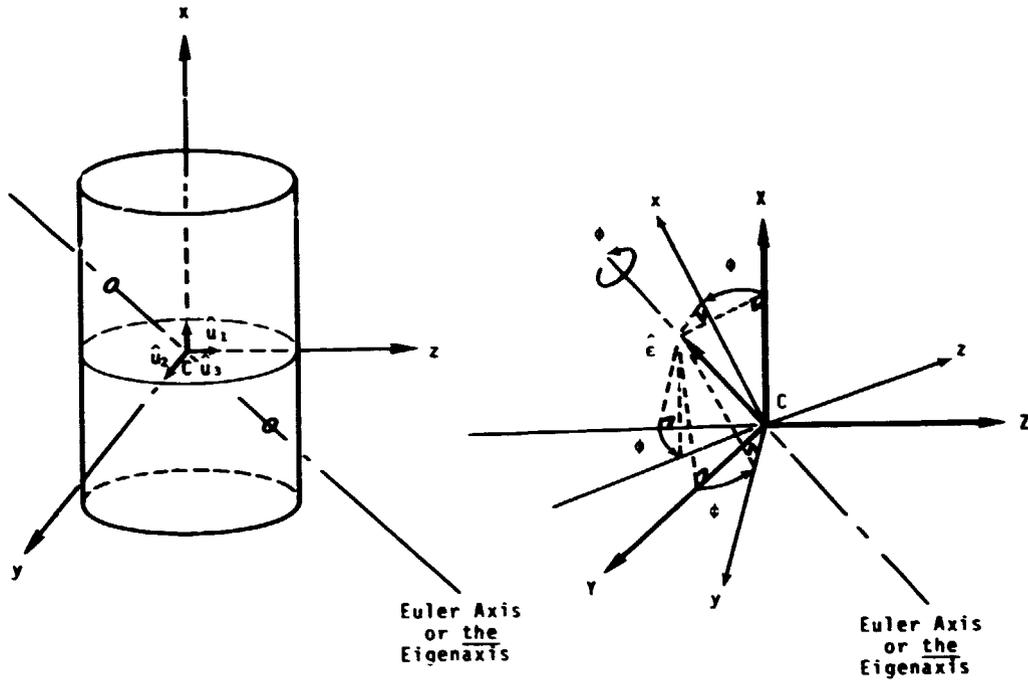
Figure 1. The Euler axis and Euler axis rotations.

$$[\hat{e}_1\hat{e}_2\hat{e}_3]^T = \underline{A}[\hat{e}_1'\hat{e}_2'\hat{e}_3']^T$$

$$\underline{A} = \underline{A}(\psi,\theta,\phi) = \underline{A}(\alpha_0,\alpha_1,\alpha_2,\alpha_3)$$

$$\alpha_0 = \cos(\phi/2) \qquad \underline{\alpha} = \sum_{j=1}^{3} \underbrace{\{[\sin(\phi/2)]\hat{\epsilon}\cdot\hat{e}_j'\}\hat{e}_j'}_{\alpha_j}$$

$$Q = \alpha_0 + \underline{\alpha} \qquad Q^{-1} = \alpha_0 - \underline{\alpha}$$

$$\hat{e}_j = Q\hat{e}_j'Q^{-1} \qquad \ell_j = \hat{\epsilon}\cdot\hat{e}_j', \quad j = 1, 2, 3.$$
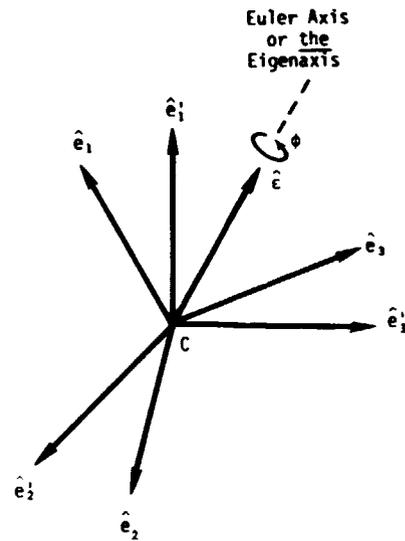
Figure 2. Attitude change logic.

described in Cochran et al., 1975. The way in which such a system is defined is briefly summarized in figure 3.

$$\hat{e}_\ell \cdot \hat{e}_I$$

$$\hat{e}_I \cdot \hat{u}_j \qquad \ell = 1,2, \text{ or } 3$$

$$\hat{e}_m = \hat{e}_\ell \times \hat{u}_n / |\hat{e}_\ell \times \hat{u}_n|$$

$$\hat{e}_n = \hat{e}_m \times \hat{e}_\ell$$
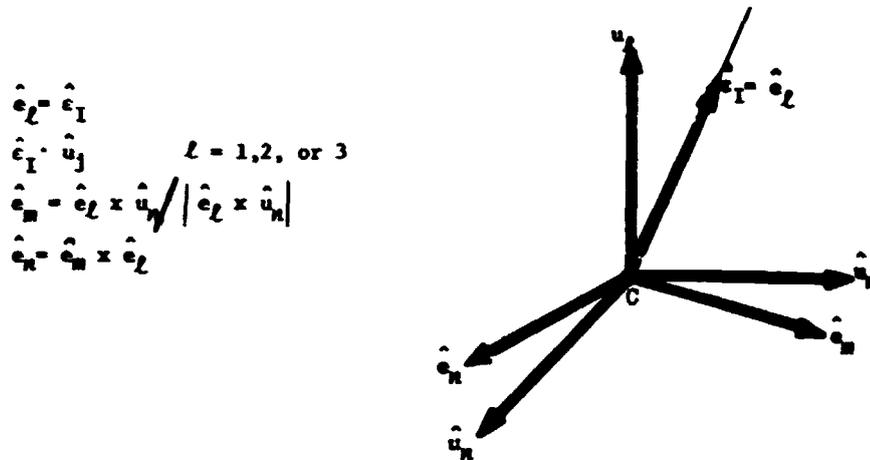
Figure 3. The eigenaxis system.

Figure 4 indicates how attitude errors in the form of small Euler angles ϕ_m and ϕ_n may be specified by using the body-fixed eigenaxis system $Ce_\ell e_m e_n$ which ideally has its $\hat{e}_\ell$-axis directed along the principal line.

$$\sin\phi_m = 2(\alpha_m \alpha_0 - \alpha_n \alpha_\ell)$$

$$\tan\phi_n = 2(\alpha_n \alpha_0 + \alpha_m \alpha_\ell)/(\alpha_0^2 + \alpha_\ell^2 - \alpha_n^2 - \alpha_m^2)$$

$$\tan\phi_\ell = 2(\alpha_\ell \alpha_0 + \alpha_m \alpha_n)/(\alpha_0^2 + \alpha_n^2 - \alpha_\ell^2 - \alpha_m^2)$$

$$\phi_\ell \simeq \phi$$

$$\phi_m, \phi_n - \text{"small" error angles}$$
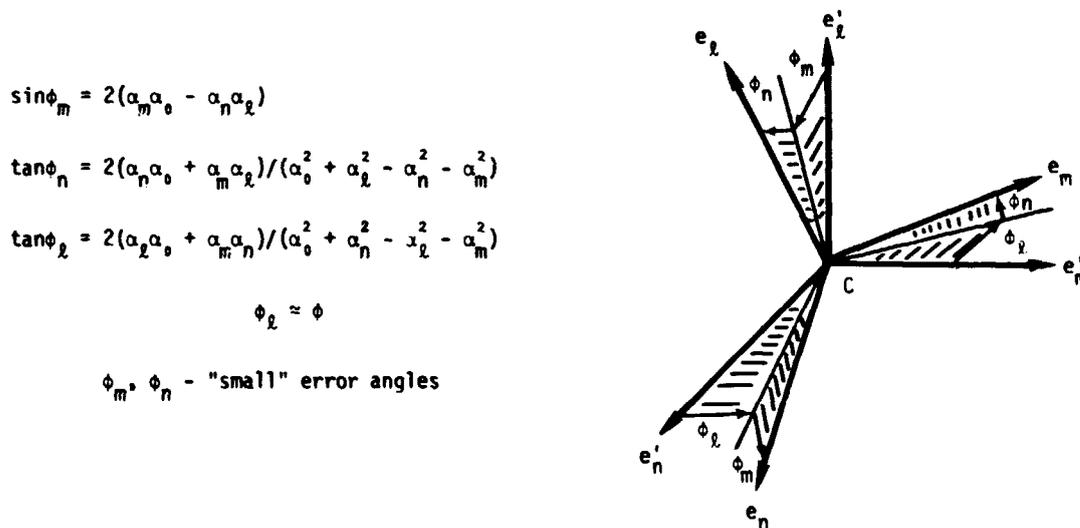
Figure 4. Attitude errors.

The dynamical equations for a spacecraft which contains n control moment gyros (CMGs) are given in figure 5. This equation, the control torque equation, and CMG steering law also given in figure 5 were used in a recent study (Cochran et al., 1975) of the feasibility of controlling single axis rotations using CMGs and several linear controllers.

119

Dynamics: $\underline{I}\,\dot{\underline{\Omega}} + \tilde{\underline{\Omega}}\,\underline{I}\,\underline{\Omega} = \underline{T}_{ex} + \underline{T}_c$

Control Torque: $\underline{T}_c = -\underline{F}\,\dot{\underline{\delta}} + \tilde{\underline{h}}_G\,\underline{\Omega}$

CMG Steering Law: $J = 1/2\,\dot{\underline{\delta}}^T\,\underline{W}\,\dot{\underline{\delta}}$

$\dot{\underline{\delta}} = -\underline{W}^T\,\underline{F}^T\,(\,\underline{F}\,\underline{W}^{-1}\,\underline{F}^T\,)^{-1}\,(\underline{T}_c - \tilde{\underline{h}}_G\,\underline{\Omega}\,)$
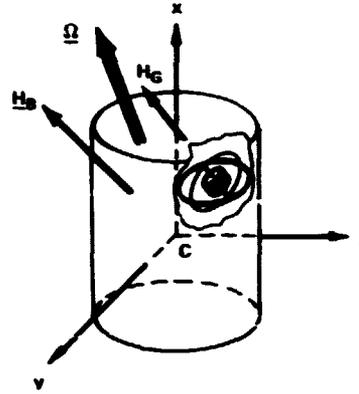
Figure 5. Attitude dynamics and CMG steering law.

The following equations are the nonlinear matrix forms of the equations of rotational motion and approximate linear equations derived assuming small angular velocity magnitude, small errors and a linear controller of angular acceleration (for more details see Cochran et al., 1975).

$$\underline{I}_e\,\dot{\underline{\Omega}}^e + \overbrace{\tilde{\underline{\Omega}}e\,\underline{I}_e\,\underline{\Omega}^e}^{\approx\,0} = \underline{T}^e_{ex} + \underline{T}^e_{c}$$

$$\dot{\underline{\Omega}}^e \simeq (\dot{\phi}_1\dot{\phi}_2\dot{\phi}_3)^T$$

$$\ddot{\phi} = \underline{I}_e^{-1}\underline{T}^e_{ex} + \underline{I}^{-1}\underline{T}^e_{c}$$

$$\ddot{\phi} = \underbrace{-\underline{K}_1(\dot{\phi} - \dot{\phi}_c) - \underline{K}_2(\underline{\phi} - \phi_c) - \underline{K}_3 \int_{t_0}^{t} (\phi - \phi_c)dt}_{\text{Linear Feedback}}$$

$$\underbrace{+\ \underline{I}_e^{-1}\underline{T}^e_{ex}}_{\text{External Disturbance}}$$

One of the controllers used in the study reported in Cochran et al. (1975) is depicted schematically in figure 6. The controller is a proportional-plus-integral-plus-derivative, or PID, controller modified by using a "model follower" commanded rotation angle generator which serves two purposes. First, it allows maintaining the difference in the actual angle of rotation ϕ about the principal line close to the commanded rotation angle ϕ_{ϱ_c} (hence higher

120

gains and tighter control) and second, it provides a means of specifying the nominal rotation rate ω^* a priori so that allowable CMG gimbal rates will hopefully not be exceeded. Attention should be drawn to the form of the function ϕ_{c_ℓ}. This function is such that the commanded rotation angle connects the initial value for $\overset{\varsigma}{\phi}$, i.e., zero, and the desired final value of ϕ, ϕ_f, with a smooth curve.

$$\begin{cases} \phi_{c_\ell} = \phi_f/2 \ (1 - \cos\omega^*t) & \omega^*t \leq \pi \\ \phi_{c_\ell} = \phi_f & \omega^*t > \pi \end{cases}$$
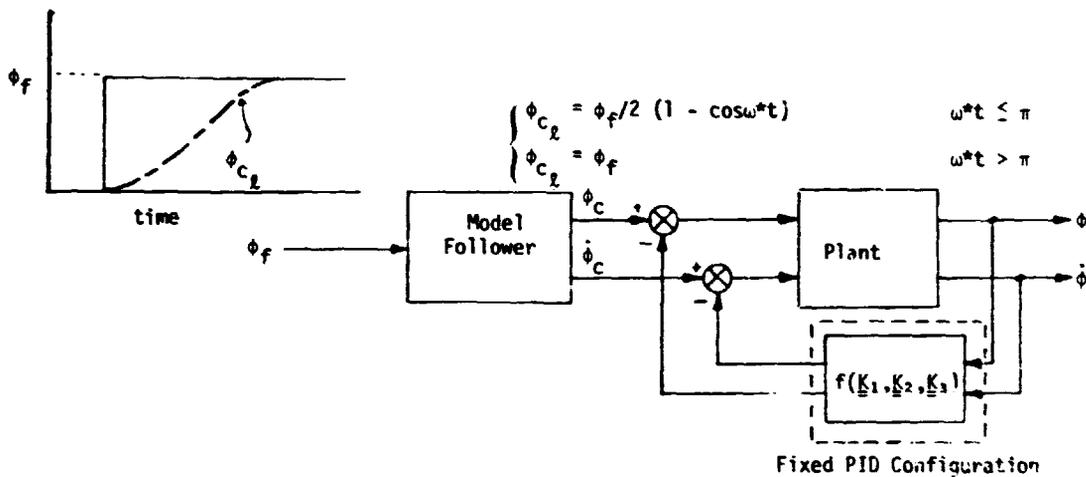
Figure 6. PID model-follower.

Some typical response curves for the rotation angle are shown in figure 7. Four different controllers were used to generate the curves by numerically simulating the attitude motions of a Large Space Telescope type spacecraft using four single gimbal CMGs as torque sources. The full nonlinear equations were used in the simulations (the reader is again referred to Cochran et al. (1975) for more details). The PID model-following controller has been discussed and the PID and PD are simpler controllers. In figure 7, MRAS refers to a model reference adaptive system controller which utilizes Lyapunov's second method to generate variable control gains.

In the study reported by Cochran et al. (1975), the control of single axis rotation in the presence of disturbances was found to be feasible using rate limited CMGs.

TRANSITION TRAJECTORIES

The basic idea for the second method of performing attitude maneuvers was motivated by the use of the function ϕ_{c_ℓ} in the PID model-following controller and previous use of the concept of weighting functions in the areas of geodesy and gravity modeling (Jancaitis and Junkins, 1974). In figure 8, this idea, the use of an averaging concept for definition of transition maneuvers, is summarized. The functions α_f (t) and α_b (t), shown in the upper left-hand portion of figure 8, represent an attitude variable, α (t), say one of the α_j, j = 0, 1, 2, 3, as it would appear as a function of time if the spacecraft were rotating freely in its initial state (subscript f) and similarly its final, or desired, state (subscript b). The dashed

curve represents a transition curve for the variable α. Note that $\alpha(t)$ is constructed by using the unforced forward integration of α from time t_0 using the actual value of α at t_0 as an initial condition and the unforced backward integration of α from time t_f with the desired final value of α as a final condition.
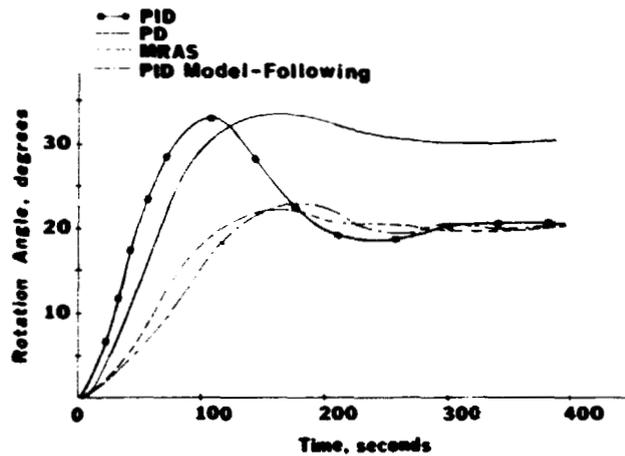
Figure 7. Rotational response.
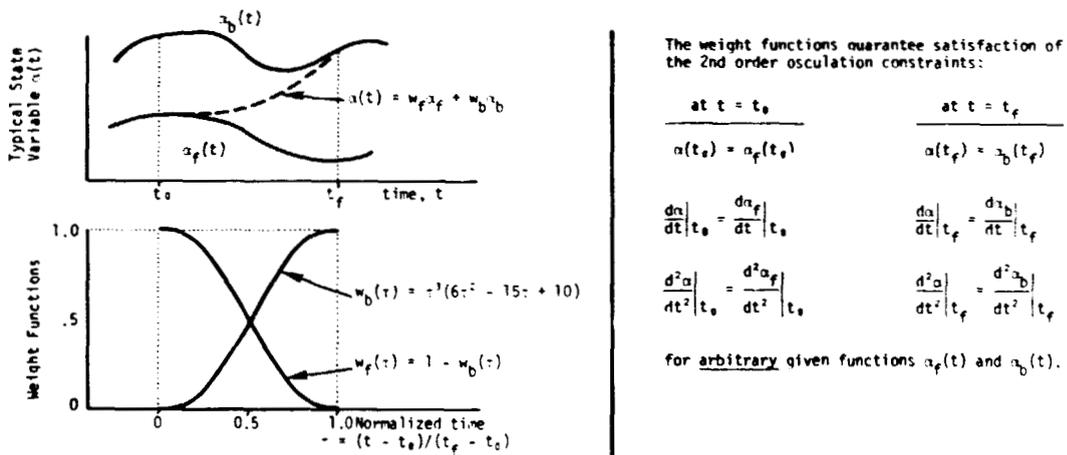
Figure 8. Averaging concept for definition of transition maneuvers.

122

The weighting functions, W_f and W_b, shown as functions of normalized time τ, are used in defining α (t), so that the second-order osculation constraints (see right-hand side of figure 8) of agreement in value and the first two time derivatives at times t_0 and t_f are satisfied. Note that W_f and W_b are relatively simple functions and that they provide a method for defining a smooth function which generates a transition curve between two arbitrary, but smooth, functions of time.

Recalling that α is an attitude variable (it may also be a vector of variables), it is obvious that the proposed method provides a means for explicitly determining the torque required to make the spacecraft attitude follow a prescribed trajectory in phase space. Thus, the trajectory departs smoothly from the initial state and ends in the desired final state. The explicit determination of the torque depends only on the availability of the first two time derivatives of three, or more, attitude variables.

We assume that, during the time required for the maneuvers, the external torques acting on the spacecraft are neglible. Furthermore, in obtaining the results presented here, we have assumed that the spacecraft is a single asymmetric rigid body with known inertia characteristics. These assumptions allow the use of an analytical solution for the free rotational motion of an asymmetric rigid body (see Morton et al., 1973, and Kraige and Junkins, 1974) in computing the forward and backward states and the necessary time derivatives used in constructing the torque required to perform the maneuver.

The analytical solution for the torque-free rotational motion of asymmetric rigid body which was used is summarized in the following list.

Analytical Solution for Torque-Free Motion of Asymmetric Body.

Angular Velocity	Euler Orientation Parameters

Angular Velocity

$$u = \Omega t + \phi_0$$

$$\omega_1(t) = \omega_{1m} dn(u,k)$$

$$\omega_2(t) = \omega_{2m} sn(u,k)$$

$$\omega_3(t) = \omega_{3m} cn(u,k)$$

where

$$\{k, \Omega, \phi_0, \omega_{1m}, \omega_{2m}, \omega_{3m}\}$$

are constants defined in terms of inertias and initial conditions.

Euler Orientation Parameters

$$\{\alpha(t)\} \equiv \begin{Bmatrix} \alpha_0(t) \\ \alpha_1(t) \\ \alpha_2(t) \\ \alpha_3(t) \end{Bmatrix} = \begin{bmatrix} \gamma_0 & -\gamma_1 & -\gamma_2 & -\gamma_3 \\ \gamma_1 & \gamma_0 & -\gamma_3 & \gamma_2 \\ \gamma_2 & \gamma_3 & \gamma_0 & -\gamma_1 \\ \gamma_3 & -\gamma_2 & \gamma_1 & \gamma_0 \end{bmatrix} \begin{Bmatrix} \beta_0(t) \\ \beta_1(t) \\ \beta_2(t) \\ \beta_3(t) \end{Bmatrix}$$

where

$$\beta_0(t) = \sqrt{\tfrac{1}{2}[1 + asn(u,k)]}\ \cos\phi_0(t)$$

$$\beta_1(t) = \sqrt{\tfrac{1}{2}[1 - asn(u,k)]}\ \cos\phi_1(t)$$

$$\beta_2(t) = \sqrt{\tfrac{1}{2}[1 + asn(u,k)]}\ \sin\phi_0(t)$$

$$\beta_3(t) = \sqrt{\tfrac{1}{2}[1 - asn(u,k)]}\ \sin\phi_1(t)$$

$\{a, \gamma_0, \gamma_1, \gamma_2, \gamma_3\}$ are constants defined by initial conditions and inertias.

and

$\phi_0(t)$ and $\phi_1(t)$ are functions involving incomplete elliptic integrals of the third kind.

The body-fixed components of angular velocity are denoted by ω_1, ω_2, and ω_3 and these are functions of the time t and constants defined in terms of principal moments of inertia and initial conditions. The Jacobian elliptic functions dn (u, k), sn (u, k), and cn (u, k) are the basic time functions involved in the solutions for ω_1, ω_2, and ω_3.

For the attitude description, Euler orientation parameters were chosen. The body's inertial attitude is defined by the α_j, j = 0, 1, 2, 3, which are expressible as functions of a set of four constant Euler parameters γ_j, j = 0, 1, 2, 3, (which define the orientation of a nonrotating angular momentum coordinate frame), and four time varying Euler parameters β_j, j = 0, 1, 2, 3, (which define the orientation of the principal axes of the body relative to the angular momentum frame). The β_j may be expressed as functions of time by using Jacobian elliptic functions, incomplete elliptic integrals of the third kind and, of course, initial conditions and inertias.

Transition trajectories may, in principle, be defined in terms of any set of attitude variables. Two particular four parameter sets were chosen. The Euler parameters α_j, j = 0, 1, 2, 3, are a rather obvious choice; however, preliminary studies have indicated that the set composed of the principal angle of rotation ϕ and the directions cosines ℓ_j, j = 1, 1, 2, 3, of the Euler axis may be a more desirable set. These will be referred to as the principal rotation parameters. The construction of transition trajectories using these two sets of variables is summarized in the following list.

Definition of Transition Trajectories

Principal Rotation Coordinates

$(\alpha_0, \alpha_1, \alpha_2, \alpha_3) \Rightarrow (\phi, \ell_1, \ell_2, \ell_3)$ Transformation

$$\left.\begin{array}{l} \phi_f(t) = 2\cos^{-1}(\alpha_{f_0}) \\[2mm] \ell_{f_i}(t) = \alpha_{f_i}/\sin\dfrac{\phi_f}{2} \end{array}\right\} \quad f \to b$$

Forward Trajectory

$\phi_f(t)$ = Function (inertias, actual initial state at t_0, t)

$\ell_{f_i}(t)$ = Function (inertias, actual initial state at t_0, t)   i = 1, 2, 3

Backward Trajectory

$\phi_b(t)$ = Function (inertias, desired final state at t_f, t)

$\ell_{b_i}(t)$ = Function (inertias, desired final state at t_f, t)   i = 1, 2, 3

Transition Trajectory

$\phi(t) = w_f(\tau)\phi_f(t) + w_b(\tau)\phi_b(t)$

$\ell_i(t) = w_f(\tau)\ell_{f_i}(t) + w_b(\tau)\ell_{b_i}(t)$ i = 2, 3

$\ell_1(t) = \pm\sqrt{1 - [\ell_2^2(t) + \ell_3^2(t)]}$

124

Forward Trajectory

$\{\alpha_f(t)\}$ = Function (inertias, actual initial state at t_0, t)

Backward Trajectory

$\{\alpha_b(t)\}$ = Function (inertias, desired final state at t_f, t)

Transition Trajectory

$$\alpha_i(t) = w_f(\tau)\alpha_{f_i}(t) + w_b(\tau)\alpha_{b_i}(t) \quad i = 1, 2, 3$$

$$\alpha_0(t) = \pm\sqrt{1 - [\alpha_1^2(t) + \alpha_2^2(t) + \alpha_3^2(t)]}$$

Note that when four parameters are used appropriate constraints must be introduced.

The transition trajectory concept has been used to generate transition trajectories and the associated torque time histories for several pairs of initial and final states. Figures 9 and 10 show results for a case in which the principal rotation parameters were used to generate the transition trajectory. The principal moments of inertia picked for the example are $I_1 = 3$, $I_2 = 2$, and $I_3 = 1$. The maneuver required was to change the rotational state of the spacecraft from one in which $\alpha_0 = \sqrt{3}/2$, $\alpha_1 = \sqrt{15}/8$, $\alpha_j = 1/8$, $\alpha_4 = 0$, $\omega_1 = 1$, $\omega_2 = 0.10$ and $\omega_3 = 0.0$ at $t = t_0 = 0$ to one in which $\alpha_0 = 1/4$, $\alpha_1 = \sqrt{15}/4$, $\alpha_2 = \alpha_3 = 0$, $\omega_1 = 0.101$, $\omega_2 = 0.0$ and $\omega_3 = 0.0$ at $t = t_f = 5.0$. In this maneuver the inertial components of angular momentum were changed from (2.93, 0.47, - 0.48) at $t = 0$ to (0.303, 0.0, 0.0) at $t = 5$. Basically, a state in which the spacecraft is rotating rapidly with an initial nutation angle of about $12°$ is changed by the maneuver into a state of much slower (an order of magnitude less) spin about the principal axis of maximum moment of inertia, with the orientation of the body's angular momentum vector also changed.

The time histories of the angular momentum components and the Euler parameters are presented in figure 9. The principal rotation parameters were averaged to produce the transition maneuver, but the angular velocity and Euler parameters are, of course, also averaged in the sense that the desired final state is reached in a smooth manner. On each plot in figure 9, the solid curve represents the time history of the indicated variable which results from unforced forward integration, the dashed line has a similar interpretation, but is derived from the backward integration of the desired final state, and the bold curve is the transition curve. Very smooth transitions of all seven variables are evident.
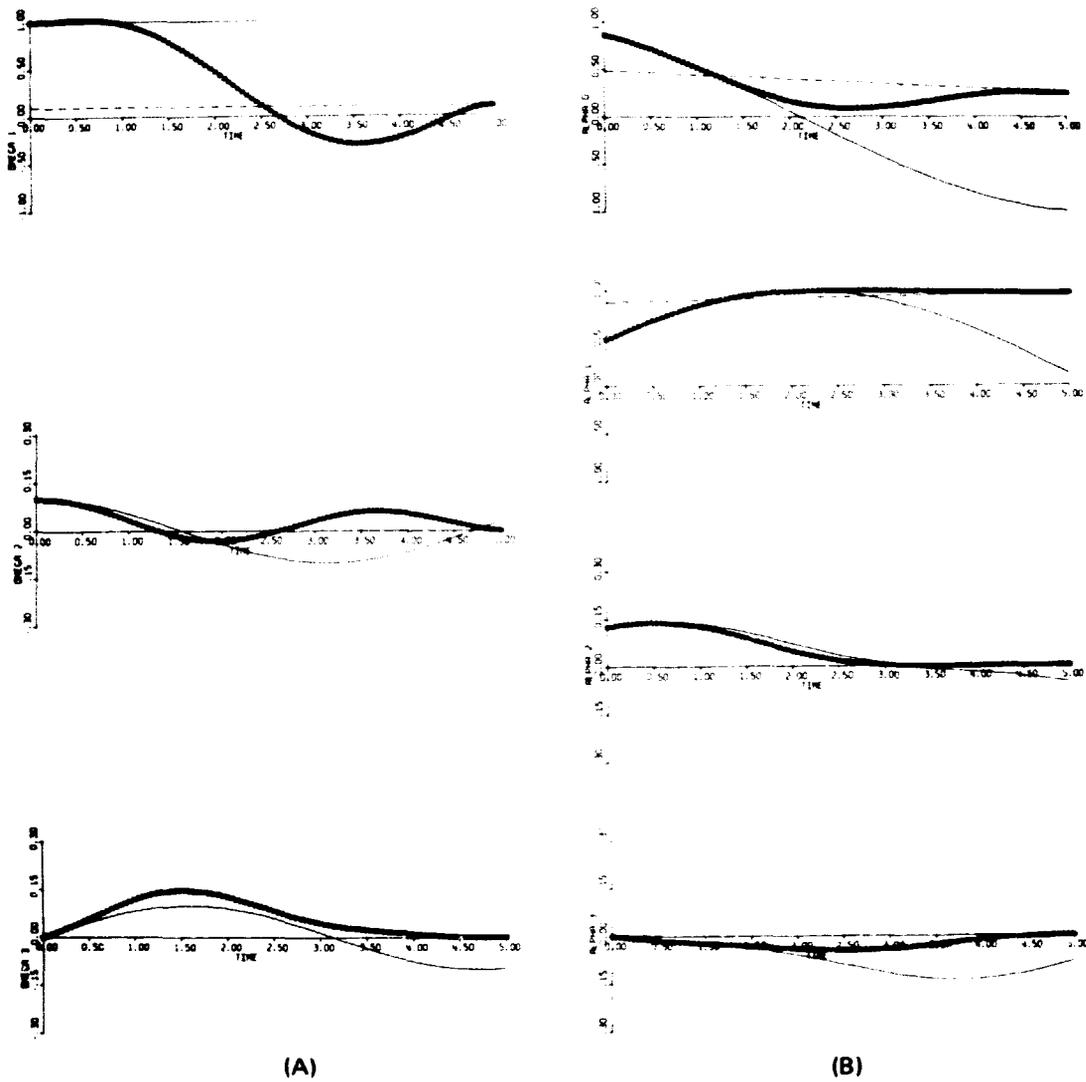
Figure 9. A - Angular velocity; B - Euler parameters.

Time histories for the variables which were averaged (i.e., the principal rotation parameters) are shown in figure 10. Also in figure 10 are included the time histories of the body-fixed components of the torque needed to generate the transition maneuver. The three curves in each of the plots indicated as LHAT1, LHAT2, LHAT3, and PHI are analogous to those previously described. In the torque plot, the 1-component is indicated by the solid line, the

126

2-component by the dashed line, and the 3-component by the bold line. The difference in the magnitudes of the initial and final angular velocities is apparent from the radically different slopes of the curves for the forward and backward solutions for the principal angle.

(B)

(C)

(A)
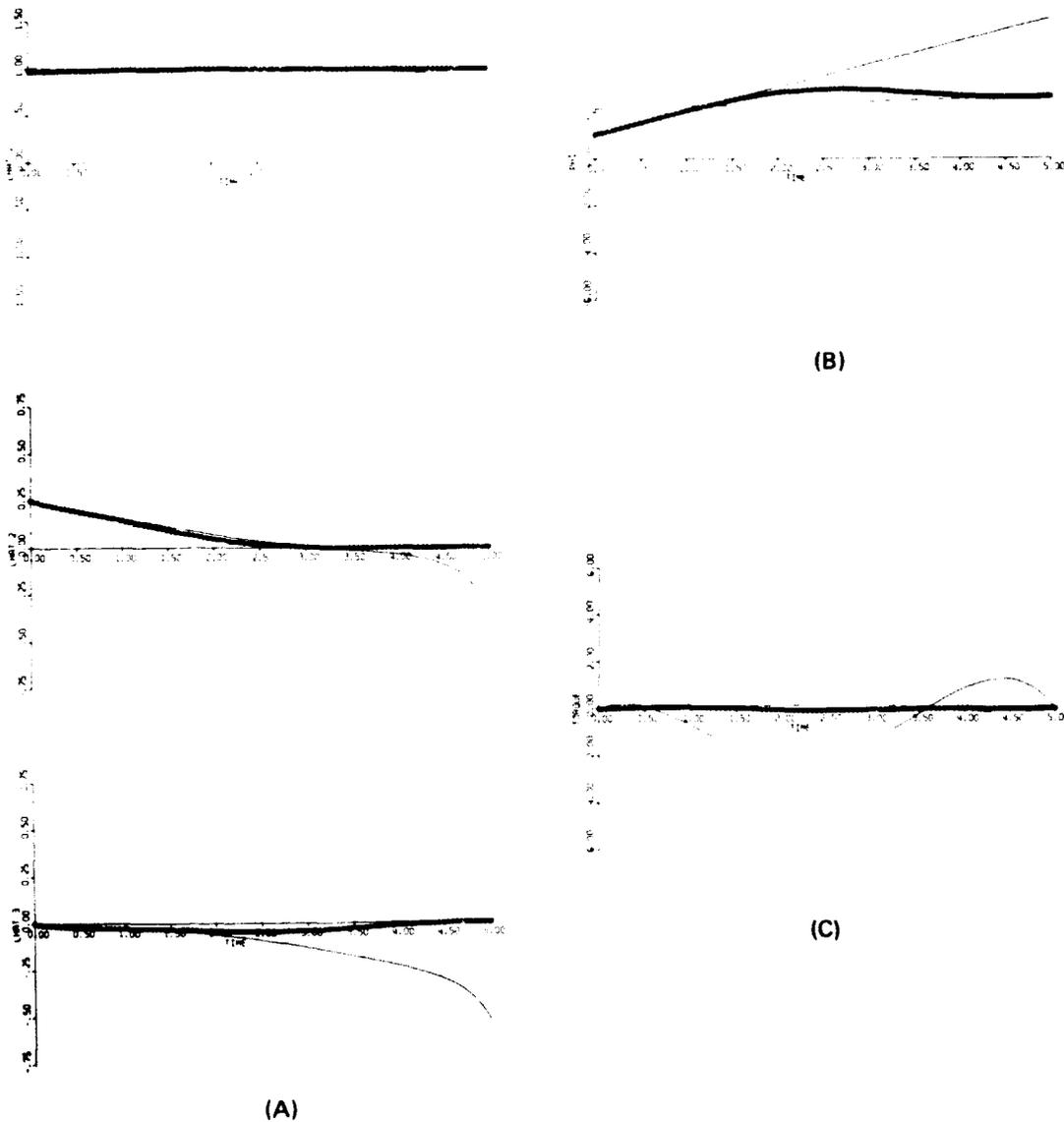
Figure 10. A - Euler axis direction cosines; B - principal angle; C - torque history.

Considering the torque history in more detail, we note that the second-order osculation constraints embodied in the functions W_f and W_b result in zero torque at t = 0 and t = 5. All three components of the torque are smooth and bounded; the largest magnitude of any one component is about 2.15.

127

Referring to the list of transition trajectories, the transformation from the Euler parameters to principal rotation parameters embodies a singularity whenever ϕ is an integer multiple of 2π; resulting in ambiguous definition of the Euler axis. Thus, in the absence of some remedial action, the transformation equations and their derivatives do not provide an acceptable basis for defining multirevolution transition maneuvers. We are currently studying means of circumventing this difficulty and thereby allowing application of this method to the multirevolution case.

From the work which we have done to date on the attitude maneuver problem, we have drawn the following conclusions:

- Single-axis maneuvers are not necessarily optimal, but provide a reasonable basis for quiescent-state-to-quiescent-state attitude maneuvers using onboard computations and continuous torques, especially if the spacecraft is asymmetric.

- Control of such single-axis maneuvers in the presence of disturbances is feasible.

- Transition maneuvers provide an explicit solution to a more general class of maneuver problems.

- Control of transition maneuvers looks feasible.

- An important feature of both methods is that iterative solution of a two-point boundary value problem (TPBVP) is avoided.

- Transition maneuvers provide starting solutions (which satisfy the boundary conditions) for iterative solution of TPBVPs.

REFERENCES

Crisp, R., D. Keene, and M. Dixon, 1967, "A Method of Spacecraft Control," *International Astronautical Federation, 17th International Astronautical Congress*, Gordon and Beach, New York.

Cochran, J. E., B. K. Colburn, and N. D. Speakman, "Adaptive Spacecraft Attitude Control Utilizing Eigenaxis Rotations," AIAA Paper No. 75-158, AIAA 13th Aerospace Sciences Meeting, Pasadena, California.

Dixon, M. V., T. N. Edelbaum, J. E. Potter, and W. E. Vandervelde, 1970, "Fuel Optimal Reorientation of Axisymmetric Spacecraft," *Journal of Spacecraft*, 7, pp. 1345-1351.

Jancaitis, J. R., and J. L. Junkins, 1974, "Modeling in n Dimensions Using a Weighting Function Approach," *J. of Geophys. Res.*, 79, pp. 3361-3366.

Kraige, L. G., and J. L. Junkins, 1974, "Perturbation Formulations for Satellite Attitude Dynamics," AIAA Paper No. 74-785, AIAA Mechanics and Control of Flight Conference, Anaheim, California.

Meyer, D., 1966, "On the Use of Euler's Theorem on Rotations for the Synthesis of Attitude Control Systems," NASA TN D-3643.

Morton, H. J., Jr., J. L. Junkins, and J. N. Blanton, "Analytical Solutions for Euler Parameters," *Celestial Mechanics*, in press; also 1973, AIAA/AAS Astrodynamics Conference paper, Vail, Colorado.

MISSION OPERATIONS FOR THE LOW COST
MODULAR SPACECRAFT

R. L. des Jardins
Goddard Space Flight Center
Greenbelt, Maryland

The low cost modular spacecraft (LCMS) was developed by Goddard Space Flight Center to provide a standard spacecraft bus which could easily be configured to support virtually any near-space unmanned mission to be flown in the 1980s. The LCMS features subsystem modularity allowing great flexibility and on-orbit servicing, yet achieving benefits of widespread standardization. Also, the LCMS design incorporates a high-performance onboard computer as a remote controller for most spacecraft subsystems. The LCMS is described briefly and its implications for mission operations is explored.

ONBOARD ORBIT DETERMINATION USING SERIES SOLUTIONS

T. Feagin
University of Tennessee Space Institute
Tullahoma, Tennessee

An iterative, linear sequential estimation algorithm is presented which is suitable for use in a small onboard digital computer. The solution is obtained in the form of a finite series of Chebyshev polynomials. The series-solution provides a close approximation to the actual orbit which is valid for a given interval of time. A Kalman filter is used to combine new observational data with the old estimate of the state and its associated error covariance matrix in order to update the series-solution and thus to provide a new optimal estimate and covariance matrix.

HIGH ALTITUDE AUTONOMOUS NAVIGATION

Howard A. Garcia
Martin Marietta Corporation
Denver, Colorado

PURPOSE OF STUDY

The applied research described in this paper pertains to a high altitude autonomous na 'ga-tion system which was the subject of a Phase 0 Preliminary Design and Feasibility Study under contract with SAMSO, United States Air Force Systems Command. This contract had the expressed objectives of selecting a particular design configuration by means of a trade study involving several candidate sextant concepts and carrying out a preliminary design based on the final selected sextant subsystem. In addition, the contract also called for an analytic evaluation of the general navigation concept by a numerical analysis which included a parametric sensitivity study and a performance demonstration by a Monte Carlo analysis.

SYSTEM REQUIREMENTS

Air Force requirements specified that the system be autonomous to the extent that no dedicated earth emission would be necessarily invoked and that the system would operate effectively to at least 120,000 n.m. The space sextant system that was adopted relies upon no earth referenced missions, either passive or dedicated. The navigation accuracy has been shown to be constant for any of the tested orbits, irrespective of orbit shape, orientation, or altitude. The Air Force requirements further specified that the system should have a demonstrated accuracy (by numerical analysis) of at least 1 n.m. (1σ rss) at a confidence level of 95 percent and, where large trajectory errors are presumed to exist, should converge in at least 10 hours from the onset of navigation. The numerical analysis has shown that the system converges to less than 1 n.m. in about 6 minutes and has demonstrated steady-state navigation accuracies of about 800 feet (1σ rss) after 15 to 18 hours of measurement processing. Other design goals established for the system include mission versatility, satellite versatility, insensitivity to reasonable parameter variations, insensitivity to satellite maneuvers, a 5-year lifetime, and the utilization of existing technologies.

NAVIGATION CONCEPT

The navigation concept is simple and direct. Navigation is accomplished by means of measured angles between the brighter stars (visual magnitude < 2) and the bright limb of the moon. Reduction to the moon's center, including compensation for asphericity effects

132

and lunar terrain, is accomplished by onboard software. The essential data required to determine the navigation position are the measured angle, the moon's ephemeris, and precise time. In principle, it may be shown that angular measurements from each of two stars to its nearest limb on the moon establishes a line of position for the spacecraft. Similar measurements made on the earth's limb provide a second line of position. The intersection of the two obtains a complete navigation fix in as short a period of time as is necessary to complete these measurements.

High navigation accuracy is achieved by further improving this position (and velocity) knowledge by recursively filtering subsequent star-moon measurements over the next several hours.

ANGLE MEASUREMENT SUBSYSTEM

The basic sextant instrument consists of two Cassegrainian telescopes, an angle measurement head, and two gimbals providing for two additional degrees of angular freedom.

The electronics package consists of an oscillator, registers, A to D converters, a digital microprocessor, and the wheel speed control servo. The total device, sextant and electronics, would weigh less than 25 pounds.

The principle of operation is quite simple. A spinning element inside of the measurement head, running at constant angular velocity, intercepts the optical path of a ray originating at a star observed by one telescope, and subsequently intercepts the path of a ray originating on the moon's limb observed by the second telescope. The time elapsed between the reception of these two signals, which may be recorded with great precision, is directly translatable into arc measure. This associated servo system incorporates two independently operated subsystems: an in-plane servo which positions the star (S) and the limb (L) trackers precisely on these respective targets and a cross-plane servo which orients the measurement head (wheel and both optical tracking telescopes) into the plane of measurement defined by the S X L vector.

MEASURING HEAD OPTICAL SCHEMATIC

Two optical trains are utilized in the operation of each tracker: the tracker ray and the timing pulse ray. The tracking ray enters the telescope aperture, reflects off the primary mirror, then the secondary mirror, and finally impinges on the detector. The timing pulse ray, originating at an internal light source, passes through the collimator lens and is reflected off two mirrored surfaces in a prism that is common to both trackers and that rotates with the wheel. This timing pulse ray is then reflected off this primary and secondary and impinges on the same detector as the tracking ray. The detectors are two-stage, four quadrant, differential detection types, with the first stage for acquisition and the second stage for precise tracking the timing pulse generation. The timing pulse is generated by zero crossing detection of the timing pulse ray as it crosses two detectors whose output is differenced. One advantage of this type of detection is the accuracy that can be

achieved with zero crossing detectors and another is its insensitivity to a mismatch in detector output responsivity.

The sextant trackers are designed for total symmetry and reciprocity so that either tracker can be used for star or limb tracking. This feature also allows for attitude measurement and onboard self-calibration using two stars.

SYSTEMATIC ERROR COMPENSATION

High measurement precision and stability is achieved by means of a phase-locked loop and self-compensation for radial runout and encoder disk systematic errors. The phase locked loop drives the wheel assembly at an angular velocity of approximately 50 rad/s. The commanded rate originates with the oscillator and the position feedback is derived from an optical transducer disk by means of a read head. When the wheel is in motion, the output from the read head is frequency. The actual disk contains inscribed $\sin 2^{11}$ and $\cos 2^{11}$ functions. These functions permit the extraction of phase information and make a wideband, high gain phase loop possible.

Systematic errors in the encoder disk are on the order of 10 arc-seconds until self-compensation procedures are activated. Other error sources which include bearing noise, sensor noise, and data sampling become dominant after self-compensation; however, the combined effect is to yield a total measurement error of about 0.5 arc second over a one second measurement time interval. The automatic tracking provision allows for continuous measurements during low thrust maneuvers. During high acceleration maneuvers, however, the sextant will be caged, but may resume operation within one minute following the maneuver.

NAVIGATION PERFORMANCE

The principal outcome of the analytic investigation of the system performance was to demonstrate that the system is capable of exceeding Air Force requirements by a substantial margin, both with regard to navigation accuracy as well as convergence time. A Monte Carlo simulation consisting of 59 samples (with no outliers) was necessary to ensure a 95 percent confidence level in the order statistics, constituting the primary investigative tool used in the performance analysis.

Two orbits were used as the models for the Monte Carlo analysis. Orbit A is a highly eccentric, 12-hour Molnyia type orbit, and Orbit B is an equatorial, circular, geosynchronous o.u.t. The Monte Carlo analysis considered only star/lunar limb measurements; consequently, these results show the high dependence of convergence time upon orbit geometry, for instance, 7 hours for Orbit A and 12 hours for Orbit B. By definition, convergence time is the time from the onset of navigation to the last major inflection of the navigation error curve; however, system accuracy continues to improve with additional data processing so that ultimate steady-state accuracy is finally achieved after several days of sextant navigation where the moon has completed a significant segment of its orbit. The accuracy is on the order of 800 feet and is a reflection primarily of the uncertainty in the lunar ephemeris itself.

134

A later analysis which employed star/earth limb measurements to augment the star/lunar limb measurements showed that the convergence time could be reduced to a few minutes. The final system accuracy would be achieved in less than 20 hours, owing to the vastly improved geometry resulting from the intersection of the second line of position. In either case, the ultimate navigation accuracy depends upon the more precise lunar limb data which is the primary mode of navigation, the earth limb data being used only to speed up convergence and to supplement the lunar limb data when the moon is occulted by either the earth or the sun.

STATISTICAL AGREEMENT

The performance analysis used several statistical methodologies to represent the expected system accuracy, all of which demonstrated good relative agreement, indicative of a fundamental internal consistency and providing a firm basis for the main conclusions drawn from the study. Four curves, all representative of the $1\ \sigma$ case, were computed and plotted for the two demonstration orbits:

- 67% - 67% population coverage derived from histogram data across 59 samples;
- σ - ensemble statistics standard deviation across 59 samples;
- σ_{cov} - square root of the summed position eigenvalues from a covariance analysis; and
- σ_3 - square root of the second central moment derived by a time averaged (moving window) technique along a single sample simulation.

An apparent disagreement between the covariance analysis and the Monte Carlo results at the initial time was due to the methods used to initialize the respective trajectory errors. The initial state covariance for these orbits was set at the estimated $1\ \sigma$ values; whereas, the initial trajectory offset for simulation purposes was set at $3\ \sigma$ values for all six state elements (a probability of occurrence of only $7 \cdot 10^{-20}$). Furthermore, the σ_3 curve, being one sample from the Monte Carlo set, is also shown to deviate initially from the other curves. The important result, however, is the fact that all of the statistical methods converge to essentially the same values at steady state for each of the two performance test cases, Orbits A and B.

SENSITIVITY ANALYSIS

A sensitivity analysis was carried out on three high altitude orbits (Orbit C, 14,350 n.m.; Orbit D, 68,000 n.m.; Orbit E, 115,000 n.m.) in addition to Orbits A and B. First and foremost, these sensitivity analyses have demonstrated that the system is totally indifferent to altitude in the earth-moon domain. Of course, this result is not unexpected because the prime observable is the moon and not landmarks on the earth. In the absence of augmented observations using the earth's limb, the rate of convergence appears to obey a logarithmic function based on orbit period. However by exploiting earth limb measurements,

all orbits converge in the period of a few minutes and obtain steady-state navigation accuracies of less than 0.2 n.m. in a matter of hours.

The sensitivity analysis also considered a range of model parameter errors of up to twice nominal values. These parameters included the lunar ephemeris (1 σ = 600 feet), lunar terrain height, (1 σ = 1700 feet), sensor noise (1 σ = 0.566 arc sec), and initial trajectory errors, the latter being dependent upon the particular orbit type. The principal results were as follows:

- The system is virtually insensitive to expected lunar ephemeris errors, even for the twice nominal case;
- 2 X σ lunar terrain errors are acceptable, but this also means that onboard compensation for terrain height will be required;
- Nominal sensor errors are near optimal in view of the contribution of other modeled system errors; and
- Large dispersions in initialization errors were completely suppressed by the recursive filtering process.

OCCULTATION OF THE MOON BY THE EARTH OR SUN

A phenomenon that must be acknowledged by the system concerns the possibility of an occultation of the moon by either the earth or the sun. The effect upon the navigation system was investigated by simulation, and it was found that the navigation accuracy was largely unaffected so long as the augmented measurement mode (earth limb) was employed during these critical periods.

In the specific example tested, worst case geometry was assumed for Orbit B (24-hour, circular orbit), where the earth itself is twice occulted by the sun in 24 hours, and the moon is concurrently obscured by the sun for 30 hours. Prior to either of the occultations in this example, the large initial trajectory errors were reduced by combined earth limb and lunar limb measurements. The earth and moon were then presumed to enter simultaneously the 9° look angle constraint zone centered about the sun. No navigation data could be acquired until the earth was again visible after 1.5 hours, and a slight increase in navigation error may be noted. Earth measurements were then commenced for the next 22.5 hours when it was again occulted; however, the growth of navigation errors this time were sufficiently suppressed so that no noticeable increase in navigation error occurs during the second occultation. Lunar limb measurements were resumed after 30 hours.

PRECISION ATTITUDE REFERENCE SYSTEM

The principal feature of the Space Sextant Navigation System is the high precision of the angular measurement. This same feature conduces to make the device an attitude reference sensor as well. The latter capability shows promise of becoming one of the most accurate onboard attitude sensing systems in existence. As an attitude sensor, it will be

136

necessary to add a platform reference mirror and a precision three axes gyro package. An autocollimation light source would also be added to the basic instrument in order to permit one telescope at a time to align itself with the reference mirror. Two axis angular reference may be achieved either with a second orthogonal reference mirror or a precision base encoder to measure the yaw angle. The relative advantages of these two alternative modes of obtaining two angular measurements of a single star have not been assessed at this time; however, it is anticipated that the system will ultimately be capable of 0.1 arc sec, three axes orientation under steady-state conditions.

SS-HANS DESIGN SUMMARY AND CONCLUSIONS

A fundamental included angle accuracy of 0.5 arc sec (1 σ) by the Space Sextant makes navigation practical in cislunar space to a high degree at accuracy (< 0.2 n.m.) and at the same time provide the highest level of autonomy possible. An attitude reference system of 0.1 arc sec precision is also feasible, employing the basic sextant instrument modified to perform autocollimation in conjunction with a fixed mirror system. The sextant and its associated electronics will weigh less than 25 pounds and will require 7.5 watts average power, 50 watts peak power, and 30 watts during actual measurement. Design lifetime is 5 years with redundancy and parts derating, bearings included.

The Space Sextant is designed to be functionally subservient to the spacecraft computer system and to impose no cycle time restrictions on the computer. Software functions including navigation, on-orbit calibration and health monitoring will require 15K of 16 bit words of memory. Read-only mass storage for a 5-year lunar ephemeris and lunar terrain height data will require up to 140K of 30 bit words. The latter needs may be fulfilled either by a solid-state ROM of less than 4 pounds or by magnetic tape units. The read-only provision greatly enhances the long life and reliability of either type of mass storage device.

UTILIZATION OF LANDMARK DATA IN
ATTITUDE/ORBIT DETERMINATION

H. Siddalingaiah
P. S. Desai
Computer Sciences Corporation
Silver Spring, Maryland

Picture data are taken both by geostationary and medium altitude satellites primarily for meteorological purposes. Abundant availability of picture data suggests that, both for navigation and picture registration for earth resources and meteorological purposes, the possibility of using landmarks is attractive. (Techniques of pattern recognition for identifying known landmarks are being developed currently at Goddard and by other contracting companies and universities, therefore, my talk will not address itself to this aspect.) One may find usage of landmarks in:

- Reduction of tracking requirements,

- Autonomous navigation,

- Potential improvement in attitude accuracy, and

- Improvement in geographic analysis of picture data.

One has the following options in using picture data from satellite fixed camera to determine:

1. Position given attitude,

2. Attitude given position,

3. Both attitude and position given:

   (α) enough landmarks

   (β) realistic attitude and orbit dynamic models

The problem is to express landmark coordinates in terms of satellite position, attitude, and camera scan angle.

This presentation will describe a mathematical model for determination of satellite position, velocity, and attitude using landmark coordinates as observables. This model, although developed with respect to earth-stabilized missions, Tiros-N and Nimbus-G in particular, is applicable to any earth-stabilized satellite in general.

138

As is usual in any mathematical discussion of flight mechanics, one has to use several coordinate systems simultaneously. The coordinate systems used here are:

1. (x^I, y^I, z^I) — Inertial, earth-centered

2. (x^R, y^R, z^R) — Rotating, earth-centered

3. (x^B, y^B, z^B) — Satellite body fixed

4. (x^A, y^A, z^A) — Instantaneous auxiliary orbital, earth-centered

5. (x^0, y^0, z^0) — Instantaneous orbital, earth-centered,

where

$$\hat{x}^A = -x^0; \hat{y}^A = -\hat{z}^0; \hat{z}^A = -\hat{y}^0$$

$$\vec{r}^A = F\vec{r}_0; F = \begin{bmatrix} -1 & 0 & 0 \\ 0 & 0 & -1 \\ 0 & -1 & 0 \end{bmatrix}$$

If $\hat{n}$ is a unit vector along the line of sight of the landmark, then,

$$\hat{n}^B = G(\alpha, \beta, \gamma)\,\hat{n}^0 \tag{1}$$

where $G(\alpha, \beta, \gamma)$ is the attitude matrix associated with 2-1-3 rotation.

If ξ, η, and ζ are the angles made by the line of sight with the positive direction of the axes, then

$$\hat{n}^B = (\cos \xi, \cos \eta, \cos \zeta) \tag{2}$$

Let

$$\hat{n}^A = (n_x^A, n_y^A, n_z^A) \tag{3}$$

Then

$$\hat{n}^0 = G^T \hat{n}^B \tag{4}$$

$$\hat{n}^A = FG^T \hat{n}^B \tag{5}$$

If (x_L^A, y_L^A, z_L^A) are the coordinates of a landmark sighted, then

$$\frac{x_L^A}{n_x^A} = \frac{y_L^A - (R_s + h)}{n_y^A} = \frac{z_L^A}{n_z^A} \tag{6}$$

where $(0, R_s + h, 0)$ are the coordinates of the spacecraft.

Since

$$(n_L^A)^2 + (y_L^A)^2 + (z_L^A)^2 = R_L^2 \tag{7}$$

139

we have

$$x_L^A = \frac{n_x^A}{n_z^A} z_L^A \tag{8}$$

$$y_L^A = \frac{n_y^A}{n_z^A} z_L^A + (R_s + h) \tag{9}$$

$$\frac{z_L^A}{R_L} = \frac{-B - \sqrt{B^2 - 4AC}}{2A} \tag{10}$$

where

$$A = \left[\left(\frac{n_x^A}{n_z^A} \right)^2 + \left(\frac{n_y^A}{n_z^A} \right)^2 + 1 \right] \tag{11}$$

$$B = \left[2 \frac{R_s + h}{R_L} \frac{n_y^A}{n_z^A} \right] \tag{12}$$

$$C = \left[\left(\frac{R_s + h}{R_L} \right)^2 - 1 \right] \tag{13}$$

Finally

$$\vec{r}_L^T = E^T (\phi, \theta, \psi) \vec{r}_L^A \tag{14}$$

$$\vec{r}_L^R = RE \vec{r}_L^{T \to A} \tag{15}$$

where

E   is the 3-1-3 rotation matrix

R   is the transformation matrix from the inertial to the earth-fixed system

ϕ is the longitude of the ascending node, and

ψ $= \omega + \nu - \dfrac{\pi}{2}$

140

where

    ω is the angle of perigee

    ν is the true anomaly

In the light of relations (3) and (6), one can also consider the camera angles as observables.

SOURCES

Caron, R. H. and K. W. Simon, "Time-Series Estimator for Rectification of Spaceborne Imagery," *J. of Spacecraft and Rockets,* 12.

Chan, F. K. and E. M. O'Neill, "Feasibility Study of a Qaudrilateralized Spherical Cube Earth Data Base," CSC, EPRF TR 1-75 (CSC).

Dambeck, W. J., 1972, "Geostationary Satellite Position and Attitude Determination Using Picture Landmarks," NOAA, Technical Memorandum NESS 21.

Garcia, Howard A., "An Analysis of Recent Advances in Autonomous Navigation for Near Earth Applications, AIAA Paper No. 73-875.

Paulson, D. C., 1972, "Autonomous Satellite Navigation From Strapdown Landmark Measurements," Proc. Conf. Non-Linear Estimation Theory, San Diego.

Phillips, D. and E. Smith, "Geosynchronous Satellite Navigation Model," Space Science and Engineering Center, University of Wisconsin, Madison, Wisconsin.

Sugihara, S., "Attitude Determination Using Known Landmarks," Report No. TOR-0172 (2120-01)-50, The Aerospace Corporation.

Chan, F. K. and E. M. O'Neill, "Feasibility Study of a Quadrilateralized Spherical Cube Earth Data Base," CSC, EPRF TR 1-75 (CSC).

THE APPLICATION OF IMAGE PROCESSING TO
SATELLITE NAVIGATION

R. M. Hord
Earth Satellite Corporation
Washington, D. C.

ABSTRACT

Given the locations of several landmarks on a satellite acquired image and their true geographic coordinates, the position and orientation of the satellite can be determined. Two methods for automatically locating the image coordinates of specified landmarks are described. The first, a particularly fast sequential similarity detection algorithm for template matching was originally described by Nagel and Rosenfeld. The second method involves iteratively resampling the picture function in the vicinity of the anticipated landmark. A variety of other speedup methods is also described. An application to SMS imagery is envisioned.

INTRODUCTION

An important role in satellite navigation is played by the recognition and location of landmarks on images of the earth's surface as viewed by the satellite. Given the locations of several landmarks on the image, and their true geographical locations, the position and orientation of the satellite can be determined. The mathematics of this process, and its error analysis, will not be recapitulated here. (See, for example, Phillips and Smith, 1972.)

We shall assume here that the approximate position and orientation of the satellite are already known, and that we want to use the landmark data to obtain more accurate estimates. This implies that we know approximately where, on the image, landmarks should appear— perhaps to within a few dozen picture elements (pixels). We shall ignore here any errors in our estimation of the orientations and sizes of the features; it is reasonable to assume that if the error in estimated position is small, then the errors in estimated orientation and size are negligible.

If we regard the orientations and sizes of the landmarks on the image as shown, and their positions as approximately known, then the problem of landmark identification and location can be solved by a template matching process. This basically involves comparing a template or small image of the landmark with the picture, in the range of positions where the landmark could be located. If a good match is obtained, the landmark has been detected, and the position of this good match gives the location of the landmark.

There are many different template matching processes that could be used for this purpose, and the matching can be implemented in various ways (digitally, optically, or by a human operator). We shall consider here only automated digital techniques.

The objective of this proposed effort is to make the template matching as computationally efficient as possible, while keeping machine storage requirements at the minicomputer level.

The standard digital template matching technique, which is based on cross-correlation, is relatively slow. Substantially faster results can be obtained by using an absolute difference measure of mismatch (sometimes known as the sequential similarity detection algorithm (SSDA). This approach is not only cheaper computationally, but also lends itself to the us of efficient search techniques for speeding up the detection of mismatches, as shown by Nagel and Rosenfeld, 1972. It can be combined with various pre- and post-processing techniques that should increase the sharpness of the matches obtained, thus increasing the accuracy, as well as the speed, with which landmarks can be located.

TEMPLATE MATCHING

Use of the Absolute Difference Mismatch Measure

The most commonly used measure of the match between a template, t (x, y), and a picture p (x, y), is the correlation coefficient (or normalized cross-correction)

$$\frac{\iint_T t\,(x, y)\, p\,(x + u, y + v)\, dxdy}{\sqrt{\iint_T t^2\,(x, y)\, dxdy \quad \iint_T p^2\,(x + u, y + v)\, dxdy}}$$

where (u, v) is the displacement of the template relative to the picture. Here the area of integration, T, is the area occupied by the template. This coefficient takes on values between 0 and 1, and has value 1 only when t (x, y) and p (x + u, y + v) are identical (over the area T) except for a multiplicative constant. In the digital case, the expression for the correlation coefficient is identical, except that the integrals are replaced by sums over picture element arrays.

Computation of the correlation coefficient is relatively slow, because it involves a large number of multiplications of template values by picture values for each position of the template relative to the picture. The process can be speeded up by using Fourier transform techniques to compute the cross-correlation; however, this approach is more costly in computer memory requirements, and will not be discussed further here.

A more quickly computable measure of the mismatch between a template and a picture is the integrated (or summed) absolute difference.

143

$$\iint_T \left| t(x,y) - p(x+u, y+v) \right| \, dxdy$$

This measure is zero wI. 'n t and p are identical (over the area T). Computation of this measure involves no multiplications; many fewer arithmetic operations are required than in the case of the correlation measure (for a quantitative comparison see Barnea and Silverman, 1972). In addition, use of the absolute difference measure makes it possible to take advantage of significant shortcuts in the matching process.

Stopping Criteria

A major advantage of the sum of the absolute differences as a mismatch measure is that this measure grows monotonically with the number of points whose absolute differences have been added into the sum. This means that if we are looking for a point of best match in a given region, we can stop adding up absolute differences in a given position (u, v) as soon as the sum has grown larger than the smallest sum so far obtained in any position (u_0, v_0), since we now know that (u, v) cannot possibly be the position of best match.

We can do even better if we set up an absolute threshold, such that if the mismatch measure exceeds θ at a given point, we will not accept that point as a point of match. It is now sufficient to add up terms of the sum until θ is exceeded; when this happens, we can reject the given point and move on to the next point.

By using both mismatch comparison and absolute thresholding, the process of finding a best match (below the mismatch threshold) can be speeded up considerably. For points where the match is poor, the threshold should be exceeded rapidly so that only a fraction of the terms in the sum need be computed for such points. Even for points where the match is good, we need not always compute all the terms of the sum, since we can stop as soon as we exceed the smallest previously obtained sum.

Optimum Matching Sequences

It has been pointed out by Nagel and Rosenfeld (1972) that the expected amount of time required to exceed a mismatch threshold can be reduced by matching template pixels against the corresponding image pixels in a preselected order. To illustrate this idea, let us consider a simple example. Suppose that the template and image contain only three gray levels, e.g., 0, 1, and 2, and that, in the given region of the image, these levels occur with relative frequencies of $1/2$, $1/3$, and $1/6$, respectively. If the template is not at or near the correct match position, we can assume that the image pixel that coincides with a given point of the template is uncorrelated with the template gray level at that point. Thus, we can compute the expected absolute gray level difference between template and image at a point as follows:

144

Template Gray Level	Probability of Difference					Probability of Absolute Difference			Expected Absolute Difference
	-2	-1	0	1	2	0	1	2	
0	1/6	1/3	1/2	0	0	1/2	1/3	1/6	2/3
1	0	1/6	1/3	1/2	0	1/3	2/3	0	2/3
2	0	0	1/6	1/3	1/2	1/6	1/3	1/2	4/3

In other words, the expected absolute difference between template and image at a template point having gray level 0 or 1 is 2/3; but, at a template point of gray level 2, the expected absolute difference is 4/3. Thus we can expect, on the average, a faster rate of growth of the sum of absolute differences if we compute the difference first for template points that have gray level 2. Thus, the mismatch threshold (or the lowest level of mismatch previously found) is likely to be exceeded sooner if we compare template points with image points in a special order—namely, first using template points of gray level 2—rather than using the template points in an arbitrary order.*

Generalizing the example just given, it is easily seen that the mismatch threshold (absolute or relative) will be exceeded faster on the average if the template points are compared with the corresponding image points in decreasing order of expected absolute gray level difference. The degree of speed-up achievable in this way depends, of course, on the probability distribution of gray levels in the given region of the image: if all gray levels are equally likely, no speedup is possible by this method.

The method just described should be even more effective when we are matching multispectral, rather than gray scale, images. This is because a probability distribution of multispectral vector values should be even more nonuniform than a distribution of gray levels would be. Thus it should be possible to select template points whose expected absolute differences from the corresponding image points should be quite large. Here the differences must, of course, be defined in vector terms, e.g., as sums of absolute differences of the individual vector components.

The speedup obtainable by this method will not be the same for all landmarks. But the best results should be obtained for landmarks in whose vicinity the distribution of gray levels, or multispectral values, is highly nonuniform. Given a set of available landmarks, one can determine, for each of them, how much speedup can be expected, and one can select preferred landmarks for which the expected speedup is greatest.

---

* It may take more time to locate the desired template points than it would if we tested them, perhaps in a simple raster sequence; but Nagel and Rosenfeld (1972) have shown that their method is faster than raster matching in spite of this.

145

The position of best match, determined by any method, may not be sharply defined, since there may be a set of nearby positions for which the match is nearly as good. It has been known for at least 20 years that match sharpness can be improved by differentiating or by high-pass filtering the image and the template before matching them. In other words, outlines of regions give sharper matches than do solid regions.* It would be of interest to investigate whether the matching speedup process described above is improved by using differentiated or outlined images and templates. This will certainly be the case if the differentiated image has a less uniform distribution of gray levels (or spectral values) than the original image, as we would normally expect.

ITERATIVE RESAMPLING

Match positions can be determined to within closer than a pixel by resampling the image (at a grid of points that have fractional coordinates, in terms of the original sampling grid) and assigning gray levels to the new pixels by interpolation. The match at such an interpolated position may be better than the match at any of the original (intercoordinate) position. The investigation of interpolated match positions is probably best done as a fine tuning of a coarse match position found without use of interpolation. The interpolated images will tend to have more uniform gray level or spectral distributions than the original image, so that the matching speedup process will probably not be as effective during this fine tuning stage as at the coarse search stage.

A refinement allowing more accurate (part pixel) registration, when such accuracy is warranted, may be described as follows:

Let $F(x, y)$ be the cross-correlation function in terms of picture displacements (x, y) from the assumed best match point, $x = 0$, $y = 0$. Fit a quadratic to $F(x, y)$ of the form

$$F(x, y) = ax^2 + 2h + by^2 + 2gx + 2fy$$

We may determine the coefficients from the values of F at a few points. At $x = n$, $y = 0$, for example:

$$F(n, 0) = an^2 + 2gn$$

Similarly,

$$F(-n, 0) = an^2 - 2gn$$

hence

$$a = [F(n, 0) + F(-n, 0)]/2n^2$$

$$g = [F(n, 0) - F(-n, 0)]/4n$$

---

* It may be of further advantage to use a thresholded outline image so as to reduce the effects of overall gray level differences due to seasonal changes, and so forth.

146

We can also find

$$b = [F(0, n) + F(0, -n)]/2n^2$$

$$f = [F(0, n) - F(0, -n)]/4n$$

$$h = [F(n, n) - F(n, 0) - F(0, n)]/2n^2$$

Differentiating, $F(x, y)$ is a maximum when*

$$ax_0 + hy_0 + g = 0$$

and

$$by_0 + hx_0 + f = 0$$

so that,

$$x_0 = (hf - bg)/(ab - h^2)$$

$$y_0 = (gh - af)/(ab - h^2)$$

Then shift origin to (x_0, y_0) and repeat with $n/2$ area size. Since only 5 values of F need to be obtained per iteration, the speed of such a procedure may prove to be adequate.

As an example in one dimension, consider the following template:

$$3 \quad 1 \quad 9 \quad 1 \quad 3$$

and the image line gray values:

$$6 \quad 6 \quad 4 \quad 8 \quad 5 \quad 6 \quad 6$$

Take $(F(x)) = ax^2 + 2gx$.

$$F(-1) = \frac{(3 \times 6) + (1 \times 6) + (9 \times 4) + (1 \times 8) + (3 \times 5)}{\sqrt{(3^2 + 1^2 + 9^2 + 1^2 + 3^2)(6^2 + 6^2 + 4^2 + 8^2 + 5^2)}}$$

$$= 0.6208 = a - 2g$$

$$F(1) = \frac{(3 \times 4) + (1 \times 8) + (9 \times 5) + (1 \times 6) + (3 \times 6)}{\sqrt{(3^2 + 1^2 + 9^2 + 1^2 + 3^2)(4^2 + 8^2 + 5^2 + 6^2 + 6^2)}}$$

$$= 0.6656 = a + 2g$$

$$a = 1/2 (F(1) + F(-1)) = 0.6432$$

$$g = 1/4 (F(1) - F(-1)) = 0.0112$$

---

* After determining coefficients, we require that F be positive definite, i.e., $ab > h^2$, to guarantee a true maximum of F.

Differentiating, F (x) is a maximum when $ax_0 + g = 0$, i.e., for $x_0 = -g/a = -0.0174$ we see:

Gray Scale	Old Coordinate	New Coordinate
6	-3	-2.9826
6	-2	-1.9826
4	-1	-0.9826
8	0	0.0174
5	1	1.0174
6	2	2.0174
6	3	3.0174

In this new coordinate system we will need F(-0.5), hence by interpolation we will need the gray level values at $X = -2.5, -1.5, -0.5, 0.5, 1.5, 2.5$.

If linear interpolation is used, then

$$G(x) = G(x_1) + \frac{(G(x_2) - G(x_1))}{(x_2 - x_1)} (x - x_1)$$

thus,

$$G(-2.5) = 6.0000$$
$$G(-1.5) = 5.0348$$
$$G(-0.5) = 5.9304$$
$$G(0.5) = 6.5522$$

and so forth.

Then a new iteration is undertaken and the process continues until the origin shift indicated is satisfactorily small.

OTHER SPEEDUPS

A possibility for still further improvement in matching efficiency, not discussed here up to now, is to identify locations in the image where the match can be expected to be good. This is typically done by making some simple local measurements on the image, and finding positions where the values of these measurements are close to their values for the template. In the present application, the positional uncertainty of the landmarks is not expected to be very large, so that it seems likely that much will be gained by the use of this approach.

There is, however, an important possibility for reducing the number of match positions that need be tried, once a match has been found for the first landmark. If this match is correct, the positional certainty of the remaining landmarks has now been reduced, since there are now fewer degrees of freedom. This is true even if the match is regarded as only approximate. Thus, after the first match is found, the next match can be searched for over a

148

relatively smaller region. After enough matches have been found, additional matches have very little positional uncertainty, so that we can search for them over very small regions. Of course, if the subsequent matches are not found in the expected places, they must be sought for over wider regions, and the original matches must be reevaluated. Thus a feedback process can be used to zero in on a best combination of match positions.

TECHNICAL DISCUSSION

The specific application to which this research is directed is the navigation of the Synchronous Meteorological Satellite (SMS). In time it is hoped that the processing of recognized landmarks for navigation (both for location error correction and relocation) can take place in quasi-real-time, which in this context is approximately 5 minutes. Before this can come about, there is a need to determine landmark processing algorithms that are rapid, accurate, reliable, and economical in storage.

It is recognized that several operational questions influence the utility of the algorithm development results. In particular, eventual implementation may be effected on a minicomputer with a hardware dot product. The availability of such a feature would have some significance to the efficiency of algorithms in the multispectral domain.

Also, error budgeting will play a central role. It may not be useful, for example, to process the image data with extreme accuracy since the errors in the landmark surveys may well predominate (current landmark accuracies are believed to be about $1/100$th of a degree in latitude and longitude, and may have a systematic bias). Hence it may be useful to concentrate on using the same landmarks repetitively for relative image-to-image geometric transformations rather than absolute geodetic location determination.

Thirdly, cloudcover distribution probability functions will affect the ability to use the landmarks. The geometric relationships require a well distributed set of control points if orientation and orbit parameters are to be determined accurately. Inadequate or ill-distributed control point data give rise to ill-conditioned matrices and the calculations become unreliable.

REFERENCES

Barnea, D. and H. Silverman, 1972, "A Class of Algorithms for Fast Digital Image Registration," *IFEE Trans. on Computers* C-21.

Nagel, R. N. and A. Rosenfeld, 1972, "Ordered Search Techniques in Template Matching," *Proc. IEEE* 60.

Smith, E. A. and D. R. Phillips, 1972, "Automated Cloud Tracking Using Precisely Aligned Digital ATS Pictures," *IEEE Trans. on Computers* C-21.

SOURCES

Hall, D. J., R. M. Endlich, et al., 1972, "Objective Methods for Registering Landmarks and Determining Cloud Motions from Satellite Data," IEEE Trans. on Computers, p. 768.

Lam, C. F. and R. R. Hoyt, 1972, "High Speed Image Correlation for Change Detection," *NAECON Proceedings*.

Webber, W. F., 1973, "Techniques for Image Registration," LARS, *Proc. Machine Processing of Remotely Sensed Data*.

CLOSED FORM SATELLITE THEORY WITH
EQUINOCTIAL ELEMENTS

R. Broucke
University of Texas
Austin, Texas

A computer software system has been developed to generate the closed-form literal first-order perturbations due to any harmonic in the potential. In a first approach, classical elements and the true anomaly are used. In another approach, equinoctial elements and the true longitude are the basic variables. The solution in equinoctial elements does not have any zero eccentricity or zero inclination singularities.

In the case of tesseral and zonal harmonics, the rotation of the central body is neglected. The expansion of the potential is done with simple recurrence formulas.

FORMULATION OF AN ARBITRARY GEOPOTENTIAL TERM
(TESSERAL) IN EQUINOCTIAL VARIABLES

P. Cefola

Computer Sciences Corporation
Silver Spring, Maryland

Previously, general formulas for the averaged disturbing potential were obtained (AIAA preprint 75-9) in equinoctial elements for the zonal and third-body harmonics. In addition, methods were given for recursive computation of these potentials. The current paper extends the applicability of this model by giving an explicit expression in equinoctial elements for the arbitrary geopotential term:

$$U = \frac{\mu}{r} \left(\frac{R_e}{r} \right)^n P_{nm} (\sin \phi) [C_{nm} \cos m\lambda + S_{nm} \sin m\lambda]$$

Expressions for the spherical harmonics $P_{n,m,}(\sin \phi) \cos m\lambda$ and $P_{n,m}(\sin \phi) \sin m\lambda$ are obtained in terms of Jacobi polynomials with the argument $(1 - p^2 - q^2)/(1 + p^2 + q^2)$ (p and q are equinoctial elements), polynomial functions which are straightforward generalizations of the C_s and S_s polynomials appearing in the zonal potential, the true longitude, and the Greenwich sidereal time, θ is fixed during the averaging period. However, an expansion of the true longitude in terms of the mean longitude and the equinoctial elements k and h would allow the consideration of resonant cases. Finally, consideration is given to recursive computation of the averaged potential for tesserals.

AN ANALYTIC METHOD TO ACCOUNT FOR ATMOSPHERIC
DRAG WITH AN ANALYTIC SATELLITE THEORY

N. Bonavito and R. Gordon
Goddard Space Flight Center
Greenbelt, Maryland

The motion of an artificial earth satellite in the presence of air drag and the earth's gravitational potential is considered. In contrast to the classical methods of numerical integration, this approach presents a quadrature algorithm employing analytical expressions for the variation of orbital elements produced by the air drag. These expressions are well-defined over expanded subintervals of the solution, and produce accurate agreement with profiles of tabular density. This procedure then allows a flexibility in the selection of end points of the subintervals, which in turn ensures a minimum error bound on the required analytical function.

In this method the effect of oblateness is accounted for by either the Vinti spheroidal theory, the Brouwer orbit theory, or the Brouwer-Lydanne theory. The changes due to atmospheric resistance for a nonrotating sphere are accounted for by the solutions of the variational equations, evaluated with the appropriate theory.

NUMERICAL IMPLICATIONS OF STABILIZATION
BY THE USE OF INTEGRALS

Paul R. Beaudet

Computer Sciences Corporation
Silver Spring, Maryland

The subject matter of this paper is some numerical experiences that we have had involving some of the celebrated notions of dynamic stabilization. Figure 1 demonstrates Ljapunov stabilization, which is an analytic notion, and the example given is one of circular motion under an arbitrary attractive central force field. There is some particle moving around in a circle at some distance from an attractive center. The attractive force is designated by -f(r), the velocity of the spacecraft is v, and the centripetal acceleration is v^2/r. By equating the centripetal acceleration to the attractive force, we can get an expression for the angular frequency that is the square root of the attractive force over $r(\sqrt{-f/r})$.

Notions of stabilization involve questions associated with what happens to this motion under slight perturbation of initial conditions. Let us start out with some satellite or particle moving in a circular orbit at a radius of α; there will be a certain angular rate associated with that motion. If we cause a slight change to occur in the initial conditions so that the radius of the orbit is no longer α but is $\alpha + \Delta\alpha$, then it may happen that the angular rate may differ from that of the original orbit. These initial conditions should be selected in such a way that the motion will still be circular in this example.

As a result of the possible different rates in the angular frequency, the mean anomalies (ϑ's) between both satellites will be different and their difference will increase linearly in time. Such motion is dynamically unstable because the motion of the initial problem and that of the perturbed problem (that is, the problem with slightly perturbed initial conditions) will deviate arbitrarily; the deviation in the mean anomaly will be as great as desired if a sufficient length of time is allowed to elapse:

$$\omega = \frac{2\pi}{T} = \frac{v}{r} = \sqrt{\frac{-f(r)}{r}}$$

for any

$$\Delta\alpha > \epsilon \quad \theta_1(t) - \theta_2(t) \geqslant \delta$$

for sufficiently large t.

154
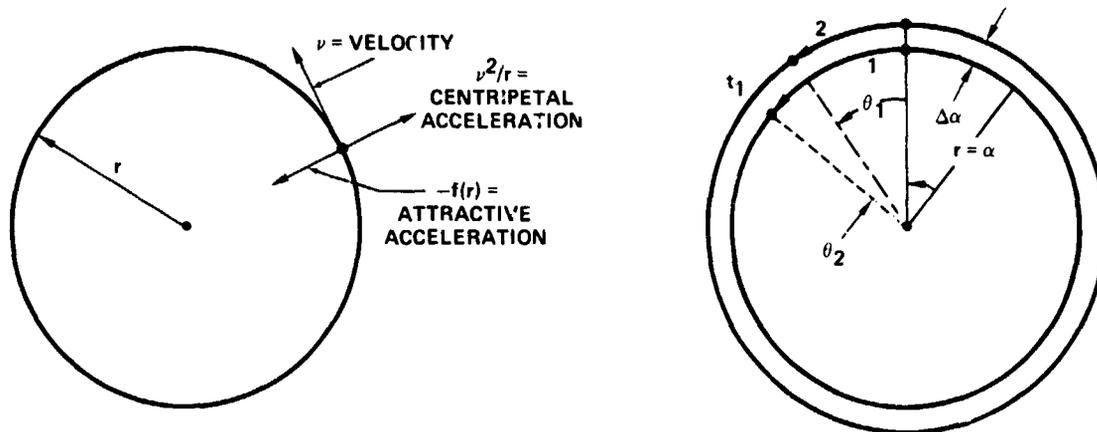
Figure 1. Ljapunov stability, circular motion under arbitrary attractive central force.

The single exception to this rule is the case where the angular frequencies are in fact the same for all possible radii. This implies that the force law should be given by $-\omega^2 r$, which is the simple harmonic oscillator:

$$\omega_1 = \omega_2 = \omega \rightarrow f(r) = -\omega^2 r.$$

Since the orbit (Keplerian) problem involves the force law, which is inversely proportional to the square of the field, this implies that the Keplerian problem is Ljapunov unstable:

$$f(r) = \frac{K^2}{r^2}$$

A dynamic problem is going to be either Ljapunov stable or unstable This is a physical concept and depends on the particular problem. The notion of stabilizing an unstable problem must then involve a change in the problem itself. We must look for another problem that happens to have the same solution as the original problem, and how this can be done will be explained later in the presentation.

The reason for looking at analytic concepts of stability is to try to improve the accuracies associated with numerical integration. Two basic approaches have been examined: With the two-body motion, one possibility (A) is to find a different formulation of the equations of motion, which are dynamically stable (that is, Ljapunov stable). Such examples are given by Baumgarte or the simple harmonic oscillator Kustaanheimo Stiefel (KS) theory. For such formulations, the frequency of the motion—the energy—is an a priori constant. A

155

second procedure (B) is to add a constraint (for example, an energy constraint) in addition to the equations of motion.

$$H(X,X) = -P_0 = \text{constant}$$

If there were such a constraint, then, when initial conditions were perturbed, those initial conditions would have to satisfy the constraints. Variations in the initial conditions that change the energy (in the case of frequency constraint) would not be permissible alterations in the initial conditions.

So it happens that, for the two-body problem, concepts A and B are analytically, but not numerically, equivalent, as will be shown later.

With perturbed motion, the Baumgarte and KS theories are not Ljapunov stable. In fact, they are unstable, but the degree to which this instability occurs is of the order of the perturbations and numerically this does not present any difficulty (concept A). On the other hand, employing an energy constraint (B), the negative energy P_0 may or may not be a constant. If we had a J_2 problem, the Keplerian energy would be a constant, yet the Baumgarte or the KS theories would still be unstable. So, for perturbed motions, concepts A and B are not equivalent, and the question arises as to whether it is better for numerical integration to look for Ljapunov stable or nearly Ljapunov stable equations of motion or to apply some kind of energy constraint. All of the evidence indicates that slightly better answers are obtained, at least for nearly circular motions, by using energy constraints.

We now take a look at some of the methods of dynamic stabilization, by which is meant either formulations that are Ljapunov stable or nearly Ljapunov stable and/or applying an energy constraint. The crux of all the stabilization procedures that exist are presently being investigated: The Baumgarte approach; a recent approach that was proposed by Stiefel, with which we have not yet had any numerical experiences; the Baumgarte-Stiefel stabilization procedure, which is an energy-constraint-type formulation; and a formulation of applying an energy constraint directly, which is due to Nacozy and will be discussed later.

The Baumgarte procedure involves a Ljapunov-stable system of equations for the two-body problem and is based on a method of Poincaré. If we start with a Hamiltonian, which is a function of the position and conjugate momentum (velocities), then the Keplerian equations of motion are given by the following canonical equations:

$$H(X,P) \rightarrow \dot{X} = \frac{\partial H}{\partial P} \quad \text{and} \quad P = -\frac{\partial H}{\partial X}$$

In numerical integration, it is very often desirable, especially for eccentric motion, to make a transformation from time as an independent variable to some other independent variable, an S variable. This S variable could be the eccentric anomaly for certain cases or a mean anomaly in another case, but it does not matter. The type of equation which will relate time with the new independent variable is given by dt/ds as some function and, in general, that function may be a function of both position and momentum:

156

$$\frac{dt}{ds} = \mu(x,P)$$

Poincaré defined a new Hamiltonian, which is related to the old Hamiltonian by the function (dt/ds) times the old Hamiltonian plus a constant, and it turns out that, with this new Hamiltonian, the equations of motion for both the space variables and the ti.. e variable are canonical, as shown below:

$$X' = \frac{\partial \hat{H}}{\partial P} = \mu \frac{\partial H}{\partial P} + \frac{\partial \mu}{\partial P} (H + P_0)$$

$$P' = \frac{\partial \hat{H}}{\partial X} = -\mu \frac{\partial H}{\partial X} - \frac{\partial \mu}{\partial X} (H + P_0)$$

$$t' = \frac{\partial \hat{H}}{\partial ..} = \mu + \frac{\partial \mu}{\partial P} (H + P_0)$$

$$P'_0 = -\frac{\ }{\partial t} = 0$$

$$P_0 = \text{constant such that } [H + P_0] \equiv 0$$

There are three equations here that are the correct equations for dynamics, except for certain terms which are called control terms. The equation for P_0, which is the momentum conjugate to the time, defines P_0. The S-derivative of P_0 should vanish, and this implies that P_0 is a constant. If that constant is chosen to be equal to the negative of the energy or the value of the Hamiltonian, then the control terms would be numerically equal to zero, but dynamically they are not. Dynamically, they are some function of r and the constant energy. So this new canonical system of equations is really an entirely different problem that happens to have the same solution as the old problem.

Baumgarte noticed that for the function $\mu = r$ the equations of motion with respect to the new, independent variable S (that is, the spatial equation of motion with respect to the new, independent variable S) are dynamically stable in the Ljapunov sense and, in fact, can be transformed to the KS simple harmonic oscillator equations. The time equation, $T' = r$, is not dynamically stable, but there are ways of getting around that problem as will be shown later in the paper.

Even though the control term, $H + P_0$, is analytically equal to zero from the analytic solution, when these equations of motion are numerically integrated, the control term may develop some error. We will then want to know how this error is going to behave dynamically.

157

To examine this formulation in the time domain, we use the following equation:

$$\ddot{\vec{X}} = - \frac{K^2}{r^3} \vec{X} + \frac{\vec{X}}{r^2} \underbrace{[H + P_0]}_{\text{CONTROL TERM}}$$

We can derive an equation of motion for the control term by multiplying (dot product) this equation by the velocity and doing some manipulation. The general solution of this equation has the control term as a constant multiplied by r. For circular motions this would basically be a constant. This solution tells us that if we develop some numerical (nonzero) errors in the control terms, then those errors are going to persist. Hence, from a numerical point of view, the orbital state will not be on the correct energy surface.

This is different from our analytical approach, in which we saw that, for the two-body problem, Baumgarte stabilization (or Ljapunov stabilization) and applying an energy constraint are, in a way, equivalent. From the numerical point of view we see that this is not true, because in numerical integration we create errors and those errors persist in the Baumgarte approach, so the state is not forced back onto the correct energy surface. Thus, applying the Ljapunov stable system of equations does not ensure that the state is going to be on the correct energy surface.

There are other methods of stabilization. The Stiefel approach involves multiplying the forcing terms of the differential equations by the a priori energy constant divided by the Hamiltonian:

Given

$$\ddot{\vec{X}} = f(\vec{x}, t)$$

use

$$\ddot{\vec{X}} = \left(\frac{-P_0}{H} \right)^{3/2} f(\vec{x}, t).$$

Now this parentheses is ideally equal to 1 for the analytic solution. If we raise the exponent to the 3/2 power, numerically it does nothing, but from a stability point of view, it does. This Stiefel system of equations is dynamically stable in the Ljapunov sense.

The Baumgarte-Stiefel control term is similar to the Baumgarte control term, except that the multiplie is proportional to the velocity vector over the square of the velocity. The multiplier is sometimes called a dissipative term, because, by looking at the equation of motion that governs the control term, it can be seen that it has a solution which decays in time:

158

$$\ddot{\vec{X}} = \frac{K^2 \vec{X}}{r} - \frac{\gamma \dot{\vec{X}}}{\dot{X}^2} \, [H + P_0]$$

leads to

$$\frac{d}{dt} \, [H + P_0] = -\gamma \, [H + P_0]$$

$$[H + P_0] = \text{constant} * e^{-\gamma t}.$$

Hence, the Baumgarte-Stiefel control term forces the state back onto the correct energy surface, because the control term is forced to decay to zero.

In the Nacozy approach, at each step of the integration, the control term is forced to zero by a virtual displacement made in the state, such that the new energy after such a displacement should be the correct energy.

$$\delta X = - \frac{[H + P_0] \, \vec{F}}{\vec{F}^2} \qquad \vec{F} = \text{acceleration}.$$

It happens that the Nacozy procedure is not compatible with multistep integration processes because of the discontinuity that occurs in the state variables. The numerical results using single-step numerical integration methods apparently work; with the multistep methods, there are problems, as will be shown later.

We now turn to the perturbed problem, where we have nonconservative perturbation, such as drag or solar radiation pressures, conservative forces, which are derived from the grading of some potential, and control terms:

$$\ddot{\vec{X}} = - \frac{K^2}{r^3} \, \vec{X} + \vec{P} - \vec{\nabla}V + [\text{control term}]$$

There are two types of integral constraints to discuss: The Keplerian energy is a near integral of the motion and has the equation:

$$\frac{d}{dt} \left[\frac{\dot{\vec{X}}^2}{r} + V - \frac{K^2}{r} \right] = \dot{\vec{X}} \cdot \vec{P} \, .$$

There is also a term not included here, which is the partial of the potential with respect to time. In the absence of perturbation, this is zero, so it is a near constant of the motion. Instead of having a P_0 that is a constant, we have to numerically integrate it. The following is a comparison of that integration of P_0 with the computation of the Hamiltonian in a

conservative system. The sum of H and P_0 is ideally zero and will be used as a control term:

$$S_0 \quad \boxed{\begin{array}{l} \dfrac{d}{dt} P_0 = -\vec{\dot{X}} \cdot \vec{P} \\[2em] H = \dfrac{\vec{\dot{X}}^2}{2} - \dfrac{K^2}{r} + V \end{array}}$$

The other type of integral constraint is a Jacobi integral, which is what the energy looks like in the rotated coordinate system of the earth. It is an exact constant of the motion for the full J_2 potential including tesseral harmonics; it is given by the Hamiltonian for the inertial energy plus the angular velocity of the earth dotted into the angular momentum. When V is time-dependent due to the earth's rotation (tesseral harmonics):

$$\frac{d}{dt} [H + \vec{\omega} \cdot (\vec{R} \times \vec{\dot{R}})] = + (\vec{\dot{X}} - \vec{\omega} \times \vec{R}) \cdot \vec{P} = 0 \text{ IF } \vec{P} = 0.$$

A control term based on this integral of motion can be applied, designated in later equations by R, indicating the energy in the rotating coordinate system:

$$[H + \vec{\omega} \cdot (\vec{R} \times \vec{\dot{R}}) + P_0]$$

where

$$\frac{dP_0}{dt} = - (\vec{\dot{X}} - \omega \times \vec{R}) \cdot \vec{P}$$

None of these equations are integrated in the time domain. They are integrated usi g the eccentric anomaly as an independent variable and, in addition, the time equation must be integrated.

Baumgarte dynamic stabilization also requires a time equation that is dynamically stable. There are five options for the time equation. The normal one would be $t' = r$, the defining relationship between t and s.

If we differentiate this equation with respect to s, we get $t'' = r'/K$. The reason we consider this is that second-order systems of equations are often easier to integrate using class 2 methods.

The next option is the ordinary time element option:

$$t = \tau - \frac{Kr'}{2P_0}$$

The equations of motion are essentially a constant term plus perturbation:

$$\tau' = \frac{K}{2P_0} \left\{ 1 + \frac{r}{K^2} \ [\vec{R} \cdot (\vec{P} - \bar{V}V) - 2V] - \frac{r'P_0'}{P_0} \right\}$$

This is a constant when the energy P_0 is a constant. If the energy P_0 has to be integrated, then some errors in P_0 might be expected to crop up; if those errors are significant, then there can be secular error type terms that will grow. There will then be timing errors associated with the integration of t'.

This analysis leads to a third system of equations, in which a new eccentric anomaly is related to the old eccentric anomaly by the following combination of variables:

$$\frac{d\eta}{ds} = \frac{K}{2P_0} \qquad \frac{d}{ds} = \frac{K}{2P_0} \frac{d}{d\eta}$$

Here the energy P_0 is in the denominator. We can transform all of the equations of motion by using this relationship.

The time is then related to a new time element, t^*, by adding to it a modified eccentric anomaly; as the equations of motion for t^* involve only perturbations, in the absence of such perturbations, the anomaly is zero:

$$t = \tau^* + \eta \cdot \frac{Kr'}{2P_0}$$

$$\frac{d\tau^*}{d\eta} = \frac{r}{K} \ [\vec{R} \cdot (\vec{P} - \bar{V}V) - 2V] - \frac{\gamma'P_0'}{P_0}$$

The fifth possibility for deriving the time as a function of s is to use a third-order differential equation as shown here:

$$t''' + 2P_0 t' = K$$

We have not had any numerical experiences doing this, but this equation is dynamically stable, as are the time element equations.

Tables 1 through 7 give the numerical errors of the GEOS-B test orbit from computer simulations. The errors are given in units of 10^{-6} kilometers (millimeters) after integrating the GEOS-B orbit over 50 revolutions. The perturbations are a 15-by-15 geopotential field, and the results are given over a range of 60 to 100 integration steps per orbit. In the first column, an I indicates the integration of the inertial energy, and an R indicates the integration of the rotational or body-fixed energy. The second column provides the particular time equation used to get the time from the eccentric anomaly. A zero indicates the t''

time equation, 1 corresponds to the t' equation, 2 is the ordinary time element equation, and 3 is the modified time element equation. The last four columns give the errors for the Baumgarte dynamic stabilization procedure (B); the Baumgarte-Stiefel control term, which forces the state ̀ack onto the correct energy surface (BS); the experiences using the Nacozy approach (N); and the ordinary time-regularized formulation, which does not have any control term and is dynamically unstable (TR), respectively.

Related to these tables are the experiences associated with integrating Cowell's equations of motion using time as an independent variable. Since the motion is nearly circular, equal step sizes in time will correspond very closely to equal step sizes in eccentric anomaly.

̀ the last four columns of the tables, the three numbers in each entry correspond to intrack .atial errors, crosstrack spatial errors, and a timing error (which is also an intrack error), respectively. There are three errors here because we are integrating spatial equations and a time equation with respect to eccentric anomalies. The final time at the end of the run is one in which the eccentric anomaly has reached a final fixed value at the end of 50 revolutions. The results of these runs are as follows: The time element with the Baumgarte control terms works with the timing error and the intrack error is still somewhat large compared to the crosstrack error. This result might be expected, because the state is no longer on the exact energy surface but persists off the energy surface. When a modified time element is applied, the timing error almost completely disappears, but only at the expense of intrack errors in the spatial equation. So all the modified time element has done for us is to shift the timing errors to spatial errors. The Nacozy process has really done nothing for us either, and the reason for that is the discontinuities in the state. Taking finite differences just adds errors in a multistep integration process. If we had a single-step integration process, these problems would disappear, as other experiences have indicated. The time-regularized processes are unstable and about two-thirds of the intrack error is in the timing and about one-third is in the spatial equations. This is in agreement with analytic work that has been done by Baumgarte.

It is the Baumgarte-Stiefel control term that gives the best answers. If, for example, the Jacobi integral is used, we get very little timing error. The spatial errors are still a little bit larger, but this control term gives us the best overall results. An important note is that the Baumgarte-Stiefel control term does not require a time element. In fact, the best results were achieved when the time element was not used and when the T'' equations or the T' equation were integrated. This is very important. Basically, the timing error results from consistent errors in r; $T' = r$. If there are consistent errors in r, timing errors will develop in integrating that system, the double integral problem.

By applying the energy constraint, the radius r is adjusted so that consistent errors in the time do not occur, and this has led to the results presented here. It is recommended that an energy constraint can be applied without worrying about the timing problem at all.

162

Table 1

Numerical Errors of the GEOS-B Test Orbit

for the BDSP. 60 Steps Per Orbit

ENERGY	ITELEM	B	BS	N	TR
I	0	UNSTABLE	−127.07899 28.97938 561.96729	−5802.32261 84.70741 12330.44769	−5326.43758 13.81227 12123.72627
I	1	UNSTABLE	−127.07197 28.97945 282.55283	−5802.18569 84.70873 6753.60074	−5326.43611 13.81225 11831.85920
I	2	UNSTABLE	−127.11421 28.98998 244.29093	−5803.50299 84.74010 1405.50988	−5327.36544 13.81054 665.25084
I	3	UNSTABLE	−341.064 28.773919 42.056	5693.628 87.159853 1136.962	−5244.249 6.950228 438.872
R	0	UNSTABLE	− 22.85710 29.93991 331.36557	UNSTABLE	SAME AS I0
R	1	UNSTABLE	− 22.84957 29.93998 50.23874	UNSTABLE	SAME AS I1
R	2	UNSTABLE	− 22.84268 29.95027 12.51864	UNSTABLE	−5327.29464 13.81072 1799.09322
R	3	UNSTABLE	− 22.84268 29.95027 12.41565	UNSTABLE	−5327.29498 13.81074 1798.98859

NOTES:

In the last four columns, the three numbers in each entry (given in units of 10^{-6} km) correspond to intrack spatial errors, crosstrack spatial errors, and a timing error (which is also an intrack error), respectively.

By integrating Cowell's equations of motion with time as an independent variable, the intrack spatial error was 3401.4027, and the crosstrack spatial error was 26.77772.

Table 2
Numerical Errors of the GEOS-B Test Orbit
for the BDSP, 65 Steps Per Orbit

ENERGY	ITELEM	B	BS	N	TR
I	0	-114.19500 2.53846 1828.84252	-115.66616 14.78646 339.48653	-2006.31579 45.74424 4266.29205	-1814.58633 1.25166 4120.60271
I	1	-114.19606 2.53844 1867.57285	-115.66429 14.78647 261.06752	-2006.27240 45.74470 2416.86411	-1814.58677 1.25165 4031.98843
I	2	-114.18013 2.53900 204.35943	-115.69274 14.79099 259.28441	-2007.21942 45.76519 648.56484	-1815.31460 1.25176 399.31962
I	3	-337.19 3.09228 11.296	-338.474 14.558205 43.667	2117.405 46.343831 409.824	1936.262 3.169659 175.349
R	0	-101.88979 2.52544 1825.45528	- 29.81388 15.44724 148.96701	UNSTABLE	SAME AS I0
R	1	-101.89076 2.52543 1858.42729	- 29.81174 15.44727 7.00168	UNSTABLE	SAME AS I1
R	2	-101.87554 2.52593 307.78874	- 29.80779 15.45175 65 45256	UNSTABLE	-1815.25454 1.25175 667.86354
R	3	-101.87549 2.52593 307.55044	29.80778 15.45176 65.31316	UNSTABLE	-1815.25555 1.25173 667.72535

NOTES:

In the last four columns, the three numbers in each entry (given in units of 10^{-6} km)
correspond to intrack spatial errors, c   crack spatial errors, and a timing error (which is
also an intrack error), respectively.

By integrating Cowell's equations of motion with time as an independent variable, the intrack
spatial error was 3401.4027, and the crosstrack spatial error was 26.77772.

Table 3
Numerical Errors of the GEOS-B Test Orbit
for the BDSP, 70 Steps Per Orbit

ENERGY	ITELEM	B	BS	N	TR
I	0	− 56.39602 3.11021 − 83.00906	− 55.74016 3.72737 110.25181	89.17622 9.39301 − 190.00997	59.21339 3.54422 − 144.20532
I	1	− 56.39740 3.11020 − 32.41277	− 55.74068 3.72737 126.90710	89.17136 9.39302 − 39.18658	59.21225 3.54421 − 130.56524
I	2	− 56.41604 3.10982 108.19045	− 55.75580 3.72860 136.67825	88.64037 9.40287 109.40972	58.77161 3.54320 129.18683
I	3	−172.115 2.960583 2.72	−171.421 3.569666 25.41	1.232 8.767146 7.63	31.457 3.383486 15.855
R	0	− 18.50051 3.14627 −127.93949	− 22.49304 3.90129 36.38436	UNSTABLE	SAME AS I0
R	1	− 18.50192 3.14625 − 77.63998	− 22.49356 3.90129 52.98888	UNSTABLE	SAME AS I1
R	2	− 18.518117 3.14591 15.28445	− 22.49164 3.90259 60.43499	UNSTABLE	58.81103 3.54332 35.63308
R	3	− 18.51815 3.14591 15.35058	− 22.49178 3.90258 60.50244	UNSTABLE	58.80972 3.54331 35.70119

NOTES:

In the last four columns, the three numbers in each entry (given in units of 10^{-6} km) correspond to intrack spatial errors, crosstrack spatial errors, and a timing error (which is also an intrack error), respectively.

By integrating Cowell's equations of motion with time as an independent variable, the intrack spatial error was 3401.4027, and the crosstrack spatial error was 26.77772.

Table 4
Numerical Errors of the GEOS-B Test Orbit
for the BDSP, 75 Steps Per Orbit

ENERGY	ITELEM	B	BS	N	TR
I	0	− 19.62149 1.84296 −545.21889	− 19.12725 .99247 10.04084	631.43636 5.75062 −1342.56385	534.84907 2.43962 −1222.06456
I	1	− 19.62227 1.84295 −515.99802	− 19.12819 .99247 44.14811	631.41960 5.75071 − 698.77660	534.84874 2.43962 −1187.46233
I	2	− 19.64372 1.84251 41.23325	− 19.13503 .99227 53.53911	631.16381 5.74633 − 77.89860	534.62285 2.43881 9.64151
I	3	64.153 1.592328 .078	63.651 .5224b 12.097	588.847 5.790954 − 119.748	492.282 1.808203 31.944
R	0	9.20689 1.86947 −581.840	− 13.39047 1.023638 − 2.75868	UNSTABLE	SAME AS I0
R	1	9.20615 1.86948 −551.67891	− 13.39146 1.02364 31.42207	UNSTABLE	SAME AS I1
R	2	9.18710 1.86908 − 64.66871	− 13.39082 1.02341 39.45957	UNSTABLE	534.64250 2.43889 − 142.20691
R	3	9.18710 1.86908 − 64.61750	− 13.39086 1.02342 39.51002	UNSTABLE	534.64266 2.43889 − 142.15558

NOTES:

In the last four columns, the three numbers in each entry (given in units of 10^{-6} km) correspond to intrack spatial errors, crosstrack spatial errors, and a timing error (which is also an intrack error), respectively.

By integrating Cowell's equations of motion with time as an independent variable, the intrack spatial error was 3401.4027, and the crosstrack spatial error was 26.77772.

Table 5
Numerical Errors of the GEOS-B Test Orbit
for the BDSP, 80 Steps Per Orbit

ENERGY	ITELEM	B	BS	N	TR
I	0	− 3.88340 .85629 −459.15306	− 3.74365 1.48006 − 15.88953	547.01168 7.57810 −1161.99962	462.17194 1.23206 −1052.62631
I	1	− 3.88368 .85629 −448.19016	− 3.74432 1.48006 9.26784	546.99724 7.57919 − 619.64184	462.17242 1.23206 −1026.10445
I	2	− 3.89834 .85601 10.98153	− 3.74692 1.48023 15.50786	546.89183 7.57760 − 96.19190	462.07088 1.23162 − 21.79383
I	3	− 16.867 .699993 .639	− 16.724 1.182493 4.999	530.505 7.653788 − 105.966	446.289 .752743 32.042
R	0	12.32661 .86888 −480.49666	− 6.75389 1.54807 − 9.24393	UNSTABLE	SAME AS I0
R	1	12.32631 .86888 −468.66261	− 6.75457 1.54807 15.97804	UNSTABLE	SAME AS I1
R	2	12.31317 .86863 − 59.98543	− 6.75434 1.54821 21.53818	UNSTABLE	462.07985 1.23164 − 134.05535
R	3	12.31314 .86863 − 6C.08864	− 6.75426 1.54821 21.43652	UNSTABLE	462.079696 1.23164 − 134.15899

NOTES:

In the last four columns, the three numbers in each entry (given in units of 10^{-6} km) correspond to intrack spatial errors, crosstrack spatial errors, and a timing error (which is also an intrack error), respectively.

By integrating Cowell's equations of motion with time as an independent variable, the intrack spatial error was 3401.4027, and the crosstrack spatial error was 26.77772.

Table 6
Numerical Errors of the GEOS-B Test Orbit
for the BDSP, 90 Steps Per Orbit

ENERGY	ITELEM	B	BS	N	TR
I	0	1.94060 .17462 −135.07205	1.88804 .65661 − 9.08666	172.74506 3.25877 − 365.23276	144.39606 .21146 − 326.48960
I	1	1.94069 .17463 −137.79058	1.88791 .65661 − 3.40434	172.74175 3.25882 − 198.53333	144.39652 .21147 − 319.98778
I	2	1.93719 .77468 − 1.66455	1.88796 .65678 − 1.60664	172.73643 3.25888 − 36.33632	144.38806 .21146 − 13.10179
I	3	1.632 .212515 .340	1.581 .342734 .362	170.214 3.062124 − 33.904	142.24 .192607 − 10.976
R	0	4.84812 .17485 −139.27516	− .91961 .68519 − 2.84861	UNSTABLE	SAME AS I0
R	1	4.8481 .17485 −141.66259	− .91983 .68519 2.84094	UNSTABLE	SAME AS I1
R	2	4.84502 .17489 − 18.61224	− .91976 .68534 4.51218	UNSTABLE	144.38850 .21146 − 43.66740
R	3	4.845096 .17489 − 18.82819	− .91971 .68534 − 4.29666	UNSTABLE	144.38868 .21146 − 43.88346

NOTES:

In the last four columns, the three numbers in each entry (given in units of 10^{-6} km) correspond to intrack spatial errors, crosstrack spatial errors, and a timing error (which is also an intrack error), respectively.

By integrating Cowell's equations of motion with time as an independent variable, the intrack spatial error was 3401.4027, and the crosstrack spatial error was 26.77772.

Table 7

Numerical Errors of the GEOS-B Test Orbit
for the BDSP, 100 Steps Per Orbit

ENERGY	ITELEM	B	BS	N	TR
I	0	1.00589 .078112 − 10.73311	.99013 .15110 − .96997	19.86950 .65629 − 40.52781	16.67995 .072534 − 36.09153
I	1	1.00598 .078109 − 13.79768	.99015 .15109 − 1.27553	19.86833 .65628 − 22.83707	16.68023 .07253 − 36.10359
I	2	1.0 .97 .078140 − .59675	.99046 .15116 − .92698	− 19.87749 .65649 − 4.78582	16.68774 .072546 − 2.22072
I	3	.775 .241308 .155	.790 .171367 .180	17.38 .348605 − 3.891	14.315 .236638 − 1.423
R	0	.83340 .078159 − 10.70273	.24629 .15553 .68240	UNSTABLE	SAME AS I0
R	1	.8?356 .078162 − 13.68274	.24624 .15553 .38025	UNSTABLE	SAME AS I1
R	2	.83348 .07819 − 1.26500	.24621 .15559 .71750	UNSTABLE	16.68663 .072566 − 4.77124
R	3	.83348 .07819 − 1.31470	.24632 .15559 .66760	UNS⁻ABLE	16.68570 072560 4.82004

NOTES:

In the last four columns, the three numbers in each entry (given in units of 10^{-6} km) correspond to intrack spatial errors, crosstrack spatial errors, and a timing error (which is also an intrack error), respectively.

By integrating Cowell's equations of motion with time as an independent variable, the intrack spatial error was 3401.4027, and the crosstrack spatial error was 26.77772.

SOURCES

Baumgarte, J., "Numerical Stabilization of the Differential Equations of Keplerian Motion." *Celestial Mechanics*, 5, pp. 490-501, 1972.

Baumgarte, J., "Stabilization of Constraints and Integrals of Motion in Dynamical Systems." *Computer Methods in Applied Mechanics and Engineering*, 1, pp. 1-16, 1972.

Baumgarte, J. and E. Stiefel, "Examples of Transformations Improving the Numerical Accuracy of the Integration of Differential Equations," (presented at the Conference on Numer   ' Solution of Ordinary Differential Equations, Austin, Texas, October 1972).

LaSalle, J. and S. Lefschetz, *Stability by Ljapunov's Direct Method*, Academic Press, 1961.

DISCUSSION

VOICE: In the   ..ulation of the Baumgarte-Stiefel stabilization procedure, corrections are applied in only one direction of a six-dimensional manifold. Wouldn't you expect more than errors in time? Is all the instability controlled by just the energy constraints?

BEAUDET: Yes.

VOICE: It seems that you ought to do more than just force your solution back into the correct energy surface.

BEAUDET: That is in fact correct, but when you look at it, you have to ask yourself the question: "What direction in this six-dimensional state manifold corresponds to the unstable direction, the direction in which errors are going to consistently grow?"

It's like that first diagram I gave you (figure 1). It is the fact that the frequency is in error that gave rise to an ever-increasing mean anomaly. It is an intrack error. In other words, when we integrate, we don't worry at all about crosstrack radial errors. It's intrack errors that are going to grow in time.

It turns out that the uncertainties in the frequency of the motion cause these errors and, since the frequency is somewhat related to the energy, at least in the two-body problem, applying an energy constraint solves the stability problem.

VOICE: But there is no constraint that will give a stable manifold, except for very special problems, which indicates that most problems should be unstable.

BEAUDET: In the perturbed problem that is the case and, if we apply J_2 perturbation, we're going to have an instability associated with the rotating plane of the orbit. In that direction, the manifold space is going to be unstable, even though we might apply an energy constrai..'. We're simply fixing up the worst part of the things associated with two-body-type motion.

VOICE: What have you done to take care of the high drag case?

BEAUDET: I haven't added anything into the energy to take care of drag. We have integrated orbits where drag was a perturbation and in which I knew that drag was not too severe a perturbation. We still get stabilization as a result. Of course, we have to integrate the energy equation, and drag appears on the right-hand side. The question is always associated with how accurately we can integrate this energy equation.

VOICE You mean you can stabilize the problem in the case of drag?

BEAUDET: If the drag is not too severe. If the drag becomes very severe, we've come across another problem, that the eccentric anomaly is not the right independent variable to use. If we start hitting a big wall associated with drag, we would like to use a different independent variable than eccentric anomaly while integrating through that region. It is the difficulty associated with finding such an independent variable or using it that has given rise to our inconclusive results in high drag cases.

C. 3

SPECIAL PERTURBATIONS USING BACK-CORRECTION
METHODS OF NUMERICAL INTEGRATION

Terry Feagin
University of Tennessee Space Institute
Tullahoma, Tennessee

Previous speakers have discussed how to change the analytical formulation of various problems in order to introduce stabilizing effects or to improve the accuracy and thereby increase the efficiency of numerical integration. The present topic is concerned with how to improve the process of numerical integration itself, in order to increase efficiency in the development of accurate ephemerides for earth satellites. In particular, the subject of this discussion is a new class of linear multistep methods for the numerical integration of ordinary differential equations. These methods are distinguished from the classical methods in that they permit the solution to be corrected at certain "back" points. That is, in the case of satellite computations, the solution is corrected at certain points in the past as the integration advances in time. Algorithms have been developed for the solution of both first- and second-order differential equations, although only the second-order case is considered here.

There are two reasons for correcting the solution at back points: First, when a polynomial obtained from interpolating evenly spaced data is used for approximating a function at a point, the coefficient of the error term is smaller when the point is nearer the middle of the range of data. Therefore, by performing the last correction at an internal point of the grid, a more accurate solution (that is, smaller truncation error for a given order) is obtained. The second (and not so intuitive) reason is that the introduction of back corrections induces numerical stability. It is well known that the general stability boundaries for the predictor-corrector methods of the Stormer-Cowell type decrease geometrically with increasing order. That is, when the higher order Stormer-Cowell methods are used on a practical problem, the step size is severely constrained by stability considerations. This is not the case with the methods using back corrections. In fact, in some cases, these methods possess general stability boundaries which are 30 to 40 times larger than those of the Stormer-Cowell methods of the same order. Moreover, the stability regions of these methods do not exhibit geometrical decay but remain relatively unchanged up to the eighteenth or nineteenth order.

The back-correction methods are given by:

$$x_{n+1} = (m+2) x_{n-m} - (m+1) x_{n-m-1} + h^2 \sum_{j=0}^{k} \alpha_j f_{n-j} \qquad (1)$$

and

$$x_{n+1-\ell} = (m+2-\ell) x_{n-m} - (m+1-\ell) x_{n-m-1} + h^2 \sum_{j=0}^{k} \beta_{j\ell} f_{n+1-j} \qquad (2)$$

for $\ell = 0, 1, \ldots, m$. The position vector of the satellite at time t_n is denoted by x_n, and the acceleration vector, by f_n. The number of back corrections is m. The coefficients $\{\alpha_j\}$ and $\{\beta_{j\ell}\}$ are determined in such a way that the highest possible order is obtained for a given k. It should be noted that for m = 0, the equations reduce to those of the Stormer-Cowell method. Therefore, the back-correction methods are simply a generalization of the classical Stormer-Cowell method.

These methods can be used with pseudo-evaluations in the following algorithm, provided the acceleration can be separated according to dominant and perturbing terms:

a. Predict a value, x^0_{n+1}, for x_{n+1} using equation 1.

b. Evaluate the dominant and perturbing accelerations using this value for x_{n+1}, saving the perturbing acceleration for subsequent calculations.

c. Set $\ell = 0$.

d. Using equation 2, obtain a corrected value, $x^{\ell+1}_{n+1-\ell}$, for $x_{n+1-\ell}$.

e. Reevaluate only the dominant acceleration using $x^{\ell+1}_{n+1-\ell}$ and obtain $f_{n+1-\ell}$ by adding the previously calculated perturbing acceleration at $t_{n+1-\ell}$.

f. If $\ell = m$, proceed to the next step of the integration. Otherwise, set $\ell = \ell + 1$ and go to (d) above.

In problems involving earth satellites, the forces can readily be separated according to dominant and perturbing terms. In such problems, these algorithms are especially efficient, because all evaluations of the forces after the first are simply pseudo-evaluations requiring only the reevaluation of the dominant forces (in this case, the two-body force).

The methods using back corrections have been tested on several problems. A numerical integration of the orbit of the Applications Technology Satellite-F (ATS-F) has been performed in which case the errors were smaller by two or three orders of magnitude when compared to the classical Stormer-Cowell method using pseudo-evaluations.

The results shown in table 1 are obtained when the seventeenth-order back-correction algorithm is applied to the to the Geodetic Earth Orbiting Satellite-C (GEOS-C) orbit.

Also shown are the results obtained using the twelfth-order Stormer-Cowell algorithm presently available in the Goddard Trajectory Determination System (GTDS). The errors are obtained by comparing with the results obtained using a step size of 40 seconds. It should be noted that for reasonable step sizes, the seventeenth-order back-correction method provides greater accuracy than the twelfth-order Stormer-Cowell method. Since pseudo-evaluations are used in both methods, the computer time required per step is the same (within a few percent) for both methods.

Table 1
Numerical Results for GEOS-C Satellite

Step Size (s)	Errors in Position after 24 Hours (km)	
	12th Order Stormer-Cowell	17th Order Back-Correction Method
60	5.7×10^{-5}	1.9×10^{-7}
80	3.2×10^{-4}	8.8×10^{-7}
100	1.1×10^{-2}	1.5×10^{-4}
200	6.9×10^{-1}	2.2×10^{-1}

The stability region of the twelfth-order Stormer-Cowell method is, in fact, slightly smaller than that of the seventeenth-order back-correction method. A higher order Stormer-Cowell method would no doubt have exhibited greater accuracy than the twelfth-order Stormer-Cowell method, but the stability region would have been considerably reduced. Consequently, the largest meaningful step size attainable with such a higher order method would have been much smaller.

The methods using back corrections appear to be more efficient than the classical methods for problems in which the dominant and perturbing forces can be readily separated and in which the evaluation of the perturbing terms requires much more computer time than the evaluation of the dominant terms.

ACKNOWLEDGMENTS

SOLUTIONS OF THE MOTION OF SYNCHRONOUS SATELLITES
WITH ARBITRARY ECCENTRICITY AND INCLINATION

Paul E. Nacozy and Roger E. Diehl
University of Texas
Austin, Texas

ABSTRACT

A first-order, semianalytical theory for the long-term motion of resonant satellites is presented. The theory is valid for all eccentricities and inclinations and for all commensurability ratios. The method allows the inclusion of all the zonal and tesseral harmonics as well as luni-solar perturbations and radiation pressure.

The method is applied to a synchronous satellite including only the J_2 and J_{22} harmonics. Global, long-term solutions for this problem, eccentricity, argument of perigee, and inclination are obtained.

INTRODUCTION

The method of solution presented here is based on a modified Von Zeipel method applied to resonant satellite systems with three degrees of freedom. The method allows any inclination and eccentricity and is a first-order semianalytical theory, yielding only the long-term perturbations.

The procedure first eliminates the short periodic terms numerically by a classical Von Zeipel averaging process. Since the averaging is performed numerically, developments in the eccentricity and inclination are not necessary. For the same reason, it is straightforward to add luni-solar perturbations and radiation pressure.

After the first Von Zeipel transformation, we have an averaged Hamiltonian that is a tabulated function of the variables: argument of perigee, longitude of the node, eccentricity, and inclination. The averaged Hamiltonian is obtained as a numerical table, not an analytical function.

The next procedure is then to eliminate the angular variable corresponding to the resonance argument, or the critical argument, t. a modified Von Zeipel transformation. The principle here is that the averaged Hamiltonian at resonance is a minimum with respect to the critical argument. This principle was introduced by Hori in 1960 for his satellite critical inclination theory. It was used in a slightly different form by Musen and Bailie in their satellite tesseral resonance theory in 1962. During the transformation, the new Hamiltonian is set equal to the value of the old Hamiltonian at its minimum.

After these two canonical transformations, a one-degree-of-freedom system remains, and in that system the Hamiltonian is a constant. We are now able to analyze the new one-degree-of-freedom Hamiltonian and obtain all long-period and secular perturbations, without having to develop a series in eccentricity or inclination.

The procedure and algorithm of the modified Von Zeipel method that we are using was developed by G. Giacaglia in 1965 (and described in detail in 1969). He applied the method to resonant asteroids in a circular restricted three-body problem in 1968. It was then applied to the elliptic restricted problems in 1970 by Giacaglia and Nacozy. The results of the elliptic restricted problem are in agreement with the solutions of asteroidal motion performed by Schubart (1968) using methods of numerical averaging.

The method was applied to the Pluto-Neptune system by Nacozy and Diehl (1974) and the results agree very closely with the numerical integration performed by Williams and Benson (1971), who used methods of numerical averaging over a four and one-half million year period.

Recently, we have adapted the method to satellite systems in resonance with the tesseral harmonics and have applied it to the J_2-J_{22} problem. The adaptation and application are presented below.

DESCRIPTION OF THE METHOD

The method uses the Delaunay equations of motion. The angular variables are modified slightly so that one variable is the mean anomaly, Y_0. A second variable is the critical argument for the synchronous satellite, Y_1, and a third is the argument of perigee, Y_2. Letting the X variables refer to the conjugate momentums, and where F is the Hamiltonian, we have

$$X_0 = L - H \qquad\qquad Y_0 = \ell$$
$$X_1 = H \qquad\qquad Y_2 = \ell + \omega + \Omega + \theta$$
$$X_2 = G - H \qquad\qquad Y_3 = \omega$$
$$F = 1/2 \cdot L^2 + H + \text{geopotential} \ (+\text{luni-solar forces})$$

The first canonical transformation is the classical Von Zeipel transformation where the new Hamiltonian, F*, is defined as the average of the old Hamiltonian over the mean anomaly from 0 to 2π:

$$F^*(X_0{}^*, X_1{}^*, X_2{}^*; -, Y_1{}^*, Y_2{}^*) \equiv \frac{1}{2\pi} \int_0^{2\pi} F(X_0, X_1, X_2; Y_0, Y_1, Y_2)\, dy_0.$$

After the averaging, we replace the X and Y variables by X* and Y* and then a new Hamiltonian is obtained, free from short periodic terms. This quadrature is performed numerically, not analytically. The quadrature is performed for various values of X_1*, X_2*, Y_1*, and Y_2*, and the Hamiltonian is obtained as a tabulated function of these variables.

The new Hamiltonian, F*, has a minimum at Y_1* near 90°. This minimum corresponds to the libration center for Y_1 (also 270°). The exact value of Y_1* depends on the value of Y_2* (the perigee). The partial derivative of the Hamiltonian with respect to Y_1*, at Y_1* near 90°, is zero.

The next canonical transformation defines a new Hamiltonian, F**, to be the value of F* at its minimum value:

$$F^{**}(X_0^{**}, X_1^{**}, X_2^{**}; -, -, Y_2^{**})$$

$$= F^*$$

$$Y_1^* \cong 90° \text{ (or } 270°).$$

This canonical transformation is that used in 1960 by Hori for his critical inclination solution, and we are using the same principle here. Since F** does not depend on Y_1**, we have:

$$X_1^{**} = \frac{\partial F^{**}}{\partial Y_1^{**}} = 0.$$

This gives a quasi-integral for X_1**:

$$X_1^{**} = H^{**} = \text{constant} = \sqrt{1 - e^{**2}} \cos i^{**}.$$

This relation between e** and i** is the component of the angular momentum in the Z direction. Since F** is a constant of the motion (conservative system), we now have two relations between three variables—eccentricity, inclination, and perigee—and we can rewrite the two relations as:

$$F^{**}(e, i, \omega) = \text{constant}$$

$$H^{**}(e, i) = \text{constant}$$

These two functions define curves in an e versus ω plane with H** as a parameter or curves in an i versus ω plane, also with H** as a parameter. This then gives us the long-term solution for e, i, and ω.

DETAILS OF AN APPLICATION

The first part of the numerical results for the $J_2 - J_{22}$ problem are shown in figure 1 for F* versus the critical argument, Y_1*. Only one plot is shown here for Y_2* (or ω*) 90°, but many other plots were obtained for different values of Y_2* (ω*). We have values of eccentricity ranging from 0.0 to 0.9, but only six values are shown in figure 1. Also, only one value for

the parameter H^{**} is given, corresponding to H^{**} to 0.3. It should be noted that there is a minimum of F^* at $Y_1^* = 90°$. This corresponds to the libration center for the synchronous satellite at $Y_1^* = 90°$.

We define the new Hamiltonian to have the minimum value of the old Hamiltonian, and then we plot the new Hamiltonian. This is shown in figure 2, for F^{**} versus Y_2^{**}, where Y_2^{**} goes from $0°$ to $180°$. The problem is periodic in π, so this will repeat from $180°$ to $360°$.

The plot of figure 2 may be considered as a three-dimensional plot by visualizing an eccentricity axis as perpendicular to and coming out of the plane of the paper. This will then produce a two-dimensional surface and it can be seen that there will be a valley in the surface centered at $Y_2^{**} = 90°$ and $e^{**} = 0.44$.

Since F^{**} is a constant for a given trajectory, we can construct planes parallel to the e versus ω plane (in the three-dimensional plot), one plane for each value of the constant Hamiltonian. In other words, we take several contour levels and each of the levels corresponds to a constant Hamiltonian and hence to a certain trajectory. The contour curves give the long-term global solutions for eccentricity versus perigee and are shown in figure 3. Contour levels near the bottom of the valley produce libration. At the bottom of the valley is the libration center, and at the top of the valley there is circulation.

Consider an eccentricity of 0.1. We see in figure 3 that, for this eccentricity, there is circulation of the perigee by following the curve, beginning at e = 0.1 and $Y_2^{**} = 0$. In other words, the e^{**} versus ω^{**} on that curve corresponds to an actual trajectory, the long-term solution to the problem.

If we have an eccentricity of about 0.4, we have libration of the perigee about the value of perigee equal to 90°. At nearly e = 0.44, there is a stationary solution, and this corresponds to a periodic solution. Apparently, these periodic solutions have not been found prior to this work for the $J_2 - J_{22}$ problem.

Using the quasi-integral relation, we can obtain corresponding plots for the inclination versus the perigee, and this is shown in figure 4. The libration center that was shown in figure 3 corresponding to e = 0.44 shows up at about $i^{**} = 70°$ and $\omega^{**} = 90°$.

The stationary solution (libration center) that we have found and presented here has an eccentricity of 0.44, an inclination of 70°, and a perigee of 90°. We have found that as H^{**} is varied, these stationary solutions form a family of periodic solutions.

CONCLUSION

Our future studies will be to trace the family of periodic (stationary) solutions. We will also add more zonals and tesseral harmonics, the effects of the sun and the moon, and radiation pressure to determine what effect they will have on the family of stationary, librating, and circulating solutions.
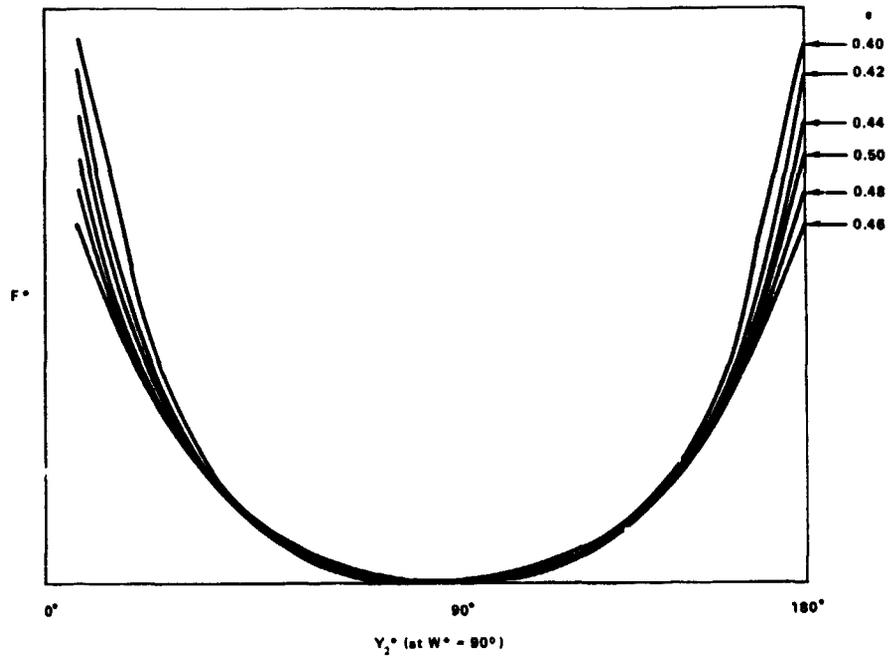
Figure 1. F^* versus ω^* for various values of e for the synchronous satellite with J_2 and J_{22}, F^* = average F and H^{**} = 0.03.
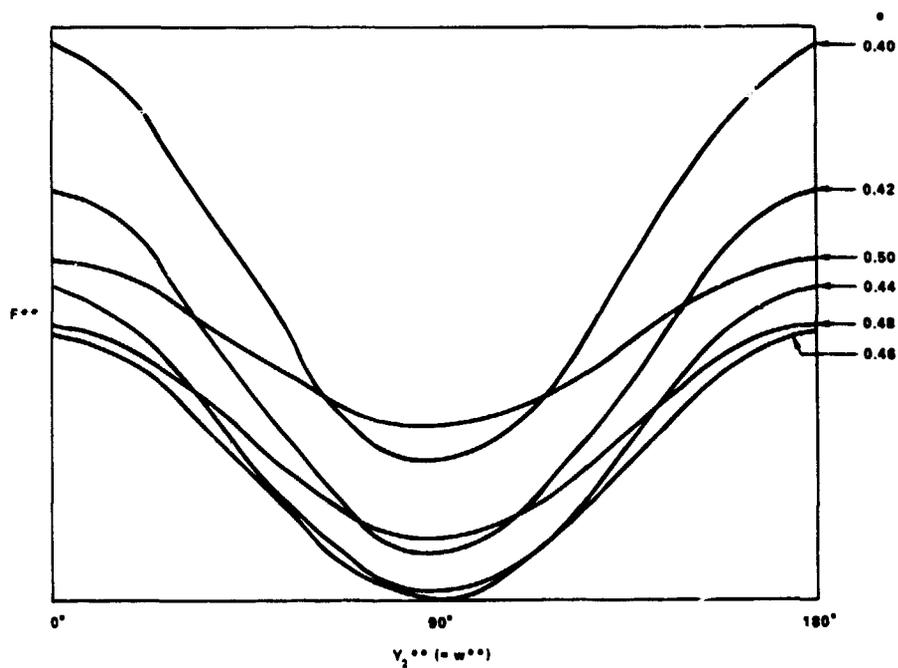

Figure 2. F^{**} versus ω^{**} for various values of e, F^{**} = minimum F^* with respect to Y_1^*.
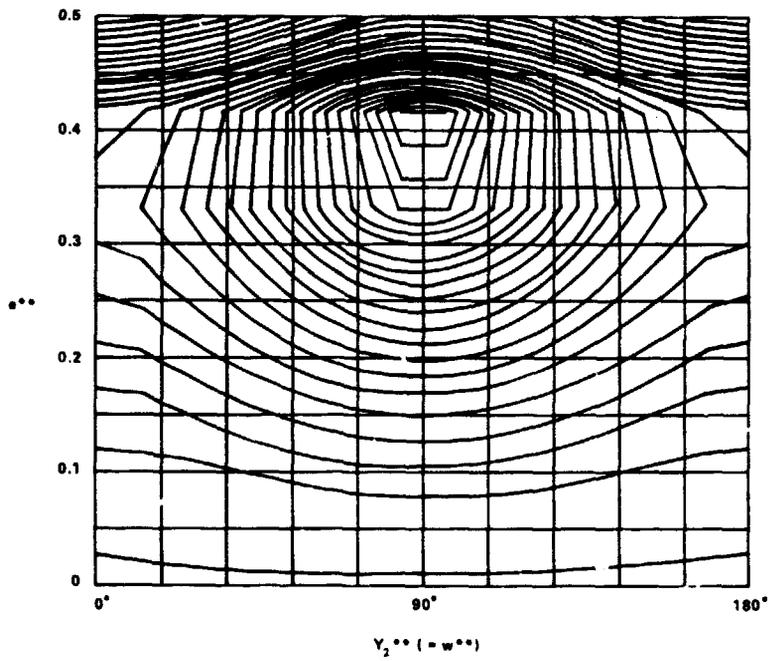
Figure 3. Phase-space diagram for e^{**} versus ω^{**} with $H^{**} = 0.3$.
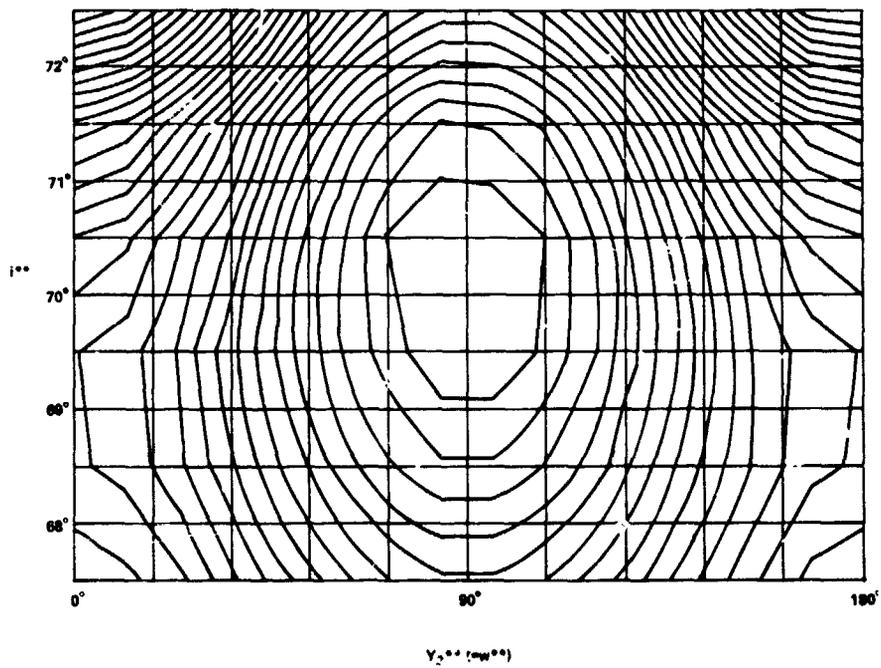

Figure 4. Phase-space diagram for i^{**} versus ω^{**} near libration center.

REFERENCES

Giacaglia, G.E.O., 1965, Doctoral Dissertation, Yale University.

Giacaglia, G.E.O., 1968, Smithsonian Astronomical Observatory Special Report No. 278.

Giacaglia, G.E.O., 1969, *Astron. J.*, **74**, p. 1254.

Giacaglia, G.E.O. and P.E. Nacozy, 1970, appears in *Peri..dic Orbits, Stability and Resonances*, ed. by G. Giacaglia, D. Reidel Publishing Co., p. 96.

Hori, G., 1960, *Astron. J.*, **65**, p. 291.

Musen D. and A. Bailie, 1962, *J. Geophys. Res.*, **67**, p. 1123.

Nacozy, P. and R. Diehl, 1974, *Bull. Astron. J.*, **6**, (2).

Schubart, J., 1968, *Astron. J.*, **73**, p. 99.

Williams, J. and G. Benson, 1971, *Astron. J.*, **76**, p. 167.

DISCUSSION

VOICE: What do you mean by stable stationary solutions?

NACOZY: I mean stability in the sense that if you place a particle on any one of the contour curves (corresponding to a trajectory), any slight deviation from the curve will cause the particle merely to move to another adjacent curve.

VOICE: What do you mean by a quasi-integral?

NACOZY: The integrals that I h , presented are accurate only to first order and hence are often re⁻·rred to as quasi-integrals.

SYSTEM DESIGN IMPACT OF GUIDANCE AND NAVIGATION ANALYSIS FOR A SEPS 1979 ENCKE FLYBY

Philip Hong
Martin Marietta Corporation
Denver, Colorado

This is a report on a study that Martin Marietta did for Rockwell, who in turn was doing a feasibility study for the solar electric propulsion stage (SEPS). The emphasis was on system feasibility, and we tried to merge the guidance and navigation requirements into the total system. The primary emphasis was the 1979 Comet Encke flyby, which at that time was the first proposed SEPS mission. We also looked at some system requirements for other missions.

Many of the system parameters are affected by guidance and navigation requirements. The most important ones are thrust control authority (that is, how much additional control is needed in the thrust subsystem to implement trajectory corrections), thrust performance tolerances, thrust vector control, propulsion time, the additional time required for adjusting the trajectories, fuel requirements, guidance updates, and the types of earth-based navigation and communications needed. Other parameters affected are the onboard navigation subsystem (how good must it be, if it is indeed needed) and the type of trajectory and terminal errors that occur (that is, control and knowledge). Control is the dispersion of the actual about the reference, and knowledge is the dispersion of the estimated about the actual.

The baseline mission for this particular stage was a launch in March 1979 and encounter in November 1980. Figure 1 shows an ecliptic projection of the flyby.

L = LAUNCH POSITION
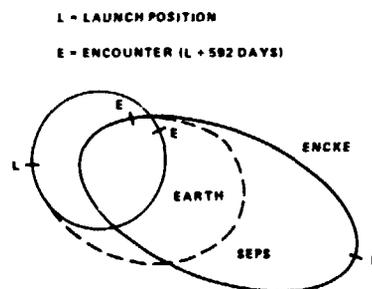
E = ENCOUNTER (L + 592 DAYS)

Figure 1. Ecliptic projection of the 1979 earth-to-Encke flyby.

One of the first things we did was to take the mission analysis results that Rockwell generated and produce a more realistic, optimized and targeted trajectory in which we imposed reasonable control policies. Listed below are the mission data:

- Launch date—March 25, 1979
- Arrival date—November 7, 1980
- Launch VHE—7.18 km/s
- Initial mass—1988 kg
- Initial power—21 kW
- Housekeeping power—0.650 kW
- Thruster efficiency—64 percent
- Propulsion time—523 days
- Coast time—Initial, 64 days; final, 5 days
- Arrival VHP—3.16 km/s
- Arrival RCA—1100 km
- Arrival mass—1456 kg

We employed constant cone, clock, and thrust over fixed time segments, and we imposed whatever constraints were necessary; for example, the final coast time of 5 days was the minimum acceptable for science. There was also an initial coast and a total thrust time of 523 days. We arrived at 3 km/s at 1100 km closest approach. The encounter was 30 days prior to perihelian for this particular study.

The baseline guidance and navigation strategy—and we are talking mostly about the approach phase now—assumed simultaneous or continuous coverage from three Deep Space Network (DSN) stations over the last 40 days. We assumed an onboard optical system similar to Mariner-10. Optical or onboard observations were taken twice per day starting at 30 days prior to encounter, and each optical measurement contained Encke and three identifiable stars. We estimated the vehicle state, thrust biases, and the Encke ephemeris, and we considered the process noise that is generated by the thrusters. Guidance uⱼ 'ates were performed every 4 days, and we assumed that we could control the trajectory just by biasing the nominal thrust controls. The baseline strategy was not intended to meet all the system requirements, but it was our first try at it.

The dynamic and measurement error sources that we assumed are listed below:

- Dynamic error sources
    a. Launch error — Position, 3 km; velocity, 5 m/s; mass, 1 kg
    b. Thrust bias — Magnitude, 2.2 percent; direction, 0.035 rad

c. Thrust noise – Magnitude, 3.5 percent; correlation time, 5 days; direction: 0.010 rad; correlation time, 3 hours

d. Encke – Position, 10,000 km; velocity, 1000 km/day

- Measurement error sources

a. DSN station location – Spin radius, 1.5 m; longitude, 3.0 m; height, 10.0 m

b. Doppler noise – Two-way, 1 mm/s; three-way, 0.1 mm/s

c. Range noise – Two-way, 3 m; three-way, 10 m

d. Optical – Resolution, 30 arc-seconds; center finding, 10 km

SEPS is launched with the Titan-Centaur, so we had typical insertion uncertainties. The thrust uncertainties consisted of both bias and noise. We estimated the bias and the noise, which has a time-varying component, hence the correlation times associated with them were considered. The values listed are for a single thruster; there are eight operating thrusters for this vehicle. The a priori error for Encke was assumed to be very pessimistic, although at that time it was a reasonable uncertainty of 10,000 km and 1000 km per day, or about 10 m/s.

Typical station location uncertainties were assumed. Since we used simultaneous range and range rate data from earth to the spacecraft, we also included three-way uncertainties. Our onboard optical uncertainties consisted of an error or 30 arc-seconds noise and an uncertainty of 10 km to approximate the uncertainty between the comet's center of brightr and the center of gravity.

One of the first things we studied was the approach geometry, to see if we could get an idea of what was happening. Figure 2 is a view of the last 30 days prior to encounter. It can be seen that the thrust vector is almost retrograde, which means that it is on a flat trajectory relative to Encke, and there is very little curvature. There is also the possibility of the thrust plume interfering with any instruments that are sensing as Encke is approached. However, cutoff occurs at 5 days prior to encounter. The position of the earth is changing very rapidly both in direction and in declination, which would indicate that earth-based tracking of the spacecraft would be very good. On the other hand, because of the flatness of the trajectory, the onboard optics probably will not be as good.

Figure 3 is a plot of the inertial position uncertainties due to the estimation of both Encke and SEPS. Because simultaneous data are employed, we get near-ballistic results for the spacecraft. However, our onboard optics just barely get below the a priori level.

Most of this is along-track error. However, a 6000-km along-track error is about 10 minutes uncertainty, and that would seriously affect pointing and slewing rate. Because the stage and Encke are dynamically uncoupled, the Encke relative uncertainty is basically the RSS of these two, which is then dominated by the Encke uncertainties.
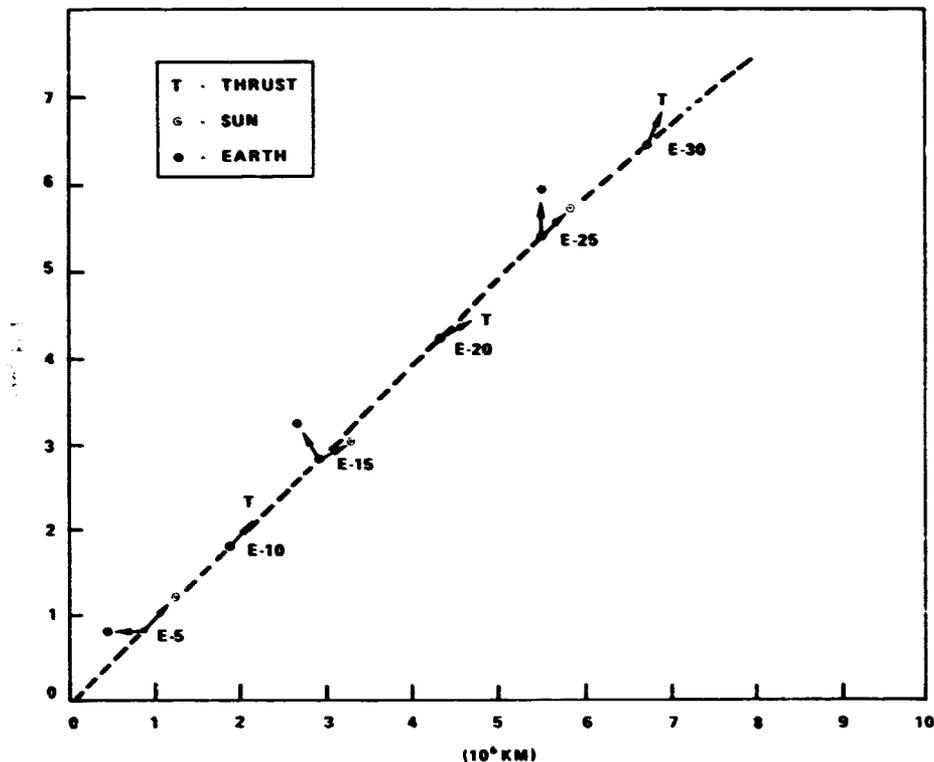
184

Figure 2. Encke flyby relative approach geometry for last 30 days prior to encounter.

As shown in figure 4, the velocity shows only fair improvement. It is still not very good, either that of Encke or of the stage.

Since we found that the Encke relative uncertainties are dominated by the a priori ephemeris error, we looked at a number of different a prioris and found that Encke relative uncertainties are a priori sensitive, primarily in the velocity component (figure 5). For example, we found that, if we have no velocity uncertainty, we will get very good estimation errors. However, if we have any reasonable amount of a priori velocity uncertainty, the optics cannot compensate, which means that the comet's relative uncertainty remains unchanged.

We did take some covariances from Bob Farquhar and used them as our a priori. They looked more like our zero velocity case, although not quite as good, or about 400 km terminal uncertainty.

Figure 6 illustrates the magnitude of the thrust guidance corrections, that is, biases to the nominal thrust control policy. The biases never exceed more than 3 percent in thrust magnitude and are irregularly shaped because of our strategy. The curve could have been smoothed out by placing the guidance updates at different intervals and by employing a different control policy. But in magnitude, the bias is not more than 3 percent, and in pointing, it is less than 2°, 1σ.
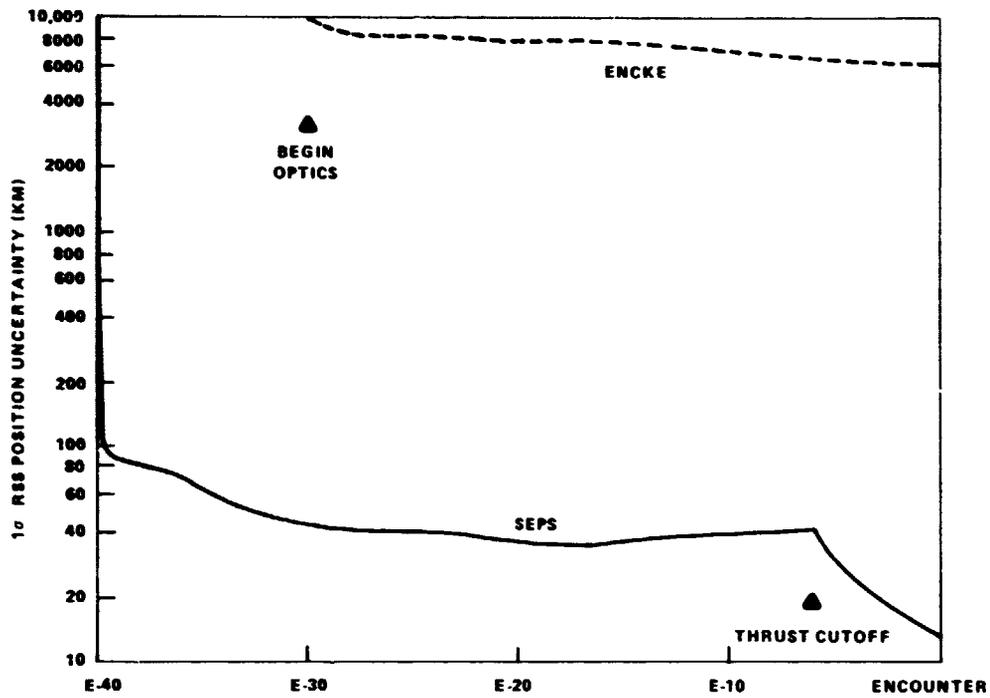
185

Figure 3. Encke flyby approach phase baseline position uncertainties.
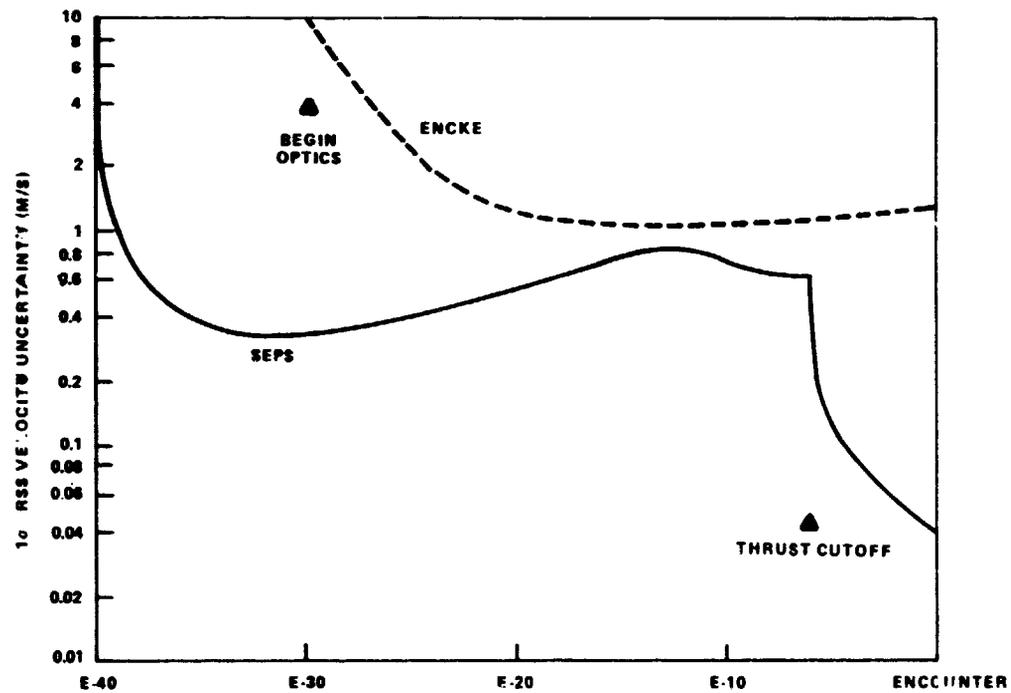

Figure 4. Encke flyby approach phase baseline velocity uncertainties.
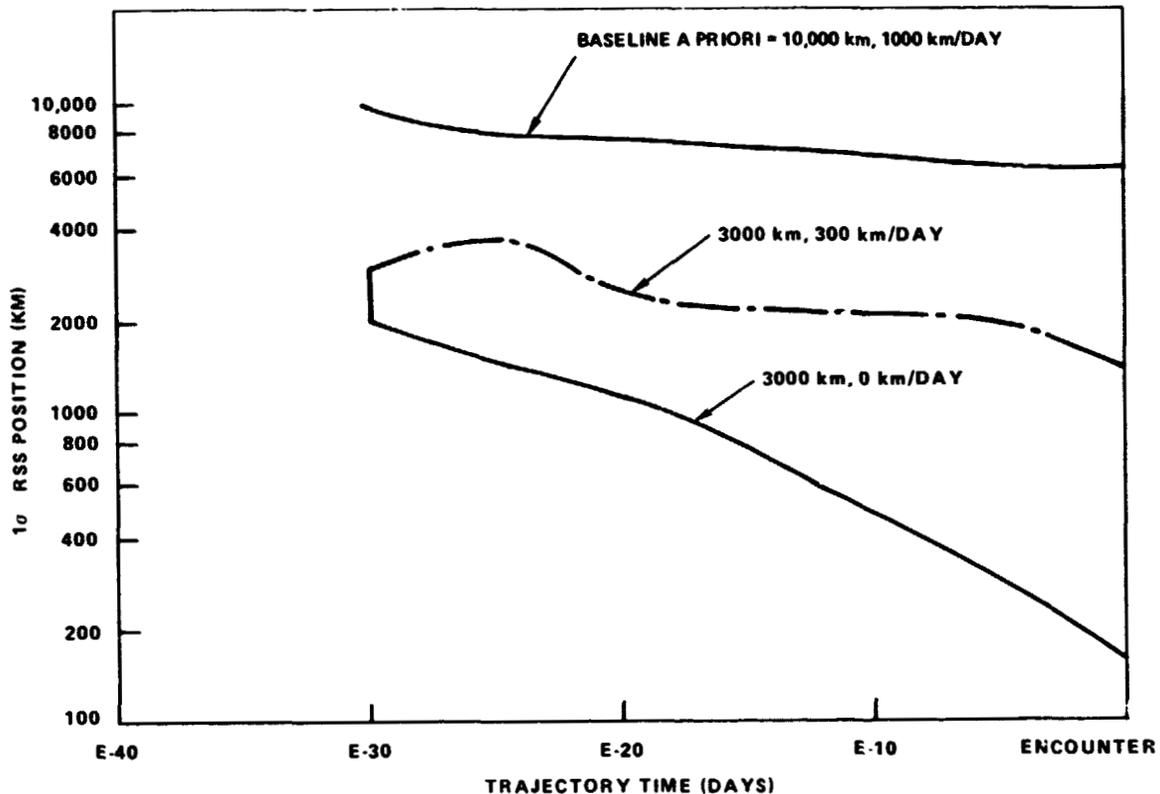
Figure 5. Encke ephemeris uncertainty.

Figure 7 illustrates the terminal control error; that is, the error obtained after all the orbit determination and guidance have been employed. The shaded area is the inertial spacecraft uncertainty, and the total bar is the Encke relative uncertainty. We chose 1000 km as a guidance success zone, which is our maximum acceptable error for a successful mission. Obviously our baseline missed that by quite a bit. If we look at the effect of a priori ephemeris uncertainties, we could get within the success zone if we have zero velocity uncertainty in Encke. However, that is not a realistic case. If we assume some currently reasonable error, we will probably just barely make the guidance success zone. Because of the dominance of the ephemeris uncertainty, even if we eliminated earth-based ranging of the stage, the Encke relative uncertainty would not be affected, but the stage uncertainty would be. If we ever do reduce the ephemeris error down to some low level, we will still need earth-based ranging, and the same thing goes for simultaneous range and range rate data from the earth.

The conclusions for this particular study are as follows: Cruise guidance and navigation requirements (not discussed) were minimal compared to the approach phase. The Encke relative approach error was dominated by the ephemeris uncertainties, particularly the

187

Figure 6. Encke flyby thrust guidance corrections.

Figure 7. Encke encounter uncertainties (1σ).

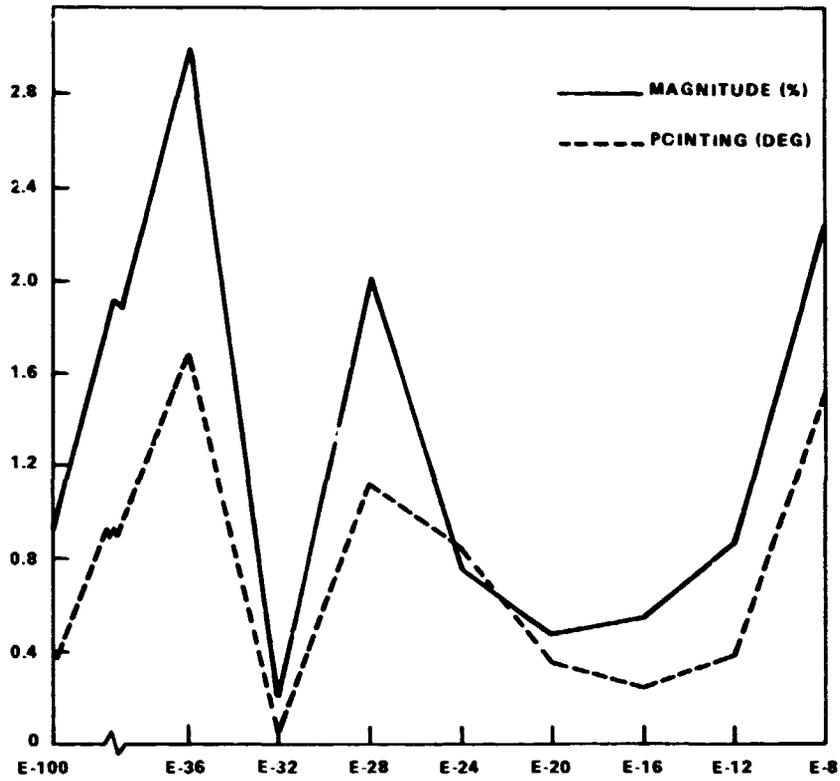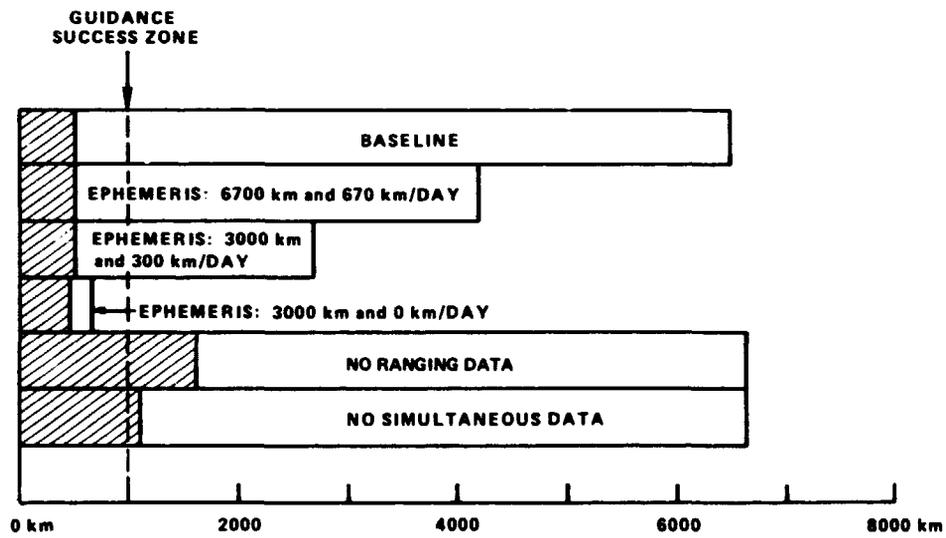velocity components. The earth-based tracking was very good; however, quality three-way data are still needed from the DSN stations. Optical navigation was only fair, due primarily to the flat trajectory. Finally, the thrust control authority, that is, the thrust updates, were within acceptable tolerances.

Table 1 lists some other missions which might drive the design of this stage, which is supposed to be a multimission spacecraft, and we identified a few missions which might drive the guidance and navigation subsystem design. One was the Encke flyby, because that was the first proposed SEPS mission. The next was an earth-orbital mission, because of its unique characteristics. The Encke rendezvous was chosen primarily because it might place great demands on an onboard sensor and also because it was the second interplanetary mission. The Mercury orbiter was chosen because it had a high thrust acceleration at approach, which meant that the process noise in the thrust would dominate this particular mission. Finally, we chose an outer planet mission, or an outbound mission, in this case a Phobos/Deimos rendezvous. The data in the table are just guesses as to what the impact might be on these subsystems.

Table 1
Mission/Subsystem Impact*

Mission	Launch	Flight Time (days)	Approach Guidance	Thrust	Thrust Vector and Attitude Control	Earth-based Tracking	Operations and Communications	Science
Encke Flyby	1979	630	M	L	L	M	L	H
Earth Orbital	1980	50-100†	H	H	H	H	H	–
Encke Rendezvous	1981	1100	H	H	M	M	M	H
Mercury Orbiter	1984	400	–	H	H	H	M	M
Phobos/Deimos Rendezvous	1984	260	H	M	M	M	H	H

*(L = low, M = moderate, H = high).

†Per one-way trip.

If we dismiss ephemeris uncertainties for the time being, the limiting factor is the thrust uncertainty; that is, the noise or uncertainty in the performance of the engines. Figure 8 shows the closest approach uncertainty. The Encke flyby is relatively insensitive to thrust magnitude uncertainties, primarily because of the good tracking from the earth, which can minimize the effect of the thrust uncertainties. The Encke rendezvous in 1981, which is a 1984 encounter, does not do as well, because the earth geometry relative to the spacecraft and Encke is not as good. The Mercury orbiter, because of the high acceleration at approach, is very sensitive to thrust error. Of course, this means that if we have a 1000-km guidance success zone, we had better reduce the thrust errors considerably for the Mercury orbiter.
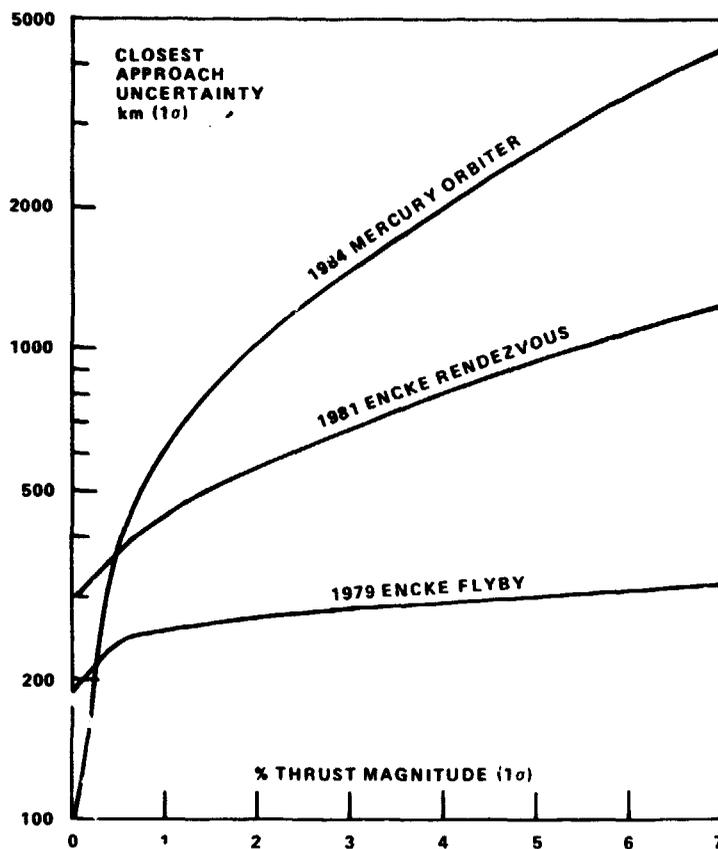
Figure 8. Sensitivity of encounter error to thrust error.

The following recommendations were made and will probably be conducted in a follow-on study:

- Improve the small body, both comet and astroid, ephemeris determination. Part of this involves integrating the earth-based telescope observations of Encke with the DSN and onboard optics measurements.

- Reduce thrust noise level, either through hardware changes or through better orbit determination and measurement.

- Continue development of the simultaneous and/or differenced data types, that is, the quality earth-based three-way data.

- Investigate the impact of other missions and combine their requirements into a common spacecraft.

- Study alternate mission strategies. For example, since we do have thrust at the end, we might shape the trajectory and possibly get some curvature to minimize the along-track error.

190

GROUND TRUTH APPLICATIONS TO ORBIT REFINEMENTS

Robert L. White
The Charles Stark Draper Laboratory
Cambridge, Massachusetts

During the past few years, the C. S. Draper Laboratory has been performing various studies for Goddard Space Flight Center pertaining to the determination and use of spacecraft attitude and orbital ephemeris data to improve the mapping accuracy of an earth-observing multispectral scanner. These studies were conducted for an Earth Observation Satellite (EOS) that is assumed to be in a circular, sun-synchronous orbit with an altitude of 1000 km.

At present, an investigation is being made into the use of known ground targets (that is, landmarks) in the earth sensor imagery, and also stars in combination with known ground targets, to estimate the spacecraft attitude, orbital ephemeris, and the bias drifts of three strapdown gyros. The present study is a covariance analysis where both the Kalman filter and Fraser two-filter smoother are used to process star and landmark measurements to obtain a statistical indication of performance. Star measurements are used to update attitude and gyro bias drift (that is, 6 parameters), and landmark measurements are used to update all 12 state parameters. This study is, for the time, restricted to the use of landmarks in the continental United States, Alaska, and Hawaii, since the primary interest in spacecraft attitude and orbital ephemeris is assumed to be during the observation passes over these regions.

The geometry of a typical pass over the United States is shown in figure 1. The spacecraft maintains a local vertical orientation as shown in the figure, where the body axis, Z_B, is always directed toward the subsatellite point. The star tracker is assumed to be a body-fixed instrument whose optical axis is directed toward zenith. As the spacecraft circles the earth, the stars pass through the 8° square field-of-view (FOV) and are electronically tracked. For the purposes of this study, these stars are artificially generated with random positions in the FOV at the times of measurement. These measurements are uniformly distributed throughout the orbit and only one measurement is made on each star as it passes through the FOV.

On board the spacecraft, there is assumed to be a multispectral scanner whose beam is directed downward and sweeps back and forth across the ground track to generate a swath of imagery 145 km (90 miles) wide (see figure 1). In the present study, a landmark measurement represents the line-of-sight (LOS) of the scan beam at the time of landmark observation. This LOS is completely defined in body coordinates by the scan beam angle for which a random value (within ±4.8°) is selected for each landmark measurement.

Figure 1. Geometry of typical observation pass.

Table 1 defines the five different landmark observation cases used in this study. The case numbers denote the number of orbital passes made over the regions of interest. A pictorial representation of case 4 is shown in figure 2, where the plus signs (+) indicate the nominal locations of the landmarks used for update purposes.

The nominal conditions used to generate most of the performance results are listed below:

- Orbit — Sun-synchronous circular orbit with an altitude of 1000 km

- Gravity model — Central force field

- Spacecraft attitude history — Local vertical with rotation only in pitch

- Star measurements — Error: 5 s (1σ)/axis; number: 20 per orbit (evenly distributed)

- Landmark measurements — Position error: 15 m (1σ) in downrange and crosstrack; number: two/pass

- Gyro error — Random drift rate (1σ) = 0.01°/hr (white noise; quantization (1σ) = 0.1 s

It can be seen that relatively simple models were adopted for the spacecraft attitude history and the gravitational model, since it was felt that these would be sufficient for the purposes of this investigation. Previous studies of attitude determination have shown that the performance results for a nominal attitude history are in fairly close agreement with those for an
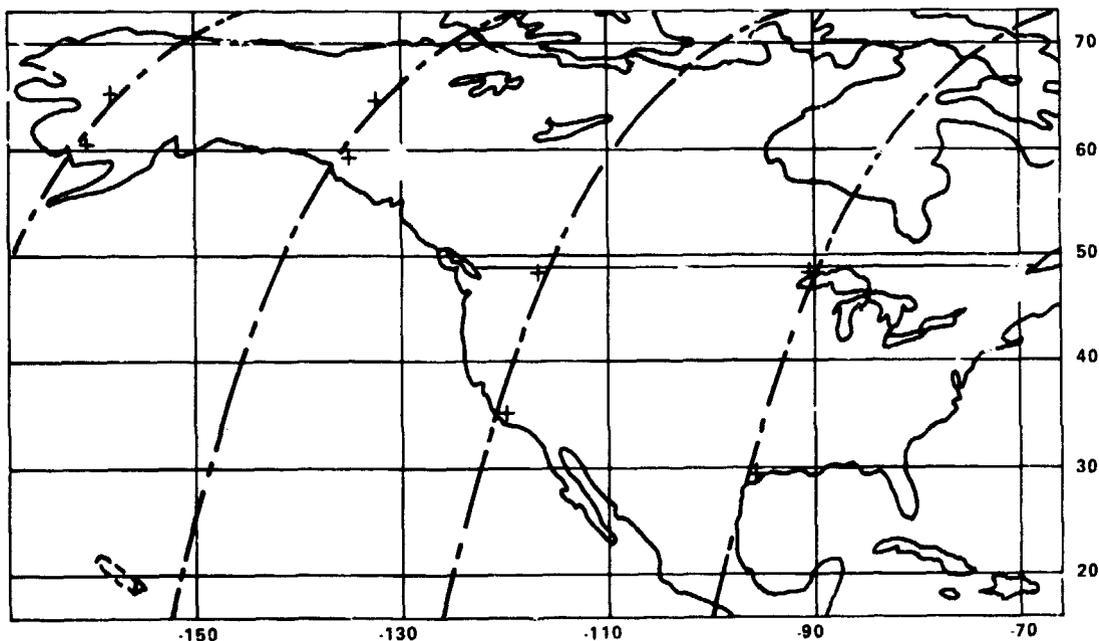
Figure 2. Landmark observation case 4

193

Table 1
Landmark Observation Cases

Case Number	Pass Number	North Latitude (deg)		Region*
		At Start	At End	
1	1	50	30	USA
2	1	50	30	USA
	2	50	30	USA
3	1	50	45	USA
	2	50	30	USA
	3	50	45	USA
4	1	50	30	USA
	2	50	30	USA
	3	65	60	Alaska
	4	65	60	Alaska
5	1	50	45	USA
	2	50	30	USA
	3	50	45	USA
	4	65	60	Alaska
	and at		20	Hawaii
	5	65	60	Alaska

*USA denotes continental USA.

attitude history that deviates from nominal by the amount anticipated in EOS. Deviations in attitude due to the various disturbing torques can be accurately indicated by the spacecraft gyros. A central force field was used for the gravity model. It was felt that the inclusion of J_2 and the higher gravitational harmo~ ~ ~vould add undue complexity to the problem without shedding any additional light on the merits of using star and landmark measurements. With the possible exception of J_2, the inclusion of the ~~ harm~ nics does not produce a significant change in the geometry of the bas~ ~ ~ ~ the period of

interest (a few orbits). Consequently, if the higher harmonics were included in the simulation and were accurately accounted for in the propagation of ephemeris data (that is, no harmonic uncertainties), it is felt that the performance would be somewhat the same. With regard to the existence of uncertainties in these harmonics, it is felt that this is a problem which all techniques must face.

The nominal landmark measurement error adopted for this study was 15 meters (1σ) in downrange and crosstrack. This value does not represent the most recent estimate of what is anticipated for the proposed EOS; it merely represents the anticipated uncertainty in establishing the location of a ground control point (landmark) on the earth by other means (for example, surveying). In a more realistic situation, we would also include the error in determining the scan beam angle at the time of observation and also the errors associated with image resolution and the method used to identify landmarks in the imagery. Since most of these other sources of error had not been firmly established for EOS at the beginning of this study, they were not considered when adopting the present nominal value. This was felt to be an acceptable approach, since the plan was to generate sufficient sensitivity data to show the effect of using different values of the important error sources and parameters.

The nominal values used for the initial state uncertainties are as follows:

- Attitude (pitch, roll, yaw) — 60 arc-s (each)

- Gyro bias drift — $0.03°$/hr (each)

- Ephemeris position

  a. Altitude — 20 m

  b. Downrange — 50 m

  c. Crosstrack — 20 m

- Ephemeris velocity

  a. Altitude — 0.05 m/s

  b. Downrange — 0.02 m/s

  c. Crosstrack — 0.02 m/s

In figures 3 and 4, the performance in estimating spacecraft position is shown for both the Kalman filter and the Fraser two-filter smoother. The results are for landmark observation case 4. This case, like all others, was initiated at the ascending node of the orbit and completed one pass over the north polar region before making the first pass over the United States. It is seen that the Kalman filter does an effective job in reducing the position uncertainties after two passes over the continental United States, and with only two landmark updates per pass. The significant improvement in filter performance after two passes is primarily due to the large reduction in the velocity uncertainties on the second pass. Both
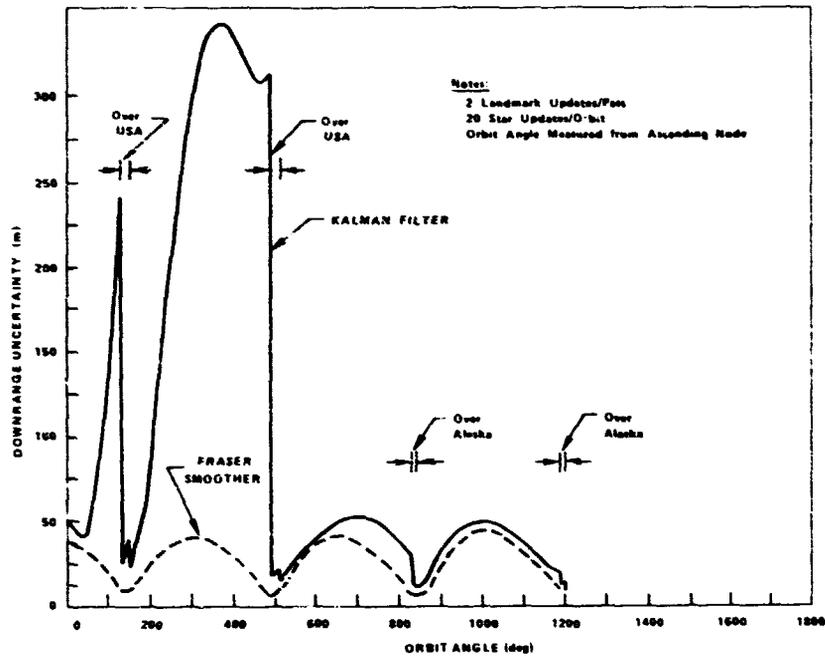
195

Figure 3. Kalman filter and Fraser smoother downrange estimation uncertainties for landmark observation case 4.
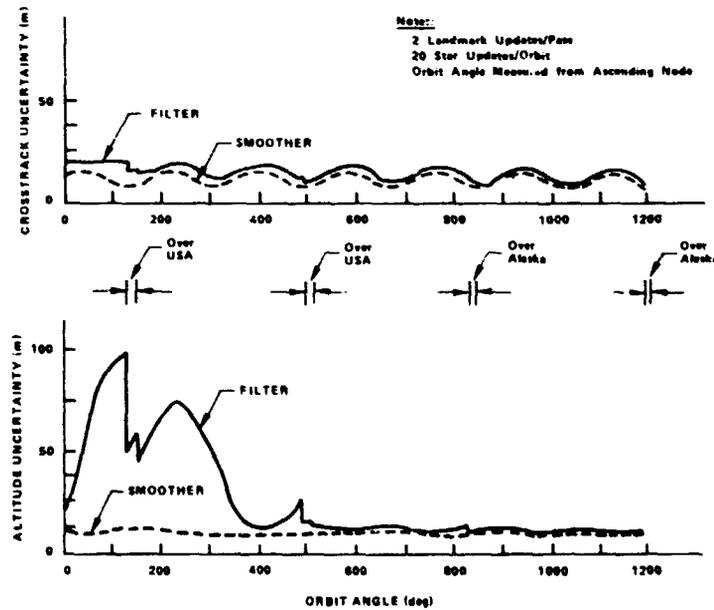

Figure 4. Kalman filter and Fraser smoother estimation uncertainties for crosstrack and altitude for landmark observation case 4.

figures 3 and 4 show that the smoother does a much better job than the filter for those portions of the orbit away from the United States. It should be noted that each smoother curve exhibits somewhat the same minimum during each pass over a landmark update region, while those for the filter are reduced from pass to pass. It is also noted that the filter performance eventually approaches that of the smoother, and it is for this reason that the filter was used in place of the more complicated smoother to generate most of the performance results of this study.

In table 2, the performance in estimating all 12 state parameters is shown for both the filter and the smoother. The filter data represents the uncertainties at the end of the last pass, while that for the smoother is for a time at the end of the first or second pass. Note that the attitude performance is very good. This is primarily due to star updates. The reason that the yaw performance is not as good as that for pitch and roll is due to the fact that very little yaw information is obtained directly from the star tracker because the stars are close to zenith.

Table 3 illustrates the performance when either landmark or star updates are not used. The first set of data is a repeat of the nominal performance of table 2 (using star and landmark updates) and is shown here for purposes of comparison with the other two data sets. The second set of data represents the performance when only landmark updates are used. It is seen that the uncertainties in pitch and downrange position (designated "range" in the table) continue to grow as one goes from landmark observation case 1 to case 5. This clearly indicates a lack of observability in this approach. It is also interesting to note that the downrange uncertainty in meters is numerically about five times larger than the pitch uncertainty in arc-seconds. Since 1 arc-s subtends about 5 m at a distance of 1000 km, the results indicate that the filter, after overcoming the initial state uncertainties, ends up applying the same equivalent update to both pitch and downrange position. The landmark measurements provide very little information to distinguish between the two state parameters. Consequently, the existing uncertainties in gyro bias drift and spacecraft velocity cause the pitch and downrange position uncertainties to grow with time. It should be noted that the same numerical relationship (5 to 1) occurs between roll and crosstrack; however, the uncertainties in these parameters do not grow with time since they are bounded by nature. On the basis of the pitch and downrange performance, it would therefore seem that there is no useful purpose to be gained in using only landmarks. However, it has been found that very strong negative correlations do occur between the errors in pitch and downrange position and also between the errors in roll and crosstrack position. These correlations are such as to greatly nullify the effects of these errors on a mapping process that makes use of attitude and ephemeris data updated with only landmark measurements.

The third set of data in table 3 shows the performance when only star updates are used. These data were generated as a matter of interest, since star measurements can only be used to update attitude and gyro bias drift. It is seen that the attitude performance is almost as good as that of the first set. The uncertainties shown for the spacecraft position components represent the natural growth of these quantities, and it is seen that the downrange position uncertainty grows more rapidly than that in the second data set.

Table 2
Kalman Filter and Fraser Smoother Estimation Uncertainties
for Different Landmark Observation Cases

Landmark Observation Case	Filter (F) or Smoother (S)	State Estimation Uncertainties (1σ)											
		Attitude (arc-s)			Gyro Bias Drift ($10^{-\cdot}{}^\circ$/hr)			Position (m)			Velocity (m/s)		
		Pitch	Roll	Yaw	X	Y	Z	Alt.	Range	Track	Alt.	Range	Track
Initial State Uncertainties (All Runs):		60	60	60	30	30	30	20	50	20	0.05	0.02	0.02
1	F	3.1	3.1	20	20	2.1	4.0	41	21	14	0.05	0.03	0.02
	S	2.5	2.3	20	20	2.1	4.0	30	18	14	0.04	0.02	0.02
2	F	1.9	1.6	14	14	0.4	1.0	14	15	10	0.02	0.01	0.02
	S	1.2	1.5	14	14	0.4	1.0	14	13	10	0.01	0.01	0.02
3	F	1.5	1.4	12	12	0.2	0.7	14	12	8	0.02	0.01	0.02
	S	0.8	1.3	12	12	0.2	0.7	14	8	8	0.01	0.01	0.02
4	F	1.3	1.3	9.8	9.8	0.1	0.6	12	11	7	0.02	0.01	0.02
	S	0.8	1.1	9.7	9.8	0.1	0.6	12	7	7	0.01	0.01	0.02
5	F	1.2	1.3	8.7	8.7	0.1	0.5	9	10	7	0.01	0.01	0.01
	S	0.8	1.1	8.7	8.7	0.1	0.5	9	7	6	0.01	0.01	0.01

Note: Smoothed data are for the time at the end of the second pass over the United States except for cases 1 and 2 where data are for the time at the end of the first pass. Filter data are for the time at the end of the last pass.

Table 3
Kalman Filter Performance for Cases With and Without Landmark or Star Updates

Landmark Observation Case	STATE ESTIMATION UNCERTAINTIES (1σ)*					
	Attitude (arc-s)			Position (m)		
	Pitch	Roll	Yaw	Alt.	Range	Track
Initial Uncertainties Are:	60	60	60	20	50	20
Nominal Performance with 2 Landmark Updates per Pass and 20 Star Updates per Orbit						
1	3	3	20	41	21	14
2	2	2	14	14	15	10
3	2	1	12	14	12	8
4	1	1	10	12	11	7
5	1	1	9	9	10	7
Performance with 2 Landmark Updates per Pass and No Star Updates						
1	44	5	32	66	213	20
2	90	5	27	54	441	20
3	161	4	22	50	782	20
4	229	4	19	38	1111	20
5	277	4	17	29	1342	20
Performance with No Landmark Updates and 20 Star Updates per Orbit						
1	3	4	24	101	291	20
2	2	2	15	101	747	20
3	2	2	12	101	1226	20
4	1	1	11	99	1712	20
5	1	1	10	99	2243	20

*Gyro bias drift and spacecraft velocity uncertainties are not shown.

Table 4 shows the sensitivity of performance to variation in the number of landmark updates per pass and the number of star updates per orbit for landmark observation case 2. It is seen that fairly good performance is obtained even with one landmark update per pass and that there is no significant improvement when going from two (nominal) to five landmark updates per pass. It is also seen in the second set of data of table 4 that some variation can be allowed in the number of star updates per orbit without seriously affecting the results.

Table 5 gives the sensitivity of performance to variation in the star and landmark measurement errors for landmark observation case 2. These data give some indication of the measurement accuracies needed in order to obtain a desired level of performance. More recent results (not shown) have been generated to show the effect of larger variations in these measurement errors.

Table 4
Sensitivity to Number of Landmark Updates Per Pass and Number of Star Updates
Per Orbit for Landmark Observation Case 2

Updates Per Pass or Orbit	State Estimation Uncertainties (1σ)*					
	Attitude (arc-s)			Position (m)		
	Pitch	Rcll	Yaw	Alt.	Range	Track
Initial Uncertainties Are:	60	60	60	20	50	20
Landmarks**						
1	1.9	1.6	15	16	18	11
2 (Nom.)	1.9	1.6	14	14	15	10
3	1.9	1.6	14	13	13	9
5	1.9	1.6	12	13	12	9
Stars**						
5	3.3	2.5	19	13.4	21	13
10	2.5	2.1	18	13.4	17	11
15	2.1	1.8	16	13.4	16	10
20 (Nom.)	1.9	1.6	14	13.4	15	10
25	1.7	1.5	12	13.4	14	10

*Gyro bias drift and spacecraft velocity uncertainties are not shown.

**Other type measurement (star or landmark) was nominal.

Table 5
Sensitivity to Star and Landmark Measurement Error for Landmark Observation Case 2

Measurement Error (1σ) (Per Axis)	State Estimation Uncertainties (1σ)*					
	Attitude (arc-s)			Position (m)		
	Pitch	Roll	Yaw	Alt.	Range	Track
Initial Uncertainties Are:	60	60	60	20	50	20
Star Measurement Error						
2 s	0.8	0.8	7	13.3	12	8
5 s	1.9	1.6	14	13.5	15	10
10 s	3.6	2.7	18	13.8	21	13
15 s	5.4	3.3	20	14.1	29	16
Landmark Position Error (Downrange and Crosstrack)						
7.5 m	1.9	1.6	12	10	11	8
15 m	1.9	1.6	14	14	15	10
30 m	1.9	1 7	15	16	24	13
45 m	1.9	1.7	15	16	34	16

*Gyro bias drift and spacecraft velocity uncertainties are not shown.

ATTITUDE DETERMINATION USING
DIGITAL EARTH PICTURES

Lawrence P. Gunshol
Computer Sciences Corporation
Silver Spring, Maryland

We at Computer Sciences Corporation have developed a computer program called PICATT, which stands for picture attitude determination. This paper describes the particular satellite to which this technique of attitude determination has been applied, describes the method of solution, and discusses the results that have been attained using the PICATT program.

The satellite to which we have applied the PICATT technique is the Applications Technology Satellite-3 (ATS-3), which has been operational since 1967. The mission characteristics of ATS-3 are as follows: It is in a geosynchronous, circular orbit, with very low eccentricity; currently the inclination is on the order of 5°. It is spin stabilized at approximately 100 rpm. The dominant torque on the spin axis is the solar radiation torque, which varies from 10 to 60 arc-seconds per day, depending upon the time of year.

Observable misalignments have developed between the ATS-3 principal axis of spin and the geometric axis of spin. This phenomenon was originally detected by Westinghouse Corporation, using a graphical technique for processing pictures. When Computer Sciences developed the PICATT program for ATS-3, we also detected the misalignments between the principal axes and the geometric axes. Due to the fact that there are misalignments between the principal and the geometric axes, there is a cross-coupling effect on the spin axis whenever an east-west stationkeeping maneuver is performed. ATS-3 is positioned at 70° west longitude, and east-west stationkeeping maneuvers are performed at approximately 3-month intervals; whenever one is performed, the attitude is perturbed.

The Soumi camera has a variable elevation that covers an approximately 18° field of view. At synchronous altitude, the earth subtends an angle of approximately 17.4°, and ATS-3 is able to view the entire earth when it is oriented properly. The elevation angle range covers 9° above the plane normal to the spin axis to 9° below the plane normal to the spin axis. The resolution of the camera, when it is pointing directly at the local vertical, or nadir, is approximately 3.7 km (2 n.m.). The spectral bandpass is 4720 Å to 6300 Å; hence, it is a visible system. The analog video signals are processed to form an image on a film, and the National Oceanic and Atmospheric Administration (NOAA) produces prints of the earth image. ATS-3 originally had the capability of taking a color photograph and was the first satellite to take a color photograph of the earth from synchronous altitude. Currently, the

capability exists only for taking black-and-white, spin-scan, cloud-cover pictures. It is also possible to record the video signals onto a digital tape; these processed digital tapes are used for our attitude determination efforts.

The attitude control requirement for ATS-3 is to maintain the spin axis attitude to within $1°$ of orbit normal. More precisely, NOAA desires to take pictures of the earth 2.5 hours prior to high noon and 3.5 hours after high noon, for a total elapsed time of 6 hours, or one-quarter of an orbit. NOAA also wants to see $55°$ north latitude and above during this time interval.

As shown in figure 1, we use the standard celestial inertial coordinate frame, where the X_E axis points toward the vernal equinox and Z_E points toward the north celestial pole. Right ascension is measured in the conventional sense, counterclockwise from X_E. Declination is measured positive above the equatorial plane.
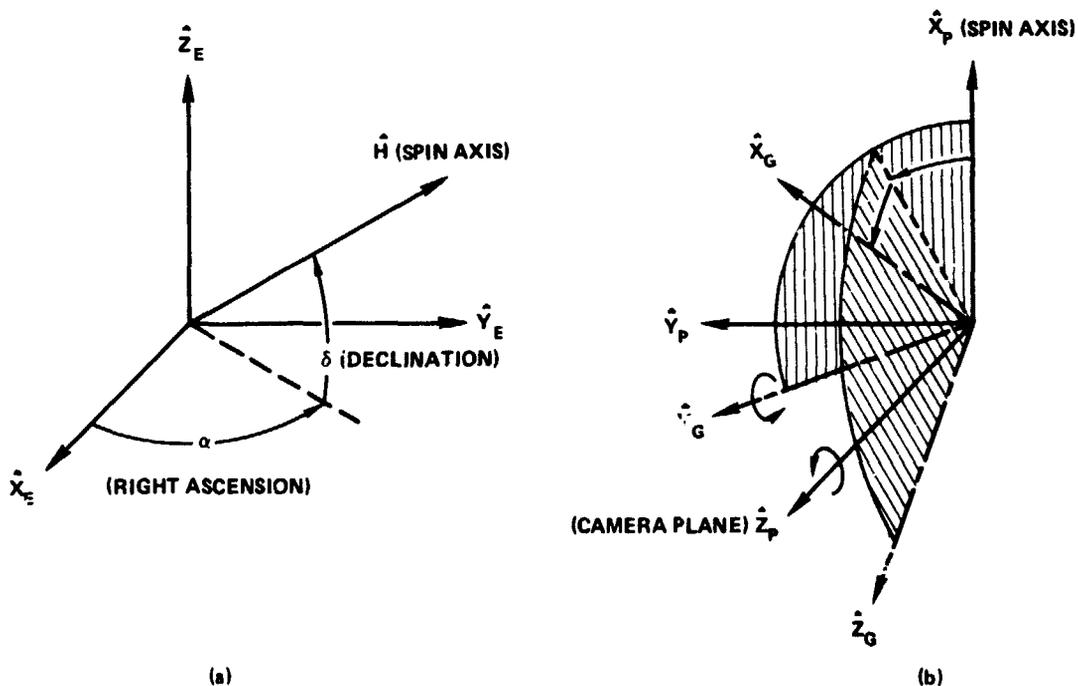

Figure 1. Coordinate systems. (a) Spin axis attitude angles; (b) principal and geometric axes.

As mentioned before, there are misalignments between the ATS-3 principal and geometric axes. These misalignments are described by two rotation angles: A geometric system is defined whereby the X geometric axis points along the symmetric axis of the spacecraft; the Z geometric axis points toward the plane of the camera on board ATS-3. We define the

204

offset between the principal and geometric axes by first rotating around the Z principal axis through the angle ψ (which we call a skew misalignment angle) and then rotating about the Y geometric axis through the angle θ (which we describe as an offset misalignment angle).

As seen in figure 2, the reference pulse for ATS-3 is provided by the sun. Given the orbital and the spin axis characteristics, there is an angle, β, between the sun reference and the local vertical vector. This angle β and the time rate of change, $\dot{\beta}$, are precomputed and stored on the ground in the processing equipment. It should be remembered that the Soumi camera on ATS-3 is constantly on and scans the earth disk and the darkness of space as well. The digital processing occurs on the ground.
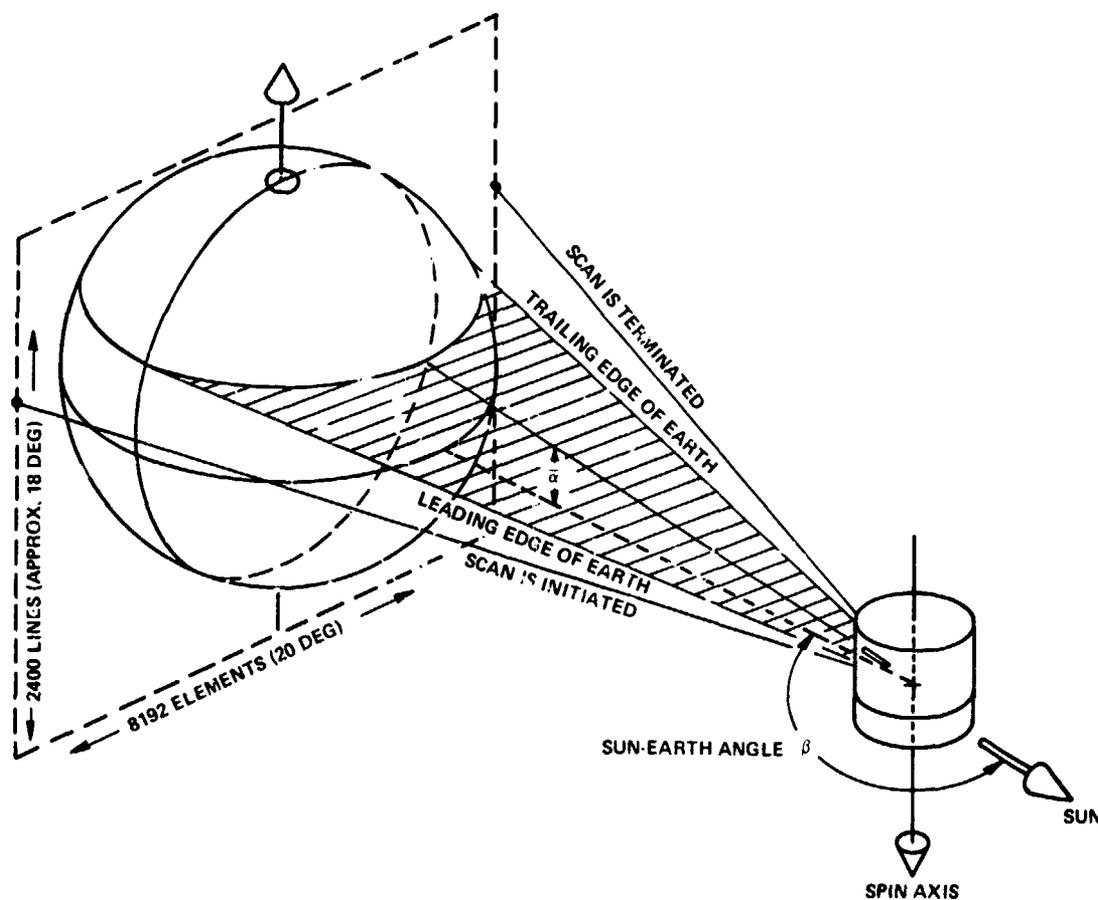

Figure 2. Camera scan geometry

Again referring to figure 2, the camera steps from 9° above the plane normal of the spin axis to 9° below the plane normal to the spin axis. For a typical elevation angle, $\bar{\alpha}$, the

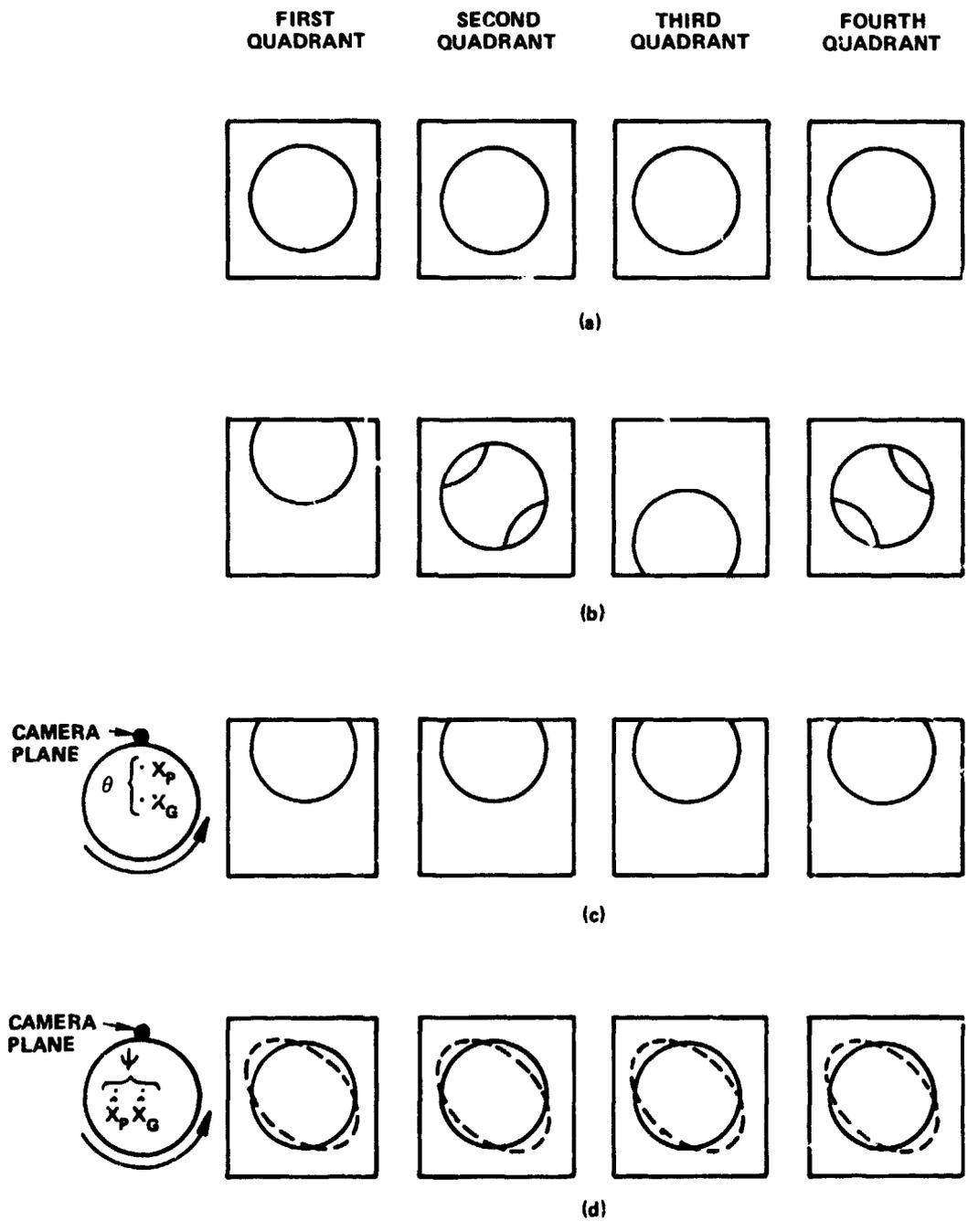| | FIRST QUADRANT | SECOND QUADRANT | THIRD QUADRANT | FOURTH QUADRANT |

(a)

(b)

(c)

(d)

Figure 3. Misalignment effects on pictures. (a) Spin axis at orbit normal and no misalignments; (b) spin axis off orbit normal and no misalignments; (c) spin axis at orbit normal and bias misalignment; (d) spin axis at orbit normal and skew misalignment.

206

ground equipment initiates recording at a point which is a function of the precomputed angle, β, and the angular rate of change, $\dot{\beta}$. During the scan, the leading edge of the earth is observed as well as the entire earth disk. At the point where the trailing edge of the earth is observed, the scan is terminated. The spacecraft then rotates, the camera is stepped to the next discrete elevation angle, and the process is repeated.

The result is a matrix consisting of 2400 scan lines (corresponding to the 18° field of view) and 8192 samples per scan line (the analog signal is sampled 8192 times over the duration of the recording). The recording is synchronized with the spin rate such that a 20° scan is obtained. The matrix is searched by a preprocessor program called EDGE, and EDGE extracts either the leading edge of the earth or the trailing edge of the earth, depending upon which is the most sharply defined. Prior to high noon, we process the right earth edge. After high noon, we process the left earth edge. (Since this is a visible system, only one edge per picture is processed.)

The effects of spin axis orientation and misalignments are illustrated in figure 3 with four limiting cases. Case a depicts a purely circular synchronous orbit with the spin axis at orbit normal and no misalignments present between the principal and the geometric axes. In this particular case, we would see a perfectly centered earth throughout four points in the orbit, each separated by 90°. The effects of terminators are not illustrated in the figure. With a visible system, terminators would be present within these four pictures.

If no misalignments are present but the spin axis is perturbed off orbit normal (case b), the top of the earth would be cropped at one point in the orbit. The bottom of the earth would be cropped one half orbit later. One quarter and three quarters of an orbit later, the earth would be centered perfectly in the picture.

In case c, an orbit-normal attitude is represented, and a bias misalignment, θ, is present. It should be noted that if the total misalignment angle between the geometric axis of spin and the principal axis of spin is a biased misalignment, then the camera plane, the X-principal axis, and the X-geometric axis are all coplanar. With this particular geometry throughout the orbit, a constant cropping of either the north or the south of the earth within the frame would occur.

Finally, with case (d), an orbit normal attitude is represented, and the total misalignment angle is the skew misalignment angle ψ. In this case, there is a stretching of the earth, a distortion, because the angle β is computed by assuming that there are no skew misalignments. If there is a skew misalignment, recording will be sooner than desired at the top of the picture and later than desired at the bottom of the picture.

In general, the spin axis is not at orbit normal, and misalignments are present. The objective is to use the orbital information and then estimate the spin axis attitude angles as well as the misalignment angles ψ and θ.

The basic problem of estimation in PICATT can be outlined as follows:

PICATT Estimation Problem

Constants C

Ω	=	Right ascension of ascending node
$\bar{\omega}$	=	Argument of perigee
M	=	Mean anomaly
i	=	Inclination
$\bar{\alpha}$	=	Camera elevation angle
ϵ	=	Earth optical radius
τ	=	Spin period

State variables X

$\alpha, \delta, \psi, \theta$

Measurement Y

ω	=	Sweep angle from initiation of recording to earth edge

The standard orbital parameters are known constants. The semimajor axis and eccentricity are not included. PICATT actually does account for the complete orbital state in the mathematical model. At synchronous attitude, with a very low eccentricity, there is only second-order effect from those two parameters. We use the argument of perigee and the mean anomaly to describe the intrack position. In addition to intrack position, the inclination is also required to define the orientation of the local vertical relative to the spin axis. The camera elevation angle is also assumed to be exactly known, as is the earth optical radius (the angular width of the earth as viewed from synchronous altitude, approximately 17.4°) and the spin period (needed to convert the 8192 discrete digital counts to a sweep angle). These known parameters—the orbital information, camera elevation angle, earth optical radius, and spin period—are all assumed to be known with zero uncertainty.

A four-parameter state variable array includes the right ascension (α), declination (δ), the skew misalignment angle (ψ), and the bias misalignment angle (θ). The precession of the spacecraft due to solar radiation torque is ignored because picture information is obtained over only a quarter of an orbit. In other words, 6 hours of information, rather than 24 hours, is obtained. Over the computational period in which the pictures are taken, it is assumed that α and δ are inertially fixed.

Finally, the measurement Y is the sweep angle from the initiation of the recording to the detection of either the leading edge or the trailing edge of the earth. This measurement is obtained by converting the edge counts to an angle of sweep, using the spin period, τ.

PICATT uses the weighted least-squares batch filter with memory and requires knowledge of the Bayes matrix, Λ_0^{-1} (the inverse covariance matrix of error and the initial state estimate):

208

$$\hat{x}_{i+1} = (A_i^T W^{-1} A_i + \Lambda_0^{-1})^{-1} [A_i^T W^{-1} y_i + \Lambda_0^{-1} \bar{x}_i]$$

where

$$x_i = X - \hat{X}_i$$

$$\bar{x}_i = X_0 - \hat{X}_i$$

$$y_i = Y - f(\hat{X}_i, C)$$

$$A_i = (\partial f / \partial X)_i$$

W^{-1} = Weighting matrix

Λ_0^{-1} = Bayes matrix

The x_i is the residual between the unknown true state and a current best estimate of the state; $\bar{x}_i$ is the residual between the initial state estimate and the current best estimate of the state; y_i is the residual between the measured sweep angle Y and the predicted sweep angle, which is a function of our current best estimate of state as well as the known constants. The A matrix is the matrix of partial derivatives of the observation equation, and W is the weighting matrix. In PICATT, the data are weighted as a function of the computed standard deviation of the residuals between the measured and observed sweep angles.

How well does PICATT work? Prior to the development of the PICATT program, the operational attitude determination program for ATS-3 was the ATBAY program, which used sun sensor information and polarization angle measurements (POLANG). The problem with ATBAY was the POLANG. Real-time Faraday rotation measurements normally were not available. In addition, the stations tended to have biases that could not be estimated. It was felt that this was no better than a $1°$ accuracy system.

Prior to the development of the PICATT program, we would perform an attitude maneuver on ATS-3 at approximately 2-month intervals. That was a very inefficient procedure as far as performing attitude maneuvers—trying to erect the spin axis to orbit normal and then finding out that the spin axis actually precessed in some other direction. As a result, we were maneuvering approximately every 2 months. With the advent of the PICATT program, the requirements for maneuvering ATS-3 have been reduced to a frequency on the order of one maneuver every 8 months. Because of the increased accuracy of PICATT, the efficiency has been significantly improved as far as the attitude control.

The following is a comparison between the ATBAY program and PICATT, for the time period covering August 1970 to December 1971. During this time, we were not receiving pictures on a weekly basis as we are now, so we did not have a large volume of PICATT solutions. Normally, the ATBAY solutions were computed out of phase. For this statistical study, we selected spin axis attitude estimates at points that are separated by no more than 1 or 2

days between ATBAY and PICATT. With this ground rule, there were 11 samples. The residuals are the differences between ATBAY and PICATT. It is assumed that PICATT is correct. Listed below are the mean (μ) and the standard (δ) deviations for these 11 samples:

	μ	δ
Right ascension	0.512	13.486
Declination	–0.195	0.225
Pointing error	0.496	0.302

The most important characteristic is the pointing error. With this statistic, the mean is almost 0.5° with a standard deviation of 0.3; 8°. The sum of the mean and standard deviation approach the 1° total error in the sun sensor/polarization angle method of attitude solution.

This is a relative comparison: To find out the actual operational results on ATS-3, an intermediate computational program called the latitude scan program is used. This program takes the orbital information, the attitude and bias state estimate (α and δ as well as the misalignment angles ψ and θ), and redicts the latitude that will be : ·ned in the center of the picture as a function of · lay.

The first scale on figure 4 .sents right ascension, which ranges from 0° to 360°. Time of day can be related to righ cension in inertial space, since the earth is moving 360° in one day. Likewise, lo al high n. n as a function of time of year can be correlated as a function of right ascension. The solid line indicates a prediction for observing the maximum north latitude scanned on the pictures as a function of time, using the PICATT state estimate and the orbit parameters. The portion that is fairly flat indicates that the camera is scanning over the top of the earth. The sharply curved portions indicate that the camera is scanning into the earth disk. The triangles represent latitudes which have been read off gridded weather pictures. It should be remembered that not only do we get the digital pictures, but we can also obtain a corresponding print by processing the video signals from the camera.

It is seen that, the farther the spin axis is located from orbit normal, the more the scan cuts into the earth. At the point that the scan starts cutting into the earth, seeing lower and lower, and approaching the 55° north latitude limit, the better observability we have as far as the correctness of the PICATT solution is concerned. From the figure, it is seen that we are predicting very accurately where the cutoff occurs between the point where we scan over the top of the earth and the point where we start cutting into the center of the earth. Normally, we find that right ascension is the most difficult parameter to define; we usually detect a bad solution by finding a horizontal shift in the prediction. We generally get fairly good agreement on the vertical scale or latitude.

It has been indicated previously that cross-coupling of attitude perturbations with the east-west stationkeeping maneuvers occurs. The last stationkeeping maneuver was performed December 5, 1973. Figure 5 presents the ATS-3 state since then. There is a general trend in right ascension and declination with some scatter. There is even more scatter in the total
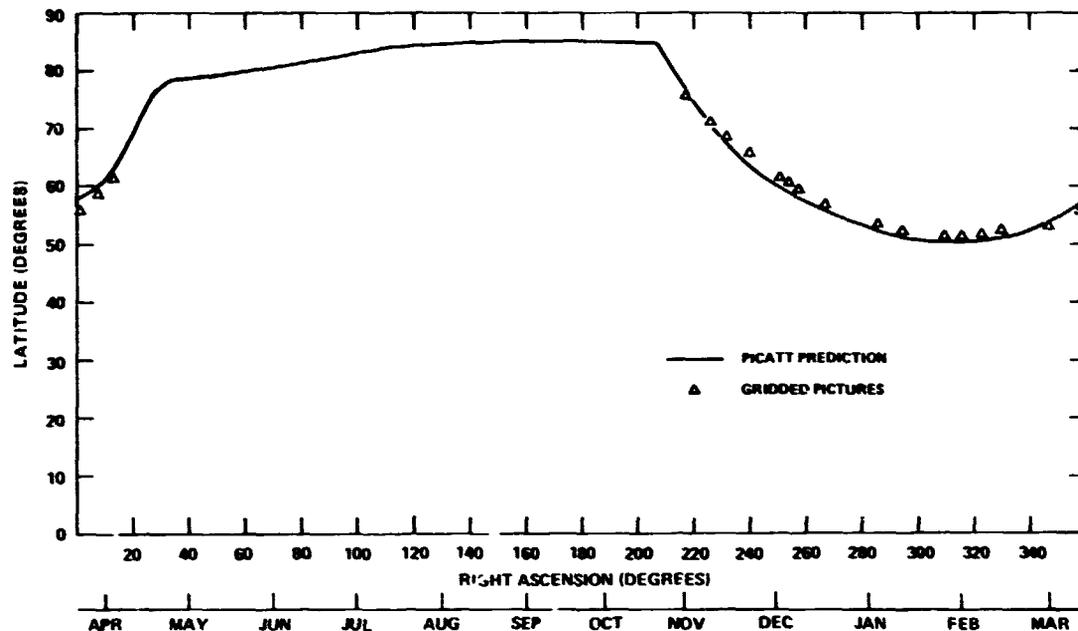
210

Figure 4. Typical latitude scan plot.

misalignment angle, as seen in figure 6 (total misalignment angle being the included angle between the geometric axis of spin and the principal axis of spin). The problem illustrated is traceable to the fact that we get only a quarter orbit of information, and the spin axis is fairly close to orbit normal. Being close to orbit normal, the PICATT program has difficulty relating the bias misalignment angle, θ, to the declination state, δ. There is a trade-off between θ, which is the primary contributor toward the total misalignment angle, and the declination, δ.

We currently are obtaining erratic results, this would improve if we were to have information over a full orbit. Of course, being a visible camera system, we cannot get that information over a full orbit. Included in figure 6 is a statistical study on the misalignment information. We are predicting a mean misalignment of 0.348° with a standard deviation of 0.112° and a total misalignment angle on the order of 0.5°, although earlier in the development of the PICATT program, it appeared that the misalignment angle was on the order of 1°. Every time an east-west stationkeeping maneuver is performed, more fuel is used and the misalignments change.

The PICATT program has been extremely successful, as far as maintaining the attitude on ATS-3 within the given requirements. I think that the program has more capability if it can be used on a satellite that has digital earth pictures over a complete orbit. This is possible with the Synchronous Meteorological Satellite-A (SMS-A), launched May 16, 1974, which has an infrared capability and takes pictures over the complete orbit. We expect SMS to get much more consistent estimates of the misalignment angles as well as the attitude angles, α and δ.
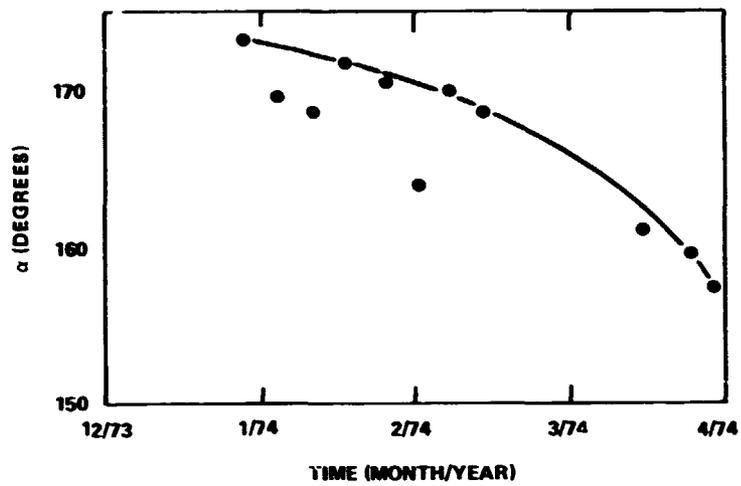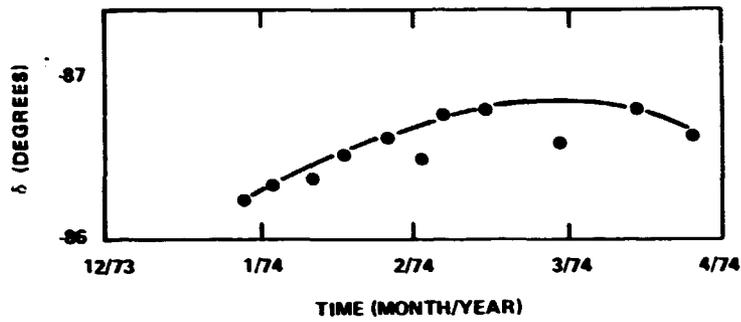
211

Figure 5. ATS-3 attitude time-history following December 5, 1973, stationkeeping maneuver.
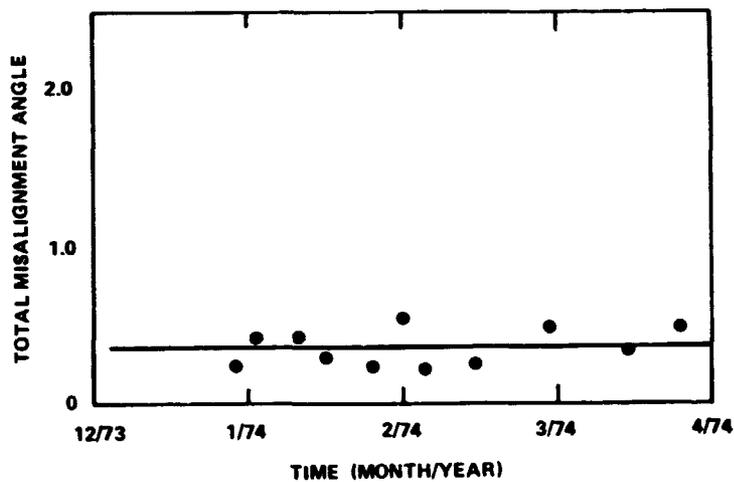

Figure 6. ATS-3 Misalignment time-history following December 5, 1973, stationkeeping maneuver. (Misalignment angle statistics: $\mu = 0.348°$, $\sigma = 0.112°$.)

DETERMINATION OF INTRACK ORBITAL
POSITION FROM EARTH AND SUN
SENSOR DATA

Myron Shear
Computer Sciences Corporation
Silver Spring, Maryland

By intrack orbital error is meant a constant time adjustment, ΔT, that is applied to a set of
ephemeris data which is otherwise correct. The ephemeris data may be in the form of an
orbit tape or in the form of orbital elements with an associated orbit generator. The ΔT is
simply added to the time before the ephemeris routine is accessed. It is implicit here that
ΔT is a constant throughout the pass of data that we are considering, where the pass of data
is typically a fraction of one orbit.

In terms of Keplerian orbital elements, we are applying an adjustment to one of the six orbital elements, and the other five are assumed to be correct. Why would we want to assume
that five of the six orbital elements are correct? Those who are familiar with orbit determination problems understand that there are cases, particularly with a predicted orbit, where the
predominant source of error will be an intrack error. We have seen numerical examples from
real, predicted orbit tapes compared with later definitive and more accurate orbit tapes, which
show that as much as 99.9 percent of the orbit error in a predicted tape can be removed,
simply by applying a constant time adjustment throughout an orbit. Table 1 shows an example of intrack orbit error for the Small Scientific Satellite-A (SSS-A), which has an apogee
height of 26,500 km, a perigee height of 220 km, and a period of 7 hours and 20 minutes.
The error in the predicted orbit tape is determined by comparison with the definitive tape.
The predicted tape is accessed at a time about 2 weeks beyond the available data used in
the predicted tape.

Table 1
Example of Intrack Orbit Error

	Error in Predicted Tape (km)	Optimum Time Adjustment (s)	Error After Time Adjustment (km)
Near Apogee	123.	59.13	1.83
Near Perigee	586.	59.24	0.50

The primary motivation for determining this intrack adjustment is to improve the accuracy
of our attitude determinations, particularly in cases where we are forced to determine an

213

attitude in near real time within an hour of the time the data are received. In these cases, we have to use a predicted orbit tape; we do not have time to wait for a definitive orbit tape to be generated. Potentially, this technique has the capability of improving orbit determination for other users as well or of attaining the same orbit accuracy that we have now, but using less orbit data. That has not yet been done, but we are working on combining the orbit and attitude problems, that is, processing orbit tracking data with earth and sun sensor data in one system and thereby improving both the orbit accuracy and the attitude accuracy with the available data.

Figure 1 explains these attitude sensors, which have been used on at least four different missions—the Radio Astronomy Explorer-2 (RAE-2), the Interplanetary Monitoring Platform (IMP), the Small Scientific Satellite (S³), and the Atmospheric Explorer (AE)—and which are planned to be used on the Synchronous Meteorological Satellite (SMS) and the Communications Technology Satellite (CTS). What all these missions have in common is an earth sensor telescope of some type, mounted at an angle to the spin axis so that the earth sensor scans a cone; if this cone intersects the earth, then the earth sensor will be triggered. The telescope may be sensitive to either infrared or visible light. In addition, there is a sun sensor on the spacecraft with a slit parallel to the spin axis; when the plane of that slit crosses the sun, the sensor triggers and also measures the angle between the spin axis and the sun direction.

The raw telemetry includes the angle between the spin axis and the sun, (β); the time that the sun sensor slit plane crossed the sun; the times that the earth sensor triggered on and off; and the inertial spin period, as defined by the time between two successive sun sightings.

As shown by figure 2, it is easier to visualize the information if it is considered in terms of the geometric parameters which it defines. It happens that all the information in a single frame of data defines only three angles in space. One of them, of course, is the sun angle, the angle between the spin axis and the sun, because it is measured directly. The other two geometric parameters are the dihedral angles labeled A_{in} and A_{out} in figure 2: A_{in} is the dihedral angle from the plane of the spin axis and the sun to the plane defined by the spin axis and the horizon vector, that is, the vector from the spacecraft to the horizon at the earth-in triggering; A_{out} is the same thing for the earth-out triggering. It is worth noting that these two horizon vectors are unknown quantities. Even if the vector from the spacecraft to the earth is known, the vector from the spacecraft to the horizon crossing points would not be known. The data define two dihedral angles measured with respect to unknown vectors.

We will now examine the resolution of these devices for the missions considered. The data are of course digitized before we receive them, so the value of the least significant bit is a lower limit on the resolution of the sensor. This is not to be confused with the accuracy of the sensor, because there may be systematic errors much larger than the resolution.

For the sun angle, the least significant bit typically has a value ranging from 0.25° to 1°, making the sun sensor a relatively coarse sensor. The earth-in and earth-out measurements are somewhat more sensitive. For these, the resolution depends on the clock rate of the spacecraft in relation to the spin period, and the resolution ranges from 0.01° to 0.7°. We
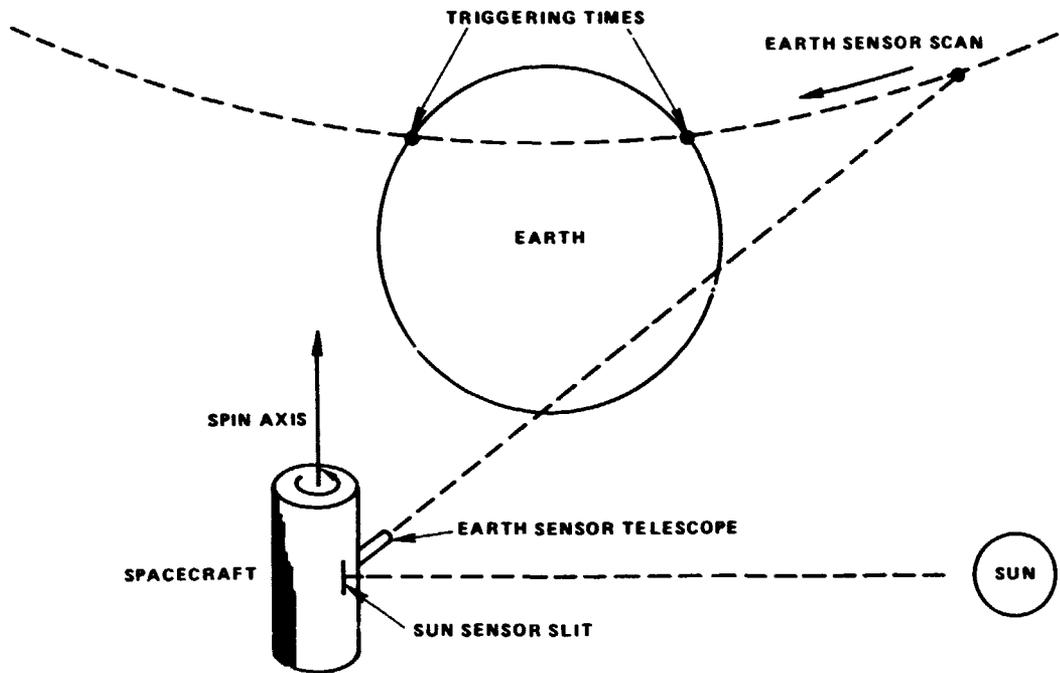
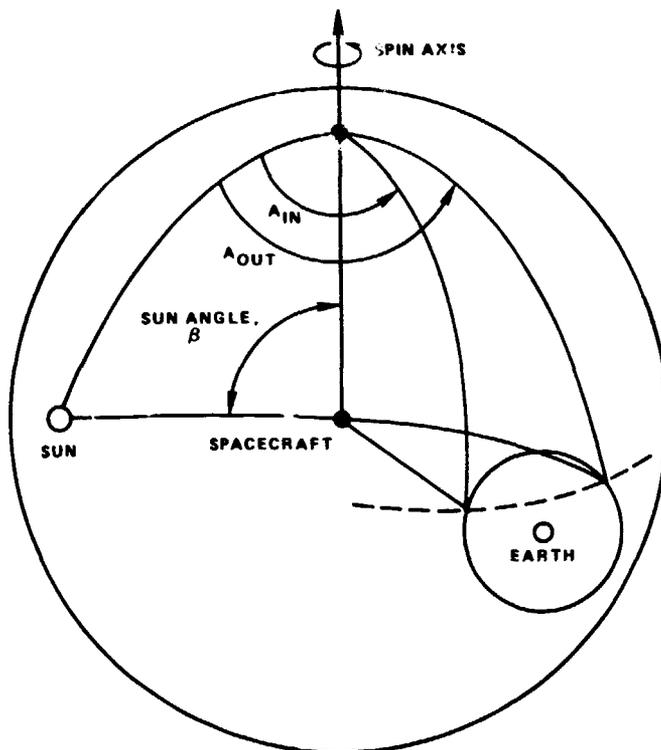Figure 1. Earth and sun sensors.

Figure 2. Geometrical observables from earth and sun sensors.

are mainly interested in missions where the resolution is closer to 0.01° because, in that case, the earth sensor is potentially a rather sensitive device, assuming that we can remove systematic errors, which may be as large as 1° or more, and which will be discussed later.

This is what the data look like in a single frame, and now I want to define the unknowns in this problem. The first is the attitude of the spacecraft, because that is what the sensor was put on board to determine. The attitude can be described by a two-element state vector, right ascension (α) and declination (δ), if we assume that the attitude is constant and there is no nutation. I am assuming throughout this presentation that any nutation in the spacecraft is negligible. Therefore, attitude is a two-element state vector. The second unknown is the intrack time adjustment, Δt, which is the primary topic of this paper. We are assuming that we have a source of orbital ephemeris, which is correct, with the possible exception of this intrack time adjustment.

So these are three primary state parameters: two for attitude and one for time adjustment. In the ideal case, those would be the only three unknowns in the problem, and the problem would be relatively simple. In practice, it has been found that, on all of the missions we have supported, there are significant systematic biases in the sensors that have to be removed when the data are processed in order to meet the attitude requirements of the mission, which may be, for example, ±1° for attitude.

Therefore, some additional parameters must be determined from the data. In general, the unknowns include the elevation of the earth sensor with respect to the spin axis, the azimuth of the earth sensor with respect to the sun sensor, and the elevation of the sun sensor with respect to the spin axis, that is, a bias in the measured sun angle. In addition, there is a possible earth sensor triggering threshold or sensitivity error. These earth sensors do not have a very narrow field of view; the field of view may be as wide as 3° in diameter. If the sensor threshold is not accurately known, there may be an uncertainty of several degrees as to where the sensor is pointing at the time it triggers. Finally, there is the possibility of a constant time delay on either the earth-in or the earth-out triggering due to electronic delay between the time the event occurs and the time it is recorded.

In principle, all of these quantities can be measured on the ground before the spacecraft is launched. In practice, they are subject to change. The alignments, of course, could change due to thermal distortion of the spacecraft. It is even more likely that the apparent alignments with respect to the spin axis would change because the spin axis shifts with respect to the geometric body axis, for example, due to uneven fuel usage between fuel tanks. Also, the electronic parameters can change, for example, if the temperature of the electronic components changes.

To model all these sources of error, it is necessary to introduce five additional angular parameters. These are biases with nominal values of zero. There is a bias on the earth sensor elevation and a bias on the earth-in or the earth-out rotation angle. This includes both the effect of an azimuth offset between the earth and sun sensors and a possible difference between the time delays for the earth-in and the earth-out triggerings. There is also a bias on sun angle and a bias on the apparent angular radius of the earth as seen from the spacecraft.

216

The bias on the angular radius of the earth is intended to correct for the earth sensor triggering threshold. Without discussing the details, it can be shown that, for an earth sensor with a circular field of view, any constant triggering threshold can be exactly compensated for by adding or subtracting a constant bias on the apparent radius of the earth.

Thus, the total number of unknowns includes five angular biases and three primary state parameters, for a total of eight parameters that have to be determined. However, a frame of data includes only three observables: sun angle and earth-in and earth-out angles. Clearly, on the basis of a single frame of data, we could determine, at most, three of these unknowns. To have any hope of determining all eight unknowns, we need more than one frame of data, and the frames have to be independent in some sense. This is where the real problem occurs.

Typically, we do have a large number of frames of data, but the sun angle may be constant throughout the entire block because, as mentioned previously, the sun sensor is a relatively coarse sensor, and the sun angle is changing very slowly. So it is not uncommon for the measured sun angle to be constant throughout the pass, in which case, regardless of the number of frames of data, there is only one actual observable for the sun angle.

The earth-in and earth-out angles are more useful, because they do vary with the spacecraft position. Still, two frames of data taken at nearby positions in the orbit will be redundant. Speaking qualitatively, in order to determine all eight of these parameters, it is clear that we need a significant fraction of an orbit of data in order to have independent observables and not just the three observables that occur in one frame.

We have developed a program called OABIAS, which processes data of the type described and determines a state vector, including the unknowns listed below:

- Attitude (α, δ)
- Earth sensor elevation bias
- Bias on earth-in angle, A_{in}
- Bias on earth-out angle, A_{out}
- Bias on angular radius of earth
- Bias on sun angle, β
- In-track orbit time adjustment, Δt

The program is a standard, weighted least-squares recursive estimator. Any number of the above listed parameters can be fixed at constant values and not determined.

The program works as a standard recursive estimator: the state vector is used to predict the observables, the residual is computed for each observable, and the partial derivatives of each observable with respect to each element in the state are computed. Then the residuals and partial derivatives are used to update the state vector. The partial derivatives can be computed analytically for every case except the case of interest here, the intrack orbital time adjustment.

217

If the partial derivative of any arbitrary observable is considered with respect to the time adjustment, Δt, it is equal to the partial derivative of the observation with respect to the spacecraft position vector, $\vec{R}$, multiplied by the partial derivative of the spacecraft position with respect to Δt:

$$\frac{\partial \text{ (observation)}}{\partial \Delta t} = \frac{\partial \text{ (observation)}}{\partial \vec{R}} \cdot \frac{\partial \vec{R}}{\partial \Delta t}$$

$$= \frac{\partial \text{ (observation)}}{\partial \vec{R}} \cdot \vec{V}$$

The derivative of the spacecraft position with respect to Δt is one that cannot be computed analytically, because we do not have an analytical expression for spacecraft position as a function of time. However, it is not necessary, because we can get the velocity $(\vec{V})$ of the spacecraft from the orbit tape.

In practice then, we analytically compute the derivation of each observation with respect to $\vec{R}$, then multiply that by the velocity vector obtained from an orbit tape. The important point here is that this method is not restricted to any particular type of orbit. We are not assuming, for example, a Keplerian orbit. Any orbit that can be described by an orbit tape can be handled correctly using this technique.

Figure 3 shows some results obtained using simulated data for the Communications Technology Satellite, which is scheduled to be launched next year. The data were simulated for transfer orbit, with a perigee of 190 km and an apogee of 36,000 km. The attitude in this case is pointing 49° below the plane of the orbit; the earth sensor is an IR sensor mounted at 85° from the spin axis. These facts together imply that the earth sensor will scan the earth only during the indicated portions of the orbit. For the rest of the orbit, the earth sensors will miss the earth; there will be no useful data from the earth sensor for those periods.

Both of these sections of the orbit were simulated and the data were combined. The data includes 100 frames evenly spaced over 240 minutes over both of those segments of the orbit—40 minutes near perigee and 200 minutes near apogee. Gaussian noise of 0.012° is applied to the earth rotation angles, the earth-in and earth-out angles. That corresponds to the clock rate expected for the spacecraft.

We were attempting to determine the complete eight-element state vector, so biases of 1° were applied to each of the angular parameters that describe the bias on the sun angle, the earth-in and earth-out azimuth angles, the earth sensor elevation, and the apparent angular radius of the earth. For the time adjustment, an error of 60 seconds was applied to the ephemeris data, which corresponds to a very large, 6° error in spacecraft position at perigee, which would make the perigee data virtually useless for attitude determination without correcting for it. But the time adjustment corresponds to an error of only 0.15° true anomaly at apogee.
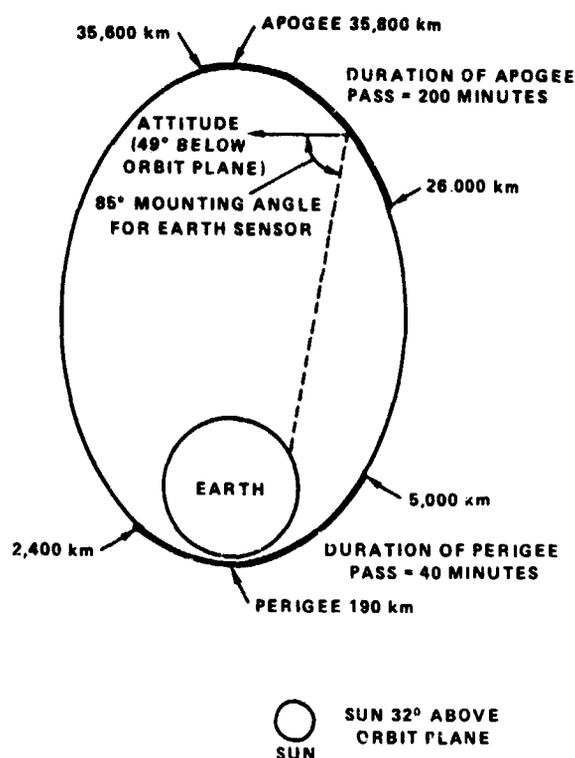
Figure 3. Example of position determination with simulated data for the Communications Technology Satellite.

The results for these simulated data are shown in table 2. The biases are initially estimated at zero, because they are unknown quantities; the initial attitude was obtained from a deterministic processing of the data, before correcting for biases. It can be seen that this initial attitude is more than $2°$ off, which would violate mission constraints for this mission, since we have a $1°$ attitude accuracy requirement. The final result from the program shows that all of the unknowns are determined to an accuracy of $0.05°$, and the intrack time adjustment is determined to an accuracy of one-half second. This indicates that, first of all, the program works. Secondly, it means that the problem is feasible. That is, we really should be able to determine all eight of these state parameters, assuming that we have a sufficient amount of data and that there are no substantial systematic errors that have not been considered in the state vector.

This brings us to the case of the real data. We have processed real data from four spacecraft—IMP, S^3, RAE-2, and AE—but the results cannot be presented in this form because the true state is not known for any of these spacecraft. In fact, since the attitude changes, or is changed, from one day to the next, we do not generally have more than one pass of data to examine to define a given state vector.

Table 2
OABIAS Results*

Parameter	True State	Initial Estimate	Final Result
Attitude $\{ \begin{matrix} \alpha \\ \delta \end{matrix}$	330.00 / -21.75	329.50 / -23.88	330.02 / -21.80
Earth Sensor Elevation Bias	-1.00	0.0	-1.01
Earth-in Azimuth Bias	-1.00	0.0	-0.99
Earth-out Azimuth Bias	-1.00	0.0	-0.96
Bias on Angular Radius of Earth	1.00	0.0	1.01
Sun Angle Bias	-1.00	0.0	-0.99
Intrack Time Adjustment	-60.00	0.0	-59.59

* All values are in degrees, except intrack time adjustment, which is in seconds.

Thus, only three things can be said about the real data: either it can or cannot be fitted. or we can find an infinite number of state vectors which would fit the data equally well to within the noise level. It happens that this third cause is not uncommon for the missions that we examined. The reason is that, when trying to determine an eight-element state vector on a small section of an orbit, it is to be expected that the entire state vector will not be determinable.

However, we have generally found that the results are consistent with what we would expect, based on simulation. That is. where there are enough data to find the state vector, it can be determined uniquely. Where there is not enough information, we can determine any number of state vectors that would fit the data. We have not, as a rule, encountered the other problem, that of not being able to find any state vector that fits the data; this would indicate the presence of some systematic error that we have not modeled.

It should be pointed out that, if the misalignment parameters and biases could be eliminated and the state vector thereby reduced from eight elements to three elements, it would obviously be a simpler problem. It would take much less data to determine the state. In fact, since there are three observables in a single frame of data, and as there would be only three unknowns in that case, the time adjustment and the attitude could be determined, based on just a single frame of data. But, based on our experience, it is not feasible to ignore all of these systematic bias parameters.

DISCUSSION

VOICE: Is this technique being used operationally?

SHEAR· It has been applied operationally to all four spacecraft mentioned; currently, the operational work is concentrated on AE-C. It has improved the attitude determination accuracy for those missions. It is not used to process every pass of data. It is used on the initial passes of data in the mission to try to determine the biases that will be used throughout the mission.

VOICE: Are the simulation results that you've shown for the same static attitude estimator? When you generated data, did you use the model you have in your estimator?

SHEAR: That's right. It's the same model. There are no systematic errors that aren't accounted for.

VOICE: There are no attitude dynamics?

SHEAR: Correct, there are no attitude dynamics.

VOICE: In the case of the real data, the accuracy of your intrack time adjustment could be checked against orbit tracking data, couldn't it?

SHEAR: It is possible to get an independent confirmation of the intrack orbit error. I think our problem has been more often that we can't determine all eight state parameters including the time adjustment; consequently, if the time adjustment does not agree with the orbit data, we don't know whether we've got the right answer for one of those biases or not.

I think that it is feasible to determine the intrack time adjustment on the S^3 spacecraft. The S^3 has an orbit that is fairly similar to the orbit I just showed you for the simulated example. In that case, I think it's feasible, but we haven't processed S^3 data extensively yet.

VOICE: I have worked on some of the problems of bias determination and the biases are usually so highly correlated with what you're trying to measure that they can't be separated. Is your simulation realistic?

SHEAR: Well, there are different geometry cases to be considered. I could point out, for example, a circular orbit. For any circular orbit, we cannot determine this complete eight-element state vector, regardless of the attitude of the spacecraft, the sensor mounting angles, or the amount of data. It can be proven that there is a perfect correlation between the intrack error and the sensor misalignments; we can find an infinite number of state vectors that will fit the data.

Referring back to figure 3, if we were to delete either one of these passes of data, I don't think it would be feasible to do the problem; the complete eight-element state vector could not be determined with either pass alone. Of course, if we could reduce the state vector to fewer elements, it could be done. But we were not able to solve for all eight elements, even on simulated data, with just one of those sections.

VOICE: As a practical problem, can you get track-in data when you're at perigee?

SHEAR: Probably not directly at perigee, for such a low perigee. But it should be possible to get most of these data. The S^3 spacecraft, which has the same orbit except for a slightly lower altitude, frequently obtains a pass of data which covers most of what is indicated here as the perigee pass.

VOICE: For your simulated data, where did the sun lie with respect to the orbit flight?

SHEAR: The sun is shown in figure 3, but I didn't mention it. The sun is $32°$ above the orbit plane, and it's roughly in the direction shown in the figure.